Tailoring on-surface chemistry of (hetero)aromatics on transition metal surfaces

Memoria presentada para optar al grado de Doctor en Ciencias Físicas por

Anna Lisa Pinardi

Dirigida por **Prof. José Ángel Martín Gago**

Tutor **Dr. Alejandro Gutiérrez**

Madrid, Junio 2013

Contents

Abstract

Organic molecules such as Polycyclic Aromatic Hydrocarbons (PAH) have the potential of substituting the silicon-based technology in electronic circuits, and are also widely spread in Organic Light Emitting Diodes (OLED) and in new designs of solar cells. The bottom-up construction of such devices with organic molecules as the building blocks is one of the bases of nanotechnology. The ability of manipulating the electronic properties and the relative position of the molecules with respect to each other is a great challenge for controlling the outcome at the atomic scale to obtain new nanoarchitectures.

On-surface chemical modification of molecules is an excellent approach to obtain a controlled manipulation of the organic functional molecules. In particular, transition metal surfaces are uniquely prone to engineer desired outcomes from the pristine molecules, as some of the resultant structures cannot be achieved otherwise. To this extent, many scientists focused in manipulating precursors in perfect systems such as on single crystal metal surfaces in Ultra High Vacuum (UHV). The employment of such tools has the object to control separately each parameter to achieve a desired outcome.

Depending on the electronic structure of a particular transition metal, the effect that the surface may have on a PAH varies completely. In this thesis we focus on three organic molecules, namely $C_{57}H_{33}N_3$ (a crushed triaza-fullerene), $C_{40}H_{24}N_2$ (an open N-doped nanographene flake) and C_{60} (fullerene) on different metal surfaces. The latter molecule is in general very stable due to its symmetric shape; however, the first two precursors differ from the fullerene, as when deposited on a surface they undergo chemical modification upon thermal activation. The metal surfaces catalyse the cleavage of the C-H bonds, thereby leaving unstable C dangling bonds which combine with either dangling bonds of the same or of another molecule, creating new C-C bonds, or with the surface, forming new bonds between the carbon and the metal. This process is named cyclodehydrogenation if new aromatic rings are generated, and dehydrogenation if no new rings arise from the new bond.

When depositing submonolayer coverage of a PAH on a highly reactive surface such as Pt(111), the molecules stick where they land, and therefore, as the C-H bonds cleave upon annealing, only intramolecular modification is allowed because the molecules are fixed. Due to a bonding with the surface, there is no interaction with other precursors and the molecule cyclodehydrogenates to modify its structure and its electronic properties. $C_{57}H_{33}N_3$ transforms into a triaza-fullerene, while $C_{40}H_{24}N_2$ into a N-doped nanographene.

On the other hand, if the PAHs are deposited on a weakly interacting surface such as Au(111) or on other coinage metals, the molecules are free to move at room temperature as they do not bind with the metal. Upon annealing, they (cyclo)dehydrogenate and link together to form covalent chains: this is possible because the activated molecules can meet each other because surface diffusion allows intermolecular interaction.

Abstract

The intermediate structures formed by $C_{57}H_{33}N_3$ and $C_{40}H_{24}N_2$ on different metals upon annealing have been investigated in details with different surface science experimental and theoretical techniques such as Scanning Tunneling Microscopy (STM), high resolution X-ray Photoelectron Spectroscopy (XPS), Near-Edge X-ray Absorption Fine Structure (NEXAFS) and Density Functional Theory (DFT) calculations. The shape of the precursors has been selected on purpose to obtain triaza-fullerenes and N-doped nanographene, and the employment of hetero-aromatic precursors is an elegant way of introducing dopants on the resultant outcome. Before obtaining triaza-fullerenes, the partial cyclodehydrogenation of $C_{57}H_{33}N_3$ allows to observe open-cage fullerenes. On the other hand, $C_{40}H_{24}N_2$ undergoes a two-steps hierarchical transformation: due to steric reasons, the first C-H bonds to cleave upon annealing are the internal ones, hence forming nanographene; however, further thermal energy injection also causes the edge C-H atoms to cleave, forming N-doped nanodomes. Both precursors transform into N-doped graphene when enough thermal energy is provided.

The third precursor, namely the fullerene, differs from the other two as it is much more stable, since it is highly symmetric and it lacks of C-H bonds. In this thesis, we analyse the effect of the presence of this molecule on the metal, rather than the opposite. C_{60} is well known to induce a single- or a multi-atom vacancy on transition metals, even though the mechanism of the vacancy formation is still under discussion. According to the theoretical calculations, the energy needed for the surface to reconstruct is noticeably lower in the presence of the fullerene. Our experimental observations reveal that the as-deposited fullerenes at room temperature are weakly interacting with the surface, however annealing at 450 K causes a charge transfer from the surface to the molecule. This is a metastable state in which an adatom-vacancy pair is formed, as predicted by DFT calculations. Further annealing at 700 K forces the formation of a single atom vacancy beneath each fullerene.

Resumen

Las moléculas orgánicas, como los hidrocarburos policíclicos aromáticos (PAH), surgen como posibles substitutos de la tecnología basada en silicio en circuitos electrónicos, además de ser muy comunes en los diodos orgánicos de emisión de luz (OLED) y en nuevos diseños de células solares. La construcción 'bottom-up' (de abajo a arriba) de estos aparatos utiliza las moléculas como 'ladrillos', y es una de las bases de la nanotecnología. Lograr la manipulación de las propiedades electrónicas y de las posiciones relativas de las moléculas, es crucial para controlar el resultado a escala atómica para obtener nuevas nanoarquitecturas.

La modificación química de moléculas sobre superficies es una manera excelente de obtener una manipulación controlada de las moléculas. En particular, las superficies de metales de transición son únicas para controlar y obtener el resultado deseado a partir de un precursor. En este sentido, algunos grupos científicos investigan la manipulación de moléculas precursoras sobre sistemas perfectos, como son las superficies de cristales en condiciones de ultra alto vacío (UHV). El uso de estas herramientas tiene el objetivo de controlar cada parámetro por separado para obtener el resultado deseado.

Dependiendo de cómo sea la estructura electrónica del metal de transición elegido, el efecto de su superficie sobre un PAH puede cambiar completamente. En esta tesis, nos focalizamos sobre tres moléculas orgánicas: $C_{57}H_{33}N_3$ (triaza-fullereno abierto), $C_{40}H_{24}N_2$ (nanografeno dopado con N abierto) y C_{60} (fullereno). Este último precursor es muy estable debido a su forma simétrica; sin embargo, los dos primeros precursores difieren del fullereno, ya que cuando son depositados sobre una superficie se modifican químicamente tras una inyección de energía térmica. Las superficies de los metales catalizan la ruptura de enlaces C-H, dejando carbonos cargados que se enlazan con otros carbonos. Si de este proceso nace un nuevo anillo orgánico, esta transformación se llama ciclodeshidrogenación. Si no se crea ningún anillo, se llama simplemente deshidrogenación. Alternativamente, estos C se pueden enlazar con la superficie.

Si evaporamos menos de una monocapa de un PAH sobre una superficie reactiva como el Pt(111), las moléculas no difunden y permanecen donde se depositan. Tras calentar, la ruptura de enlaces C-H causa una modificación intramolecular, ya que las moléculas no se pueden mover y no pueden interaccionar con otras moléculas. Entonces los precursores ciclodeshidrogenan y cambian sus estructuras y sus propiedades electrónicas. $C_{57}H_{33}N_3$ se transforma en un triaza-fullereno, mientras $C_{40}H_{24}N_2$ lo hace en un nanografeno dopado con N.

Por otro lado, si se deposita el PAH sobre una superficie poco reactiva, como puede ser Au(111) o en cobre, las moléculas pueden difundir, ya que la baja interacción lo permite. Tras calentar, los precursores (ciclo)deshidrogenan y se enlazan entre sí, formando cadenas covalentes. Esto es posible porque en la superficie las moléculas activadas se pueden encontrar debido a la difusión de las mismas, teniendo lugar la interacción intermolecular.

En esta tesis, investigamos también en detalle las estructuras intermedias formadas por $C_{57}H_{33}N_3$ y $C_{40}H_{24}N_2$ sobre distintos metales tras calentar. Empleamos varias técnicas experimentales y teóricas de física de superficies, como el microscopio de barrido de efecto túnel (STM), técnicas de espectroscopia con radiación

sincrotrón y cálculos de teoría. La estructura de los precursores se ha seleccionado deliberadamente para obtener triaza-fullerenos y nanografeno dopado con N. Utilizar hetero-aromáticos como precursores es una manera elegante de introducir dopantes en la estructura final. Antes de obtener triaza-fullerenos, la ciclodeshidrogenación parcial de $C_{57}H_{33}N_3$ nos permite observar fullerenos 'open-cage'. Por otro lado, $C_{40}H_{24}N_2$ se puede transformar en dos estructuras distintas, dependiendo de la temperatura. Así pues, debido a razones estéricas, los primeros enlaces C-H que se rompen son los más interiores, formando nanografeno; tras calentar más, los átomos de hidrógeno en los bordes también se separan, y se forman nano-cúpulas. Finalmente, para ambos casos, $C_{57}H_{33}N_3$ y $C_{40}H_{24}N_2$, si sometemos cada sistema a bastante temperatura, los dos precursores se rompen y se transforman en grafeno dopado con N.

El tercer precursor, el fullereno, es muy distinto de los otros dos ya que es mucho más estable debido a su simetría y a la falta de enlaces C-H. En esta tesis analizamos el efecto de la presencia de la molécula sobre el metal. Se conoce que el C_{60} induce una vacante mono- o multi-atómica sobre la superficie de metales de transición; sin embargo, el mecanismo de la formación de la vacante es aún desconocido. Los cálculos teóricos indican que la energía necesaria para la reconstrucción de la superficie baja notablemente en presencia del fullereno. Our experimental observations reveal that the as-deposited fullerenes at room temperature are weakly interacting with the surface, however annealing at 450 K causes a charge transfer from the surface to the molecule. This is a metastable state in which an adatom-vacancy pair is formed, as predicted by DFT calculations. Further annealing at 700 K forces the formation of a single atom vacancy beneath each fullerene. Nuestros experimentos sobre C_{60}/Pt(111) nos indican que la interacción entre el sustrato y el adsorbato a temperatura ambiente es muy baja; sin embargo un calentamiento a 450 K causa una transferencia de carga de la superficie a la molécula. En este es un estado metaestable, un 'adamos-vacancy pair' se forma, como predicen los cálculos de DFT. Un ulterior calentamiento a 700 K causa la formación de una vacante debajo de cada fullereno.

1. Introduction and motivation

Nanotechnology stands as the engineering and manipulation of objects at the molecular or atomic scale to build functional items for a useful purpose. The spreading of this concept began with Prof. Richard Feynman's famous lecture named 'There is plenty of room at the bottom' (Caltech, 1959)[1] in which the Nobel Prize winner supported the possibility to manoeuvre single atoms and array them in a desired way. This was the beginning of the 'bottom-up' approach: the idea of building brick to brick a desired final object, and to use atoms and molecules as bricks.

A few decades after Feynman's lecture, the invention of the **Scanning Tunneling Microscope** (STM) in 1981[2] paved the way to applying the atomic and molecular manipulation at the nanoscale for the engineering of technological tools. For the first time, scientists were able to see atoms and to move them in a desired way. After this invention, the interest in the potential of nanotechnology started to grow exponentially.

Moreover, many new carbonaceous materials such as the **fullerene**[3] and the **carbon nanotube**[4,5] were discovered in 1985 and in 1991 respectively. Their unique shape and the predicted properties puzzled scientists and governments into investing more and more time and money in this new and exciting field. The recent discovery of the two-dimensional material **graphene**[6] and the confirmation of its extraordinary properties is the proof of the great recent advances in nanotechnology. Nowadays, nanotechnology is a multidisciplinary field which promises to be the millstone in future generation's technology, not only in electronics but also in other crucial fields such as medicine or clean energy achievement.

As the name 'nanotechnology' suggests, its particularity is the use or study of small objects, with an upper limit of about 100 nm. At the nanoscale, many quantum mechanical properties can no longer be ignored and are therefore exploited to improve the properties of the final product. The most important feature of so-called nano-obects is the fact that the surface to volume ratio rises, therefore the surface plays an increasingly important role. The density of state curve changes leading to the rise of new properties due to the reduced dimensionality of the object and this can be exploited in nanotechnological devices. Hence an important research field of nanotechnology is surface science, the research of the chemical and physical processes that occur at the surface of a body, or at the interface between two objects, in any of the three states of matter.

A large branch of surface science deals with ideal systems, where single crystal samples are analysed in an **Ultra High Vacuum** (UHV) environment. The employment of UHV allows perfect sample cleanliness and a very high control of the environment as well as powerful characterisation techniques. Single crystals in UHV are model systems to understand the chemical and the physical properties taking place at the surface of a material.

Uncountable systems have been characterized with surface science techniques and nowadays most standard metallic, semiconducting and insulating single crystal surfaces are well known in terms of structure and of electronic properties. In the past twenty years the interest of surface scientists shifted towards solving more complicated problems such as the interaction and the behaviour of large molecules and nanoparticles.

These systems have a very high technological impact. For example, "organic molecules are an excellent and easy way to modify the properties of metal surfaces"[7] in terms of electric, tribological and optical properties, and resistance to corrosion. Moreover, a lot of effort has been put into developing **molecular electronics** to

substitute the inorganic semiconducting technology. Molecular electronics aims at building electric circuits using single molecules or clusters which are much cheaper, versatile and smaller than the old school technologies.[7]

In order to build functional and efficient circuits with organic molecules, different problems have to be overcome. First of all, the chosen molecules have to serve the purpose, for example depending on the task they have to behave as good electron donors or acceptors. Moreover, the interaction between them or with the substrate's surface has to be well known. Covalently bonded molecular networks are ideal for this purpose[8,9] because they are much more stable and more resistant than physisorbed H-bonded or metalorganic networks.[7] Additionally, the coupling between the molecules and the electrodes affects the network's electronic properties; therefore it has to be well known in order to choose suitable molecules and suitable electrode materials. Surface science techniques are ideal to answer these important questions.

Besides, learning to combine organic molecules one by one, to place them in the desired place and even learn to manipulate them into turning into a different molecule, allows controlling with atomic precision their behaviour and forcing a desired outcome. The use of molecules as building blocks to achieve a fancied result is the base of the bottom-up approach.

The **catalytic properties of surfaces**, particularly of transition metals, can be exploited to manipulate and change the structure and properties of molecules, in particular **Polycyclic Aromatic Hydrocarbons** (PAH), by inducing chemical reactions. Indeed, "creating or connecting together large organic molecules […] by chemical reactions readily on surfaces is the first step to a true advance in the field of molecular electronics".[8] The role of the surface is twofold: first of all, it brings together the precursors; secondly, it catalyses the rupture of some intramolecular bonds to transform altogether the pristine molecule into something else.

The electronic structure of a transition metal (TM), especially its sharp d-band, is crucial to determine its catalytic activity. The electrons in the molecular orbitals of the adsorbed PAH interact and bond with the d-valence band electrons of the TM. The d-band varies its occupancy for each TM, therefore the chemical bonding of each metal with the adsorbate changes, indicating a specific activity for each reaction.

In on-surface catalysed processes, the surface can act on a molecular precursor in different ways, depending on both the precursor and on the surface. Different reactions can be promoted. Most reactions involve the cleavage of a C-X bond (X being a halogen or a hydrogen) to subsequently form new bonds. External injection of energy in the system is usually needed to overcome the activation barrier, and this energy is mainly provided by annealing the system.

A common strategy to modify the pristine molecule is via a **dehalogenation** reaction (such as Ullmann or Sonogashira reactions) which leaves a C dangling bond.[10–12] In this case, a PAH is adorned with a halogen such as Br or I, bonded to a C atom. The breakage of this bond, catalysed by the TM, leads to the formation of different structure. A classic example by Grill *et al.*[13] allows the formation of zero-, one- or two-dimensional networks, by controlling the number of Br atoms attached to the precursor. When only one Br atom is attached to a C in the molecule, the cleavage of the C-Br bond leads to one dangling C bond, and the formation of a dimer. The presence of two Br atoms in the PAH leads to the formation of one-dimensional polymer, and the presence of four Br atoms leads to two-dimensional networks. Dehalogenation reaction on

metals have been largely exploited to build porous covalent networks, and the use of precursor with different size can lead to tailored structures with different pore-sizes.[14–16]

Graphene nanoribbons (GNR) have also been synthesised by dehalogenation reactions of PAH precursors.[17–19] GNRs with widths smaller than 10 nm are semiconducting, and their band-gap is highly dependent on the width. The selection of different PAH as precursors allows tailoring these properties with atomic precision, so that the shape and the size of the GNR can be controlled hence manipulating its band-gap and its electronic properties.

Dehydrogenation reactions are equally important to dehalogenations in on-surface tailoring of PAH precursors. They involve the cleavage of C-H bonds. The ability of TM to cleave a C-H bond is so great that some molecules readily dehydrogenate on a metal surface at room temperature, as for example methane and ethylene on Pt(111).[20] However larger PAHs in general require the injection of extra external energy (as annealing) to overcome the activation barrier and to dehydrogenate.

Cyclodehydrogenation is the formation of an aromatic ring caused by the cleavage of a C-H bond in an organic molecule. This technique is very powerful to create new nano-objects from a programmed precursor. A few works which express the full potential of this technique are worth mentioning.

Otero *et al*.[21] demonstrated that surface assisted cyclodehydrogenation can be exploited to form fullerenes from their planar triangular precursors. $C_{60}H_{30}$ and $C_{57}H_{33}N_3$ were deposited on Pt(111) and annealed to 750 K: all the intramolecular C-H bonds broke and new C-C bonds formed, thus creating C_{60} and the triaza-fullerene $C_{57}N_3$. STM images registered a structural change for which the triangular shape of the pristine molecule transformed into spherical, and the apparent height rose from 0.14 to 0.38 nm.

Nanodomes have been synthesised in a similar way by Rim *et al*.[22] by annealing hexabenzocoronene on Ru(0001). Here too a structural change was clearly observed by STM when comparing the system before and after the annealing.

Treier *et al*.[23] also provided evidence for the outstanding importance of surface assisted cyclodehydrogenation by forming nano-graphene from a planar triangular precursor (cyclohexa-*o*-*p*-*o*-*p*-*o*-*p*-phenylene) on Cu(111). The particularity of their work is that the STM experimental results were combined with large-scale *ab initio* simulations which determined in detail the steps of the cyclodehydrogenation by recognising the weakest C-H bonds which were the first ones to break for steric reasons.

The works mentioned above stress on the importance of the use of the correctly designed precursor to achieve the desired outcome. Amsharov *et al*.[24] were also able to grow fullerenes (even the higher order fullerene C_{84} from $C_{84}H_{42}$). They also used two differently designed isomers of $C_{60}H_{30}$ molecules and they showed that only the one which was correctly programmed was able to transform into a fullerene.

Other on-surface chemical reactions concerning PAH involve an imine formation, which is a reaction leading to a double bond between N and C.[25–27]

The surface may act on the precursors in two ways: either by promoting an intermolecular bonding, such as in the case of Grill *et al*.[13] or of Lafferentz *et al*.,[12] or by acting on a single molecule to transform a single object.[21–24,28] The ordering of molecules on the surface depends on the adsorbate-surface interaction and on

the intermolecular interactions. For example, the first monolayer of benzene on metals usually lays flat, while beyond a single-layer thickness the same molecule tilts due to intermolecular interactions.[7] Ordered networks of molecules can be achieved on surfaces via self-assembling, and they can be formed only if the substrate-adsorbate interaction is low enough for them to diffuse but high enough to hold them in place.

Some organic molecular networks assemble via hydrogen bonding, where an H atom of a PAH binds with an electronegative atom such as O or N of another molecule.[29,30] These chains are stable, but this type of bonding is less strong than metal coordination or covalent compounds. Metal-organic frameworks can be constructed on surfaces by applying the rules of coordination chemistry: metal atoms function as mediators between the organic molecules and favour the growth of two-dimensional networks.[31–34]

Covalently bound complexes of PAH are more stable with respect to hydrogen bonded or metal-coordinated systems.[9,35,36] This is why these chains are ideal for molecular electronics applications. In a recent publication, Franc and Gourdon reviewed extensively the formation of covalent networks via on-surface catalysis in UHV.[37]

The choice of the surface is crucial for steering the catalytic reaction outcome. Bieri *et al*.[9] looked at the role of the substrate in the transformation of hexaiodo-substituted macrocycle cyclohexa-*m*-phenylene upon annealing on three different surfaces; they found that different two-dimensional outcomes arise depending on the diffusion of the precursors, which in turn depends on the surface-adsorbate interaction and therefore on the choice of the substrate. Other works also compared the outcome of on-surface catalysis of a given precursor on different surfaces.[16,38] Moreover, the use of faceted surfaces such as the (110) face of Cu have been used to confine the growth of one-dimensional covalent networks.[39,40]

A novel strategy for the growth of covalent networks was proposed by Lafferentz *et al*.[41] who suggested a multi-step procedure to drive the reaction towards one- or two-dimensional systems. The precursors included two (or more) different active sites, which activate in sequence at different annealing temperatures, therefore promoting a reaction in steps. They deposited 5,15-bis(4'-bromophenyl)-10,20-bis(4'-iodophenyl)porphyrin, namely a porphyrin with two I and two Br atoms bonded to the phenyl rings, onto Au(111). They then annealed to 390 K, so the I atoms detached leaving C dangling bonds who allowed the formation of one-dimensional polymeric or oligomeric chains. A second annealing to 520 K caused the cleavage of the Br atoms, so that two-dimensional networks formed. This hierarchical strategy was used by Dinca *et al*. to obtain pentacene from2,5,9,12-tetrabromoanthra[1,2-b:4,3-b':5,6-b'':8,7-b''']tetrathiophene on Ni(111).[28]

The **doping** of organic networks (such as graphene or other objects) is an appealing way to tune their electronic properties: indeed, the introduction of N or B in a graphene network it is known to open a band-gap transforming it into a p- or n-doped semiconductor.[42] Comprising foreign atoms in the precursor and its modification via on-surface chemistry is an elegant bottom-up strategy to dope in the outcome with atomic precision. For example, N-doped triaza-fullerenes were achieved for the first time by cyclodehydrogenation of its doped planar precursor $C_{57}H_{33}N_3$, and N-doped graphene has been obtained by Chemical Vapour Deposition of different precursors containing N substituents.[42,43]

Large organic molecules can also act on the surface to induce a reconstruction. The most famous example is obtained when depositing C_{60} on low index close-packed transition metals, such as Pt(111) or Au(111): a

one- or multi-atom vacancy is induced on the metal surface upon annealing. The role of C_{60} is to lower the energy barrier needed for the surface to reconstruct.[44,45] Other molecules can act on the surface to induce restructuring and long-range mass transport. For example, $C_{90}H_{98}$ was shown to be able to rearrange the atoms at step edges of Cu(110), by acting as a template forming metallic nanostructures of fixed size.[46]

This thesis concerns different aspects of the interaction of organic molecules with surfaces, and in particular the ability of surfaces to induce chemical reaction on large PAH. The molecules selected for the purpose are described in Chapter 2, and are: (i) the pyridyl-substituted dibenzo[5]helicene $C_{40}H_{22}N_2$; (ii) the crushed triaza-fullerene $C_{57}H_{33}N_3$; (iii) the fullerene C_{60}. We deposited these three organic molecules onto four metal surfaces (Pt(111), Cu(110), Cu(111) and Au(111)): we describe their behaviour and the effect of the catalytic properties of the different substrates, as well as the structural and electronic alteration of the molecule-surface systems. This thesis is divided into seven main chapters:

1. **Introduction and motivation.** We present the importance of the field of on-surface synthesis of new materials and we explain the role of transition metals to catalyse reactions, by showing some crucial results from the literature. Finally, we summarise the seven chapters of this thesis.

2. **Experimental methods.** In this Chapter, we introduce and describe the systems studied in this thesis together with the experimental and theoretical techniques used for their characterisation. The Scanning Tunneling Microscope (STM), together with X-ray Photoelectron Spectroscopy (XPS) have been the main tools for probing the samples. Additionally, Near-Edge X-ray Absorption Fine Structure (NEXAFS) Low Energy Electron Diffraction (LEED), Temperature Programmed Desorption (TPD), and Density Functional Theory (DFT) are introduced. We describe DiPy[5]DBH, $C_{57}H_{33}N_3$ and C_{60}, namely the three main organic molecules studied on transition metal surfaces (Pt(111), Cu(110), Cu(111) and Au(111)). In this Chapter, we also mention the groups we collaborated with during this thesis.

3. **Tailored formation of N-doped nanoarchitectures by diffusion-controlled on-surface (cyclo)dehydrogenation of heteroaromatics.** In this Chapter we describe how the role of surface diffusion of PAHs on metal surfaces influences the final outcome of on-surface reactions. We report on the possibility to control the final outcome just by selecting different surfaces: if diffusion is promoted, the formation of intermolecular polymers or oligomers is favoured (dehydrogenative polymerisation); if the diffusion is blocked, the precursors undergo an intramolecular transformation into a new object (cyclodehydrogenation).

4. **Spectroscopic and morphological study of diPy[5]DBH on different transition metals.** The behaviour of DiPy[5]DBH on Pt(111), Cu(110), Cu(111) and Au(111) is studied in detail with STM, XPS, NEXAFS and *ab-initio* calculations. The high reactivity of Pt(111) is confirmed: in this surface the molecule is not diffusing upon adsorption, hence blocking intermolecular interaction and promoting intramolecular modification of the pristine molecule. The molecule undergoes two main phase transition, first transforming into N-doped nanographene, then into N-doped nano-domes, before its rupture to form N-doped graphene islands. On the other surfaces, diffusion promotes the intermolecular interaction. We provide a detailed spectroscopic analysis of the systems to complement with the STM images at different annealing temperatures.

5. **$C_{57}H_{33}N_3$: on-surface cyclodehydrogenation steps to the formation of triaza-fullerenes.** We unveil the steps of formation of triaza-fullerene starting from its planar precursor. We provide a detailed analysis of the system by showing STM images at different temperature, compared to N1s, C1s and Pt4f XPS spectra. We show how the molecule undergoes three stages before graphene formation: open molecule, open-cage fullerene and fullerene.

6. **The mechanism of the atomic vacancy formation on the C_{60}/Pt(111) system.** The fullerene is known to induce a reconstruction on different transition metal surfaces, by promoting the formation of a single- or multi-atom vacancy. Here we show by STM and XPS that C_{60} physisorbs on Pt(111) at room temperature; the formation of the vacancy is promoted by annealing of the surface and results in a transition to a chemisorbed state, as a decrease in the apparent height of the fullerene and as a rotation of the molecule. The passage from physisorption to chemisorption is likely to be due to the desorption of an invisible layer of atomic H which passivates the surface. The vacancy formation is accompanied by an intermediate step for which there is charge transfer from the surface to the molecule as the molecule couples with an adatom: this intermediate phase was observed as an increase in apparent height of the STM, and as a shift in the C1s XPS peak.

7. **Conclusions.** In this Chapter, we summarise the main discoveries of this thesis in two languages, English and Spanish.

2. Experimental methods

The branch of physics concerning the study of solid surfaces is called surface science and it explores the electronic, structural and optical properties of last few monolayers of a solid.

Although the very first pioneering studies were performed at the end of the 18th century, only with the development of Ultra High Vacuum (UHV) techniques in the 1950s modern surface science was born. Moreover, the implementation of Auger Electron Spectroscopy (AES) in the 1950s and Low Energy Electron Diffraction (LEED) in the 1960s in laboratories, together with the achievement of the first X-ray Photoelectron Spectroscopy (XPS) spectra, were important steps towards the establishment of modern surface science as we know it. In the 1980s, due to the development of synchrotron radiation facilities, X-ray diffraction was applied to surface science by allowing a grazing incident angle between the sample and the x-ray beam in order to achieve surface sensitivity, and this was another breakthrough in the field of surface science in general and crystallography in particular.

The Scanning Tunneling Microscope (STM) developed in the 1980s and atomic resolution images were achieved. The combination of STM studies with Density Functional Theory (DFT) calculations to explain the scanned images and the energetic processes of a chemical reaction allowed surface science to become an "atomistic" view of chemistry. These concepts were applied to different disciplines and have been particularly important for understanding the fundaments of catalysis (the 2007 Nobel Prize in chemistry was won by Gerhard Ertl, "for his studies of chemical processes on solid surfaces") or to control a perfect Molecular Beam Epitaxy (MBE) thin film growth, very significant for the microelectronic technology.

These historical events show us that surface science is a relatively new science, and that it has changed quite a lot during the last few years. The experimental techniques are nowadays well established, the main surface atomic relaxation and reconstruction process on metals, semiconductors or insulator surfaces are understood and their interaction with simple objects (adatoms or small molecules) has been studied in depth. The current tendency in surface science is to focus on chemical complexity and nanotechnology, to achieve extreme capability to characterize small objects and to control the bottom-up assembling processes. In this sense, one of the new trends is to study large molecular organic molecules on surface and how they can ensemble in larger nanostructures by on-surface chemistry.

Ultra High Vacuum is an important condition to ensure the cleanliness of a surface. In a UHV chamber devoted to surface science, the base pressure is about $1x10^{-10}$ mbar, therefore the atmospheric contamination is almost absent. This allows eradicating the impurities from the surface, to have a precise control on the adsorbed material.

In this chapter I will describe the experimental system of the ESISNA group, which I have been using for the development of this thesis, I will mention the groups we collaborated with and I will describe the systems where we performed the experiments.

Moreover, during the course of my thesis, I used many different experimental techniques which allowed me to analyse a particular situation from many different points of view, in order to obtain a full description of the system. I will briefly describe them in this Chapter.

2.1 Experimental systems used in this thesis

The experiments of this thesis have been mainly carried out in the ESISNA group[47] at the Institute of Material Sciences of Madrid (ICMM – CSIC), but part of the work has also been performed in different laboratories:

- With Dr. C. F. J. Flipse and Dr. K. van de Ruit in the Molecular Materials and Nanosystem (M2N) group of the Technical University of Eindhoven (Eindhoven, The Netherlands): Low Temperature Scanning Tunneling Microscopy (STM) and Scanning Tunneling Spectroscopy (STS)
- With Dr. G. Castro and Dr. J. Rubio and their team in the Spanish Beamline (SPLINE) of the European Synchrotron Radiation Facility (Grenoble, France): Surface X-ray Diffraction
- With Dr. S. Lizzit and Dr. S. Gardonio in the SuperESCA beamline of the Elettra Synchrotron (Trieste, Italy): X-ray Photoelectron Spectroscopy (XPS)
- With Dr. R. Schennach in the Graz University of Technology (Graz, Austria): Temperature Programmed Desorption (TPD)
- With Dr. L. Floreano, Dr. A. Cossaro, Dr. A. Verdini and G. Lovat at the ALOISA beamline of the Elettra Synchrotron (Trieste, Italy): XPS and Near Edge X-ray Absorption Fine Structure (NEXAFS)
- With Dr. A. Preobrajenski at the ID1011 beamline of the MAX-lab Synctrothron (Lund, Sweden): XPS and NEXAFS
- With Dr. A. López Vázquez de Parga, Dr. S. Barja and M. Garnica at the IMDEA-Nanociencia group (Madrid, Spain): Low Temperature STM and STS

The UHV chamber of the ESISNA group is shown in Figure 2.1.1. This UHV chamber has a base pressure of about $1x10^{-10}$ mbar.

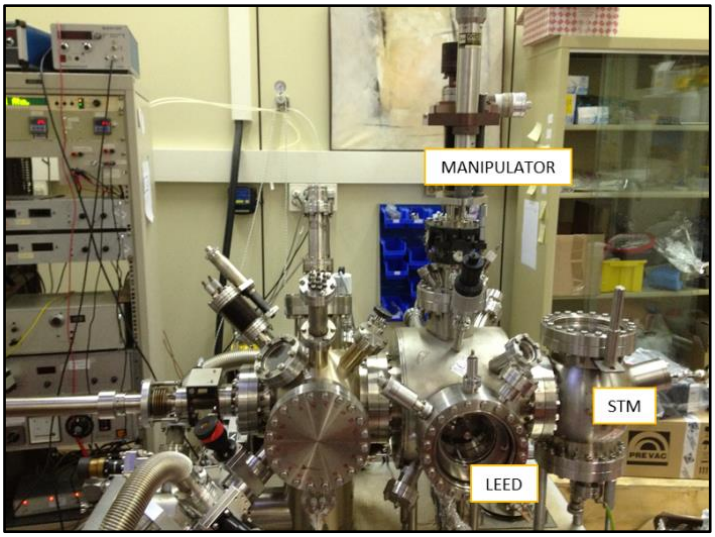

Figure 2.1.1 – *One of the experimental systems of the ESISNA group.* *This photograph shows the UHV chamber in which most of the experiments of this thesis were performed, equipped with a RT-STM and a LEED, among other tools.*

In this chamber, UHV was obtained with a turbo-molecular pump. The vacuum was maintained with the same turbo-molecular pump, with an ion pump, and a Titanium Sublimation Pump (TSP). The pressure inside was checked with a Bayard-Alpert hot filament ion gauge.

This chamber was equipped with an Omicron room temperature (RT) STM (controlled by a Dulcinea electronic from Nanotec[48]), Low-Energy Electron Diffraction (LEED) optics (Specta-LEED), a Quadrupole Mass Spectrometer (QMS), a sputtering ion gun, many evaporators of different molecules and a manipulator with range RT-1300 K. The sample was heated up by electron bombardment, by passing current through a Ta filament at its back to produce electrons while applying 1.2 kV to the sample to attract them.

This chamber has recently been updated,[47] and we implemented Polarisation Modulation Infra-Red Reflection-Absorption Spectroscopy (PM-IRRAS) together with a Multi-Channel Plate LEED. PM-IRRAS allows studying real-time chemical reactions of species adsorbed on the surface. The system is mounted so that both in-situ (UHV) and ex-situ (ambient pressure) experiments can be performed, and the Polarisation Modulation cancels the signal of the gas in the air and it is only sensitive to the species adsorbed on the surface.

2.2 Substrate preparation

The cleaning process of transition metal single crystals in UHV is well known, however, a very good pressure is needed for a successful outcome. In this thesis, we used four single crystals, namely Pt(111), Cu(110), Cu(111) and Au(111). All of them are face centred cubic (fcc) crystals.

Platinum lies in group 10 of the periodic table and due to its electronic structure (see Chapter 1) its surface is highly reactive. Copper and gold belong to group 11 of the periodic table and together with silver these metals are also referred to as coinage metals.

Pt(111) is the hardest crystal to clean at an atomic level among the ones we employed. When this sample is introduced into a UHV chamber from air, at least three annealing cycles in 1-5x10^{-6} mbar of O_2 are necessary. Contamination of the sample is mainly due to carbonaceous species and to H_2O: the annealing (1000-1200 K) processes in O_2 are needed to burn the carbon which reacts with the oxygen forming mainly CO and CO_2, which desorb from the surface and it is pumped away by the pumps in their gaseous form.

Oxygen contamination and other remnants are then cleaned with sputtering and annealing cycles. In sputtering, Ar^+ ions are fired to the surface for about 10 minutes. These ions (purity = 99.999%) are non-reactive and they are accelerated at 1.5 kV towards the surface, and they generate a current to the sample of about 10 μA. In order to reconstruct the surface after this destructive operation, we perform further annealing to about 1100-1200 K in a clean UHV atmosphere.

The achievement of clean Cu and Au surface is easier due to the fact that these surfaces are not as reactive as Pt. Sputtering and annealing cycles to about 900-1000 K are needed to obtain clean surfaces, but no annealing cycles in an O_2 atmosphere are necessary.

The lattice parameters of the surfaces are shown in Table 2.2.1.

	Pt(111)	Cu(110)	Cu(111)	Au(111)*
Lattice parameter (Å)	3.9242	3.6149	3.6149	4.0782
Nearest Neighbour distance (Å)	2.7748	2.5561	2.5561	2.8837
Distance between atomic planes (Å)	2.2656	2.5561	2.0871	2.3545

* Au(111) exhibits a surface reconstruction (22x√3), which is not considered in these calculations.

Table 2.2.1 – *Different crystallographic parameters of the four surfaces studied in this thesis.* *The lattice parameter, the in-plane nearest neighbour distances and the distance between planes are shown here for Pt(111), Cu(110), Cu(111) and Au(111).*

The fcc conventional unit cell is shown in Figure 2.2.1-a. The atoms are shown in purple. One atom is placed in the centre of each side of the cube. Figure 2.2.1-b represents the close-packed (111) orientation of a fcc crystal. The yellow atoms represent the surface, with a typical 2D hexagonal periodicity. Figure 2.2.1-c shows the (110) face of a fcc structure, with the rows of the topmost atoms in yellow. Pt, Au and Cu are all fcc metals.

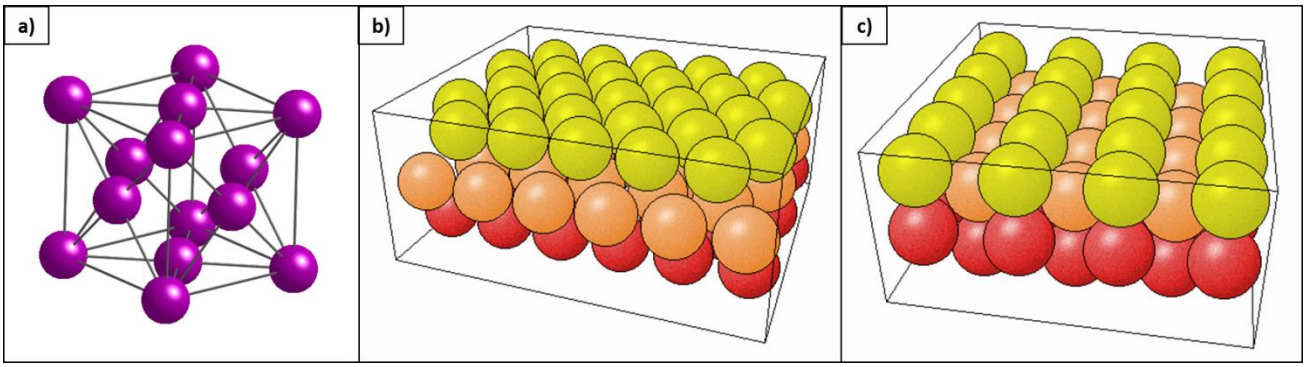

Figure 2.2.1 – *Fcc unit cell, and the (111) and (110) faces of this structure.* *From the University of Virginia web page.*[49] *a) The atoms of an fcc conventional shell are shown in purple. b) The (111) face of a fcc crystal; the yellow atoms belong to the topmost layer. c) The (110) face of a fcc crystal; the yellow atoms belong to the topmost layer, and form rows.*

2.3 Deposition of organic molecules

We deposited different organic aromatic molecules on the surfaces mentioned above. We sublimated these molecules in UHV from home-made Ta crucibles welded to two stainless steel bars (see Figure 2.3.1).

The temperature of the molecules is controlled by a type-K thermocouple welded to the crucible, because the temperature is homogeneously distributed in the entire envelope. The crucibles were filled with the molecular powder and annealed by passing current through the bars. This method is very clean and it allows the evaporation of the molecules at a reliable rate without contaminating the sample. Moreover, after the fabrication the empty crucibles were always heated in UHV to desorb the water molecules and the contamination before filling them with molecules.

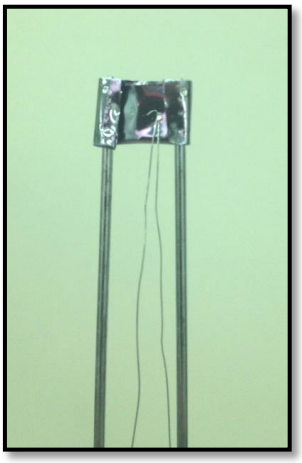

Figure 2.3.1 – *A photograph of a homemade Ta molecular source.* *The two wired welded to the Ta crucible are the thermocouple to measure the temperature of the molecules.*

In this thesis, the following organic molecules were used:

- 4,4'-dibenzo[f,l]pentahelicene-17,18-diyildipyridine (diPy[5]DBH); $C_{40}H_{22}N_2$, see Figure 2.3.2-a (deposition temperature: 575 K); the group of Dr. Ivo Starý of the Institute of Organic Chemistry and Biochemistry, Academy of Sciences of the Czech Republic, synthesised this molecule.[50]
- $C_{57}H_{33}N_3$, see Figure 2.3.2-b (deposition temperature: 700-730 K); the group of Dr. Berta Gómez-Lor of the Institute of Material Sciences of Madrid synthesised this molecule.[51]
- (C_{60}-I_h)[5,6]fullerene; C_{60}, see Figure 2.3.2-c (deposition temperature: 700-850 K); this molecule was purchased by Sigma Aldrich (purity 99%).

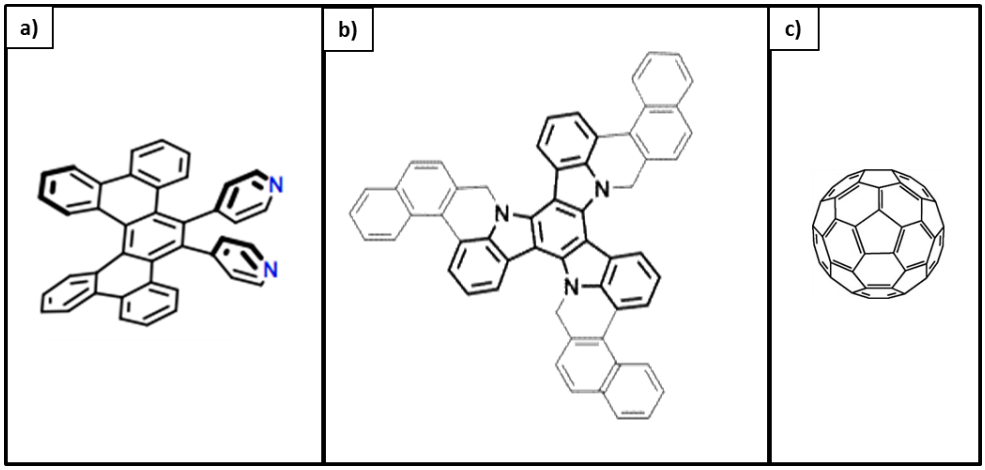

Figure 2.3.2 – *The three organic precursors selected for this thesis.* *(a) $C_{40}H_{24}N_2$. (b) $C_{57}H_{33}N_3$. (c) C_{60}.*

$C_{57}H_{33}N_3$ in Figure 2.3.2-a was synthesised by alkylation and intramolecular palladium-catalysed arylation from the symmetrical triindole, a triaza analogue of truxene.

$C_{40}H_{22}N_2$ was synthesised in six main steps (Figure 2.3.2-b).[50] In the first stage, symmetrical bisarylethyne was prepared by Sonogashira coupling with gaseous acetylene. The key compound of the whole synthesis was the aromatic triyne, which was prepared by a double Suzuki coupling using the aryl boronic ester and symmetrical bisarylethyne. Deprotection of two triisopropylsilyl group with tetrabutylamonium fluoride (TBAF) preceded terminal triyne. Then this triyne was coupled twice (by Sonogashira coupling) with 4-iodo pyridine. Finally, this triyne was transformed by Nickel mediated intramolecular [2+2+2] cycloisomerization directly into the fully aromatic dibenzohelicene (DiPy[5]DBH).

During the deposition, the pressure was always < $5x10^{-10}$ mbar. The rate of evaporation depends on the type of molecule and on the temperature of the source, and it lay in the range of 0.1 ML/min.

2.4 Scanning Tunneling Microscopy (STM)

The STM has been the main tool used in this thesis, and in this section I will briefly introduce this technique. It was developed in 1981 by Gerd Binning and Heinrich Rohrer at the IBM Research Laboratory in Zurich. The inventors won the Nobel Prize in Physics in 1986 “for their design of the scanning tunneling microscope”, and it was a real breakthrough since it allows to image directly surfaces with atomic resolution.[52]

A Scanning Tunneling Microscope works by taking advantage of quantum tunneling. This is a completely quantum mechanical phenomenon by which the probability that a particle with kinetic energy E_K can tunnel through a potential barrier with energy E for which $E_K < E$ is not zero. This would be strictly forbidden by classical mechanics and it is due to the particle-wave duality of electrons. The probability of tunneling depends (among other things) on the width of the potential barrier.

The STM works by scanning a metallic tip (usually W) very close to the surface of a conducting sample, so close that electrons can tunnel from the tip to the sample (or vice versa). The current of these tunneling electrons (i. e. the tunneling Current I_t) is then monitored and since I_t depends on the tip-sample distance, a topographic image of the sample is then achieved.

$$I_t \propto V_s\, e^{(-\,k\,d\,\sqrt{\bar{\varphi}})} \qquad (1)$$

Equation (1)[52] indicates that I_t is proportional to the voltage applied between the tip and the sample V_s, the tip-sample distance d, a constant k and the average work-function $\bar{\varphi}$. Typical tunneling currents are of the order of 0.01-10 nA. A potential difference is needed to favour a tunneling current in only one direction, otherwise it would average out; the bias is applied to the surface in the ESISNA system. Since the current is exponentially proportional to the distance, a small change in the separation between the tip and the sample will cause a big change in the current, and this is the principle of the STM.

The sample is mounted on a support which is driven by a piezoelectric material; this support can move the sample for rough adjustments towards the tip. On the other hand, the tip must move with an accuracy of better than 1 Å, and it is mounted on a highly precise holder formed by three piezoelectric columns which move the tip perpendicular and parallel to the sample. A piezoelectric is a material which extends or compresses linearly when a voltage is applied to it (or, vice versa, it acquires a charge when compressed or extended). The movements of the sample and of the tip are controlled by an interface which generates the voltage needed to move them (see Figure 2.4.1 for a sketch of the setup).

An STM image can be recorded in two different modes, namely constant height mode or constant current mode. When constant height is used, the vertical position of the tip is unchanged, and the image results from the variations of the current signal as the tip is scanning the surface; a flat surface is needed in order to avoid crashing the tip. However most experiments are performed in the 'constant-current' mode: the current is kept steady by a feedback loop and since the current is proportional to the distance between the tip and the surface, this distance must also be constant. Therefore the corrugation of the sample (such as adsorbed molecules or the atoms forming the surface) will force the feedback to compress or to extend piezoelectric support in order to keep the tip-sample distance constant, and this movement is registered and transformed in height units by the electronic of the STM, connected to the computer.

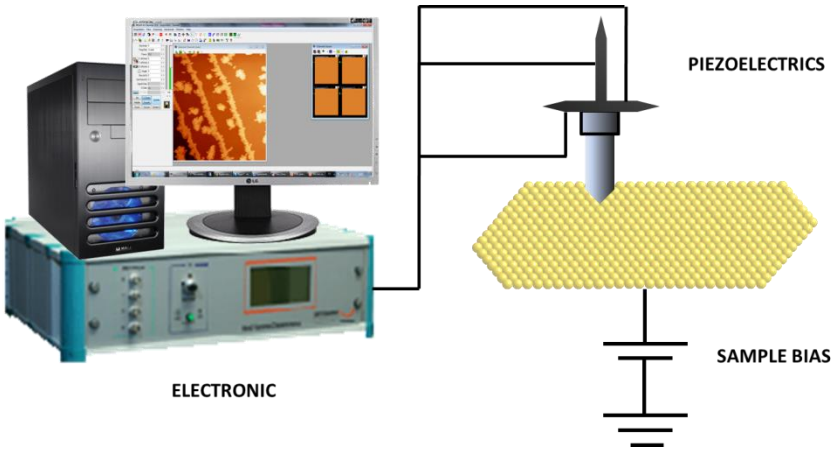

Figure 2.4.1 – *A simple sketch of the setup of the STM.* *The surface is scanned with the tip, connected to three piezo-electrics which move it with high precision. The voltage impulses are monitored by an interface and processed by a computer.*

Due to the high precision of the system, the tip and the sample are very sensitive to mechanical vibrations. To suppress them, the tip-sample system is mounted on an anti-vibrational holder which is suspended by permanent magnets. Moreover the whole chamber is also sitting on a structure which damps the vibrations of the floor. Figure 2.4.2 is a photograph of a top view of the room temperature STM of the ESISNA group: it shows the anti-vibrational stage suspended by an array of permanent magnets and the piezo-electrics of the tip.

Nowadays, the STM has greatly evolved to achieve better resolution. For example, many STMs now can operate at different temperature. Low Temperature STMs can be cooled down with liquid helium to 4 K, to

minimise the kinetic movements which can cause drift and instability of the tip; Variable Temperature STM can function both at low and at higher temperatures.

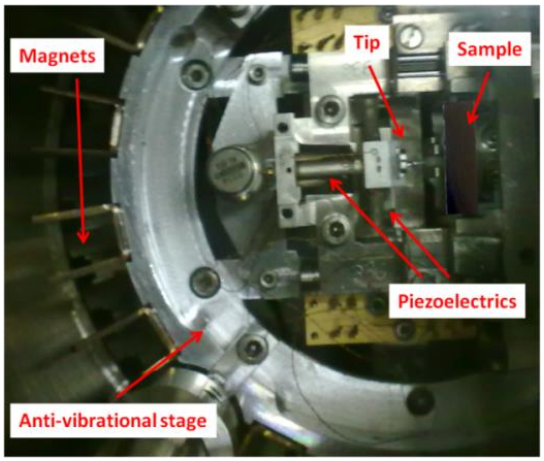

Figure 2.4.2 – *A photograph of the Omicron STM1 set-up.* *The STM is suspended by an array of permanent magnets, in order to damp the mechanical vibrations. The tip and the sample are indicated in this image, as well as the piezo-electrics which allow the tip to move with such a precision.*

The ideal tip terminates with only one atom at the apex; this is hard to achieve because the fabrication of the tip is an uncontrolled and dynamical process: however, the sharper the tip termination is, the easier it is to obtain high resolution images. The tips are usually home-made with electrochemical etching. Figure 2.4.3 shows the set-up that we have in our laboratory: a W wire (0.2 mm wide) is introduced in the metallic ring, which has been immerged in a 2.5 M KOH solution so that a KOH membrane remains on the hoop. A voltage (about 10 V) is then applied between the ring and the W wire, so that K^+ ions start to attack the surface of the wire and they etch the surface to form a sharp tip. In order to clean the tip from KOH traces such as oxides and water, the tips were always annealed to about 900 K in UHV.

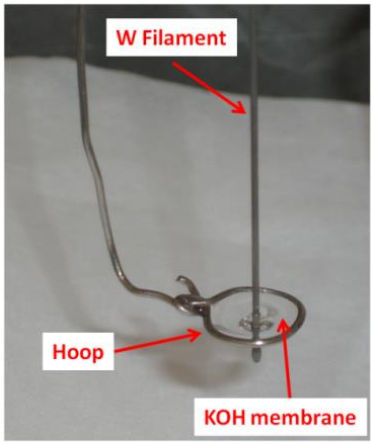

Figure 2.4.3 – *A photograph of the process of making an atomically sharp STM tip.* *The W wire is immerged in a KOH membrane, and electrochemical etching allows the tip formation.*

Figure 2.4.4-a shows a typical image of a clean Pt(111) surface, which has been one of the most used substrates in this thesis. Large and clean monoatomic terraces can be observed. Figure 2.4.4-b shows the same clean surface, with atomic resolution: each small sphere is a different atom, and the hexagonal symmetry of the fcc(111) face is observed. To achieve enough sensitivity to obtain atomic resolution of a transition metal surface, the tip-sample distance must be very short, therefore high tunneling current is needed.

All STM images shown in this thesis were recorded at constant current, with a tunneling current between 0.2 and 1 nA, unless stated otherwise.

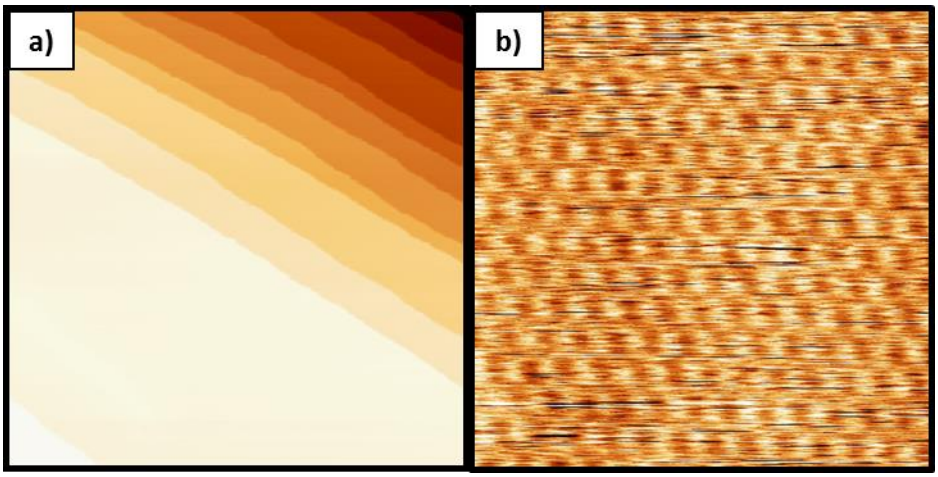

Figure 2.4.4 – *STM images of a clean Pt(111) surface.* *a) In this 100x100 nm^2 image, large clean terraces and monoatomic steps (height = 0.23 nm) are seen (V_s = +2 V; I_t = 0.2 nA). b) Atomic resolution image of a clean Pt(111) surface (4x4 nm^2; V_s = -0.001 V; I_t = 11 nA). The atoms are clearly visible in a hexagonal pattern.*

2.5 Low-Energy Electron Diffraction (LEED)

The ultimate goal of most diffraction studies on ordered systems in the determination of their structure.[53] LEED is a widely spread technique to uncover the atomic structure of the few last layers of a crystal: it is based on the principle of elastic diffraction of electrons and it allows a direct vision of the diffraction pattern. Figure 2.5.1 shows a schematic diagram of the main components of the optics of a standard LEED device.

The electrons are produced and accelerated by the electron gun towards the sample surface, with energy in the range of 10-1000 V. The electrons scattered from the sample travel in a straight line through spherical grids towards the phosphorous screen. The grids are used to retard all electrons that have not been elastically scattered: the electrons that overcome the grids are then accelerated to the phosphorous fluorescent screen, which is positively charged (+ 6 kV). Due to the crystalline nature of the surface, what appears in the screen is the projection of the magnified reciprocal space map of the structure of the surface (the Bragg diffraction spots).

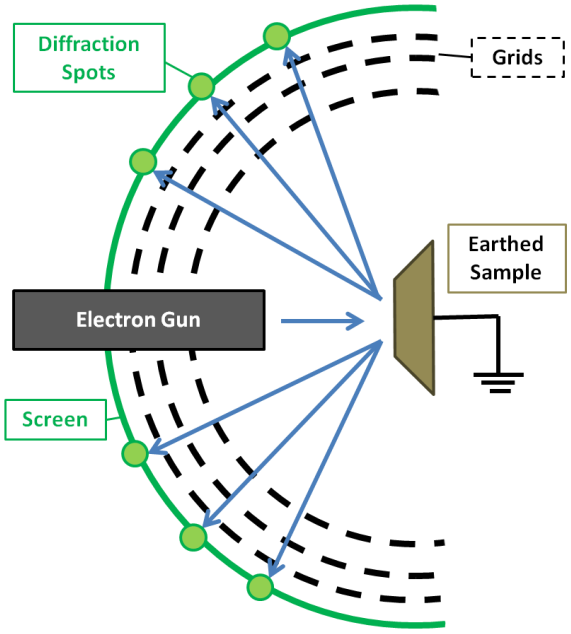

Figure 2.5.1 – *A sketch of the basic components of a LEED device.* *The electrons are shone from the electron gun to the sample, where they diffract into an ordered pattern and are observed as bright spot in a fluorescent phosphorous screen.*

As an example, a typical image of a LEED pattern of Pt(111) is shown in Figure 2.5.2. LEED is also very powerful because a detailed analysis of the intensity of the spots as a function of the energy of the electrons reveals the coordinates of the atoms in the unit cell. This process is called LEED-IV, but a full analysis is far from simple due to the difficulties in theoretically deriving the atomic coordinates from the IV curves.

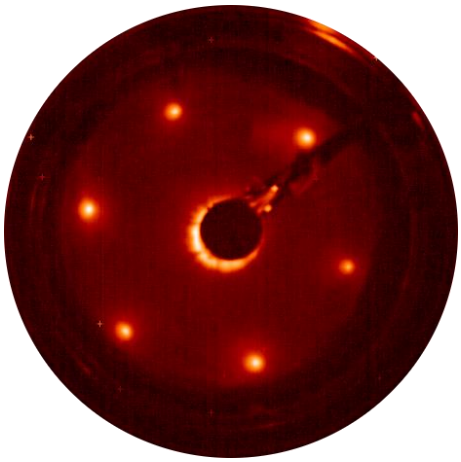

Figure 2.5.2 – *A typical LEED image of a clean Pt(111) surface.* *The LEED was recorded with an electron energy of 140 eV, and the six first order spots are shown.*

2.6 X-ray Photoelectron Spectroscopy (XPS)

Kai Siegbahn in the 1950s and 1960s developed the instrumentation and the theory of XPS to give us the technique we use today.[54] XPS provides qualitative and quantitative chemical information of all the elements present on a surface (except H and He). The principle is based on the photoelectric effect and it is very simple: when a monochromatic x-ray beam with energy hν penetrates the surface, a photon is absorbed and a core-level electron with binding energy E_B below the vacuum level is emitted from the surface with a kinetic energy

$$E_K = h\nu - E_B - \varphi \qquad (2)$$

where φ is the work function of the sample and analyser. The kinetic energy of the electrons is measured with a detector, usually a Concentric Hemispheric Analyser (CHA), and therefore knowing the hν of the x-rays, we can know the energy of the bound state. From this, since each electron coming from a particular energy level of a particular chemical element has a specific binding energy we can obtain information on the chemical composition of the surface. Figure 2.6.1 represents a sketch of the physical basis of the functioning of the XPS, showing the energy levels of Pt as an example.

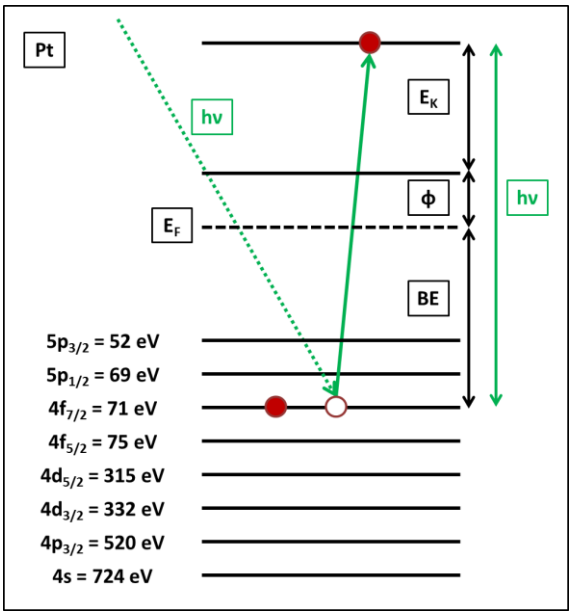

Figure 2.6.1 – *Schematic representation of the photoelectric effect for Pt.* *This sketch shows the principles for which an XPS works. A photon excited a core-level electron of the surface of the sample. The energy of this electron is recorded and its binding energy is calculated. The energy levels drawn out of scale correspond to Pt.*

X-rays can be produced either by an x-ray source such as Al Kα (1486.6 eV) Mg Kα (1253.6 eV) or from a synchrotron radiation light source. The photon flux and therefore the intensity of the signal and the resolution are highly improved by using synchrotron light.

Apart from the identification of the elements composing the sample surface, XPS is also useful to identify the chemical shifts of a particular element. The shifts are seen as slight changes (a maximum of a few eV) in the binding energy and/or in the width of the peak, and they are caused by the oxidation state, the lattice sites and bonding with other elements among other electronic processes.

As an example, the XPS Pt4f$_{7/2}$ spectrum of a clean Pt(111) sample is shown in Figure 2.6.2. It was recorded at the SuperESCA beamline at the ELETTRA synchrotron radiation facility (Trieste, Italy). This peak is fitted with a background line (light blue) and two components. The main peak (70.9 eV) corresponds to atoms in the Pt bulk structure and the second peak (70.5 eV) is the surface peak. The core-level binding energy of transition metals such as Pt is different from that of the bulk, due to the fact that atoms on the outermost surface region have fewer neighbours and therefore their electronic properties are different: this effect is called Surface Core Level Shift (SCLS).[55]

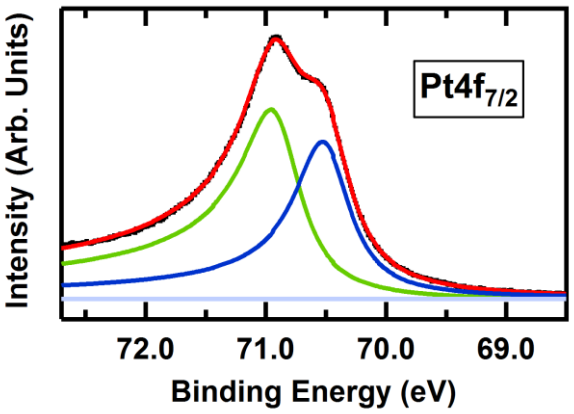

Figure 2.6.2 – *Pt4f$_{7/2}$ XPS peak of a clean sample.* *This spectrum was recorded at the SuperESCA beamline in the ELETTRA synchrotron radiation source. This peak is made up by two components, the bulk peak (70.9 eV) and the surface peak (70.5 eV) at a photon energy of 200 eV.*

The XPS spectra were analysed by using a non-commercial program developed by Hyun-Jo Kim (Department of Physics of Seoul National University, Seoul, 151-742, Korea). This program allows a fit of the width of the peaks by convoluting the Lorentzian and the Gaussian contribution to the width. The binding energy of every peak was corrected according to the Fermi Energy, which was recorded with the same parameters.

During the course of this thesis, we have recorded high resolution XPS at the SuperESCA and ALOISA beamlines (ELETTRA, Trieste, Italy) and at D1011 (MAX-lab, Lund, Sweden).

2.7 Near Edge X-ray Absorption Fine Structure (NEXAFS)

NEXAFS is an x-ray absorption technique which gives qualitative and quantitative information on the intra-molecular bonds, such as the bond length, which bonds are present in the system, and the orientation of the bonds on the surface by studying the unoccupied electronic structure.[56] NEXAFS usually probes transitions from the K-edge of atomic species and it is mostly used to detect low-Z multiple species such as O, C or N.[57]

An x-ray beam is shone on the sample, and its energy is scanned throughout the absorption edge of a given element. As shown in Figure 2.7.1 (from Hähner *et al*.[56]), when a photon is absorbed by an atom, it induces a photoelectron from a core-level to be emitted, leaving the molecule in an excited state. The relaxation process can then take the form of a photon emission, or of an Auger electron emission.

An Auger electron is observed when the system is in an excited state due to the recent emission of a core level electron (for instance, the K level). Therefore another electron from a different energy level (such as the L_3 shell) falls into the vacancy in the K shell and due to the extra energy in the system a third electron from an outer shell (L_1 for example) is then ejected to the vacuum level. This would be a KL_3L_1 Auger emission.

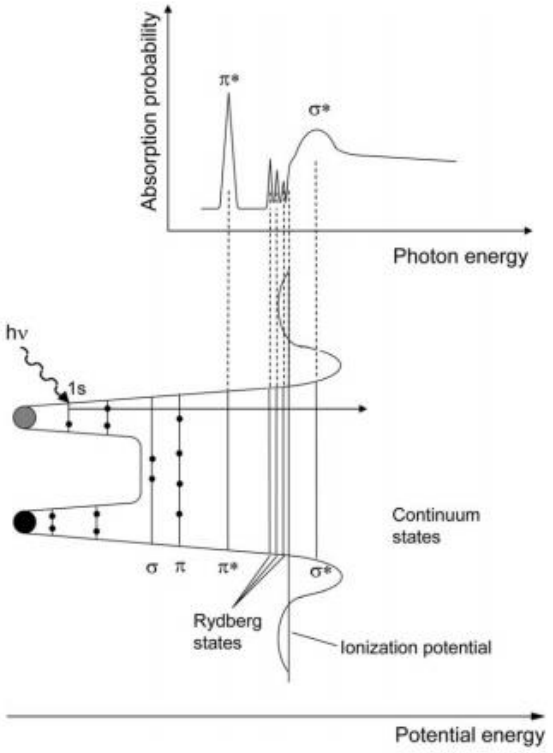

Figure 2.7.1 – *A sketch of the physical mechanisms of NEXAFS.* *From Hähner et al*[56]*. The bottom part of the image shows the x-ray absorption process. The top part shows an example of a possible outcome, showing the absorption probability in terms of the photon energy.*

For soft x-rays (used in surface science to detect low-Z elements), the ejection of an Auger electron is much more likely to occur than the radiative alternative therefore this method gives very good results. Let us assume that the studied system presents bonds with π and σ symmetry, (*eg*. an aromatic molecule, the unfilled π* and σ* orbitals are indicated with a star). The π* state usually corresponds to the Lowest Unoccupied Molecular Orbital (LUMO), while the σ* orbital is found at higher energy (see Figure 2.7.1).

A NEXAFS spectrum shows the absorption of the sample as a function of the energy of the incident beam: this cannot be obtained with a commercial x-ray lamp, therefore synchrotron radiation light is required. The energy scan can indeed by achieved with synchrotron light by adjusting the monochromator of the beamline. Moreover, synchrotron light also provides linearly polarized light: this feature is exploited to obtain the molecular orientation with respect to the surface. The probability of an absorption transition is maximized if the electric field of the light is parallel to the direction of a given molecular orbital (s-polarization), and it is minimized if the electric field is perpendicular (p-polarisation). Therefore, by measuring the NEXAFS with different absorption angles, the orientation of the molecule with respect to the surface is obtained.[57,58] For example, if an aromatic molecule is lying flat, with p-electrons pointing out of the plane of the surface, as shown in Figure 2.7.2, p-orbitals are usually perpendicular to the surface and therefore they would only be visible by the p-polarized beam.

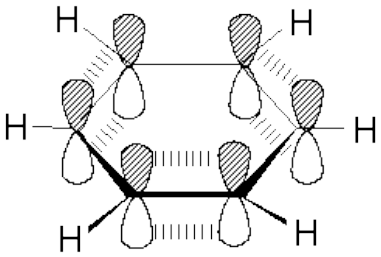

Figure 2.7.2 – *A scheme of the p-orbitals of a benzene ring.* *The six C atoms of a benzene ring are linked by σ bonds; the p electrons of the ring can participate in π bonding.*

For the case of a threefold surface symmetry (such as the (111) face of Au and Cu) and for the geometry of the system at ALOISA (ELETTRA), the angle between the aromatic ring of an organic molecule and the surface can be written as γ(R) in Equation (3):

$$\gamma(R) = \sin^{-1}\left(\sqrt{\frac{2cos^2\alpha}{R+3cos^2\alpha-1}}\right) \qquad (3)$$

where R is the ratio between the p- and the s-polarised intensity and α is the incident angle.[58]

Figure 2.7.3 represents an example of the difference between the p-polarization and the s-polarization peaks: it shows the C K-edge of diPy[5]DBH/Au(111) just after deposition (no annealing was performed). The

π* region (284-290 eV) is rich in sharp well defined peaks and each component represents a chemically different transition: for example the main peak at 284.9 eV is caused by the C1s transition of the aromatic rings to the π_1* empty state (see Chapter 4). Absorption of photons in an energy range between 290-310 eV results in broader resonances that arise from transitions to orbitals of σ*-symmetry.A sharp peak in the π* region is present for both p- and s-polarised light: as discussed above, this indicates that the π orbitals of the system are not completely perpendicular to the surface and therefore the molecule is not completely flat.

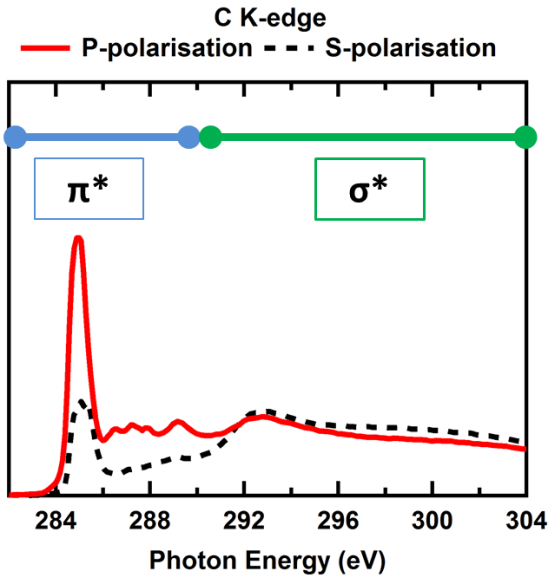

Figure 2.7.3 – *C K-edge NEXAFS spectrum of diPy[5]DBH/Au(111) at RT.* *The s-polarization and the p-polarization spectra are shown for comparison, in terms of the x-ray photon energy.*

In this thesis NEXAFS was recorded with Partial Electron Yield at the ALOISA beamline (ELETTRA, Trieste, Italy) and at D1011 (MAX-lab, Lund, Sweden). At ALOISA we recorded the spectra of DiPy[5]DBH/Au(111) and Cu(111) at different annealing temperatures, while at D1011 the ones of the same molecules on Cu(110).

2.8 Temperature Programmed Desorption (TPD)

TPD, also known as Temperature Desorption Spectroscopy (TDS), is used to understand the chemical composition of elements that are desorbed from a particular surface.

A Quadrupole Mass Spectrometer (QMS) is the main tool used for TPD. In a UHV chamber, the mass of the residual gas is determined by the QMS, which works by ionizing the atoms of the residual gas with a filament. These atoms are then accelerated between four metallic rods, which are connected electrically. By applying a radio frequency voltage between two opposite rods, only ions with a particular mass/charge ratio will make it to the end of the QMS, where they will be detected and differentiated according to their mass. A

sample is placed in front of the QMS and a programmed temperature ramp is started, so that the QMS can register the different masses that desorb from the surface at a particular temperature.

During this thesis, TPD spectra were recorded at the Technical University of Graz with Prof. R. Schennach. We documented the desorption of mass = 2 (corresponding to H_2 molecules) with temperature in the C_{60}/Pt(111) system and confirmed the presence of residual H on a clean Pt surface, due to the residual gas in the UHV atmosphere.

Unlike XPS and STM, TPD is a surface technique which is sensitive to the detection of atomic or molecular hydrogen. However, since hydrogen is the main contaminant of UHV chambers, and annealing of a filament is also known to release this element, the set-up of the experiment has to be carefully calibrated.

2.9 Density Functional Theory (DFT)

Theoretical calculations of the same systems that we have experimentally studied have been performed. These calculations can reproduce the experimental observation in a computer. The advantage is that from the calculation we can derive information about the energetic, electronic properties or atomic structure of the system in an atomistic way.

In order to calculate the correct electronic structure, theoreticians must know the optimised geometry of the systems, which is done by solving the Schrödinger equation for the desired system. The Schrödinger equation cannot be solved exactly for a many-body system therefore some approximations are needed. DFT describes and determines the ground state of a many-body structure by optimising the electron density: the system is described as a functional that represents the global electron density of the system.

The Born-Oppenheimer approximation is the basis of the first principle calculation methods, and it assumes that the movement of the electrons is much faster than the one of the nuclei, due to the much greater mass of the latter. Therefore it is possible to uncouple these movements and to solve them separately.

The DFT can describe the electron density in terms of either plane waves (for instance with the CASTEP code) or in terms of localized orbitals (*e.g.* with FIREBALL). The latter method is more efficient and less costly in terms of computational effort, although less precise than the first one.

When working with aromatic molecules, Van der Waals interactions have recently been implemented in the calculations and greatly improve the outcomes.[59,60]

During the course of this thesis, we have collaborated with several theoreticians to complement our experimental work. Dr Jose Ignacio Martinez Ruiz calculated the most stable configuration for DiPy[5]DBH on Pt(111) at room temperature, and the cyclodehydrogenation steps to obtain dihexabenzocoronene (Chapter 4). Dr Giulio Biddau and Prof Rubén Pérez performed calculations on the mechanism of vacancy formation of C_{60} on Pt(111), even though the results are not shown in this manuscript.

3. Tailored formation of N-doped nanoarchitectures by diffusion-controlled on-surface (cyclo)dehydrogenation of heteroaromatics

Surface-assisted cyclodehydrogenation and dehydrogenative polymerisation of polycyclic (hetero)aromatic hydrocarbons (PAH) are among the most important strategies for bottom-up assembly of new nanostructures from their constituent molecular building blocks. Although diverse compounds have been formed in recent years using this methodology,[8] *a limited knowledge on the molecular machinery operating at the nanoscale has so far disallowed to control the reaction outcome.*

In this Chapter, we show that the strength of the PAH-substrate interaction rules the competitive reaction pathways (cyclodehydrogenation versus dehydrogenative polymerisation). So, starting from the same molecular precursor and controlling its diffusion by the nature of the supporting surface, temperature-triggered dehydrogenation takes place to provide molecular or polymeric structures of variable dimensionality.

We employ in-situ Ultra High Vacuum Scanning Tunneling Microscopy (UHV-STM) to achieve the understanding of the self-assembling of molecular precursors on surfaces. Herein, by comparing the behaviour of two hetero-aromatic precursors on two different surfaces, we report on the control of competitive intramolecular and intermolecular dehydrogenative processes respectively called cyclodehydrogenation and dehydrogenative polymerisation by monitoring the diffusion of the precursors on the surfaces.

By choosing the appropriate N-heteroaromatic precursors and by controlling their diffusion, the on-surface (cyclo)dehydrogenation can either lead to monomolecular triazafullerenes and diazahexabenzocoronenes (N-doped nanographene), or to N-doped polymeric networks.

3.1 Introduction

The controlled on-surface formation of intricate π-electron systems may ultimately overcome the limits of the conventional synthesis, which often faces severe problems if large, fragile or insoluble molecules are to be prepared in solution and subsequently deposited on a solid substrate. Central to such efforts are complex carbon-rich molecules or materials, whose bottom-up synthesis at the nanoscale represents a great challenge today. Molecular architectures featuring π-conjugation are expected to mediate efficient charge transfer and, therefore, they are particularly attractive for future molecular electronics applications.

Since the discovery of graphene a significant progress has been made in the top-down approach to its etched or carved fragments. In contrast, on-surface synthesis appears as a key mechanism for controlling bottom-up assembling of new nanostructures.[8] Although this synthetic route is still in its embryonic state the first breakthroughs have already been reported. Thus, (hetero)fullerenes,[21,24] nanographene,[23] graphene nanoribbons,[17] domes,[22] aromatic oligomers/polymers or 2D architectures from suitable precursors have already been achieved. Therefore highly attractive π-electron systems on metal,[9,10,12,13,17,21–24,28,41] semiconductor or insulator[61] surfaces are available.

The bottom-up approach to achieve new functional nanostructures and two-dimensional (2D) materials should retain the key features of a traditional synthesis but also exploit specific phenomena such as on-surface self-assembly and on-surface reactivity of individual molecular components to covalently interconnect the outcome. This is particularly important when doping is required to modify the electronic properties of 2D materials, such as graphene. Substitutional doping is a powerful way of tailoring the material properties,[42] and the use of heteroaromatic precursors for the bottom-up reaction permits an easy and rational control of the doping in the final reaction outcome.

The emerging on-surface covalent coupling methodology[7,9–13,17,35–37,41,61–65] employs so far a limited portfolio of useful carbon-carbon bond forming reactions: cyclodehydrogenation (analogous to Scholl reaction), dehydrogenative oligomerisation[35] or polymerisation,[65] radical dimerisation[9,10,12,13,22,41] (analogous to Ullmann coupling), carbene dimerisation[36] and aryl halide-alkyne coupling[11] (analogous to Sonogashira reaction). Among these reactions, cyclodehydrogenation (intramolecular oxidative C-C coupling) and dehydrogenative oligo- or polymerisation (intermolecular oxidative C-C coupling) are especially attractive. The processes formally correspond to C-H activation of both precursors followed by their (cross)coupling.[8]

In particular, the mechanism of cyclodehydrogenation of an aromatic precursor and the role of the metal surface were studied experimentally and theoretically in details for the specific case of Cu(111):[23] cyclodehydrogenation was used to form nanographene following a rational methodology.

In this Chapter, we show that within this general frame of coupling reactions by dehydrogenation, the strength of the surface-adsorbate interaction can control the formation of new tailored nanostructures with different dimensionality. By controlling the diffusion of the precursors with the choice of the metal surface, we can drive the reaction towards the formation of zero-dimensional N-doped nano-objects, or towards the formation of covalent polyaromatic networks. A sketch is represented in Figure 3.1.1.

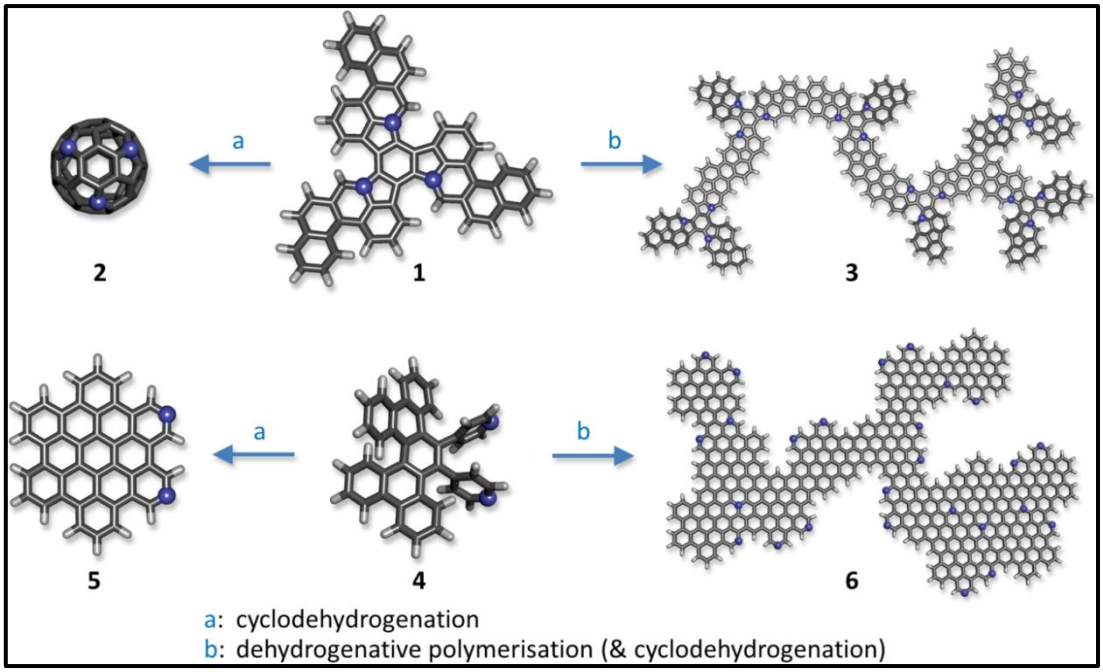

Figure 3.1.1 – *The heteroaromatic precursors 1 and 4 are subjected to controlled on-surface dehydrogenation.* *1* *and* *4* *may form respectively (i) nitrogen-doped triazafullerene* *2* *or 2,5-diazahexabenzocoronene* *5* *(both through intramolecular cyclodehydrogenation) or (ii) branched and cross-linked 2D polyaromatic architectures* *3* *or* *6* *(both through intermolecular dehydrogenative polymerisation accompanied by intramolecular cyclodehydrogenation). Nitrogen atoms are highlighted as blue balls.* *3* *and* *6* *represent only conjectural structures.*

3.2 Design of the model precursors 1 and 4

The choice of the geometry of the precursor is very important to program the outcome of the cyclodehydrogenation.[21,22,24] In order to study the substrate-controlled competition of on-surface cyclodehydrogenation *versus* dehydrogenative polymerisation, we have chosen two heteroaromatic precursors, **1** and **4** (Figure 3.1.1).

The three-fold symmetric clover-shaped and nearly flat crushed-fullerene precursor **1** ($C_{57}H_{33}N_3$) was already shown to undergo cyclodehydrogenation[21] on single-crystal platinum surfaces yielding to triaza-fullerene **2** ($C_{57}N_3$) by removing 33 H atoms and the consequent formation of new C-C bonds. This molecule was synthesised by Gómex-Lor *et al.*;[51] its shape was specifically designed to yield to the formation of a triaza-fullerene via cyclodehydrogenation. Chapter 5 of this thesis is entirely dedicated to the steps of the transformation of the pristine molecule into triaza-fullerenes.

The easily accessible[50] pyridyl-substituted dibenzo[5]helicene **4** ($C_{40}H_{24}N_2$) is a non-planar helical molecule. Precursor **4** can flatten through on-surface cyclodehydrogenation by the removal of 8 H atoms: the resultant formation of four new C-C bonds leads to the achievement of 2,5-diazahexabenzocoronene **5** ($C_{40}H_{16}N_2$), 2N-HBC, namely N-doped nanographene. In Chapter 4, we will study in details the mechanisms of transformation of this molecule.

Normally, polyaromatic precursors undergo cyclodehydrogenation rather than dehydrogenative polymerisation whenever possible due to steric factors (the loss of hydrogen is expected to occur

preferentially at sterically congested sites).[66] However, we propose that under certain reaction conditions the on-surface dehydrogenative polymerisation of **1** or **4** can compete with cyclodehydrogenation or even overwhelm it. In this scenario branched and curled nanoribbons or 2D cross-linked polyaromatic networks **3** or **6** can be formed on a metal surface.

3.3 Cyclodehydrogenation of 1 and 4 on Pt(111): a highly reactive surface

Pt is known to be a highly reactive surface and a good catalyst of dehydrogenation reaction of organic molecules.[20,21] We hence deposited precursors **1** and **4** under UHV conditions on Pt(111) at room temperature (RT), and this is represented in Figure 3.3.1. At low coverage (about 0.3 ML), the STM images show individual molecules of **1** (Figure 3.3.1-a) and **4** (Figure 3.3.1-c) scattered over the surface with no preferential adsorption at the step edges. This indicates that both precursors are well anchored to their adsorption sites and, accordingly, their diffusion is substantially restricted. However, the molecule-substrate interaction is not strong enough to disrupt the molecular structure.[67]

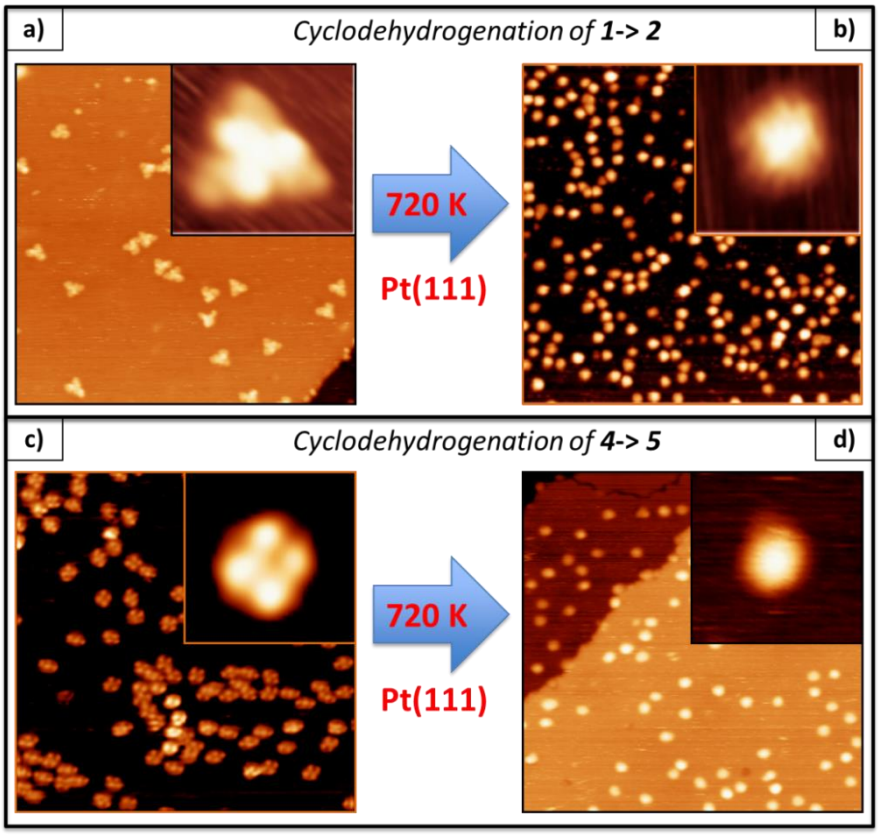

Figure 3.3.1 – Dehydrogenation of 1 and 4 on the Pt(111) single-crystal surface. *UHV STM images of about 0.3 ML of precursor **1** in (a) (30×30 nm^2, the inset 4×4 nm^2, V_s = +0.5 V) and precursor **4** in (c) (30×30 nm^2, inset 4×4 nm^2, V_s= +2.0 V) deposited on Pt(111) at room temperature show individual molecules with intramolecular structure corresponding to molecular orbitals. After annealing at 720 K, the cyclodehydrogenation process occurs and 1 is transformed into the spherical triaza-fullerene **2** in (b) (30×30 nm^2, inset 4×4 nm^2, V_s = +0.5 V) and **4** into the flat 2,5-diazahexabenzocoronene **5** in (d) (30×30 nm^2, inset 4×4 nm^2, V_s = +2.0 V).*

We performed DFT calculation for the case of **4** on Pt(111) and the results will be presented in Chapter 4. We found that the precursor **4** adsorbs 0.31 nm above the surface and reacts with the Pt by electrostatic interactions derived from Van der Waals forces with a binding energy of 1.5 eV per molecule, which is high enough to prevent its diffusion. However, the electrostatic nature of this interaction and thus the absence of covalent bonding does not modify the structure of the molecule as we experimentally observe: we can clearly distinguish in the STM images the shape of individual molecules and resolve the submolecular structure of **1** (in agreement with previous studies,[21,67] shown in the inset of Figure 3.3.1-a) and **4** (inset of Figure 3.3.1-c).

Upon annealing **1** and **4** on Pt(111) at about 720 K, they both change their shape, size and intramolecular structure (Figure 3.3.1-b and -d). The shape of **1** transforms from triangular to spherical (**2**) (Figure 3.3.1-b). The transformation of **1** to triaza-fullerene **2** is caused by the cleavage of all the C-H bonds and the spontaneous formation of new C-C bonds without rearranging the present bonds.[24] This transformation is accompanied by significant morphological changes: the width decreases from 2.2 to 1.2 nm and the apparent height increases from 0.20 to 0.35 nm. These observations are in agreement with related studies on fullerene nanostructures deposited on the same surface.[21]

Concerning precursor **4**, its internal structure with four bright lobes disappears upon annealing and rounded features are imaged with the STM (Figure 3.3.1-d). The lateral size (diameter) changes from 1.4 to 1.0 nm and the apparent height from 0.30 to 0.20 nm. This newly formed nanostructure features a loss of the intermolecular resolution (see inset) indicating the breakage of C-H bonds to form 2N-HBC, N-doped nanographene **5**. This agrees with previous studies on forming and imaging hexabenzocoronene structures on surfaces.[22,68,69] Finer details of this transformation will be discussed in Chapter 4.

The transformation of **1** into **2** is a process of complete cyclodehydrogenation, as the thermal activation involves the cleavage of all the C-H bonds, and all of the C dangling bonds link to form new cycles. However, only partial cyclodehydrogenation occurs in the process of transformation of precursor **4** into **5**, since only the inner H atoms detach while the peripheral ones are maintained.

3.4 Dehydrogenation of 1 and 4 on Au(111): a weakly interacting surface

Intriguingly, we obtain an entirely different picture when changing from the platinum substrate to gold (Figure 3.4.1). In contrast to Pt(111), the Au(111) single-crystal surface is known to interact weakly with adsorbed aromatics and, accordingly, it is considered to be inert towards some catalytic reactions.[70] Indeed, after the deposition of about 0.4 ML of **1** or **4** on the Au(111) surface at room temperature no molecules are seen by STM because they diffuse faster than the scanning speed (Figure 3.4.1-a and -c, respectively). The presence of **1** and **4** in its molecular form on the surface was corroborated by XPS and NEXAFS (see Chapter 4). These spectroscopic techniques also confirm the presence of N in the molecules on the surface.

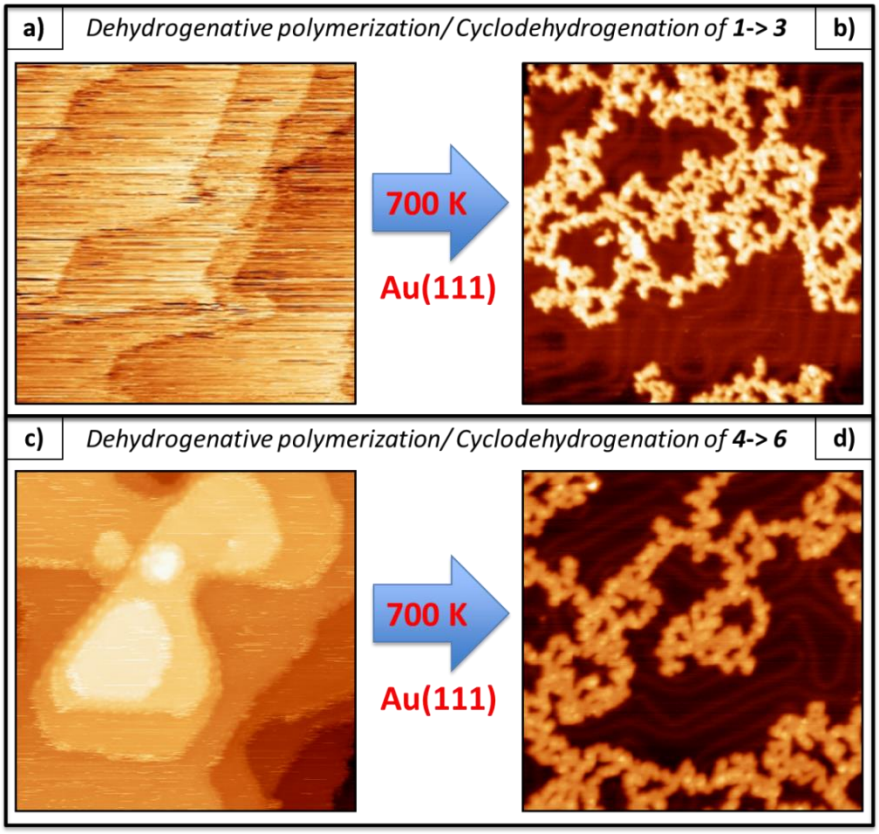

Figure 3.4.1 – *Dehydrogenation of 1 and 4 on the single-crystal Au(111) surface.* *STM images of 0.4 ML of precursor **1** in (a) (30×30 nm^2, V_s = +0.5 V) and precursor **4** in (c) (30×30 nm^2, V_s = +2.0 V) deposited on Au(111) at room temperature do not show individual molecules. After annealing **1** and **4** at 700 K, the dehydrogenative polymerisation/cyclodehydrogenation processes occur and **1** is transformed into the 2D heteroaromatic network **3** in (b) (40×40 nm^2 V_s = +0.75 V) and similarly **4** to **6** in (d) (40×40 nm^2, V_s = +2.0 V).*

However, upon annealing **1** and **4** to 700 K, we observe the formation of 2D polymeric cross-linked networks **3** and **6** (Figure 3.4.1-b and -d, respectively). The highly diffusing precursors **1** and **4** partially cyclodehydrogenate and dehydrogenate, meet other diffusing (and also dehydrogenated) adsorbed precursor and covalently bind together.

After a few molecules merge via dehydrogenative oligomerisation, the diffusion of such nanoclusters diminishes. Once these molecular seeds fix on the gold surface, a random network of branched molecules forms since polymerisation does not follow any preferential crystallographic direction. In some sections of the network, we can distinguish a triangular or round topology in their constituent units resembling that of the original precursor **1** and **4**, respectively.

Figure 3.3.1 and Figure 3.4.1 show that surface diffusion is the key mechanism driving cyclodehydrogenation and dehydrogenative polymerisation of the same molecular precursor (**1** and **4**) either to the formation of individual nano-objects (**2** and **5**) or extended networks (**3** and **6**) as schematically represented in Figure 3.1.1. The interplay between molecule-surface and molecule-molecule interactions causes the reaction to move towards either the left or the right in Figure 3.1.1.

The degree of polymerisation of the precursors **1** and **4** and, accordingly, the structure and dimensionality of the formed nano-objects can be controlled by two experimental parameters, namely by the annealing temperature and by the surface coverage (Figure 3.4.2).

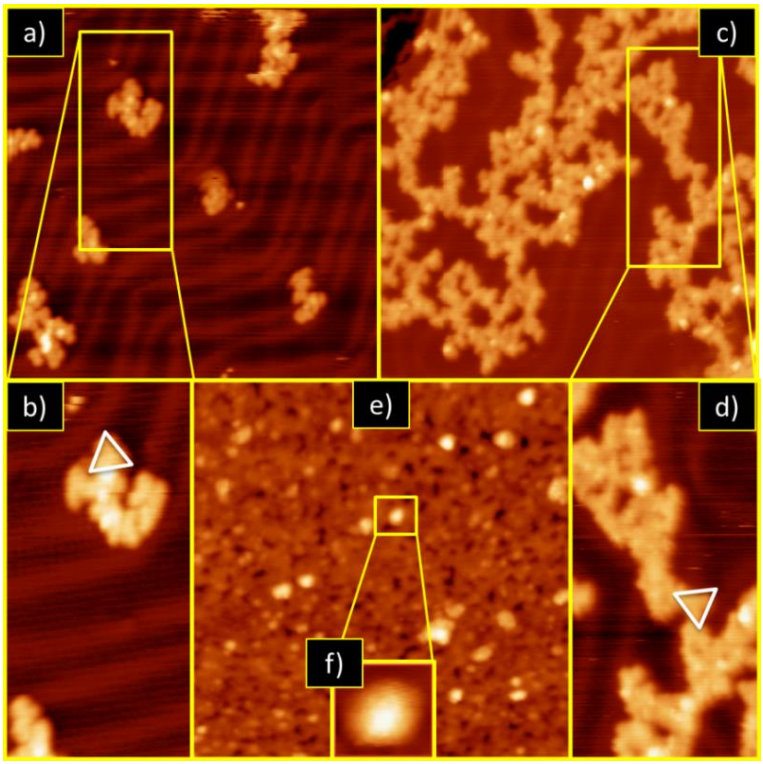

Figure 3.4.2 – *(Cyclo)dehydrogenation of 1 to form new nano-architectures with different dimensionality.* *STM images of **1** deposited on Au(111) at different temperatures and coverage. a) Small oligomeric clusters nucleate at the corner of the surface reconstruction (formation of 0-D nanostructures) if 0.1 ML is deposited at 540K (30x30nm^2). b) Zoom on one nano-aggregate (8.5x17.2 nm^2); the triangular topology that characterizes **1** can be clearly distinguished (white triangle) indicating only partial dehydrogenation. c) The formation of a linear polymeric network made up of individual molecules indicates a 2-D crosslinking of the deposited precursor when depositing 0.3 ML at 600K, (30x30nm^2). d) Detail of one of the branches of the polymer where the white triangle indicates the smallest building-block (8.5x17.2 nm^2). e) N-doped carbon 2-D layer is formed with a series of interlinked partially folded structures when 1 ML is deposited at 900 K (40x40nm^2). f) Individual heterofullerenes are observed embedded into the layer in some areas of the image (3x3 nm^2). Presence of N in all these nano-architectures was confirmed by XPS. Typical bias and tunnel current were 750 mV and 0.1 nA, respectively.*

Indeed, depositing a lower coverage of **1** (0.1 ML) on Au(111) and annealing to a lower temperature (540 K), small zero-dimensional oligomeric clusters **3** become visible by STM, as they anchor to the surface at the elbows of the herringbone reconstruction (Figure 3.4.2-a and -b) or at the step edges. High resolution STM images show that the oligomeric clusters **3** consist of a few covalently bound subunits where some retain the triangular shape of the precursor **1** (Figure 3.4.2-b, white triangle), meaning that only partial (cyclo)dehydrogenation of **1** took place, which leads to oligomerization rather than folding. These nanoclusters **3** are weakly bound to the surface since they can be easily moved by the STM tip.

Figure 3.4.3-a shows an STM image of low coverage of **1** deposited on Au(111) and annealed at 540 K. The molecules nucleate together at the corners of the surface herringbone reconstruction forming different aggregates. At this threshold temperature, we can observe the formation of one-dimensional oligomeric

nanostructures. Their height corresponds to that of individual intact molecules **1**. These nanostructures can be easily moved with the STM tip (see red circle), which manifests their weak interaction with the surface.

Figure 3.4.3-b represents the planar subunits of the oligomers parallel to the surface, which correspond to precursors **1**. The white triangles indicate the semi-intact molecules: the cyclodehydrogenation of these precursors is only partial, since they maintain their pristine shape; however the dehydrogenative oligomerisation is effective here. Curiously, the final morphology of the two different polymeric chains formed using **1** and using **4** as building blocks is similar. At low annealing temperature, the apparent height and width of the chains are in general those of a single intact molecule, meaning that most chains are unimolecular and that the cyclodehydrogenation of the building blocks is partial.

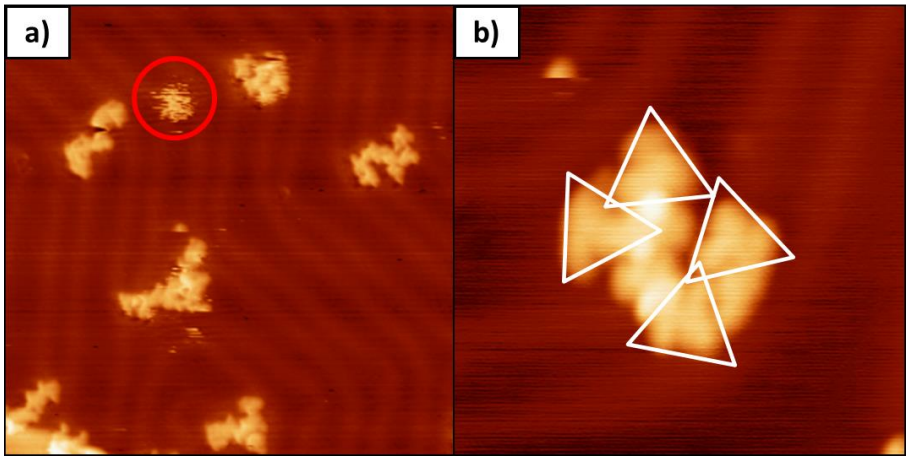

Figure 3.4.3 – ***Different oligomeric nanostructures obtained at a low coverage (0.15 ML) of 1 on Au(111) after annealing at 540 K.*** *a) The red circle in this image indicates and island which can be moved with the tip (29x29 nm^2, V_s= -1.5 V, I_t = 0.5 nA). b) The high resolution STM image of the most abundant nanostructure formed from* ***1*** *on Au(111) at 540 K (10x10 nm^2, V_s = -1.4 V, I_t = 0.2 nA); the white triangles superimposed on the image indicate the triangular molecules.*

Upon increasing the activation temperature to 600 K polymeric chains **3** topologically similar to those shown in Figure 3.4.1-b are formed (Figure 3.4.2-c and -d). However, in a few cases we can still distinguish the intermolecular structure of the original precursor **1**, as indicated by the white triangle in Figure 3.4.2-d. This shows that cyclodehydrogenation is also not complete at this temperature.

In order to form a complete two-dimensional N-doped carbonaceous monolayer, we increase the coverage to 1 ML and to favour the cylodehydrogenation process, the temperature of the substrate to 900 K. Then, all triangular-shaped substructures disappear and a dense carbonaceous sheet structure forms (Figure 3.4.2-e). Evidently, extensive dehydrogenative polymerisation took place but, at the same time, cyclodehydrogenation proceeded to a higher degree than at 600 K since open-cage and completely closed triaza-fullerene **2**, could be identified within the layer (Figure 3.4.2-f).

Thus, the layer's morphology is not fully flat but bumped. The origin of the height roughness is twofold. On one hand we have to keep in mind that N atoms are included in the layer, and the local density of states at the N sites can be much higher.[71] Secondly, **1** includes both pentagons and hexagons, and therefore the

precursor should (partially) fold upon (partial) cyclodehydrogenation. As mentioned above, the triangular features are not visible at this temperature, indicating an almost complete removal of H atoms and an intermolecular recombination process.

As we will show in Chapter 4, the formation of polymeric structures occurs for all coinage metals; moreover, similar structures will form on different Cu faces.

3.5 Conclusions

In this Chapter, we showed that the adsorbate-surface interaction plays a key role in tailoring the outcome of the on-surface dehydrogenation of suitable (hetero)aromatic precursors. Under temperature and substrate control, cyclodehydrogenation and dehydrogenative polymerisation compete to govern the on-surface reaction in favour of either individual molecular nanostructures (when their initial diffusion is minimised) or polymeric networks (when diffusion is enhanced).

We have found that either (i) a strong coupling of heteroaromatic precursors with the Pt(111) surface blocks the diffusion of molecules and, accordingly, thermally induced intramolecular cyclodehydrogenation dominates; or, in contrast, (ii) a weak coupling of heteroaromatic precursors with the Au(111), Cu(110) or Cu(111) surface allows the diffusion of activated molecules and, therefore, intermolecular dehydrogenative polymerisation takes place (along with cyclodehydrogenation).

Thus, by using the same heteroaromatic precursor, we can steer the reaction towards the formation of individual molecular nanostructures or complex heteroaromatic networks. Importantly, we demonstrated a straightforward bottom-up approach to nanoscale carbon-rich heteroarchitectures such as triaza-fullerenes, N-doped nanographene, N-doped polymeric networks and N-doped carbonaceous overlayers, which are not accessible by standard tools of chemical synthesis. In particular, the use of hetero-aromatic precursors allows a controllable way of achieving a doped result. Weakly reactive substrates such as Au(111) are also promoting surface chemistry, even though to a lower extent than the highly reactive one such as Pt(111).

4. Spectroscopic and morphological study of DiPy[5]DBH on different transition metals

In the novel subject of on-surface bottom-up formation of new architectures from functional molecular building blocks, the choice of the surface is a crucial parameter. In Chapter 3 we showed that by depositing a Polycyclic Aromatic Hydrocarbon (PAH) on different transition metals, the strength of surface diffusion of the as-deposited precursor rules the final outcome of the surface-assisted dehydrogenation. Hence on a weakly interacting surface such as Au(111), the studied PAHs diffuse at room temperature therefore, upon annealing, intermolecular dehydrogenative polymerization are favoured resulting in the formation of polymeric chains. On the other hand, a strongly interacting surface, as Pt(111), does not allow surface diffusion, impeaching the interaction with other nearby molecules. Thermal activation results in intramolecular cyclodehydrogenation, and as a consequence new "zero-dimensional" objects are created. On top of that, the selection of a correctly designed precursor is also vital to achieve the desired outcome. For example, $C_{57}H_{33}N_3$ on Pt(111) cyclodehydrogenates to form triaza-fullerenes,[21] *(see Chapter 5) and only the choice of the precursor with the right molecular design and the surface with the precise catalytic properties could have led to this transformation.*

As elaborated in Chapter 3, the pyridyl-substituted dibenzo[5]helicene (DiPy[5]DBH) can form either N-doped nanographene units, or polymerise to form covalent heteroaromatic chains. Again, the choice of the surface is responsible for driving the reaction towards one result or the other, by promoting either cyclodehydrogenation or dehydrogenative polymerisation.

In this Chapter, we study in detail the deposition of DiPy[5]DBH on four different metal surfaces, namely Pt(111), Cu(110), Cu(111) and Au(111). We report Scanning Tunneling Microscopy (STM), Near-Edge X-ray Absorption Fine Structures (NEXAFS) and X-ray Photoemission Spectroscopy (XPS) at different temperatures, and we combine the results of these techniques with Density Functional Theory (DFT). NEXAFS and XPS give precise chemical information on the surface, and are therefore very useful to understand the mechanisms of (cyclo)dehydrogenation in an atomistic way. These results are complemented with STM images, which provide a visual understanding of the situation. In the last Section, the STM data of the precursor on the four surfaces is combined to achieve a phase diagram of the stages undergone by the molecules, which gives insights on the reactivity of the studied metals.

4.1 DiPy[5]DBH on highly interacting metals: Pt(111)

4.1.1 Deposition on the surface at room temperature

The Pt(111) surface is known to be a good catalyst towards dehydrogenation of Polycyclic Aromatic Hydrocarbons (PAHs)[8,20,21,72], because of the particular electronic structure of its d-band, which allows high efficiency in the cleavage of hydrogen atoms from the organic molecule.

In some cases, such as for methane and ethylene, the molecules readily dehydrogenate at room temperature (RT);[20] however, depending on the precursor, sometimes this reaction needs to be promoted by an external injection of energy, which can be easily provided by the annealing of the sample. With this method, surface scientists have already achieved covalent networks[65] such as graphene nanoribbons,[17] and zero-dimensional structures such as nano-domes,[22] nanographene,[23] C_{60} and higher order fullerenes,[21,24] and triazafullerenes.[21]

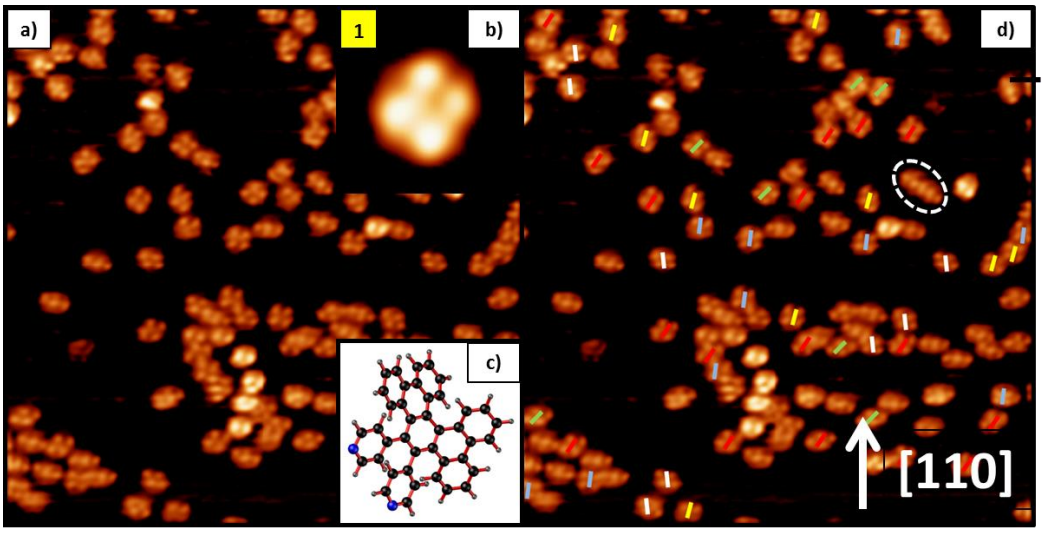

Figure 4.1.1 – *STM image of DiPy[5]DHB as deposited on Pt(111) at room temperature.* *a) 30x30 nm^2; Voltage applied to the sample (V_s) = 0.5 V. b) 4x4 nm^2 zoom of a single molecule: the intact diPy[5]DBH precursor will be referred to as **1**, as shown in yellow. c) A ball-and-stick model of **1**. d) The same image as (a) is shown, exhibiting the direction of the molecules with respect to the surface: each coloured line represents a direction. The lines have been drawn by cutting a molecule in two identical halves, and this allowed obtaining the position of their directional axis with respect to the Pt crystallographic vectors. The dashed white circle indicates two molecules with only two lobes, likely to be fragments of the pristine precursor.*

Figure 4.1.1-a represents an STM image 0.4 monolayers of the pyridyl-substituted dibenzo[5]helicene (diPy[5]DBH, $C_{40}H_{24}N_2$) on Pt(111). Randomly scattered four-lobe structures are observed. The apparent height (AH) of the objects is 0.28±0.02 nm, while the width is about 1.70±0.15 nm: since their size is comparable to the one of the molecules, we conclude that each four-lobe object represents a single molecule. The intact molecule at room temperature will be referred to as **1**. The zoom in Figure 4.1.1-b represents a single molecule, and the internal features correspond to a mixture of the topography (the tilted rings) with electronic effects (the spatial distribution of the lowest unoccupied molecular orbitals (LUMO)).

Figure 4.1.1-c exhibits a ball-and-stick model of the precursor, which indicates that the isolated molecule still maintains its three-dimensional (not flat) structure although it is fixed on the surface.

Upon deposition, the molecules stick where they land: this indicates that the interaction with the surface is stronger than the intermolecular forces, meaning that the precursors cannot diffuse and form ordered islands. The fact that we can actually observe the intramolecular resolution indicates that the interaction between the molecules and the Pt is not strong enough to disrupt the molecular structure, even though it is high enough to prevent diffusion.

When deposited, **1** sits in five different directions, represented in Figure 4.1.1-d by different coloured lines. Due to the threefold symmetry of the system, the molecular orientations turn out to be only three: at 30±5º, 15±5º and 7±5º with respect to the $[1\bar{1}0]$ crystallographic direction of Pt. Although the real angle is hard to determine, because of the error in determining the Pt's crystallographic directions from the STM, the rotational difference between the molecules on a particular image is accurate. These angles would correspond to the main directional axis of the molecules (Figure 4.1.2-a) oriented respectively along the (1,1), (1,3) and (1,6) directions with respect to the Pt(111) surface, as shown in Figure 4.1.2-b. These directions originate angles of 30º, 15.9º and 8.7º respectively, in good agreement with the angles reported by the STM.

The main directional axis of **1** (Figure 4.1.2-a) is estimated to be the only one which symmetrically cuts the precursor in two mirroring halves, however only DFT calculations can confirm this assumption. The fact that the molecule can only orient in three ways indicates that even though the molecules are not energetically allowed to diffuse, they adjust with respect to the surface in order to find the minimum energy configuration, as in the case of other large PAHs on the same surface.[67]

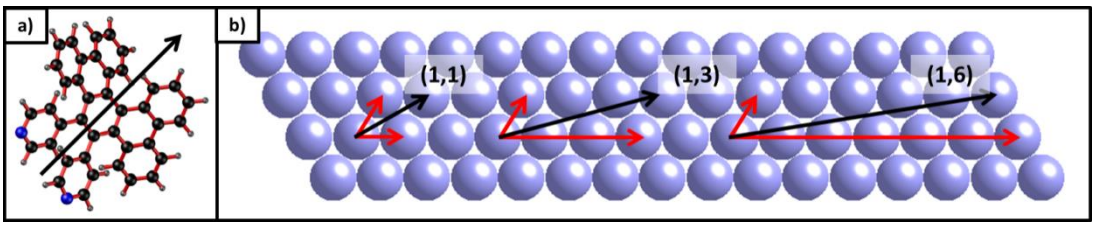

Figure 4.1.2 – ***Orientation of the main directional axis of the molecules with respect to the Pt(111) vectors.*** *a) A possible main directional axis of the molecule is indicated by a black arrow superimposed to the ball-and-stick model of diPy[5]DBH. b) The lilac spheres indicate atoms of the Pt(111) surface; the main directional axis of the molecule can orient in three different directions, namely (1,1), (1,3) and (1,6); the resultant vector is indicated by a black arrow.*

Curiously, Figure 4.1.1-a and -d (see dashed white circle) reveal that there are some exception to the four lobes configuration mentioned above: some molecules only exhibit two or three lobes. If we suppose that the four lobes of the molecular orbitals correspond to the intact molecule, the molecules exhibiting fewer lobes would indicate fragments broken in the evaporator.

Figure 4.1.3-a represents the STM image of **1** compared with its theoretical simulation (Figure 4.1.3-b), and the LUMO representation of the free molecule (Figure 4.1.3-d), obtained with an isosurface of $4x10^{-5}$ electrons/Å^2; both experimental and theoretical images are oriented as the structure shown in Figure 4.1.3-

c. We will later discuss how according to the *ab-initio* calculations, the interaction between the pristine molecule and the Pt surface is electrostatic at room temperature, and this allows the molecule to maintain its three- dimensional shape caused by its helical structure.

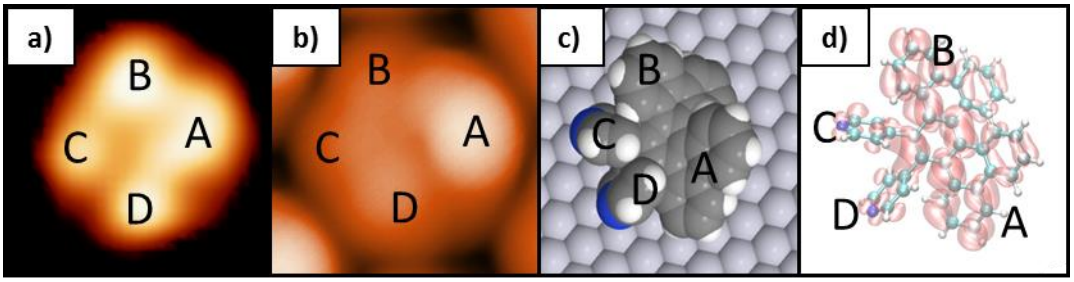

Figure 4.1.3 – *STM image, simulation and structure of a deposited molecule at RT on Pt(111).* *The letters A-D represent a different lobe. a) An experimental STM image of **1** exhibiting four bright lobes (2x2 nm^2; V_s = 2.0 V). b) The theoretical simulation of the intact molecule at RT. c) The calculated structure of the relaxed precursor at RT, oriented in the same way as (a) and (b). d) The free molecule molecular orbital (LUMO) obtained with an isosurface of 4x10^{-5} electrons/Å^2.*

The experimental STM image of the molecule presents four bright lobes, reproduced by the theoretical simulation. The similarity between the two indicates that the molecule remains intact upon deposition. Since the model structure is oriented so that they can be superimposed to the theoretical simulation and the experimental image (each letter on top of each lobe indicates an analogous feature), the brightest lobe A is caused by the phenyl ring of the helicene which is tilted with respect to the substrate. Lobes B and C are related to the two pyridine rings (ring B is standing higher than ring C) and lobe C to one of the two benzene rings. Figure 4.1.3-d represents the theoretical LUMO of the free molecule. Since it does not exhibit four clear lobes, we can conclude that the features observed with the STM are mainly due to a topographical effect rather than to an electronic one.

To understand the catalytic effects of Pt(111) on this molecule, and to try to achieve N-doped nanographene via cyclodehydrogenation of the precursor, we anneal the samples to different temperatures, up to 830 K, in steps, to have a full picture of the different chemical stages undergone by the precursor. Above 830 K, the molecules disrupt to form graphene. As displayed in Figure 4.1.4-a and -d, STM images indicate that the structure with the four lobes of the molecular orbitals is present up to about 400 K. At this point, the precursor changed aspect, and only two lobes (one brighter than the other) were visible. The change of the aspect of the molecule reflects a structural change caused by the annealing. This structure is explained in details below, and it will be referred to as **2**, as indicated in the image.

Figure 4.1.4-b, -c, -e and -f show the complete loss of molecular orbital resolution triggered when further heating the sample to 650 K and to 770 K: the molecules transform into uniform round features. The zooms (Figure 4.1.4-e and -f) clearly show that in both cases no intra-molecular resolution is present. An attentive reader may relate the absence of such feature to a poor resolution of the tip. However, we scanned hundreds of images of annealed samples and no intramolecular resolution was ever seen, while for the un-annealed samples the observation of MO was standard. Interestingly, the panorama after annealing to 650 K is different from the one after heating the sample to 770 K. Figure 4.1.4-b and -c compare two 25x25 nm^2

images after annealing at 650 and 770 K respectively, and the molecules at 650 K (referred to as **3** from now on) seem broader than the majority of the molecules at 770 K (**4**), and this is highlighted by the 7x7 nm^2 zooms (Figure 4.1.4-e and -f).

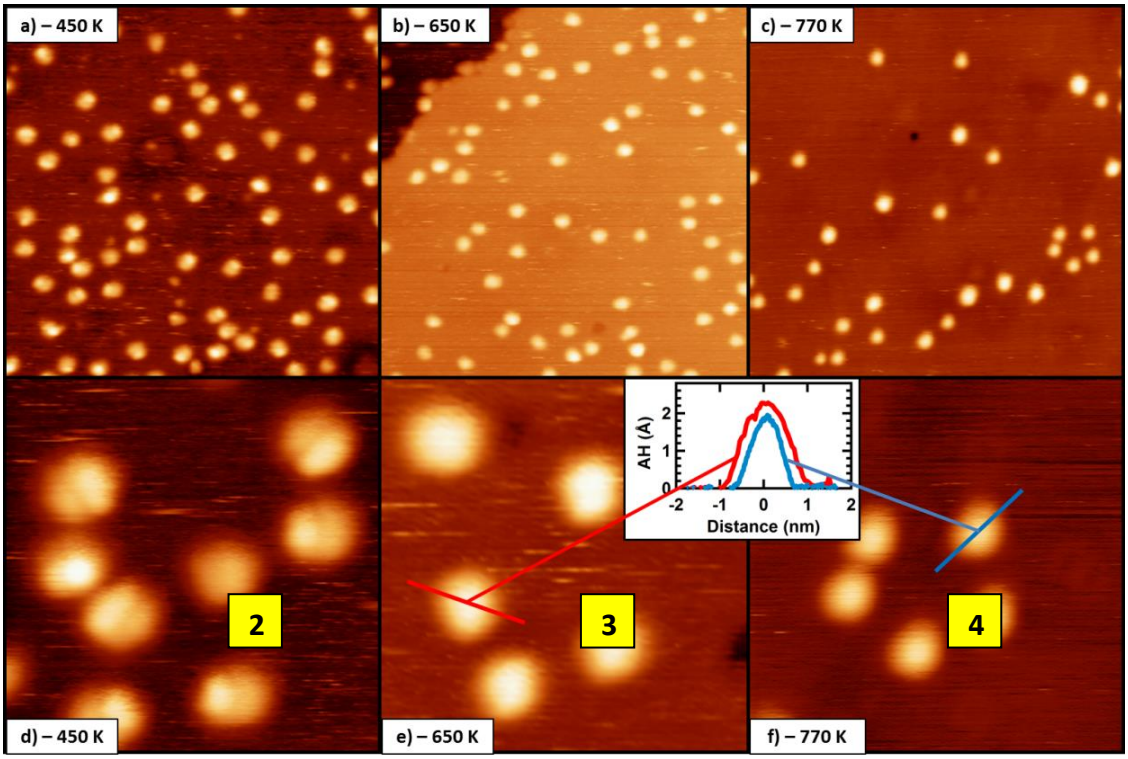

Figure 4.1.4 – ***Three different types of molecules arise when annealing DiPy[5]DHB/Pt(111) at 450 K, 650 K and 770 K.*** *The images at the top have the same size (25x25 nm^2) as the images at the bottom (7x7 nm^2). a) When the sample is annealed at 450 K, the molecule transforms and only two lobes are visible, a brighter and a dimmer one (25x25 nm^2; V_s = 2.0 V). b) As the sample is annealed at 650 K, the intramolecular resolution is lost (25x25 nm^2; V_s = 2.0 V). c) If the sample is further heated to 770 K, most molecules become smaller than the ones observed in (b) (25x25 nm^2; V_s = 2.0 V). d) A 7x7 nm^2 zoom of (a) highlights the features of the molecules at 450 K: these molecules will be referred to as* ***2****. e) A more detailed image of the sample annealed to 650 K: these molecules will be referred to as* ***3*** *(7x7 nm^2; V_s = 2.0 V). f) A smaller image of the sample annealed to 770 showing five molecules: these molecules will be referred to as* ***4*** *(7x7 nm^2; V_s = 2.0 V). The inset in between (e) and (f) shows the Apparent Height profiles of one molecule annealed to 650 K (red) compared with the one of a molecule annealed to 770 K (blue): the latter is smaller both in width and in height.*

The apparent height profiles of **3** and **4** in the inset clearly indicate that annealing the precursor at 650 K (**3**, red) triggers the formation of a molecule with a particular structure, which differs from the outcome obtained when increasing the temperature further (**4**, blue).

Table 4.1.1 schematically exhibits the typical apparent height and the typical width of an intact precursor at room temperature **1**, compared with the outcomes arising after the structural changes upon annealing at 450 K (**2**), 650 K (**3**) and 770 K (**4**). Notice how both the height and the width of the representative molecules decrease with temperature. Therefore the precursor must undergo at least three structural transformations upon annealing (before forming graphene). We recorded the apparent height profiles of about thirty molecules at each temperature, to achieve statistical validity.

Annealing T (K) + molecule type	Apparent Height (± 0.02 nm)	Width (± 0.15 nm)	Molecular Orbitals at V_s = 2.0 V
RT (**1**)	0.28	1.70	4 lobes
450 (**2**)	0.28/0.23	1.50	2 lobes
650 (**3**)	0.23	1.44	NO
770 (**4**)	0.19	1.25	NO

Table 4.1.1 – ***The apparent height and the width of DiPy[5]DBH annealed at four different temperatures.*** *The height and width of the non-annealed sample **1** (observed with four lobes in the STM) are compared with the ones of the molecule annealed at 450 K (**2**), 650 K (**3**) and to 770 K (**4**): the three molecules are different. The apparent height profiles were measured on about 30 molecules at each stage, to obtain statistical validity. The last column indicates whether molecular orbitals are observed with the STM.*

Interestingly, Figure 4.1.4-c indicates that not all the molecules annealed to 770 K undergo the full transformation from **3** to **4**: some exceptions exhibit the same size as the precursors annealed to 650 K of Figure 4.1.4-a and -b, showing that the at this temperature the structural transition is only partial and the transformation process is slow.

As mentioned above, the change of the observed intramolecular structure in **1**, **2**, **3** and **4** and the decrease in the apparent height and width imply a structural change of the molecule itself. In order to understand these variations, we performed theoretical STM simulations, which are shown in Figure 4.1.5. In this image each column represents a different temperature. The top row shows the annealing temperature, the second row the structure of the molecule (oriented as the next two rows), the third row the theoretical STM simulation of the precursor at a given temperature, the fourth row the experimental STM image (2x2 nm^2) and the last row the experimental apparent height compared with the theoretical one.

The first column of Figure 4.1.5 represents **1** at room temperature. As discussed above, the essential features of the four bright lobes of the experimental STM image are replicated by the simulation, and this also indicates that the molecule does not break upon deposition. Phase **2** is an intermediate stage between **1** and **3** and it is represented in the second column of Figure 4.1.5. Upon thermal activation at 450 K, **1** undergoes a partial cyclodehydrogenation, in which six C-H bonds break and three new C-C bonds form to create three new aromatic rings. The two tails of the helicene bind together as a consequence of cyclodehydrogenation, and the two pyridine rings bind with the benzene rings. This change is reflected in the experimental and theoretical STM images, where a drastic change occurs: three of the bright lobes of **1** merge to form a unique lobe. This result reflects the formation of three new aromatic rings in the molecule. According to the apparent height profile, the experimental STM image reveals a brighter lobe (0.28 nm) and a dimmer lobe (0.23 nm). The bright part corresponds to one of the pyridine rings being farther from the surface due to steric and geometrical effects.

Further thermal activation allows the cleavage of the two C-H bonds in between the two pyridinic rings, and the subsequent formation of a new C-C link which creates a new aromatic ring, forming **3**, diaza-hexabenzocoronene (2N-HBC), also known as N-doped nanographene. The transformation from **2** to **3** results in a structural change which is reflected in the experimental and theoretical STM as a complete loss of molecular orbital resolution, as represented in the third columns of Figure 4.1.5, which shows a molecule from the sample annealed at 650 K. The profile shows a decrease in apparent height to 0.23 nm and in width

to 1.44 nm. Curiously, the central part of the molecule is not flat, as it would be expected by a flat molecule such as this one: the reason for this may be assigned to the tip geometry: this is reproduced by the pyramidal W-tip employed in the calculations. The use of a tip with large curvature can account for the experimental shape. Other authors have also analysed similar molecules on transition metals,[22] and observed an apparent height of about 0.10 nm: this difference with respect to our system is likely to be due to their greater surface-adsorbate interaction, such as a covalent bonding between the two.

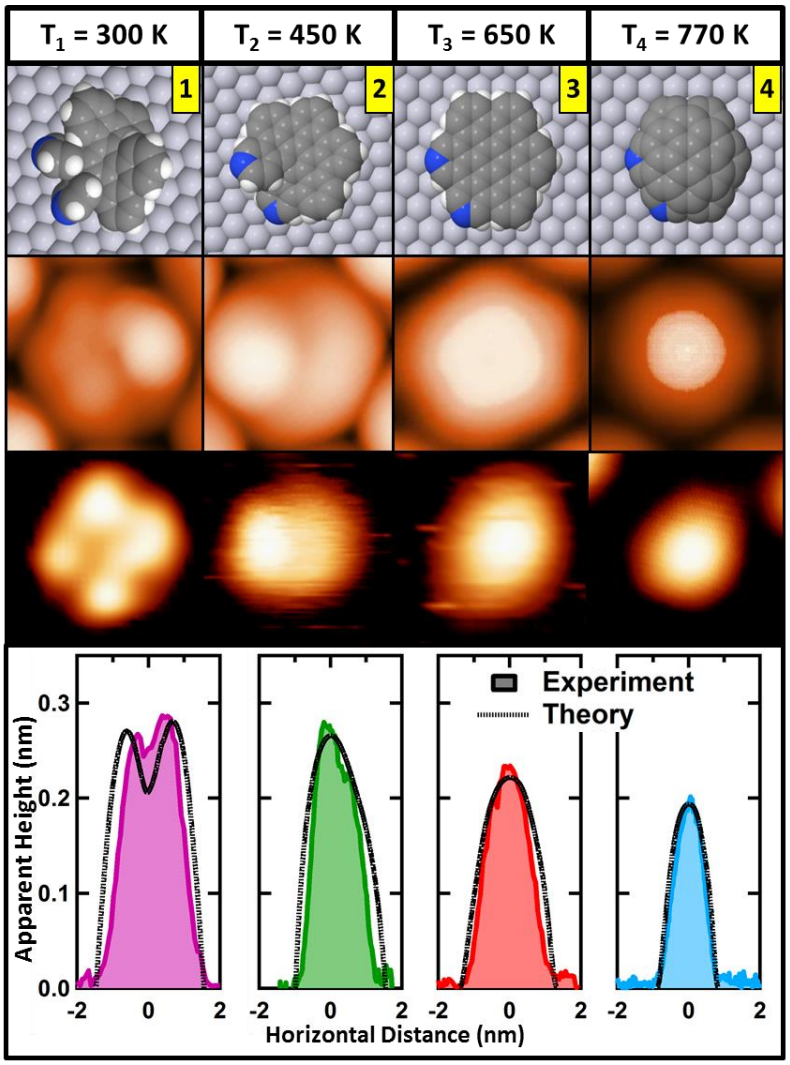

Figure 4.1.5 – ***Each column of this image represents one of the four main stages of the transformation of the pristine molecule 1 into the intermediate step 2, to N-doped nanographene 3 and to a N-doped nano-dome 4, upon thermal activation.*** *The first row represents the annealing temperature. The second panel reveals the structure of a given stage: this structure is oriented so that it can be superimposed onto the STM simulation, shown in the third panel. The fourth row represents the experimental STM image of each stage (2x2 nm^2; V_s = 2.0 V). Finally, the last panel shows the experimental apparent height (solid coloured line) as compared to the theoretical apparent height (dashed black line).*

The fourth column of Figure 4.1.5 shows the next annealing step at 770 K, which has the effect of cleaving all the remaining H atoms, namely the ones at the edges, from the molecule. As for the case of Rim *et al.*,[22] the effect of the complete dehydrogenation of the molecule is to curve the precursor into an N-doped nano-

dome (**4**). Since the breakage of the C-H bonds at the edge does not generate any organic cycle, we must refer to this process as to dehydrogenation, as opposed to cyclodehydrogenation, which is the formation of an aromatic ring caused by the cleavage of one or more C-H bonds. The energy to break the internal C-H bonds is lower than the one needed to cleave the bonds at the edge due to steric effects,[66] therefore the first H atoms to leave the molecule are the more central ones: however if we supply high enough energy to the system the edge atoms detach as well. This sequence allows obtaining a hierarchical order for the dehydrogenation of the molecule. This gives us the power to select the desired outcome, simply by controlling the annealing temperature and hence the energy supplied by the system.

As for the case of **3**, **4** does not exhibit any intramolecular resolution. However its width decreased to 1.27 nm and its height to 0.19 nm. This is somewhat unexpected, since upon this last dehydrogenation step the molecule bends, and the central core is elevated with respect to the edges, as shown in the second row of the last column of Figure 4.1.5. The reason for the decrease of the apparent height of **4** with respect to **3** is that the dangling C bonds at the edges bind covalently with the Pt underneath. So, even if **4** is three-dimensional and **3** is planar, the N-doped nano-dome is much closer to the Pt than the N-doped nanographene, whose edges are passivated by the H atoms. Therefore the nano-dome **4** appears smaller than the nanographene **3**.

This (cyclo)dehydrogenation reaction is catalysed by the Pt surface, which lowers the energy barrier needed to break the C-H bond. To better understand the cyclodehydrogenation steps of the transformation of **1** into **3**, we performed Density Functional Theory (DFT) calculations, by means of large-scale *ab-initio* simulations including all molecule-surface interactions, as Van der Waals, in a DFT framework within a Local Density Approximation. This investigation was not restricted to the ground state of the isolated species, but gave detailed insights of intramolecular C-C coupling by explicitly computing reaction barriers to explain the formation of N-doped nanographene out of our heteroaromatic precursor.

Figure 4.1.6 reveals the results of the calculations.

Upon deposition (step I), diPy[5]DBH remains intact (**1**), with its three dimensional shape, and no hydrogen atoms are lost. As described above, the pyridinic rings are not lying flat on the surface, but they are almost perpendicular, and we obtained a minimum energy structure with the precursor located at a perpendicular distance of 3.2 Å above the substrate. This indicates that the molecules are not covalently bonded with the surface, but a strong electrostatic interaction prevents diffusion and allows the molecule to remain intact upon deposition.

At this point, we propose a reaction energy path consisting in the consecutive cyclodehydrogenation of DiPy[5]DBH. The characterisation of the energy of each C-H bond forming the molecule reveals that some hydrogen atoms are participating in weaker bonds with C. The reaction energy path is composed by intermediate steps (II-VIII), as shown in Figure 4.1.6. Step VII corresponds to **2** in Figure 4.1.5.

The complete reaction is a sequence of mechanisms, involving: (a) thermal and kinetic-promoted removal of a “weak” hydrogen (energy barrier, 1.5 eV); and (b) slight rotation of the corresponding dehydrogenated aromatic ring towards the neighbouring “weak” C-H bond and the fracture of this C-H bond to form a new C-C bond by radical aromatic addition (energy barrier, 1.4-1.6 eV). These mechanisms are repeated four times to complete the formation of four C-C bonds. The full reaction pathway (Figure 4.1.6) is completed with a net energy gain of 2.48 eV in favour of the N-doped nanographene **3** reaction product.

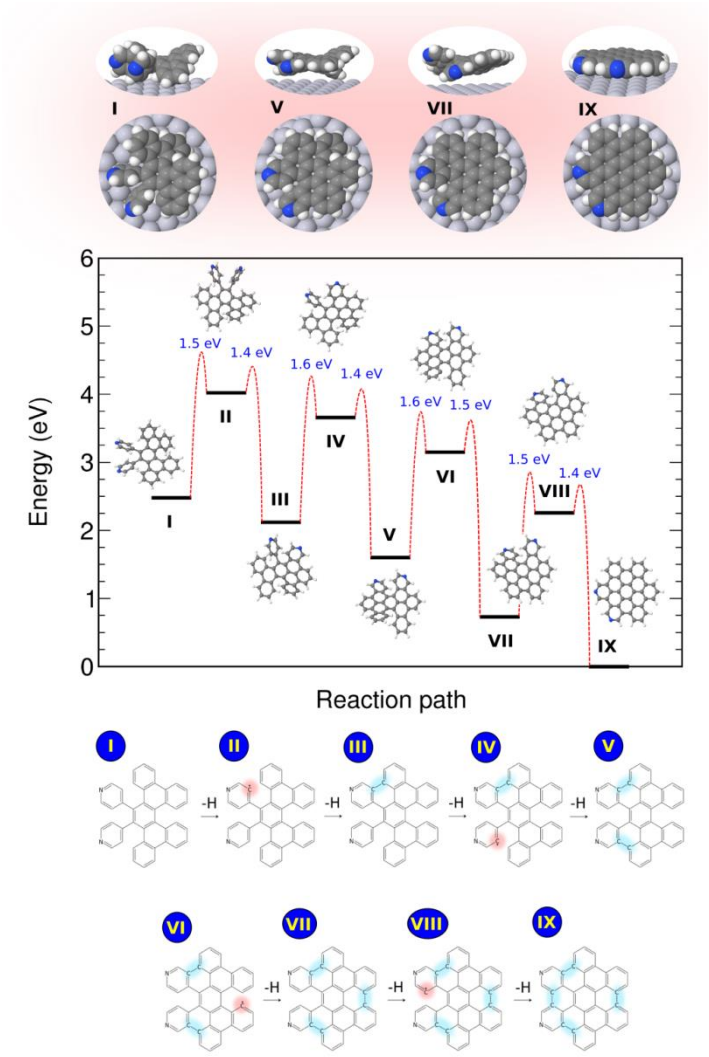

Figure 4.1.6 – *The computed reaction path of the cyclodehydrogenation of DiPy[5]DBH on Pt(111) upon annealing (steps 1 to 3).* *The reaction proceeds via seven metastable intermediates (II-VII). All energies (in eV) are referred to the final N-doped nanographene reaction product (step IX). Energy barriers (in eV) are shown for each elementary step. Images of the most representative metastable states (I, V, VII, IX) along the surface-assisted cyclodehydrogenation process are also depicted (top panels). A chemical structure diagram is included (bottom panel) to visually illustrate the different dehydrogenation steps (highlighted in red) and the subsequent C-C bond formations (highlighted in blue).*

UHV-STM on surface synthesis of nanographene was also performed by Treier *et al.*[23] by cyclodehydrogenating cyclohexa-*o*-*p*-*o*-*p*-*o*-*p*-phenylene (CHP) on Cu(111). The authors observed with the STM different stages undergone by the molecules and interpreted them as different steps of partial cyclodehydrogenation up to the formation of nanographene. Moreover, they also performed large-scale DFT. Surface-assisted cyclodehydrogenation started with a copper-promoted cleavage of the C(sp^2)-H bond to generate an aryl radical that attaches to a neighbouring aromatic units via radical aromatic addition forming thus the aryl-aryl bond. The reaction is completed by the copper-promoted removal of hydrogen and final release of recombined H_2. Importantly, as for our case, when the system overcame a given energetic barrier, it fell back to the next minimum and it needed another energy injection to overcome the next barrier.

As discussed above, according to DFT, when more energy is injected in the system, a further structural phase transition occurs after the formation of 2N-HBC **3**, which involves the full dehydrogenation of the molecule, by cleaving also the H atoms at the edge (see Figure 4.1.7).

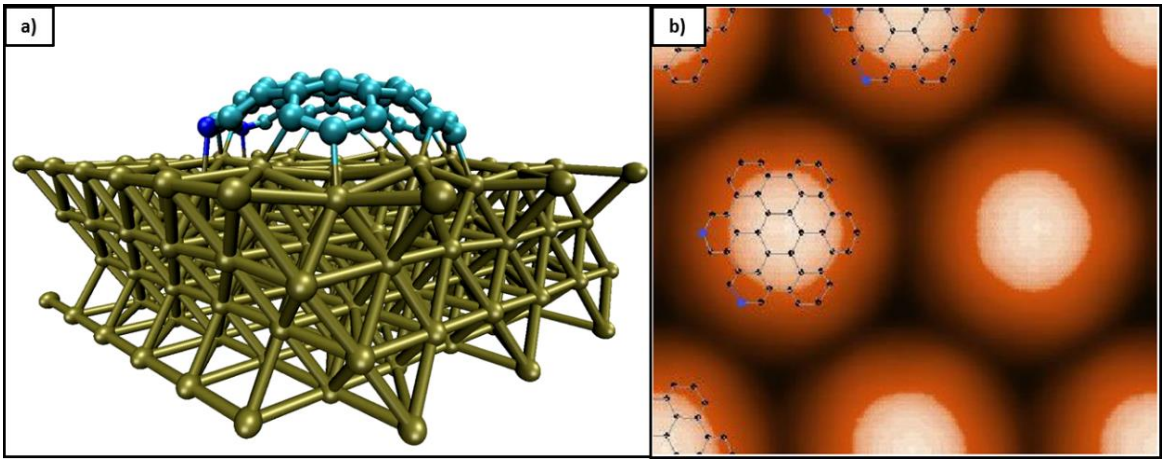

Figure 4.1.7 – *DFT representation of the complete dehydrogenation of DiPy[5]DBH/Pt(111) and subsequent formation of N-doped domes 4.* *a) A three-dimensional representation of the formation of **4** on Pt(111); the light blue atoms indicate the C and the dark blue ones the N, while the green ones the Pt. Notice how the C atoms at the edge bond with the Pt causing the bending of the molecule. b) A ball-and-stick model of the dome is superimposed to the simulation of the STM images, measured with a current of 0.1 nA and a sample voltage of 2.0 V.*

The calculations hence suggest that the dangling C atoms at the edge bond with the surface and the N-doped nanographene **3** bends into an N-doped nano-dome **4**. Figure 4.1.7-a represents a ball-and-stick model of the dome, and it indicates how the edge C atoms bond with the Pt causing a bending of the molecule: for the case of **3**, the edge C atoms were passivated by the H atoms, and this caused the molecule to lay flat on the surface. Figure 4.1.7-b shows the STM simulation of **4**: it confirms that no intramolecular resolution should be observed, as for the case of the experimental STM images.

The STM simulation of the two structural phase transition of **1** into **3** and into **4** allowed us to record the theoretical apparent height profile and to compare it with the experimental one (Figure 4.1.8).

The left panel of Figure 4.1.8 represents the experimental apparent height profiles of a typical 2N-HBC (red) and a typical N-dome (blue): as discussed above (Table 4.1.1), 2N-HBC is wider and taller than the N-dome. This is confirmed by the theoretical apparent height profiles (right panel). The width of the theoretical simulations is about 5% broader than the one of the experiment, but it lies within the error.

As discussed above, these apparent height profiles confirm the proposed evolutions of **1** into **3** and successively into **4**: the first structural phase transition at 650 K allows the cyclodehydrogenation of the weakest C-H bonds, causing the formation of N-doped nanographene flakes at about 650 K (2N-HBC); the second phase transition involves the cleavage of the remaining H atoms on the edges, and this effect causes the edge C atoms to covalently bond with the surface and the subsequent bending of the molecule into a dome. The edges of 2N-HBC are passivated with H atoms, therefore, as for the case of the intact molecule at room temperature, only an electrostatic interaction binds the molecule with Pt, and the distance with the

surface is of the order of 3.2 Å. However, when the N-domes form, the dangling bonds of the edge C atoms bond covalently with the Pt upon complete dehydrogenation, and this causes a decrease in the surface-adsorbate distance. This mutation in the interaction with the surface therefore allows the counter-intuitive decrease in the apparent height when the domes form.

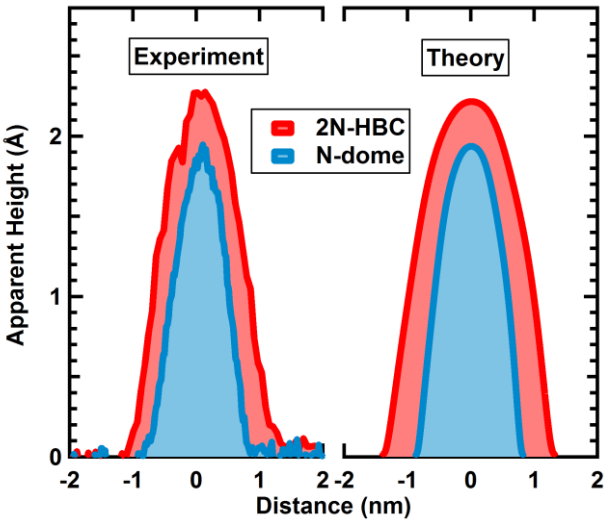

Figure 4.1.8 – *Experimental and theoretical apparent height profiles of 2N-HBC 3 and N-dome 4.* *The left (right) panel shows the apparent height profile of the experimental (theoretical) evolutions of DiPy[5]DBH, namely 2N-HBC (red) and N-domes (blue). The N-dome is shorter and narrower than the 2N-HBC. The sample voltage of both theoretical and experimental images was 2.0 V.*

The final value of the apparent height of the N-domes (0.19 nm) resembles the apparent height of the domes grown with hexabenzocoronene (HBC) on Ru(0001) by Rim *et al.*[22] (0.20 nm); in their case, the molecule was flat at room temperature, therefore the transformation into a hemisphere results in an overall increase in the apparent height.

The apparent height of 0.28 nm measured at room temperature is due to various factors, such as the three-dimensional nature of the precursor and to the electrostatic interaction with the surface (as opposed to a stronger bond which would bring the molecule closer to the surface). Moreover, the height measured with the STM is a convolution of the topographic and electronic effects, which may play a great role at room temperature, due to the presence of the N dopants. The decrease in apparent height from **1** (0.28 nm) to **3** (0.23 nm) reflects the flattening of the molecule due to the 2N-HBC formation caused by the cyclodehydrogenation.

As discussed before, further annealing to 830 K leads to the observation of large graphene flakes. Figure 4.1.9-a proves that graphene islands coexist with the N-doped nanographene domes. Upon further annealing (Figure 4.1.9-b) the STM shows no more nanographene fragments, just large graphene islands.

The mechanism of formation of graphene has been the topic of different experiments.[55] Here, the bonds that formed the molecules break to form larger graphene islands at the Pt steps. The steps are in general more reactive sites, ideal for triggering the formation of graphene.

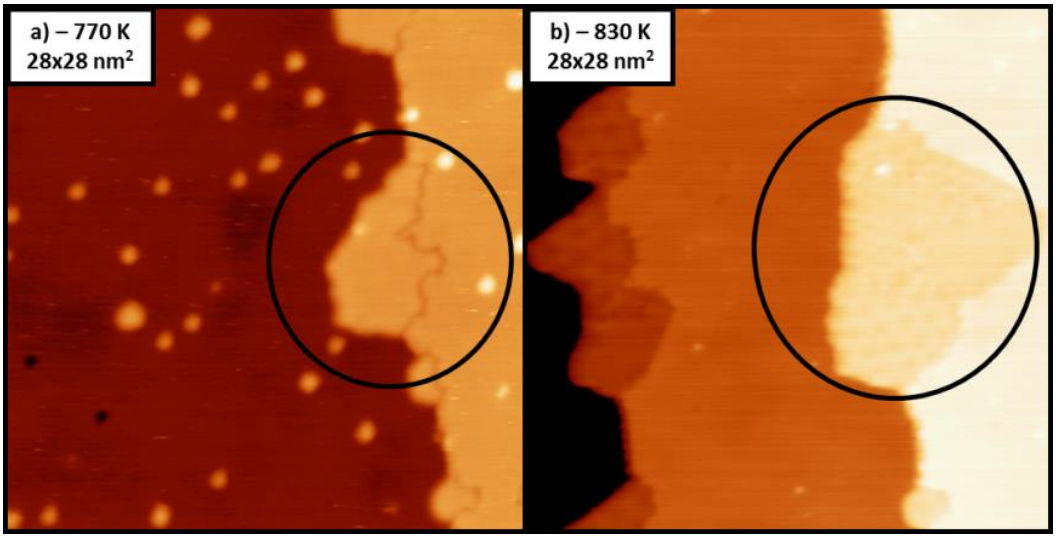

Figure 4.1.9 – *Graphene formation from DiPy[5]DBH.* *a) At 770 K large graphene islands (black circle) co-exist with N-doped nanographene flakes (28x28 nm^2; V_s = 2.0 V). b) At 830 K no more molecules are present, only graphene islands (28x28 nm^2; V_s = 0.3 V)*

4.1.2 DiPy[5]DBH/Pt(111): deposition on the hot surface

The temperature of the sample during deposition can greatly influence the kinetics of the reaction.

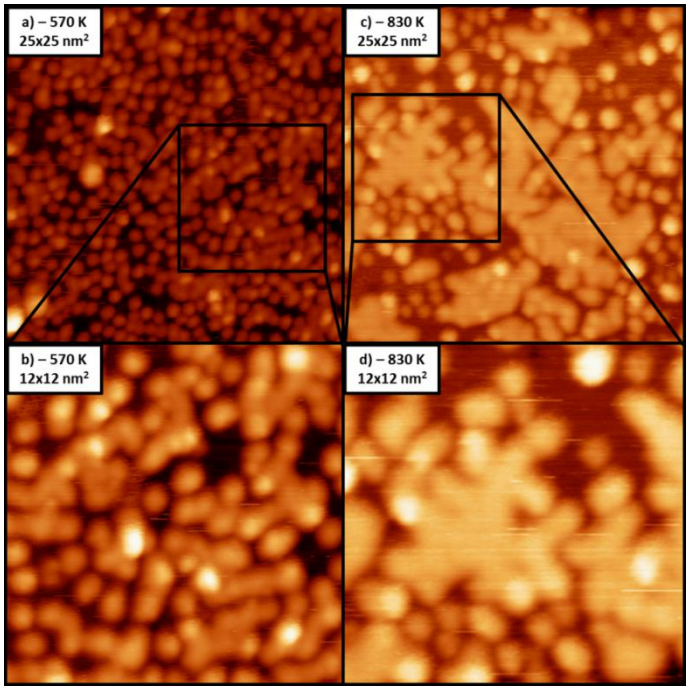

Figure 4.1.10 – *STM images of DiPy[5]DBH deposited on the hot surface of Pt(111).* *a) 0.85 monolayers were deposited on the sample kept at 570 K (25x25 nm^2; V_s = 2.0 V). b) A zoom of (a) to show the situation with more details (12x12 nm^2; V_s = 2.0 V). c) While keeping the sample at 830 K, 0.75 monolayers were evaporated (25x25 nm^2; V_s = 2.0 V). d) A zoom of (c) (12x12 nm^2; V_s = 2.0 V)*

If we evaporate the molecule on a hot sample, we may achieve different outcomes from those obtained after depositing at room temperature and post annealing at the same temperature. This is for instance the case of C_{60}/Pt(111) presented in this Chapter 6. Hence, we deposit **1** on the hot sample in order to check whether different features can be grown if a different sequence of the experimental procedure is followed. Figure 4.1.10-a shows the result of depositing **1** on the sample at 570 K: no ordered networks are observed. Even though we increase the coverage to about 0.85 monolayers to facilitate inter-molecular interaction, no change is observed. From the zoom (Figure 4.1.10-b), we know that no intramolecular resolution is present, as for the case of the room temperature deposition and subsequent anneal to similar temperatures, as shown in Figure 4.1.4-b.

We repeat the experiment by keeping the surface at 830 K, the temperature at which graphene islands were previously observed to form (Figure 4.1.10-c). In this case, we observe agglomerations of molecules. Due to the high coverage, nearby dehydrogenated molecules merge forming graphitic patches. The large amount of material allows graphene formation far from the steps. Some isolated molecules do not participate in these first stages of graphene growth.

In order to obtain a full layer of N-doped graphene, we evaporate more than one monolayer on the surface kept at 870 K (Figure 4.1.11). On many transition metals, the growth saturates when one monolayer of graphene is achieved, therefore the deposition of more material only ensures full monolayer coverage, because the surplus sticks with difficulty to the surface. As previously reported by our group,[73] the growth of graphene with large PAH as precursors and of the lowest possible temperature favours the formation of small islands of different periodicities and different angles with respect to the Pt (moirés): the same was observed when evaporating DiPy[5]DBH on the sample at 870 K.

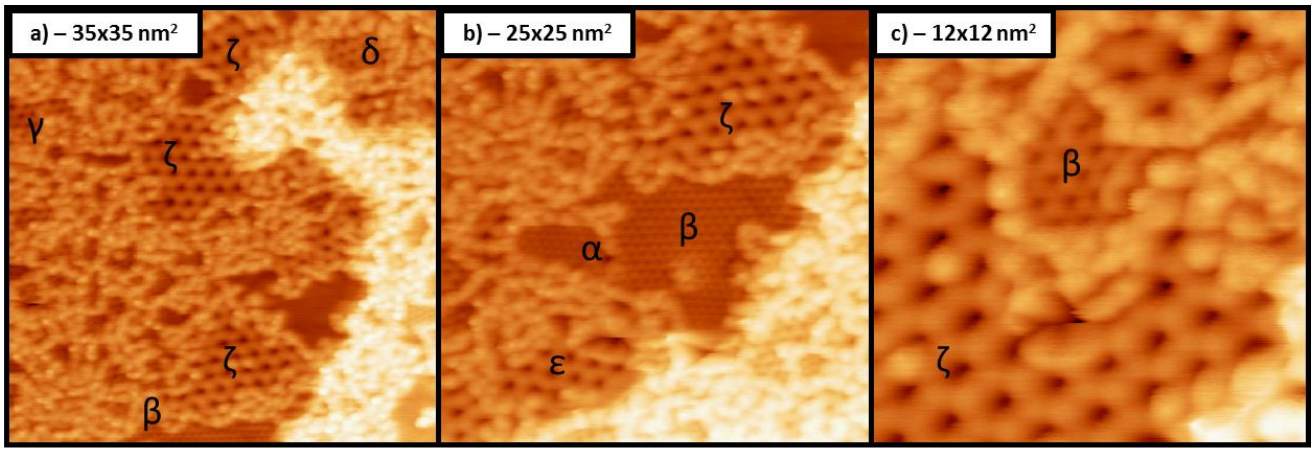

Figure 4.1.11 – *Multi-phase graphene formation from DiPy[5]DBH on Pt(111) kept at 870 K.* *All these STM images have been measured with V_s = 0.01 V. The Greek letters superimposed to the islands refer to the different phases following the nomenclature of Merino et al.[73] which describe the different moirés. a) 35x35 nm². b) 25x25nm². c) 12x12 nm².*

Figure 4.1.11-a, -b and -c show that graphene domains with a large unit cell coexist with domains with a smaller unit cell. The Greek letters refer to the different moiré structures as defined by Merino *et al.*,[73] and in the three images we see up to six different domains, namely α, β, γ, δ, ε and ζ. The large amount of moirés is due to the relatively low temperature supplied to the system. Moreover, not all the material breaks to grow into graphene but some forms N-doped carbonaceous chains around the moiré islands: these chains grow in the borders between moiré islands, and separate them. In order to achieve graphene with better quality (less defects and less domains), more temperature must be provided to the system.

The application of different voltages to the sample is well known to cause a different outcome in the topographic contrast in some moirés.[74] The same has been observed here: no resolution of the moirés was obtained for some voltages applied to the sample. An example of two images of the same zone scanned with two different voltages is observed in Figure 4.1.12: the island in the middle is clearly resolved at -0.01 V but no moiré resolution is achieved at 0.1 V.

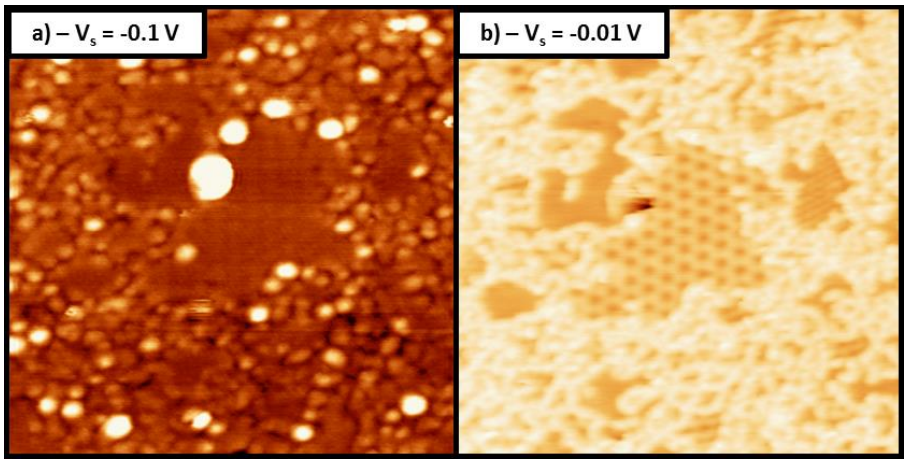

Figure 4.1.12 – *Graphene at different sample voltages.* *These are 27x27 nm^2 STM images of the same zone measured with two different voltages applied to the sample, namely -0.1 V for (a) and -0.01 V for (b).*

4.2 DiPy[5]DBH on coinage metals

As opposed to Pt(111), coinage metals such as Cu(110), Cu(111) and Au(111) are less reactive. Moreover, the different charge distribution of the electrons in the solid and the different structural properties may cause changes in the reactivity of different low index surfaces of the same element. The (110) surface of a face-centred-cubic transition metal is in general more catalytic than the (111) one due to its increased corrugation.[7]

Hence, here we are going to test the influence of the composition and the termination of the metal surface: to this aim, we deposit DiPy[5]DBH on Cu(110), Cu(111) and Au(111) and STM images are recorded after annealing the sample at different temperatures. Moreover, spectroscopic information has been recorded at

the D1011 beamline at the MAX-Lab synchrotron in Lund (Sweden) and at the ALOISA beamline at ELETTRA in Trieste (Italy).

4.2.1 DiPy[5]DBH/Cu(110)

In this Section we will present Cu(110) STM images and then combine them with the spectroscopic information in order to understand the full picture.

STM results – DiPy[5]DBH/Cu(110)

As we deposit the molecules, we observe a striking difference with the Pt(111) case: even though the evaporation methodology is the same, no molecules are observed on the sample. The reason for this is that DiPy[5]DBH is diffusing when deposited (Figure 4.2.1-a) because of the lower diffusion barrier of Cu(110) compared with Pt(111). The molecules are in a physisorbed state and diffuse faster than the STM scanning speed, making it impossible for the microscope to capture them in an image.

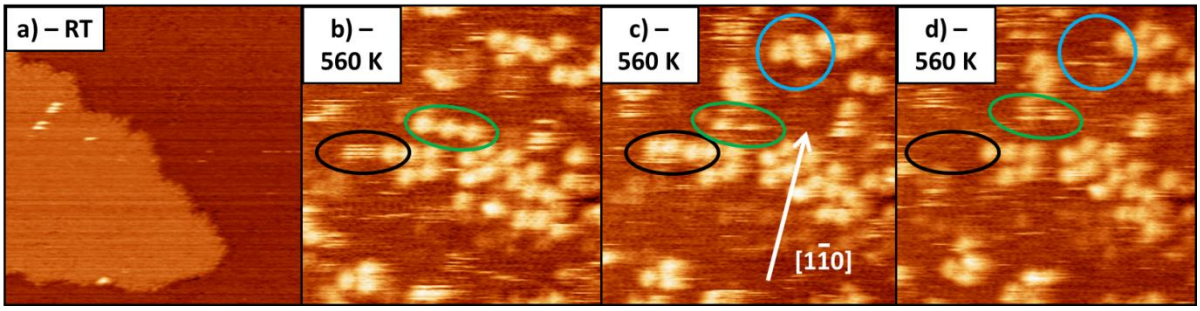

Figure 4.2.1 – *DiPy[5]DBH as deposited on Cu(110) and further annealed to 560 K.* *a) At room temperature the molecules are moving (50x50 nm^2; V_s = 2.0 V). However, if the sample is annealed to 560 K (b-c) they become visible and stick to the surface (18x18 nm^2; V_s = -2.0 V). The black circle shows the difference in two consecutive images. The white arrow shows the crystallographic direction of the Cu rows.*

After annealing the sample to 560 K, the molecules start to appear on the surface in form of dimers or very small oligomers (Figure 4.2.1-b, -c and -d), due to their partial dehydrogenation. However, even after annealing at this temperature some molecules are still diffusing. Indeed, subsequent images differ from each other, as it is shown in the figure: the two molecules in the black circle of Figure 4.2.1-b are not present neither in Figure 4.2.1-c nor in Figure 4.2.1-d. We recorded STM movies by quickly scanning the same zone overnight in order to achieve about 500 frames. These movies are available on the ESISNA web page[47] and they clarify a few factors. First of all, the molecules move mainly along the [1$\bar{1}$0] direction, indicated by a white arrow in Figure 4.2.1-c, the one of the Cu(110) rows. Indeed, the energy needed to diffuse from one row to another is higher than the one for diffusing along the rows, therefore these atomic rows can be regarded as atomic rails for the molecules. Moreover, not all molecules diffuse, some of them are fixed.

Further annealing at about 620 K allows all the molecules to covalently bond with each other and to form static polymers on the surface (Figure 4.2.2-a). In Figure 4.2.2-b, the individual molecules forming the building blocks of the linked chains can be clearly distinguished, and their size and apparent height is similar to the N-doped nanographene found on Pt(111).

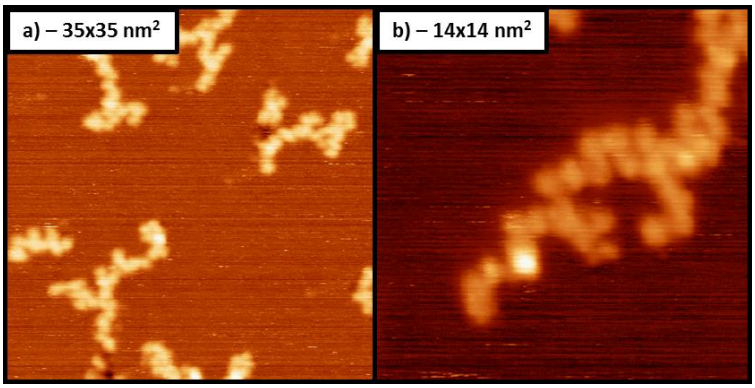

Figure 4.2.2 – *Annealing the sample at 620 K caused the molecules to form chains.* *a) 35x35 nm^2; V_s = 2.0 V. b) 14x14 nm^2; V_s = 2.0 V.*

As discussed in Chapter 3, the intermolecular bonding among monomers is caused by dehydrogenative polymerisation: the molecule cyclodehydrogenates to form N-doped nanographene, and it also dehydrogenates losing some peripheral H atoms: the C atom with the dangling bond binds with another dehydrogenated C atom of another molecule, thus forming the seeds of a polymer chain. Comparing this result with the case of Pt(111) in Figure 4.1.4, it is clear that surface diffusion is the key mechanism driving the reaction towards the formation of individual nano-objects (as for platinum) or to extended networks (as for copper) starting from the same molecular precursor.

Further annealing of the sample leads to the decomposition of the molecular chains: indeed heating to 750 K allows a graphene submonolayer to form, as shown in Figure 4.2.3. The images in Figure 4.2.3 have been measured at positive sample voltage V_s = 2.0 V; images recorded at negative sample voltages are very similar. The graphene formed by following this methodology exhibits a peculiarity: the image reveals two types of graphene islands, with different apparent heights. As shown in Figure 4.2.3-c and -d, the dim part of island on the left (A) measures 0.09 nm, while the bright part (B) 0.24 nm. Interestingly, A, and B seem to form part of the same island, just like the one of Figure 4.2.3-a and -b.

Two explanations seem reasonable to tackle the origin of this height difference. First of all, the height mismatch may be caused by an electronic effect. The apparent height measured by the STM is only partially related to the real topographic height: also the electronic configuration of the surface and the adsorbate plays a great role. So the two different islands may have different local density of states which can induce an apparent height gap between two islands.

The other possible reason is purely geometric, and it is the mass transport and etching of the Cu atoms on the surface. The Cu(110) step in the middle of Figure 4.2.3-c is 0.18±0.03 nm high (C). As discussed above, the dim part of the island (A) is 0.08±0.03 nm high and the bright one (B) 0.23±0.03 nm. Therefore, the

apparent height of island B roughly equals the AH of the dim island A plus the step height C. This suggests that the bright graphene patches are sitting on a different level with respect to the dim flakes. Large molecules are well known to induce reconstructions on transition metal surfaces[44] and the high temperature used in the annealing can favour mass transport of Cu(110).

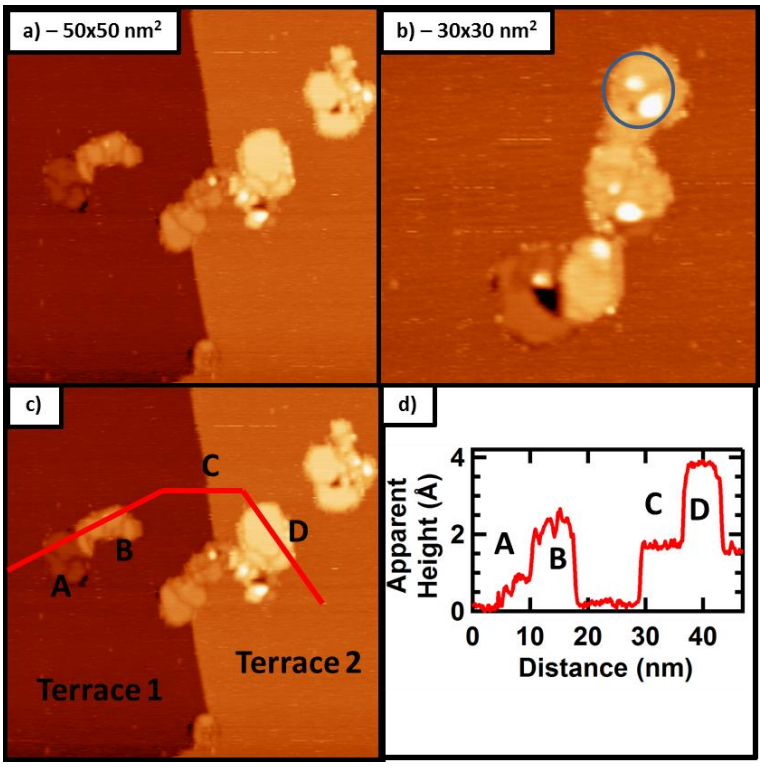

Figure 4.2.3 – *Graphene flakes obtained after further annealing at 750 K, and the islands have two different apparent heights.* *All the images were measured with V_s = 2.0 V. a) 50x50 nm² image of a few graphene islands on two different terraces. b) 30x30 nm² zoom of one particular island exhibiting two apparent heights; the blue circle highlights possible graphene nano-bubbles. c) Same as (a), the red line represents the apparent height profile shown in (d), each letter refers to a different zone in (c).*

With the information that we have so far it is hard to tell which explanation is the correct one, and we will discuss more about this in the next Section, where x-ray spectroscopy data are presented. In any case, we can advance that the most probable reason for observing two types of islands is due to mass transport of the Cu atoms on the surface.

The bright island in Figure 4.2.3-b exhibits even brighter features in the middle (indicated by a blue circle). They are likely to be strain-induced graphene nanobubbles,[75] which have been observed to exhibit Landau levels which form in the presence of strain-induced pseudo-magnetic fields.

We also performed further annealing, and we observed a similar panorama to the one just described (Figure 4.2.4). Figure 4.2.4-a represents a graphene island, and the Cu(110) rows are resolved. The zoom (Figure 4.2.4-b) shows linear moiré as it has been reported on other (110) surfaces.[76] The spacing between graphene rows is 0.23±0.03 nm, and the angle between the moiré and the crystallographic direction of Cu is 0º. The corrugation of the graphene is as low as 0.01 nm.

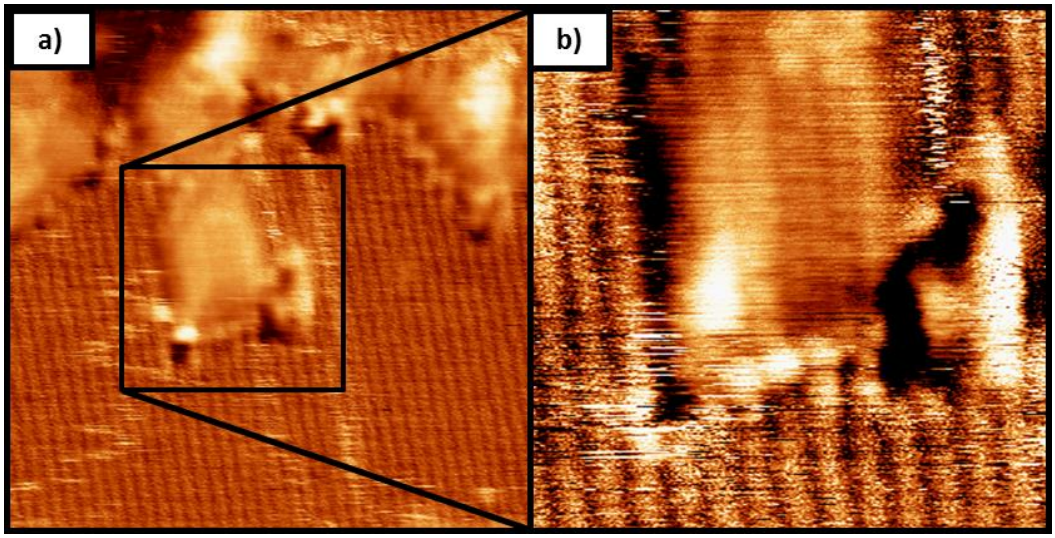

Figure 4.2.4 – *STM images of graphene on Cu(110), after annealing to about 800 K.* *a) 10x10 nm^2; V_s = 0.1 V. b) 4x4 nm^2; V_s = 0.1 V. The rows are atomic views of the Cu(110) termination on graphene.*

To summarize, on Cu(110) the molecules diffuse at room temperature and this is the key to the oligomers' and polymers' growth: surface diffusion allows them to come across each other when they dehydrogenate and bind together, as opposed to the case of Pt(111), where they stick where they land. Besides, further annealing creates graphene exhibiting two apparent heights, either due to an electronic effect or to the growth on two different Cu terraces.

NEXAFS results – DiPy[5]DBH/Cu(110)

XPS and NEXAFS for DiPy[5]DBH/Cu(110) were measured at D1011 at MAX-Lab in Lund (Sweden). These techniques help us understanding the chemical processes that the molecules undergo upon annealing, and additionally NEXAFS provides information about the orientation angle of the PAH with the surface. In this Section, I will first present the C K-edge NEXAFS spectra at different temperatures and in the next one high resolution XPS results of both submonolayer coverage and multilayer coverage and the Temperature Programmed (TP) XPS to describe the changes in real time of N1s and C1s with temperature.

In NEXAFS, the angle between the polarization of the synchrotron x-ray beam and the sample surface determines what molecular states are accessible. If the electric field is parallel to the surface, we are measuring with so-called s-polarized light, and the absorption intensity presents a maximum for molecular states oriented parallel to the surface, such as σ* orbitals in benzene rings which are sitting flat on the surface. If it is perpendicular, the p-polarized light will contribute mostly to detect the states perpendicular to the surface (π* states for benzene).

All the absorption energy scans were recorded with both s-polarised (dashed black lines) and p-polarised (solid red lines) light. The NEXAFS spectra were normalised by dividing the C K-edge of the system by the C K-edge of the clean sample. Figure 4.2.5 reveals the room temperature multilayer, estimated to be about 2.4 monolayers (ML), shown in the upper panel and submonolayer coverage (lower panel) Partial Electron Yield (PEY) NEXAFS of DiPy[5]DBH/Cu(110) at room temperature.

In general, the energy range of absorption of the π*-states of the aromatic rings lie between 284-290 eV, and above 290 eV we detect the broad continuum of σ* resonances. In the π* region, we can observe four peaks, denoted as A, B, C and D. The main peak A corresponds to the transitions of the C1s electrons of the aromatic rings to the Lowest Occupied Molecular Orbital (LUMO) at 284.4 eV.[77–82] When zooming in (see the green inset) we can see that this peak comprises two components, the second one being at 284.8 eV. The cause of this splitting is likely to be the presence of non-equivalent C sites in the molecules, which interact differently with the environment.[83,84]

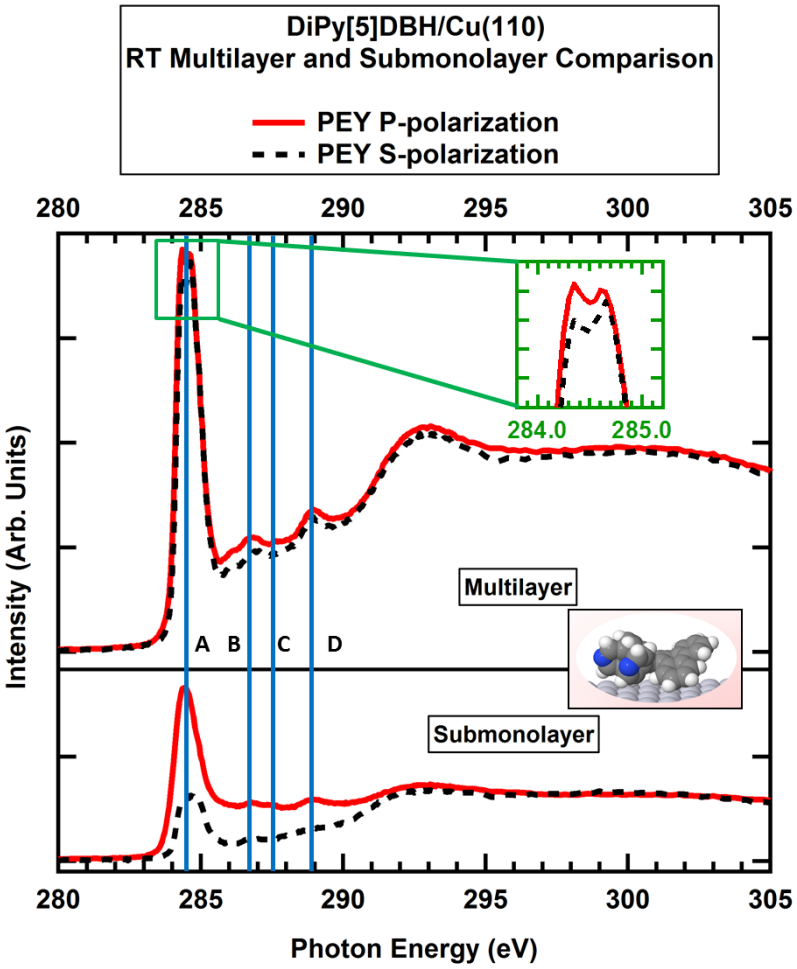

Figure 4.2.5 – *Partial Electron Yield room temperature C K-edge NEXAFS of DiPy[5]DBH/Cu(110).* *This figure compares the NEXAFS of multilayer coverage (upper panel) with submonolayer coverage (lower panel) for both s- and p-polarized light (dashed black line and solid red line respectively).The blue vertical lines indicate the positions of four peaks A, B, C and D. The green inset shows a zoom of peak A for multilayer coverage; the pink inset shows the model of an intact molecule at RT.*

In the literature, the less intense peaks B (286.8 eV), C (287.5 eV) and D (289.9 eV) have been assigned to transitions of the C1s electrons related to C-H groups.[69,79,81–83,85–87] Some groups interpret these peaks as transitions to the σ* orbitals[79,86], others to the Rydberg states,[85] and others to a Rydberg-valence mixing.[56,88] In the literature, peak C at 287.5 eV is sometimes assigned to the signature of chemisorption of the organic layer with the metal surface.[81,84,89] However, in the system we are studying the molecules diffuse at room

temperature; therefore the energy barrier to move on the surface is very low, which suggests a weak interaction of the molecule with the substrate. However, peak C can also be interpreted as arising from the carbon atoms influenced by the presence of N, namely the ones in the pyridinic rings.[90] As we will discuss later, peak C is still present upon annealing, unlike peak B and D: hence we assign B and D to the transitions of C1s electrons related to C-H groups to π* states, and peak C to transition of C1s electrons of carbon atoms belonging to the pyridinic ring. The broad features above 291 eV represent C1s transitions to the σ* orbitals.[79,80,89]

In Figure 4.2.5, we can see that the signal for the multilayer coverage is more intense than the one for submonolayer coverage, simply because more material is present for the multilayer. Moreover, the position of the peaks is identical for multilayer and submonolayer coverage; however the relative intensity of s- and p-polarised light differs for the two systems. The contribution of the π* region of the submonolayer drops by about 75% for s-polarized light. As discussed in Chapter 3, the π orbitals of the benzene rings of a PAH are normal to the ring axis, therefore if the molecule is flat on the surface their contribution should be zero for s-polarised light. The fact that the signal of the s-polarised light is not fully vanishing for the submonolayer means that the rings are not completely flat on the surface upon deposition, or that not all the rings are flat. Nevertheless, the average angle of the benzene rings of the PAH is less than 45º for submonolayer coverage. If the average angle of the pyridinic rings was exactly 45º, the s- and p-polarised intensity would be identical. In the pink inset we show the model of the molecule at room temperature, which maintains its three-dimensional character.

However, for the multilayer case (Figure 4.2.5 upper panel), the s- and p-polarised signals are indeed identical. This lack of dichroism indicates that the molecules do not orientate in a preferential way, *i.e.* the multilayer is not crystalline but randomly oriented. The reason for this is that most molecules in a multilayer do not interact with the metal, because it is screened by other molecules below, and interact more with each other: this leads to random orientation.

Upon annealing, the NEXAFS of the sample changes drastically. Figure 4.2.6 shows the changes of the s- and p-polarized scans with temperature, compared with the STM images at each stage.

At 520 K, as indicated by the STM image, some molecules have already dehydrogenated to form dimers and oligormers. Therefore the C-H signature peaks B and D between at 286.8 and 288.9 eV start to fade, unlike peak C at 287.5 eV, related to the carbon atoms in the pyridinic rings. Moreover, the width of the 284.4 eV peak begins to spread. The broadening of peak A increases with temperature, indicating a higher chemical interaction with the metal substrate.[69,80,85] As discussed above, as the C-H bonds break, the C dangling bonds can either link with another precursor to form chains, or with the surface: the molecule stop diffusing and interact more with each other and with the metal. This explains both the decrease of the C-H peaks, and the widening of the π* resonances.

The strong dichroism of the π* contribution of the NEXAFS spectrum for the two (s- and p-) polarizations at 650 K indicates the molecule flattens upon intramolecular cyclodehydrogenation as a consequence of the formation of new bonds. Due to steric constraints, the most favourable way for the pristine molecules to flatten is by cyclodehydrogenation, to form N-doped nano-graphene, as for the case of Pt. Hence the polymeric networks are formed by N-doped nanographene monomers, which bind together as a consequence of dehydrogenative polymerisation.

The π* resonances of the N-doped graphene at 785 K and 990 K are very wide, which shows that the graphene couples with the metal, as for the cases of Ir(111), Rh(111) and Ru(0001).[80] Moreover, we can see that peak C related to the carbon atoms in the pyridinic rings is still present. The NEXAFS spectra of the polymers (650 K) and of the graphene (785 and 990 K) exhibit similar shapes: in fact, the spectra look alike because each building block of the chains is a flat N-doped nanographene flake. This means that the polymeric chains grown with DiPy[5]DBH are similar to N-doped graphene nanoribbons.

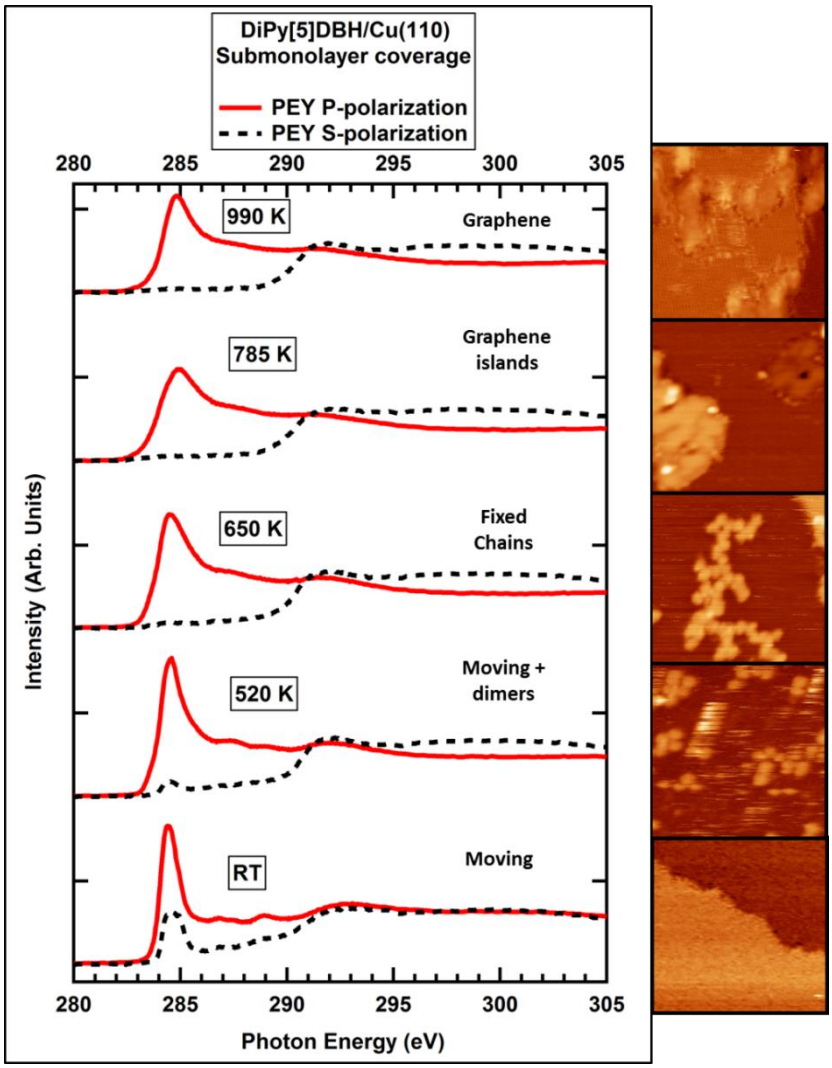

Figure 4.2.6 – *NEXAFS of submonolayer coverage of DiPy[5]DBH/Cu(110) at various annealing temperatures.* *The NEXAFS spectra were measured at RT, 520 K, 650 K, 785 K and 990 K. We employed both s- and p-polarization for each scan. On the right, the NEXAFS is compared with STM images for each situation (16x16 nm^2).*

XPS results – DiPy[5]DBH/Cu(110)

XPS complements the NEXAFS and STM information by giving insights on the chemical state of the molecule. Figure 4.2.7 shows the N1s and the C1s XPS peaks of submonolayer coverage of DiPy[5]DBH/Cu(110) at various temperatures, together with a representative STM image. The Binding Energy of each peak refers to

the Fermi edge of each scan. The peaks were fitted with a Lorentzian Width of 180 meV convoluted with a Gaussian component of about 600 meV, and by minimising the number of components for each peak.

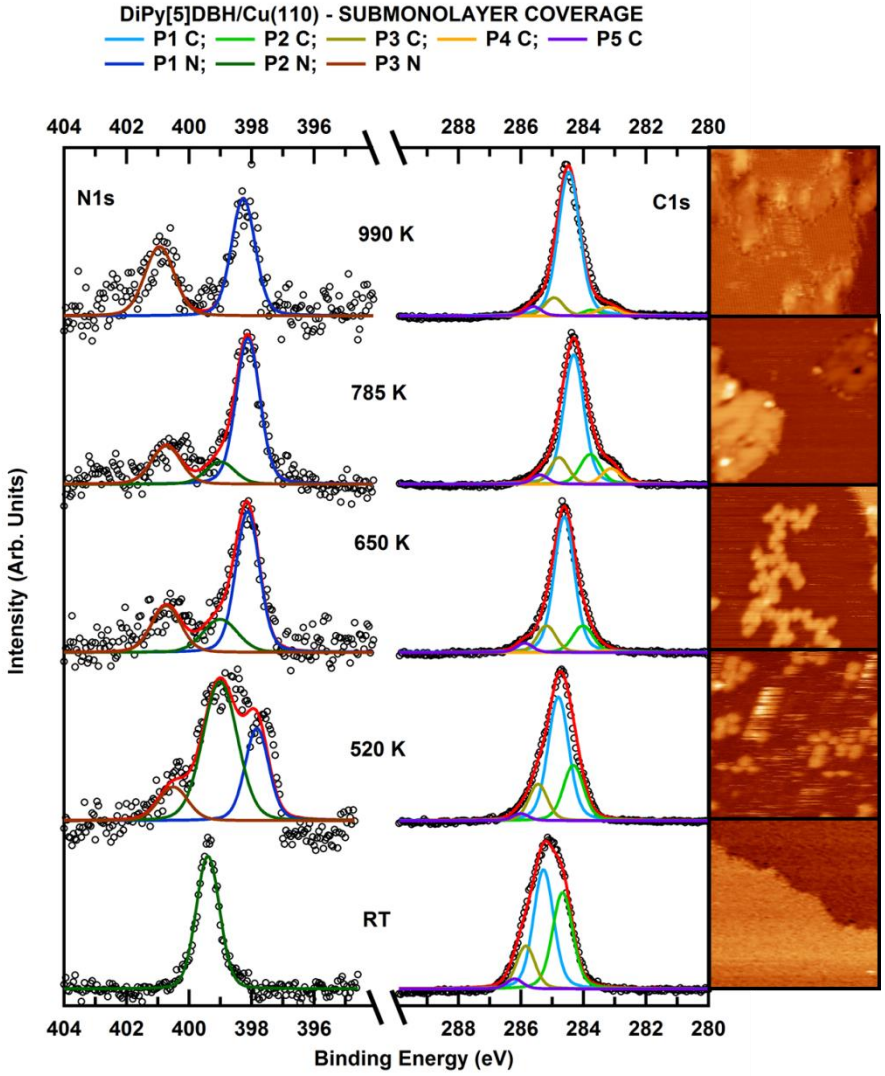

Figure 4.2.7 – *N1s and C1s spectra of submonolayer coverage of DiPy[5]DBH/Cu(110) at different temperatures.* *N1s has been fitted with three different peaks (P1-3 N in the legend), while C1s with five (P1-5 C in the legend). The XPS is compared to the STM images at each temperature (16x16 nm^2). The intensity y-axis is not in scale for C1s and N1s.*

The C1s peak of the molecule at room temperature is rich in components, as we can distinguish up to four: P1-C at 285.3 eV (blue), P2-C at 284.7 eV (green), P3-C at 285.9 (ochre) and P5-C at 286.2 eV (purple). From the STM and the NEXAFS we know that at room temperature the molecules are diffusing and are not completely flat because of their three-dimensional structure. The presence of such a high number of peaks indicates the complexity of the free, low interacting molecule, with the C atoms existing in different chemical molecular environments.

Upon annealing, the spectra transform: overall the C1s peak narrows because it loses components (or they become less important), and the whole peak moves towards lower binding energies. Moreover, at 650 K, a new component (P4-C) arises at 283.3 eV (orange). The variation of the relative importance of each contribution with temperature is very useful to understand their role and to assign the components to a specific chemical environment. To do so, we analyse the changes in the percentage of the area of a given peak with respect to the total area, as reported in Figure 4.2.8. The top left panel indicates the relative contribution of the C1s components for the submonolayer coverage of DiPy[5]DBH/Cu(110).

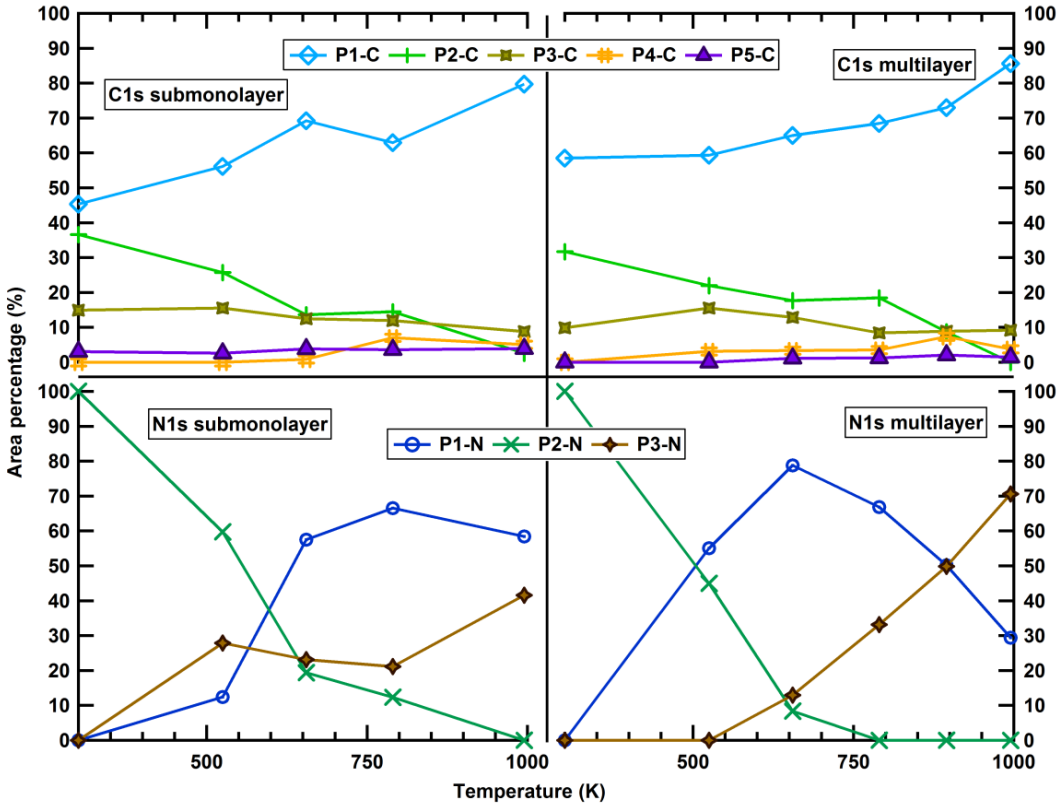

Figure 4.2.8 – *Relative area of each component of the C1s and N1s peak for DiPy[5]DBH/Cu(110) in terms of temperature.* *This figure shows the change upon annealing of the five components of C1s (upper panels) and the three of N1s (lower panels) for both submonolayer (left panels) and multilayer (2.4 ML, right panels) coverage.*

P1-C with a binding energy of 285.3 eV is the most intense peak at room temperature and this is true during the whole annealing. In fact, its relative importance increases with temperature. It represents the sp^2 C atoms in the aromatic rings.[42,77,91–98] Upon annealing, each component of the XPS peak shifts by about 0.9 eV towards lower binding energy. This indicates that the as-deposited molecules are slightly positively charged: although they are weakly bound, they still transfer some of their charge to the surface. The shift of this peak will be discussed later in more details.

The relative importance of P2-C at 284.7 eV decreases with temperature, and it indicates the C attached to the H atoms.[55,91,92,94,97,98] The binding energy distance between P1-C and P2-C (about 0.6 eV) is consistent with this assignation. Its reduction with temperature goes together with the increase in the importance of

P1-C: this further confirms the cleavage of the C-H bond and the formation of new C-C bonds as a consequence of both cyclodehydrogenation and dehydrogenative polymerisation.

P3-C at 285.9 eV represents the carbon atoms in the pyridine ring.[77,95–97,99] From the experiment we know that about 15% of the C atoms contribute to this component. Even though only four out of forty atoms (*i.e.* 10%) are directly bonded with N, the presence of this dopant does not only affect these four C, but also the neighbouring atoms comprised in the pyridinic ring. This is why the relative importance of this peak is greater than expected. This component still exists at 990 K, therefore the N-doping of graphene is effective with this recipe.

P4-C at 284.3 eV indicates the C of the molecules interacting with the Cu surface.[100,101] This component is not present at room temperature, as the molecules diffuse and do not interact with the metal. This peak appears at about 650 K, when polymeric network are present, and its relative importance increases upon annealing and stabilises when graphene is formed (see Figure 4.2.8). Lacovig *et al*.[100] propose a model for dome-shaped C nanoislands for which only the C atoms at the edges bond with the metal: the same is probably happening here.

Finally, the binding energy distance between P1-C and P5-C (286.2 eV) is constant throughout the whole annealing process (around 1 eV): therefore we tentatively assigned this component to a shake-up peak of electrons losing energy by interacting with other electrons in the surface before reaching the detector.[94]

The room temperature submonolayer N1s XPS (Figure 4.2.7 and bottom left panel of Figure 4.2.8) has only one thin component at 399.4 eV (P2-N, green), while upon annealing two new components appear and prevail, P1-N at 398.3 eV (dark blue) and P3-N at 400.5 eV. Figure 4.2.9 (from Usachov *et al*.[42]) shows all the possible N defects in a graphitic carbon grid. P2-N represents the pyridine-like N, the N that is bonded to two C atoms in an aromatic ring.[42,96,102,103] The N in the as-deposited intact molecule is pyridine-like (defect 2), therefore the observation of such component is expected.

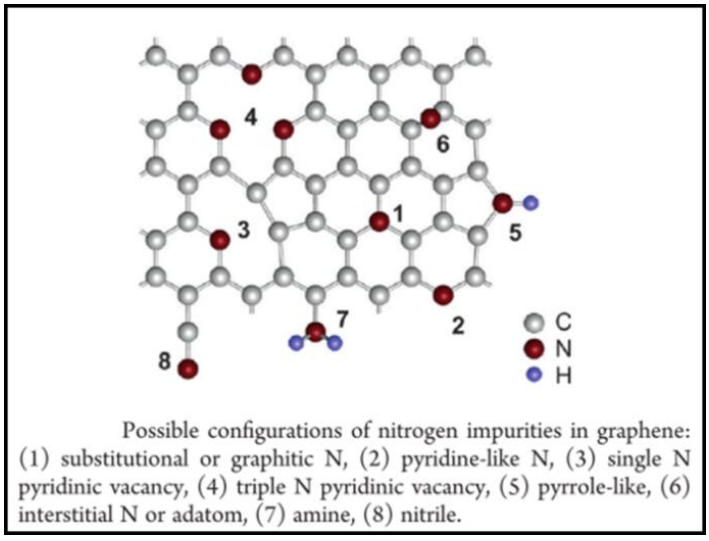

Figure 4.2.9 – *Possible N configuration in a graphitic carbon sheet.* *From Usachov et al.[42] The possible N-defects are: (1) substitutional or graphitic; (2) pyridinic-like; (3) single N pyridinic vacancy; (4) triple pyridinic vacancy; (5) pyrrole-like; (6) interstitial N or adatom; (7) amine; (8) nitrile.*

Upon annealing the N1s spectrum changes radically. As the oligomers and polymers form, the molecule flattens, and P1-N begins to dominate. P1-N (398.3 eV) represents the N atoms in the pyridine ring interacting with the Cu.[42,104,105] This is possible because cyclodehydrogenation causes the pyridinic rings to rotate; this brings the N and the Cu closer, promoting their interaction. The rotation of the aromatic rings was discussed in Section 4.1 for the case of Pt(111). The relative importance of P1-N increases with temperature, up to about 785 K: at that point, the rise of P3-N (400.5 eV) stops the increase of the N-Cu interaction.

P3-N represents the substitutional N atoms in the graphene network (defect 1 in Figure 4.2.9): these N are bonded with three sp^2 carbon atoms.[42,96,103] The 'graphitic N' component P3-N is present at 650 K: however, STM images of the sample annealed at this temperature reveal the presence of polymeric chains, not of graphene, which will appear at a higher temperature. The presence of the substitutional N in a graphene network (P3-N) 650 K indicates that some molecular chains bond via the pyridine rings, so that the linkage of building blocks in the chains involves the nitrogen atom binding with the carbon dangling bonds, hence enclosing an N atom in the hexagonal carbon lattice substituting a C atom.

Table 4.2.1 displays each component of the C1s and N1s XPS peaks. In this table, we also report the binding energy at room temperature for submonolayer coverage (when possible) and the assignation of the peaks as discussed in the text. The nomenclature of the components refers to Figure 4.2.7 and to Figure 4.2.8.

Peak	BE (eV) at RT	Assignation
P1-C	285.3	Aromatic or Graphitic C
P2-C	284.7	C-H
P3-C	285.9	C-N
P4-C	- (284.3 at 650 K)	C-Cu
P5-C	286.2	C shake up
P1-N	- (397.8 at 520 K)	N-Cu
P2-N	399.4	Pyridine-like
P3-N	- (400.5 at 520 K)	Graphitic (substitutional) N

Table 4.2.1 – *Description of each XPS peak for DiPy[5]DBH/Cu(110).* *Each peak is described in terms of the Binding Energy (BE) at RT and of its assignation as discussed in the text.*

To summarise the information we obtained so far we highlight the main behaviour of the molecule on Cu(110). At room temperature, the NEXAFS reveals that the diffusing molecule maintains its three-dimensional shape, and the presence of P2-C (C-H) indicates that DiPy[5]DBH is also intact, and it does not dehydrogenate upon adsorption. A light annealing causes a decrease in P2-C and a rise in P1-C (C-C), together with the flattening of the molecule: this indicates the starting of the surface-catalysed (cyclo)dehydrogenation process, and the formation of polymeric chains formed by nanographene building blocks. Meanwhile, P4-C (C-Cu) increases, showing a higher interaction with the surface. This is also observed in the N XPS peak with the rise of P1-N (N-Cu). Further annealing causes the formation of N-doped

graphene: this has the effect of decreasing the molecule interaction with the surface and of the substitution of the pyridinic component of N (P2-N) with the graphitic one (P3-N). P3-C (C-N) remains constant throughout the annealing process, indicating that no significant amount of N is lost, and that all the structures formed with thermal activation are N-doped.

The picture for the multilayer coverage (estimated to be about 2.4 ML) is similar to the submonolayer one and it is shown in Figure 4.2.10.

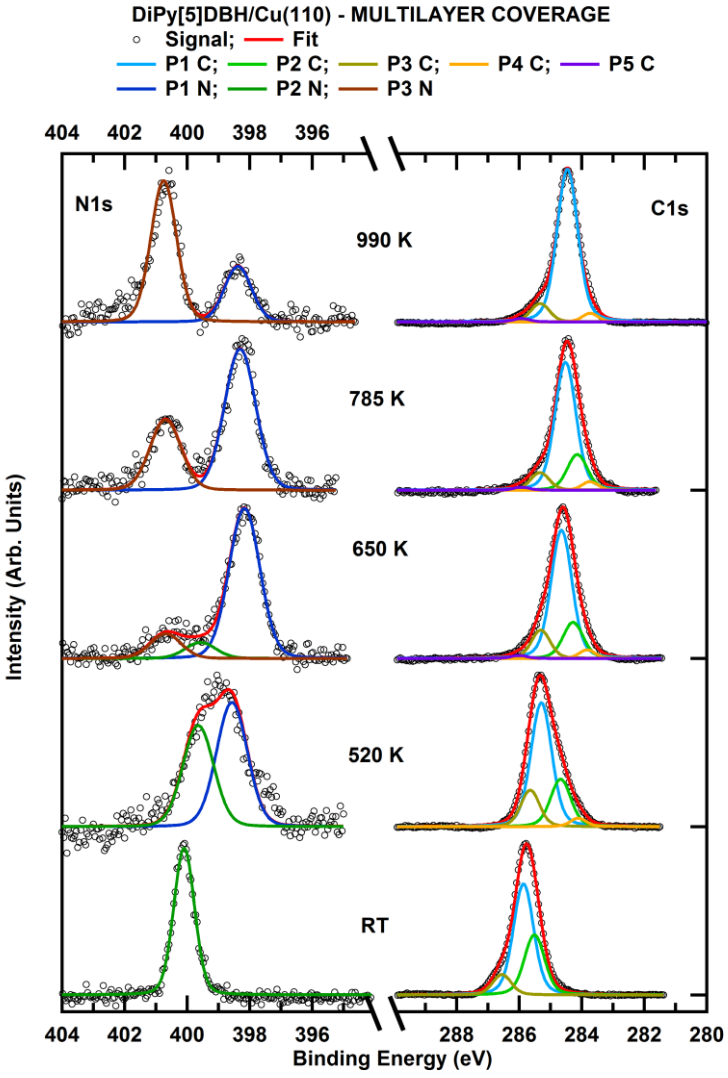

Figure 4.2.10 – *C1s and N1s peak of multilayer coverage of DiPy[5]DBH/Cu(110) at different temperatures.* *The C1s peak has been fitted with five components, while the N1s peak with three. The intensity y-axis is not in scale for C1s and N1s.*

Two main differences arise. First of all, we did not observe the shake-up (P5-C) peak at room temperature, and only appeared upon annealing at 650 K. Secondly, the Binding Energy (BE) of the peaks is higher than the submonolayer case: the main peaks of both N1s and C1s were shifted 0.7 eV towards higher BE with

respect to the previous results (P1-C at 285.9 eV and P2-N at 399.4 eV). This is because of charge effects: the electrons ejected by the sample upon x-ray exposure leave the surface in an excited state, which takes time to relax as a consequence of the insulating character of the multilayer. Hence the molecular layer becomes positively charged, and this feature increases the binding energy of the electrons. Upon annealing, the multilayer desorbs, and only one monolayer of molecules persists on the surface. This is reflected in both the C1s and N1s XPS spectra as a drop in the signal intensity by about 70% (not shown in the image). As the multilayer desorbs, the insulating character also diminishes, hence the binding energy of the whole peak shift towards lower values, until it reaches those of the submonolayer coverage. As the temperature is increased, upon (cyclo)dehydrogenation, the internal and the edge C-H bonds break and the molecules lose H atoms so P1-C decreases, and the interaction with the Cu rises, so P4-C grows with temperature.

The N1s peak also follows a similar trend to the submonolayer coverage: only pyridinic N is present on the surface, and upon annealing and oligomerisation the N starts to interact with the metal up to a point where the substitutional graphitic N prevails.

To have a tangible understanding of the binding energy shifts with temperature, we measured Temperature Programmed XPS of the N1s and the C1s for multilayer coverage.

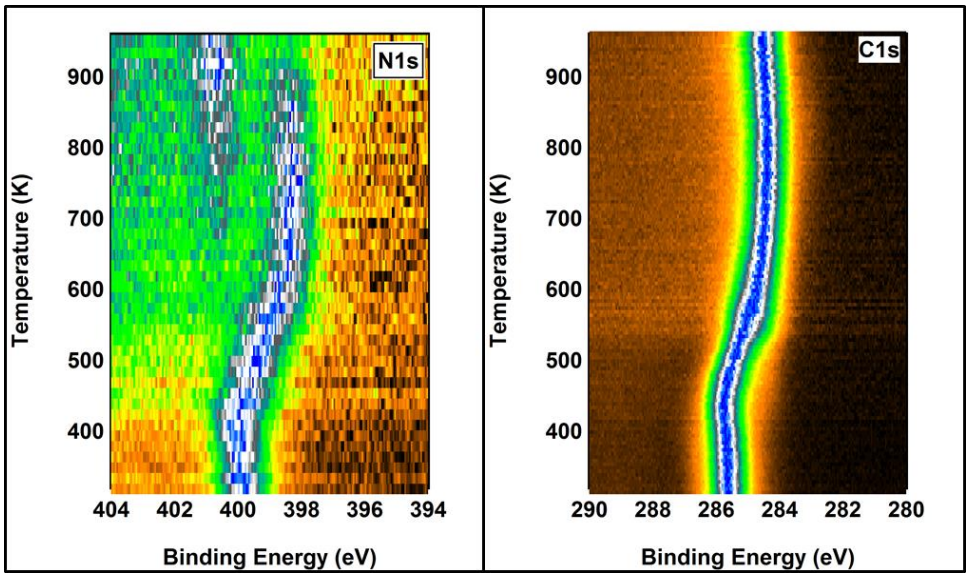

Figure 4.2.11 – *Temperature Programmed XPS N1s and C1s peaks of multilayer coverage of DiPy[5]DBH on Cu(110).* *The higher the intensity, the bluer the peak; each scan was taken every 15 K for N1s and every 5 K for C1s.*

In Figure 4.2.11, the coloured scale represents the intensity (orange/black = low; blue/white = high) of the peak in terms of the binding energy (x-axis) and of the temperature (y-axis). Each N1s and C1s peak was measured with an interval of 15 and 5 K respectively. We also monitored the Cu2p peak of the clean sample and we detected a deviation in binding energy at high temperature, caused by photoelectron diffraction effects. Since the binding energy of the Cu2p peak of the clean sample reflects the bulk material and therefore it should be independent of annealing, we corrected the Binding Energy of each temperature of the N1s and C1s peak by subtracting the deviation from the room temperature BE value of the Cu2p peak.

We can clearly detect a core-level shift towards lower BE starting at about 480 K for both the N and the C. The origin of this shift is twofold. First of all, the multilayer desorbs leaving just one monolayer, so the charge effects caused by the insulating nature of the multilayer would then decrease contributing to the shift towards lower binding energy. Secondly, the temperature of this shift coincides with the one of formation of dimers and oligomers, and it means that the molecules interact more with the surface, due to a partial dehydrogenation, and this corresponds to an increase in P4-C, which is observed at a lower binding energy with respect to the main P1-C component.

At about 700 K P3-N starts to appear: this is the signature of the appearance of substitutional N in a graphene grid. As the temperature is further increased, P3-N becomes dominant, and the C1s peak narrows which is proper of graphene.[106] The emergence of this feature is a good estimation of the graphene formation. This means that high-quality N-doped graphene is achieved, and that Chemical Vapour Deposition of hetero-aromatic molecules is a very efficient ways of substituting carbon atoms in the graphene network at the atomic level. The doping of graphene is very important for tailoring its electronic properties and modifying its band gap.

4.2.2 DiPy[5]DBH/Cu(111)

As discussed previously, we deposited DiPy[5]DBH on another face of copper, Cu(111), for comparison with Cu(110). Even though the metal is the same as the one studied in the previous Section, its surface geometry may affect its ability to catalyse reactions between molecules, and this is what motivated us to perform experiments on the Cu(111) surface.

STM results – DiPy[5]DBH/Cu(111)

Figure 4.2.12 shows the STM images obtained after depositing DiPy[5]DBH on Cu(111).

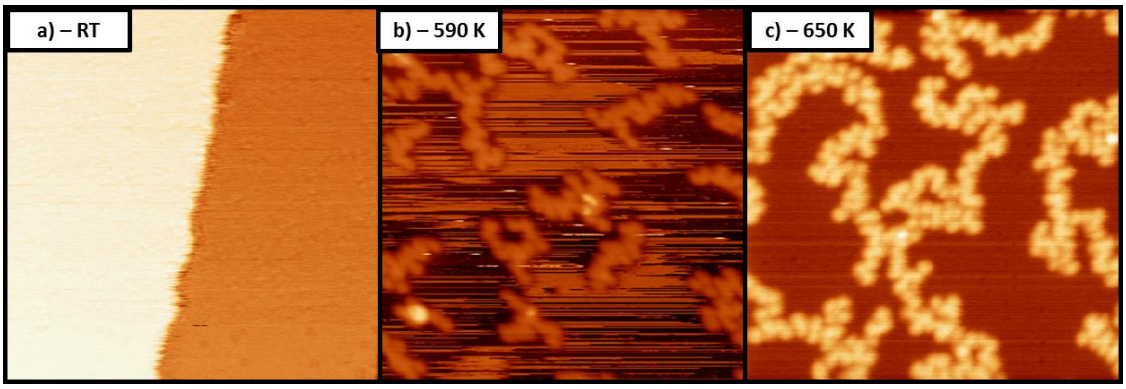

Figure 4.2.12 – *DiPy[5]DBH/Cu(111) at RT, 590 K and 650 K.* *a) At room temperature the molecules are diffusing (40x40 nm^2 V_s = 1.0 V). b) At 590 K, chains of molecules are observed together with molecules still moving (spikes) (30x30 nm^2; V_s = 2.0 V). c) At 650 K all molecules form chains fixed on the surface (30x30 nm^2; V_s = 2.0 V).*

As Figure 4.2.12-a indicates, at room temperature the molecules diffuse on the surface, so they are invisible. However upon annealing they start to dehydrogenate and polymerise forming chains: as Figure 4.2.12-b shows, at 590 K fixed chains coexist with moving molecules; therefore not all of the molecules dehydrogenated, revealing that this is a slow process, and more temperature is needed to complete the task. Curiously, in general the molecular chains have the width of one molecule and have a zigzag shape which recalls the nanoribbons synthesised by Cai.[17] This suggests that there exist more reactive sites on the molecule.

Figure 4.2.13 shows two images recorded simultaneously of the sample annealed at 590 K (the same line is recorded with different voltages in the back and forward directions). It indicates that the moving molecules behave differently from the chained molecules. At V_s = +1 V, the chains coexist with bright scratches which represent the moving molecules. Curiously, at negative voltage (V_s = -2 V) these marks are not present and we only see chains. According to the XPS of DiPy[5]DBH on Cu(110) shown in the previous Section (we will see later that this also applies to a lesser extent to Cu(111)), the molecules at RT are slightly positively charged as they transfer electrons to the surface. Therefore, a possible reason why the moving molecules are only visible at positive sample voltage is because when electrons are tunneling from the tip to the sample, the molecules are attracted towards the tip inducing instabilities and spikes. However, with negative sample voltage the opposite occurs, and the molecules are repelled away from the tip.

Going back to Figure 4.2.12-c we see that upon further annealing at 650 K all molecules link with each other, and no more 'scratches' caused by diffusing precursors are present. We can spot and distinguish the individual molecules forming the chains, which exhibit an apparent height of 0.26±0.03 nm and a width of 1.35±0.05 nm. In order to form polymeric networks, the molecules undergo dehydrogenative polymerisation and bind together by joining C dangling bonds of different molecules.

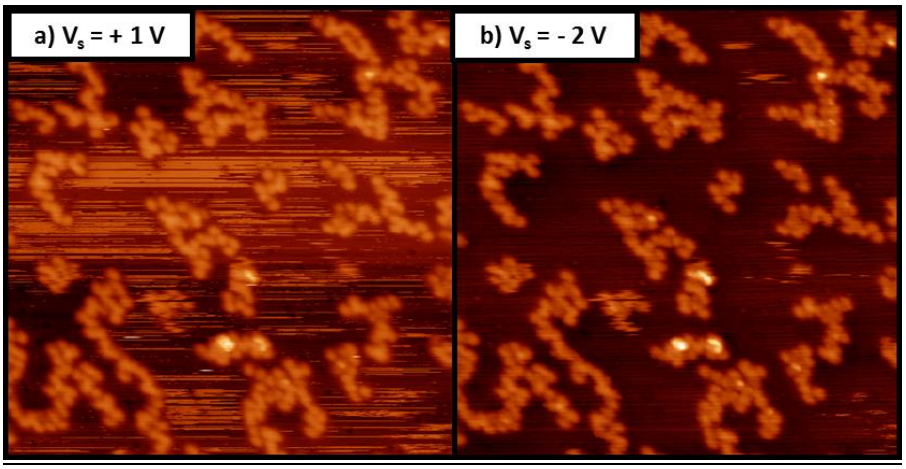

Figure 4.2.13 – *A simultaneous image of the moving molecules annealed at 590 K at different voltages.* *40x40 nm^2 images at a) V_s = 1.0 V and b) V_s = -2.0 V.*

When varying the sample voltage, the apparent height of the molecules in the polymers changes, as shown in **Figure 4.2.14**: it goes from a maximum of 0.28 nm at V_s = +2 V to being 0.08 nm around the Fermi energy, and then back to 0.20 nm at V_s = -2 V.

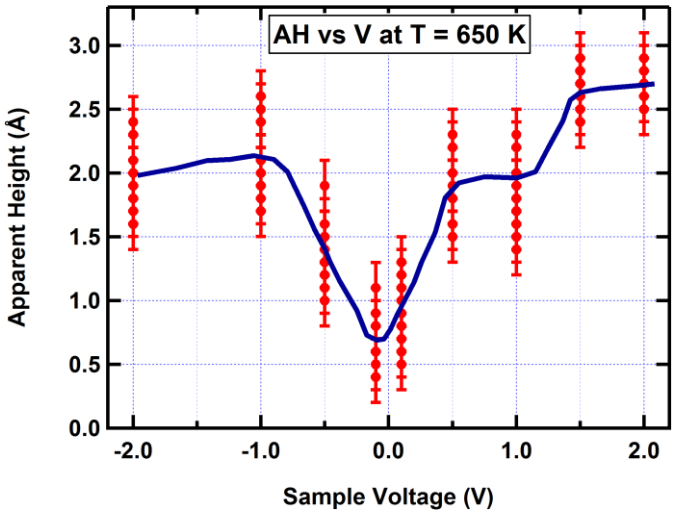

Figure 4.2.14 – *Apparent height of the molecules in the chains as a function of sample voltage.* *As V_s changes, so does the apparent height of the molecules; it was measured in samples annealed to 650 K. The blue line shows the fit line of the trend.*

These differences arise from the density of states of the molecules. We measured the apparent height of about 10 different molecules at each voltage to obtain statistical reliability in Figure 4.2.14. To a first approximation, this figure could indicate that the LUMO of the system appears at about -1.0 V, while the HOMO at 0.5 V respectively, as the first maxima below and above the Fermi Energy occur at that point.

Further heating causes the polymers to change their aspect: at 690 K, some molecules are still distinguishable but others unified with the neighbours. The chains in Figure 4.2.15-a are different than the ones in Figure 4.2.12-c, they are less uniform and show different apparent heights. Figure 4.2.15-b and -c shows that some molecules are still distinguishable: the green circles represent the size of DiPy[5]DBH as measured in the chains (diameter = 1 nm), and they have been superimposed to the intact molecules. As discussed in Chapter 3, the rise in the annealing temperature to 690 K promotes the combination of dehydrogenative polymerisation and of cyclodehydrogenation. The apparent height and width of the distinguishable molecules at 690 K decrease with respect to the ones at 650 K to 0.19 nm and to 1.0 nm respectively. This drop in size recalls the one observed on Pt, when the passage from nanographenes to nano-domes was registered as a reduction in the dimensions of the molecules. Therefore we relate the structural change in the chains as a completion of the dehydrogenation of the edges of DiPy[5]DBH and as a formation of small clusters of nano-domes.

Hence, this stage is a transition stage between the chains made up by intact molecules and the formation of graphene patches. The red oval in Figure 4.2.15 indicates a flat patch which, at first glance, looks like a graphene flake. However, the temperature is too low for this transformation to be occurring. Moreover, its apparent height is 0.22 nm and it is independent of voltage (not shown): the apparent height of graphene

usually varies with the applied voltage therefore its steadiness suggests that the patch may not be graphene. On the other hand, the distance between Cu(111) planes (*i.e.* the height of a Cu step) is 0.21 nm. Hence the flat patch in the red oval panel may be a small Cu terrace surrounded by molecules. This would mean that a Cu mass transport occurred. As we will discuss in Chapter 6, large organic molecules can induce a reconstruction on the metal surfaces, by for example lowering the energy needed to create an atomic vacancy on the metal[107,108] or by etching the step edges. However, we need more information to determine the nature of the patch, and this will be discussed later.

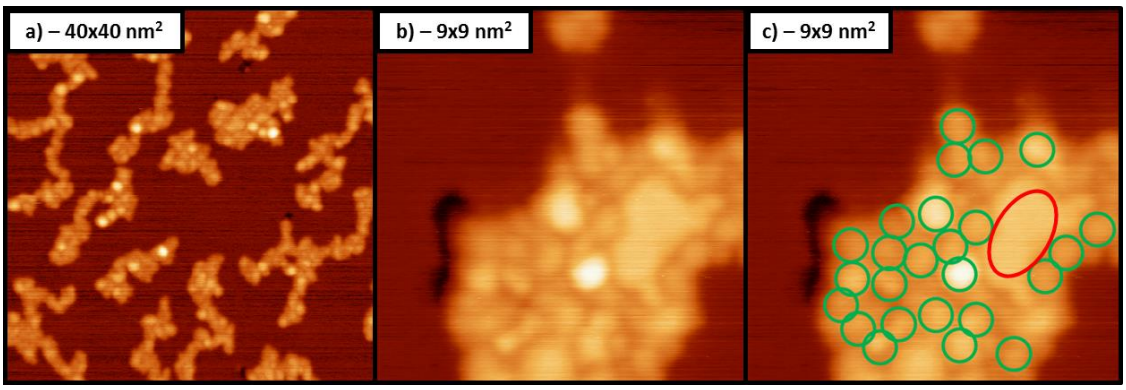

Figure 4.2.15 – *Chains of DiPy[5]DBH/Cu(111) at 690 K.* *a) 40x40 nm2; V_s = 2.0 V. b) 9x9 nm2; V_s = 2.0 V. c) This is the same image as (b), but the green circles represent the width of the molecule in the chains (with a diameter of 0.9 nm); the red oval shows a flat patch different from all the other features in the island.*

Heating up the sample at 720 K triggers a curious phenomenon: features of different height appear, as bright (above the Cu level) and dark (below the Cu level) chains emerge on the surface. Figure 4.2.16-a to -c display different size STM images of these peculiar chains. Their width varies between 0.7 to 2.0 nm. The apparent height gap between chains recalls the presence of dark and bright islands of graphene on Cu(110) in Section 4.2. As Figure 4.2.16 confirms, these chains can contain both bright and dim bits. One single chain can be bright and become dim after a few nanometres.

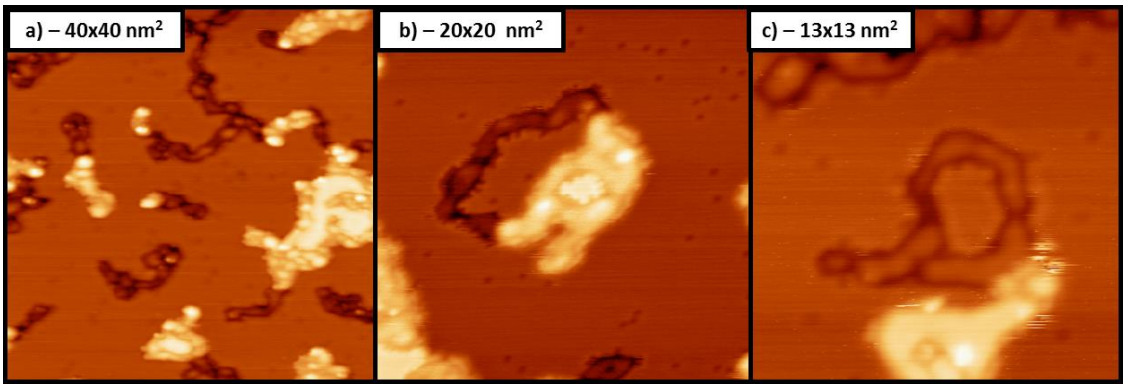

Figure 4.2.16 – *Dark and bright chains appear after annealing DiPy[5]DBH/Cu(111) to 720 K.* *All the images have been scanned with Vs = 2.0 V.*

The metal surface contains black spots, which are observed in all the images (especially clear in Figure 4.2.16-b). These features are common in Cu(111) surfaces and are caused by single-atom defects.[109,110]

At 720 K, the molecules have enough energy to completely (cyclo)dehydrogenate: the molecules in the chains are not distinguishable anymore. The C dangling bonds bind together forming N-doped chains. The apparent height within each bright or dim chain varies slightly, and remarkably in both cases the borders of the chains are much darker than the core (Figure 4.2.16-c). The complete dehydrogenation of these chains may cause the peripheral C atoms edges to bond covalently with the Cu underneath[100] and therefore to exhibit a much lower apparent height than the centre of the chain.

As for Cu(110), the coexistence of bright and dim chains can be caused by two circumstances: (i) on one hand, the divergence can be a topographic effect, in which case the chains would be sitting on two different terrace heights; (ii) on the other hand, the chains may sit on the same topographic level and their real height may be the same, so the difference may be a completely electronic effect for which the two types of chains are electronically different from each other. Indeed, the apparent height of the chains can be negative with respect to the Cu surface even though they protrude, because of electronic effects: if the chains are more insulating than the surface, the tip will have to move towards the sample to keep the tunneling current constant and will therefore register this movement as a decrease in the apparent height of what it is measuring.

To get to the root of the problem, we recorded the apparent height changes with sample voltage on different zones of the chains. Figure 4.2.17-a indicates an STM image of the zones where we recorded the apparent height shown Figure 4.2.17-b. The purple cross represents the height of a dark feature, while the green cross the one of the bright structure and the blue cross the height of a patch which is very similar to the one observed in the red oval of Figure 4.2.17-c. The heights of these three features clearly differ between each other.

Figure 4.2.17-b indicates that the apparent height of the blue cross is constant with sample voltage, but the one of the two chains varies. Moreover, the trend is similar for the two types of chains: at high sample voltages (V_s < -0.5 V or V_s > 0.5 V) the dark and bright chains are respectively -0.10±0.3 and 0.15±0.3 nm tall with respect to the Cu surface which is taken as zero. However, around V_s = 0 V, the height of both decreases by 0.18±0.3 nm. It is very important to remark that the height difference between the two chains remains constant throughout the voltage measurements – about 0.23±0.3 nm, which is (within error) the same as the height of a copper step.

Let's now focus on the bright patch, the blue cross in Figure 4.2.17: at first sight, it seems to be a graphene patch. Indeed, PAHs are known to decompose into graphene upon annealing; moreover, its smoothness recalls the one of graphene. However no atomic nor moiré resolution is achieved and the apparent height of this patch is constant at 0.24±0.3 nm at all the voltages measured, which is unlikely for graphene as in general, the apparent height of graphene is voltage dependent.[74] There exist an on-going discussion on the reported apparent height of graphene/Cu(111): some authors measured it to be 0.07 nm,[111] and some others 0.15 nm.[112] Therefore we conclude that it is unlikely for this patch to be graphene, as its height is much higher. On the other hand, its apparent height is suspiciously similar to the height of a Cu(111) step (0.21 nm): hence, the best candidate to explain this patch in between chains is a small terrace of cupper, one step higher than the rest of the surface. The fact that the apparent height curves of the bright and dim

chains differ by about 0.23 nm at all voltages suggests that the molecules in the dim chains have eroded into the Cu(111).

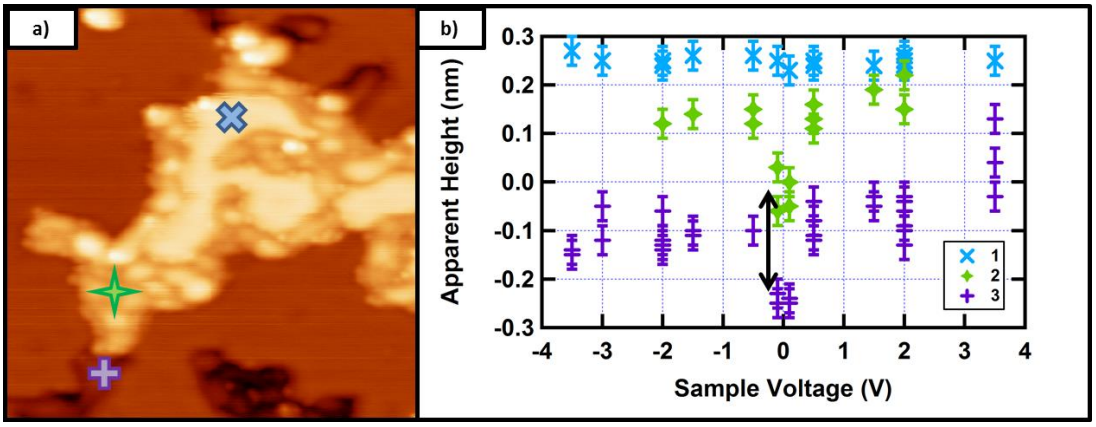

Figure 4.2.17 – *The apparent height of three zones is recorded as a function of voltage.* *a) This STM image shows where the apparent height was measured: in the three zones represented by a blue (patch), a green (bright chain) and a purple (dark chain) cross (20x20 nm^2; V_s = -2.0 V). b) The apparent height measurements of the three zones described above. Each colour represents the zone with the same colour and shape in (a).The black arrow represents the height difference between bright and dark chains, constant at 0.23 nm.*

Further annealing to 800 K triggers the growth of graphene (Figure 4.2.18). Even though we were not able to resolve neither atoms nor moirés, we conclude that we form graphene because large Polycyclic Aromatic Hydrocarbons are known to be precursors to graphene growth.[73,106]

Figure 4.2.18-a shows a panoramic image of the sample with graphene. Due to the low temperature of formation, a lot of defects appear and the shape of the islands is unusual. Curiously, we observe standing waves inside the graphene patches with our room temperature STM, as Figure 4.2.18-b reveals. The white circles highlight two graphene islands.

In Figure 4.2.18-c we see a bright island (A) and a dim patch (B): as in the case of the nanoribbons, here too the height difference between the two is about 0.23±0.3 nm, within error the same height as a Cu(111) step (see inset).

The graphene is surrounded by small round features, as the zoom in Figure 4.2.18-d shows. To a first look, they may seem intact molecules which need more temperature to break up to form graphene. However, they are smaller: the green circles in the image represent the size of an intact molecule as measured in the chains (about 1.0 nm) compared with the size of the round features at the edge of the island, which are much smaller being about 0.4 nm wide.

Chen and co-workers[111] reported the presence of similar fragments surrounding a triangular graphene island grown by decomposing 1,1'-ferrocenedicarboxylic acid on Cu(111): they assigned the features to cyclopentadienyl rings, fragments of the precursor. Due to the similarity of the case, we also think that in our case the circles surrounding the graphene are bits of the precursor which did not break to contribute to the graphene.

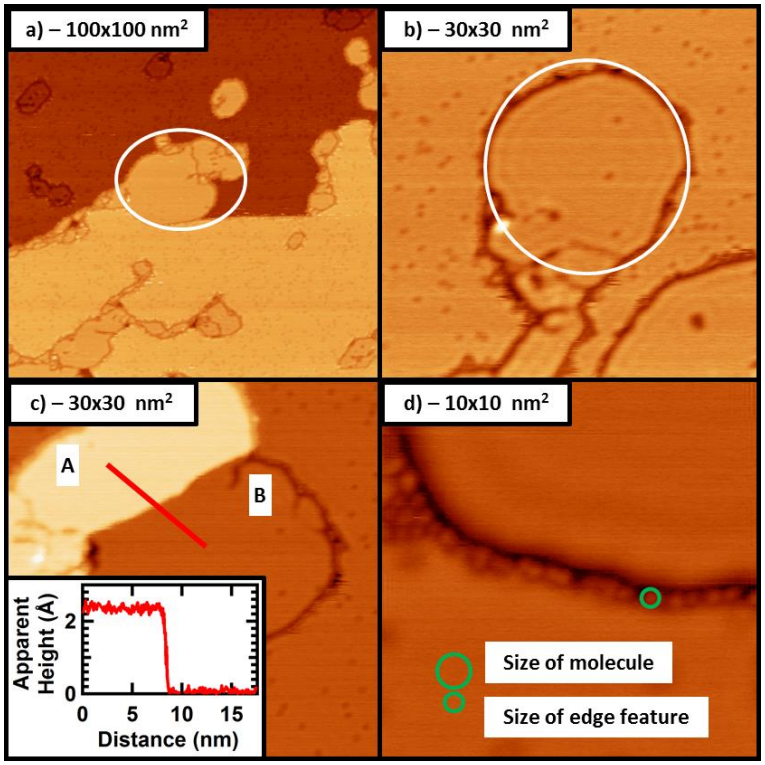

Figure 4.2.18 – *Graphene on Cu(111), after annealing the sample to 800 K.* *a) 100x100 nm²; V_s = -0.1 V. b) 30x30 nm²; V_s = 0.5V. The white circles in (a) and (b) show examples of two graphene islands. c) 30x30 nm²; V_s = 1.0 V; the inset shows the apparent height along the red line, where two islands (A) and (B) are compared. d) The size of a DiPy[5]DBH molecule is compared with the one of the features at the edge of the graphene patch (10x10 nm²; V_s = 0.3 V).*

Figure 4.2.19-b is a representation of the evolution of the apparent height with sample voltage of a bright graphene patch and of a dim graphene patch (respectively, green and purple cross in Figure 4.2.19-a). The apparent height difference between the two patches is constant (about 0.23 nm); however, it the height of both patches drops by about 0.06 nm at around 0 V. However, the apparent height of the Cu step (blue cross) is constant with voltage.

Again, the identical behaviour of the bright and the dim graphene patches suggests that the two islands are just sitting on two different copper terraces, and that surface erosion is to blame for this effect. Figure 4.2.19-c represents a side-view sketch of the phenomenon of surface etching, where the presence of graphene with different heights (or of molecular chains as in the case of Figure 4.2.16) is explained as a consequence of the erosion of the surface. Hence this evidence suggests that in fact only one type of polymeric chain and of graphene patch exists, on two different Cu levels.

The PAHs are known to induce reconstructions in the metal surfaces, and the copper surface is known for its atomic mobility. The combination of these factors can therefore induce the existence of two types of chains. The erosion of a metal by organic molecules, polymers or graphene is usually monitored at the step edges. In the present case we are observing an unexpectedly high etching of the surface in a terrace, as the dark chains and the dark graphene patch sink in the metal surface.

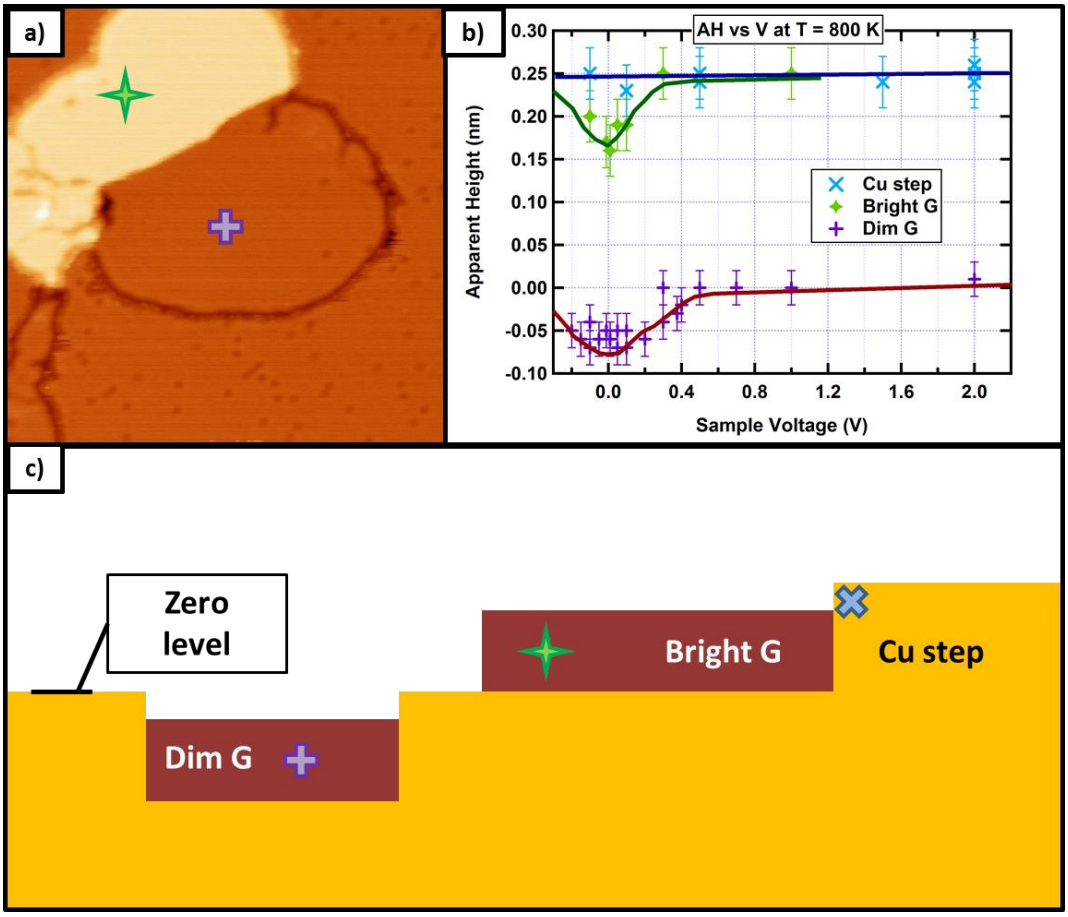

Figure 4.2.19 – *The apparent height of graphene varies with bias voltage, while the one of Cu does not.* *a) 30x30 nm^2; V_s = 1.0 V STM image of two islands of graphene (bright indicated by a green cross and dim indicated by a purple one). b) The evolution of the apparent height with sample voltages of three zones in the sample, namely bright graphene (green), dim graphene (purple) and a Cu step. The height of the Cu step is constant with voltage, while the one of the two graphene patches drops by about 0.06 nm at low voltage. c) A side-view sketch of the erosion of the Cu surface due to graphene. The black line indicates the 'zero level', the Cu plane where the apparent height is zero. As the apparent height of graphene is lower than the one of the Cu step, this is a model of the sample measured at low voltage with the STM: the Cu and the graphene have very similar (undistinguishable) heights at higher voltages.*

NEXAFS and XPS results – DiPy[5]DBH/Cu(111)

As for the case of Cu(110), we recorded NEXAFS and XPS spectra for DiPy[5]DBH on Cu(111): we carried out the experiments at the ALOISA beamline in the Elettra synchrotron. We here report the scans we obtained on a sample with one monolayer of DiPy[5]DBH.

Figure 4.2.20 shows the NEXAFS of DiPy[5]DBH/Cu(111) prior to annealing, recorded for both s- and p-polarised light (dashed black and solid red lines respectively). The room temperature PEY p-polarized NEXAFS exhibits: one asymmetric main peak A at 284.9 eV; four smaller peaks at B = 286.4 eV, C = 287.3 eV, D = 288.0 eV and E = 289.4 eV; a continuum after 291 eV. The s-polarized scan shows similar features, however, the asymmetry of peak A turned into two defined peaks, the second one being at 285.3 eV.

As for the case of Cu(110) in the previous Section, the most intense peaks at 284.9 and 285.3 eV are due to the C1s transitions to the LUMO π* states[77–82] of non-equivalent C sites in the molecules.[83,84] There is large dichroism between the s- and p-polarised signals, even though the s-polarised signal does not vanish. The π*

region is less intense for s-polarised light and the σ* region is less intense for p-polarised light. As for the case of Cu(110), this means that the molecules are not completely flat because they conserve the three-dimensional structure of an intact free molecule (see inset of Figure 4.2.20). However, the s-polarised intensity is smaller than the p- one, so the benzene rings of the molecules are laying on the surface at an average angle lower than 45º, as they try to couple their aromatic rings parallel to the surface.

Moreover, for p-polarised light, the peak at 284.9 eV is the most intense, while for s-polarised light the one at 285.3 eV is prominent. This asymmetry suggests again that the as-deposited diffusing molecule is three-dimensional since the contribution to the LUMO of the C1s electrons of carbon atoms in two different positions is geometrically different.

The small peaks B, D and E at 286.4, 288.0 and 289.4 eV can be associated to transitions of the C1s electros related to the C-H groups.[69,79,81–83,85–87] As for the case of Cu(110), peak C at 287.3 eV is likely to represent the carbon atoms in the pyridinic rings.[90] The broad features above 291 eV represent C1s transitions to the σ* symmetry.[79,80,89]

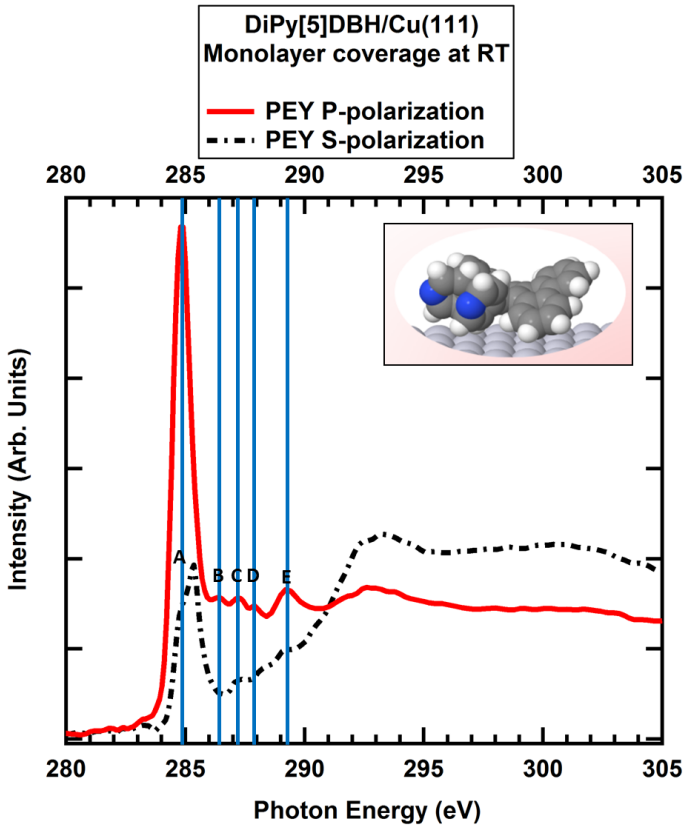

Figure 4.2.20 – *RT NEXAFS of DiPy[5]DBH/Cu(111).* *The solid red line represents the Partial Electron Yield (PEY) p-polarized scan, while the black dotted one the PEY s-polarized scan. In the inset, the three-dimensional intact molecule is shown. The blue lines indicate the position of the five peaks A–E.*

Figure 4.2.21 shows the evolution of the NEXAFS from room temperature to 620 K and to 690 K: next to the scan a sample STM image at each temperature is presented. It is clear that the NEXAFS of the molecules on

Cu(111) evolves with temperature with an identical trend as Cu(110): the main peak at 284.9 eV widens and the peaks in the C-H region fade away, which suggests that the molecule dehydrogenates and hybridises with the surface upon annealing. A small bump at 287.3 eV confirms the presence of the N upon annealing.

The middle scan of Figure 4.2.21 shows the NEXAFS of the polymeric chains where monomers can be distinguished, while the top one represents a transition phase such as the one of Figure 4.2.15-a, a stage between the polymeric chains with discernible building blocks, and the dark and bright chains. The NEXAFS scans of the annealed sample are very similar, because the chains are formed by the same units as the N-doped nanographene is the building block of both.

Moreover, as the annealing temperature is increased, the s-polarized π* resonances go to zero, maximising the dichroism with the p-polarised scan. Hence the cyclodehydrogenated molecule flattens, and this proves that the polymeric networks are formed by N-doped nanographene monomers.[69,78,80] The intensity of the p-polarised scan in the σ* region also decreases.

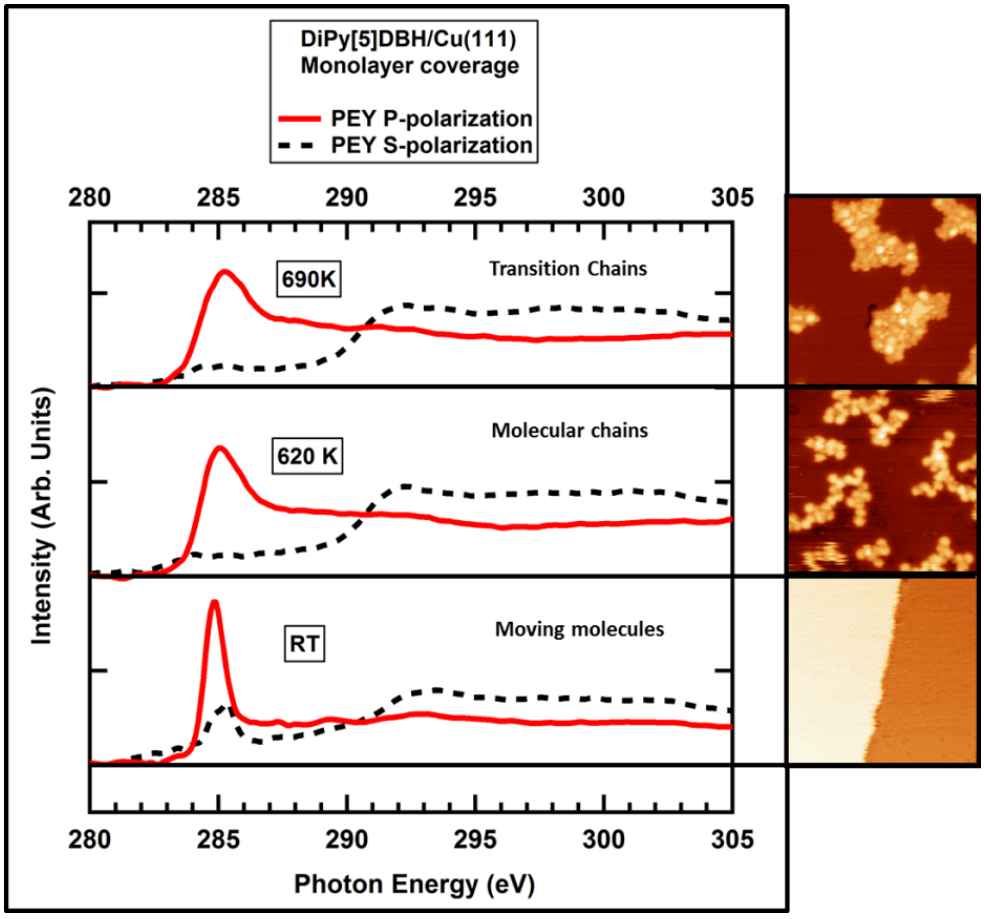

Figure 4.2.21 - *NEXAFS of one monolayer of DiPy[5]DBH/Cu(111).* *This figure shows the NEXAFS scan at three different temperatures, namely at room temperature at the bottom, at 620 K in the middle and at 690 K at the top; all the scans have been recorded at room temperature. 20x20 nm^2 V_s = 2.0 V STM images indicate each stage of the NEXAFS. Both s- (dashed black lines) and p-polarisation (solid red lines) were recorded.*

Let us now move to the N1s and C1s XPS spectra recorded at various temperatures, as shown in Figure 4.2.22. As in the case of Cu(110), the C1s scans were fitted with five peaks and the N1s with three.

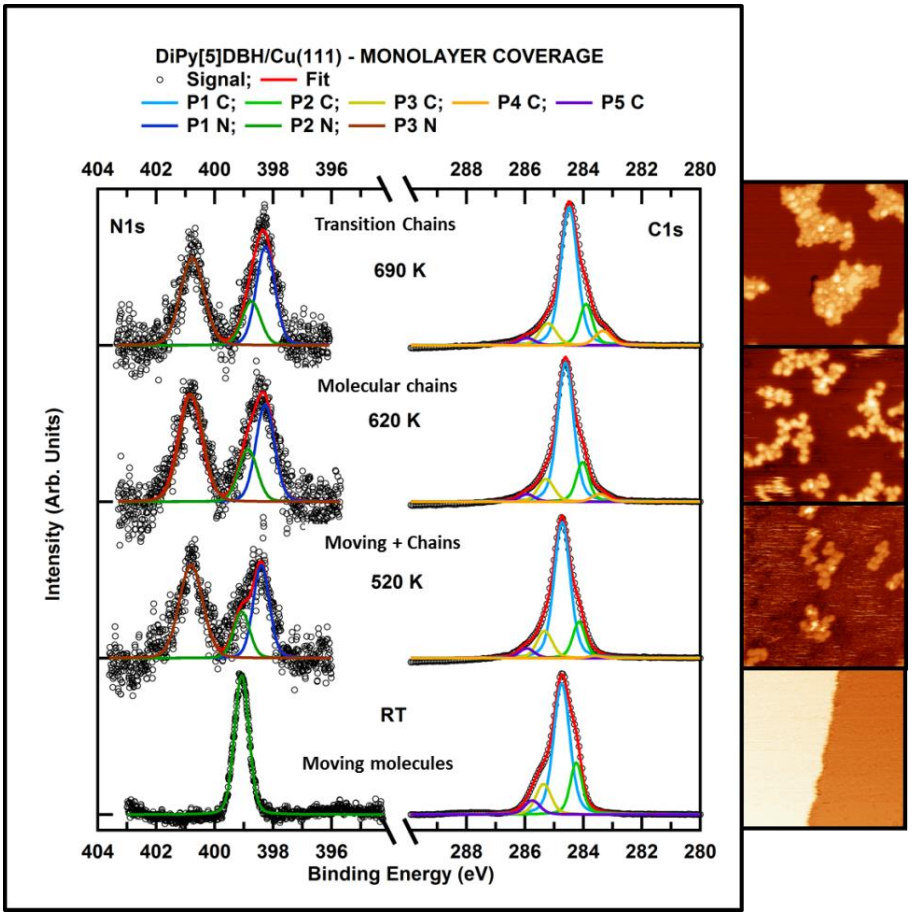

Figure 4.2.22 – *N1s and C1s XPS of one monolayer of DiPy[5]DBH/Cu(111) at various temperatures.* *The STM images on the right (20x20 nm^2; V_s = 2.0 V) represent the stage of the molecules upon the annealing. The intensity y-axis is not in scale for C1s and N1s.*

Table 4.2.2 indicates the binding energy of each peak and its assignation, which is the same as the case of Cu(110). The C1s binding energy of the main sp^2 component at room temperature of DiPy[5]DBH on Cu(111) is about 0.7 eV lower than the case of the same molecule on Cu(110). We will discuss more about this in Section 4.2.4. Unfortunately, the experimental set-up did not allow reaching the graphene formation temperature, and we stopped the annealing at the stage between polymeric molecular chains and the coexistence of dark and bright chains.

The trend of the area of each peak with temperature is similar to the Cu(110) and it helps to understand and explain the transformations of the molecules (Figure 4.2.23). P1-C (indicating C in aromatic rings) represents about 60% of the intensity, and upon annealing it peaks and then its intensity decreases: the increase is due to a decrease in P2-C (the C-H peak) caused by the dehydrogenating molecule, while the rise of the interaction with the surface (represented by P4-C) causes the final reduction.

Peak	BE (eV) at RT	Assignation
P1-C	284.7	Aromatic or Graphitic C
P2-C	284.2	C-H
P3-C	285.4	C-N
P4-C	- 283.6 at 520 K)	C-Cu
P5-C	285.7	C shake up
P1-N	- (398.4 at 520 K)	N-Cu
P2-N	399.1	Pyridine-like
P3-N	- (400.8 at 520 K)	Graphitic (substitutional) N

Table 4.2.2 – *Description of each XPS peak for DiPy[5]DBH/Cu(111).* *Each peak is described in terms of the Binding Energy (BE) at RT and of its assignation as discussed in the text for the case of Cu(110).*

The molecules diffuse at room temperature, so they interact weakly with the metal. However, as they (cyclo)dehydrogenate, they stop moving and their interaction with the surface increases. This is observed as a rise in the relative importance of P4-C. P3-C represents the contribution of carbon atoms bonded to the N dopants and it is constant throughout the annealing meaning that N atoms are not lost up to 700 K.

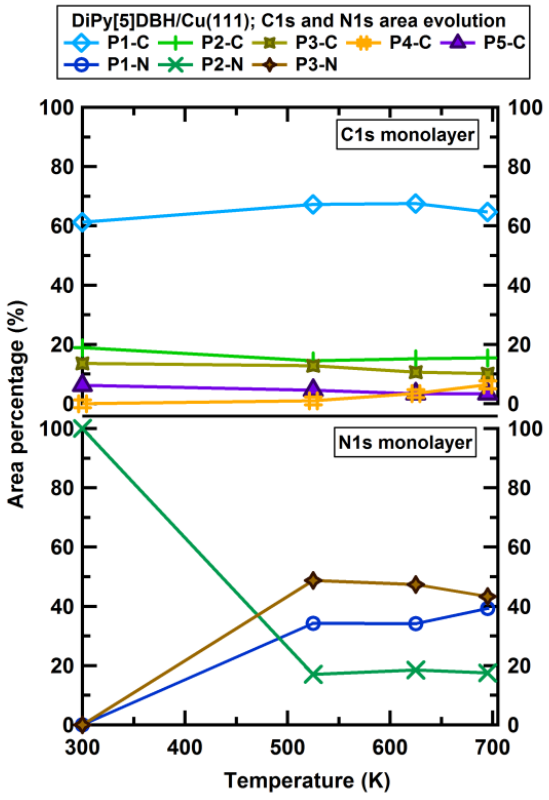

Figure 4.2.23 – *Relative area of each component of the C1s and N1s peak for DiPy[5]DBH/Cu(111) in terms of temperature.* *This figure shows how the five components of C1s (upper panel) and the three of N1s (lower panel) change upon annealing for one monolayer coverage.*

As discussed in the previous Section, the STM exhibits two types of chains of different apparent height, whose origin may be either topographic or electronic. If the bright and dim chains were electronically very different (*i.e.* if the dark chains were more "insulating" than the bright ones), the high resolution XPS spectra would show two distinct peaks, one for each type of chain. Figure 4.2.22 shows that this is not the case, and no new peaks appear in the expected range of temperatures. Therefore, the XPS suggests that the difference between the two chains is topographic.

The N1s area plot elucidates what is occurring with the pyridinic rings of the molecule. At room temperature, when the three-dimensional molecules are moving, 100% of N is in pyridinic form as indicated by the fact that only P2-N is present in the XPS. However upon annealing, P1-N and P3-N rise at the same time: the molecules dehydrogenate so the C dangling bonds meet other molecules forming graphitic N (P3-N) or bonding with the metal surface (P1-N) as a consequence of a rotation of the pyridinic ring, as explained for Cu(110).

4.2.3 DiPy[5]DBH/Au(111)

We now deposit DiPy[5]DBH on the Au(111) surface, known to be quite inert.[70] As for the previous metals, I will start by describing the STM results and in I will report then the NEXAFS and XPS results.

STM results – DiPy[5]DBH/Au(111)

As for the case of copper, at room temperature the molecules diffuse on gold (not shown) and are therefore invisible to the STM, since their motion is faster than the scanning speed. Upon annealing, the gold is able to catalyse the dehydrogenation reaction, however at a higher temperature than the copper. Figure 4.2.24 shows the system annealed to 650 K, where the molecules start to dehydrogenate and they interact with each other forming polymeric chains. The dehydrogenative polymerisation is not complete: some molecules are still moving, and they do not bind with the chains because they are still intact, with all the H atoms passivating the molecule.

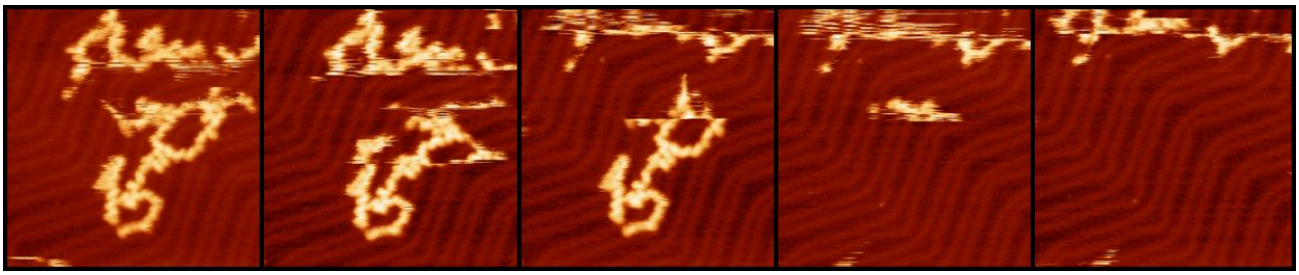

Figure 4.2.24 – *DiPy[5]DBH/Au(111) annealed at 650 K.* *The STM images (35x35 nm^2; V_s = -2.0 V) are subsequent, at first, a chain of monomers is observed, and as the images are scanned and the tip is passed on the surface, the chain and the molecules diffuse away.*

Figure 4.2.24 represents five consequent images of the same zone: the molecules interact with each other due to dehydrogenative polymerisation: however, since the molecules are not fixed on the surface, they can easily be moved by the STM tip. The herringbone surface reconstruction of gold is the reference for the relative position of the molecules in Figure 4.2.24.

Further annealing stabilises the chains on the surface, as Figure 4.2.25 confirms. In a highly stepped part of the sample, at 670 K oligomers surge from the steps themselves, since they are more reactive sites than the terraces (Figure 4.2.25-a); here the molecules are clearly distinguishable as round features, and they sit both above and below the step. Figure 4.2.25-b and -c represent the sample annealed at 730 K. At this point, the dehydrogenation is able to allow covalently bonded hetero-polymers to form: here too, as for the case of Cu(110) and Cu(111), the as-deposited molecules diffuse, therefore when they dehydrogenate they can meet and bond with each other. This is opposed to the case of Pt(111), where the molecules are energetically not allowed to move and therefore the dehydrogenation changes the structure of one single molecule.

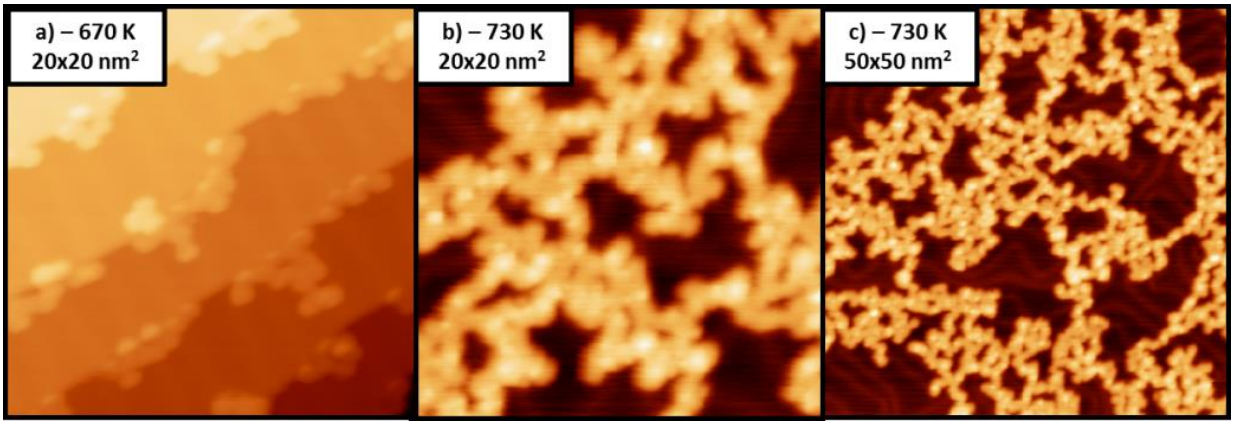

Figure 4.2.25 – *STM images of the formation of chains on Au(111) at 670 and 730 K.* *a) This image shows how in a highly stepped zone of the surface, the molecules tend to attach to the steps edges (670 K; 20x20 nm², V_s = -2.0 V). b) Further annealing completes the formation of chains (730 K; 20x20 nm², V_s = 2.0 V). c) 730 K; 20x20 nm², V_s = 2.0 V*

In Figure 4.2.25-b and -c, we see the height distribution within the molecules is not constant, ranging from about 0.25 to 0.35 nm, as brighter bumps are present. Moreover the molecules are no longer distinguishable, as opposed to Figure 4.2.25-a. The origin of the roughness is twofold. As discussed in Chapter 3, on one hand we have to keep in mind that N is included in the layer, and the local density of states at these points can be much higher.[71] Secondly, the dehydrogenation and cyclodehydrogenation forces allow the formation of the polymers and also the modification of the building blocks within the chains, like in Pt. Therefore partial (cyclo)dehydrogenation creates bumps on the surface due to the coexistence of domes and of nanographene building blocks.

When we anneal the molecules at 800 K, dark chains similar to the ones observed on Cu(111) arise, and Figure 4.2.26 displays different STM images of this phenomenon. The width of these features is between 0.6-2 nm, the apparent height is negative.

Figure 4.2.26-a is a panoramic image of the nanoribbons to depict the general state of the sample, while Figure 4.2.26-b is a scan of a smaller region. Figure 4.2.26-c and -d represent the same image with different contrasts. Figure 4.2.26-c shows an island where a bright chain surrounds different patches, similar to the ones observed in Figure 4.2.16 or Figure 4.2.18 for Cu(111). The visual contrast of Figure 4.2.26-d reveals that these patches enclosed in the dark chains exhibit the herringbone structure: this is clear evidence that for the case of Au, the bright and the dark chains are just sitting on two different gold levels. Therefore, the case of Cu(111) is likely to be the same. Figure 4.2.26-e is another example of bright and dim chains where the herringbone reconstruction can be observed in the patches. As for Cu(111), the edges of these chains on Au(111) are darker than the cores (Figure 4.2.26-f): this may be an electronic effect caused by the dehydrogenated edges bonding with the metal underneath.

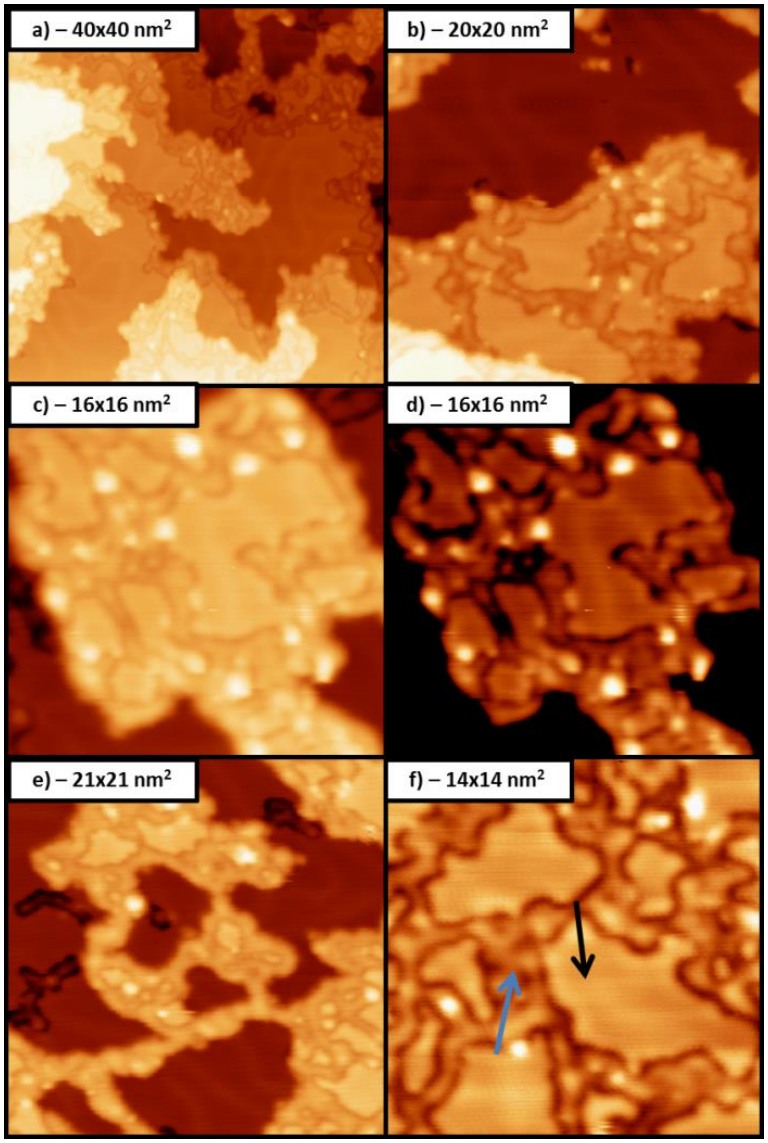

Figure 4.2.26 – *DiPy[5]DBH annealed at 800 K forms dark and bright chains with undistinguishable building blocks.* *a) 40x40 nm^2 V_s = 1.0 V. b) 20x20 nm^2 V_s = 1.0 V. c) 16x16 nm^2 V_s = 2.0 V. d) Same as (c) with a different contrast. e) 21x21 nm^2 V_s = 2.0 V. f) 14x14 nm^2 V_s = 1.5 V; the blue arrow indicates a nanoribbons and the black one indicates a gold patch.*

NEXAFS and XPS results – DiPy[5]DBH/Au(111)

In this Section I will start by showing N K- and the C K-NEXAFS edge for a multilayer coverage (about 1.5 ML) of DiPy[5]DBH deposited on Au(111) at room temperature and at 690 K (molecular chains); qualitatively, the peaks of both edges are identical to the ones of the submonolayer coverage, since their position and proportion are the same.

The N K-edge at room temperature, (Figure 4.2.27 lower left panel) is rich in components. The main peak (P1-N) lays at 398.7 and it is caused by transitions of pyridinic N1s into the π_1* orbital.[42,77,93,113,114] The other RT peaks (P2-N at 400.3 eV and P3-N at 402.5 eV) are also transitions of pyridinic N into higher Unoccupied Molecular Orbitals:[113–115] We will see later that in the XPS only pyridinic N is present at room temperature. The broad continuum above 404 eV represent transitions of the C1s electrons to the σ* orbitals.[42,116]

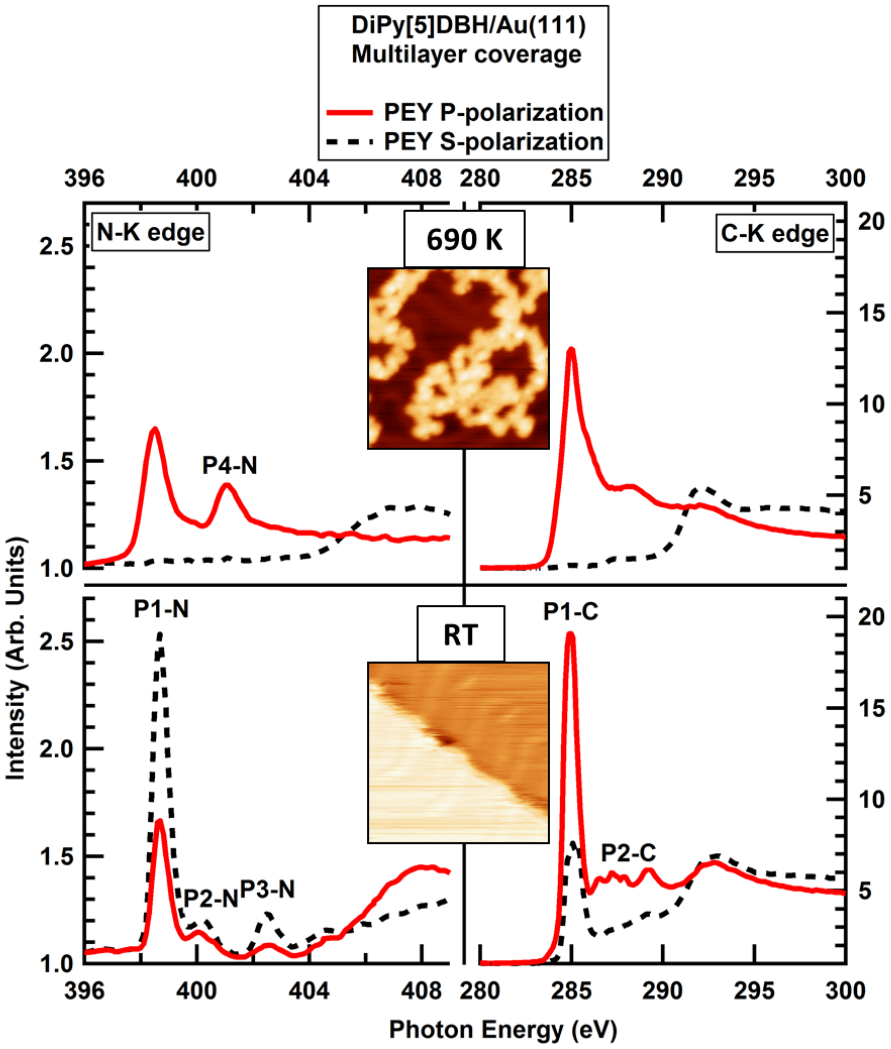

Figure 4.2.27 – ***PEY N K- and C K-edge NEXAFS of multilayer of DiPy[5]DBH/Au(111).*** *The scans were measured on the RT sample (bottom panels) and on the sample annealed to 690 K (lower panels). The red solid line represent the p-polarised scan and the blue dashed line the s-polarised one.*

Upon annealing at 690 K, the higher energy peak smears out and another more intense peak appears at 401 eV (P4-N): this new peak is the hallmark of graphitic N (defect 1 in Figure 4.2.9), the N that substitutes a C atom in the graphene network.[42,77] Since no graphene is observed with the STM at this temperature, we can conclude that the molecular polymers formed at 690 K are bonded not only via the carbon dangling bonds caused by dehydrogenation, but also with the N, by including it in the graphitic network.

The C K-edge resonance behaves similarly to the Cu(110) and Cu(111) edges. At room temperature the main peak P1-C at 284.9 eV is caused by the C1s transition of the aromatic rings to the π_1* empty state. The other peaks (P2-C at 286.6, 287.8 and 289.2 eV) indicate transitions of the C1s electros related to the C-H bond. When molecular chains are formed at 690 K, the C-H hallmarks fade away – although not completely, which indicates only partial dehydrogenation. As for the case of Cu, the peak at 287.2 eV represents the transitions of C1s electrons in the pyridinic rings. Moreover, the main peak broadens slightly, which again indicates a (minor, in this case) hybridization with the metal surface.

Let us now discuss the orientation of the molecule with respect to the surface. The C K-edge at room temperature shows that the molecules are three-dimensional, since the s-polarized signal of the π* states is not zero; however, it is less intense than the p-polarized one, therefore the angle of the aromatic rings of the molecule with the surface must be less than 45º (it would be 45º if the p- and s-polarized signals were the same).

However, the surprise comes from the N K-edge at room temperature: contrary to the C K-edge case, at room temperature the s-polarized signal of the π* states is greater than the p-polarized one; if we assume that the geometry of the molecular orbital of the pyridinic rings is the same as the one of the aromatic C rings, and that all the pyridinic rings are equally oriented, we can calculate the angle of the pyridinic rings with respect to the Au surface, by using Equation 3 of Chapter 2.

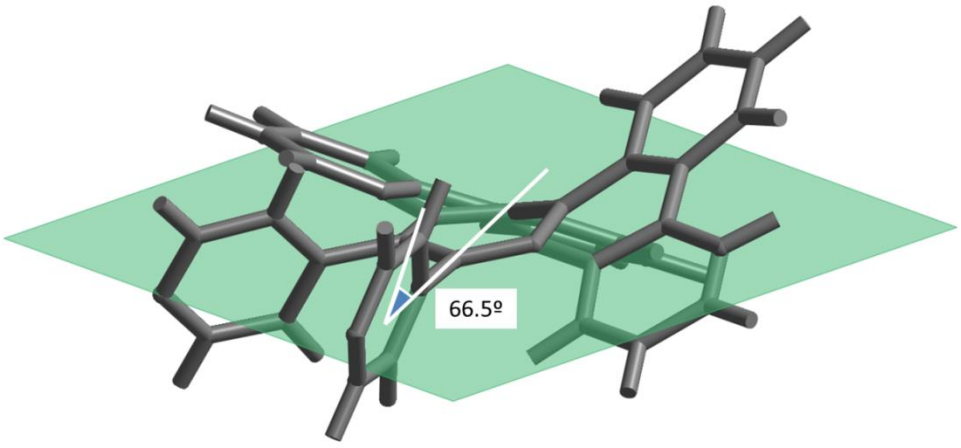

Figure 4.2.28 – ***The angle between the plane of the central benzene ring and the pyridinic rings for the free molecule is 66.5º.*** *The green rhomb indicates the plane of the central benzene ring.*

The resultant angle of the plane of the pyridinic ring to the surface is 64.5º. The calculated angle between the pyridinic rings and the plane of the central benzene ring for the free molecule is found to be 66.5º,

remarkably similar to the one obtained with the NEXAFS scans. Figure 4.2.28 is a graphic representation of the free molecule, and the angle between the central benzene ring (green plane) and the two pyridinic rings (blue circles) is predicted to be 66.5º. The similarity between the observed and calculated angle of the ring suggests that the structure of the as deposited molecule on Au(111) is not affected by the presence of the metal, thereby confirming the low surface-adsorbate interaction.After annealing, when the chains form, the molecule flattens. The intensity of the s-polarized beam around the π edges goes to zero for both the N K-edge and the C K-edge.

Figure 4.2.29 shows the N1s XPS peak for the multilayer and the C1s peaks for multilayer and submonolayer coverage. The XPS scans of Figure 4.2.29 represent the moving molecule at room temperature, the moving molecules after annealing the sample to 580 K (some molecules already dehydrogenate), and the molecular chains at 690 K.

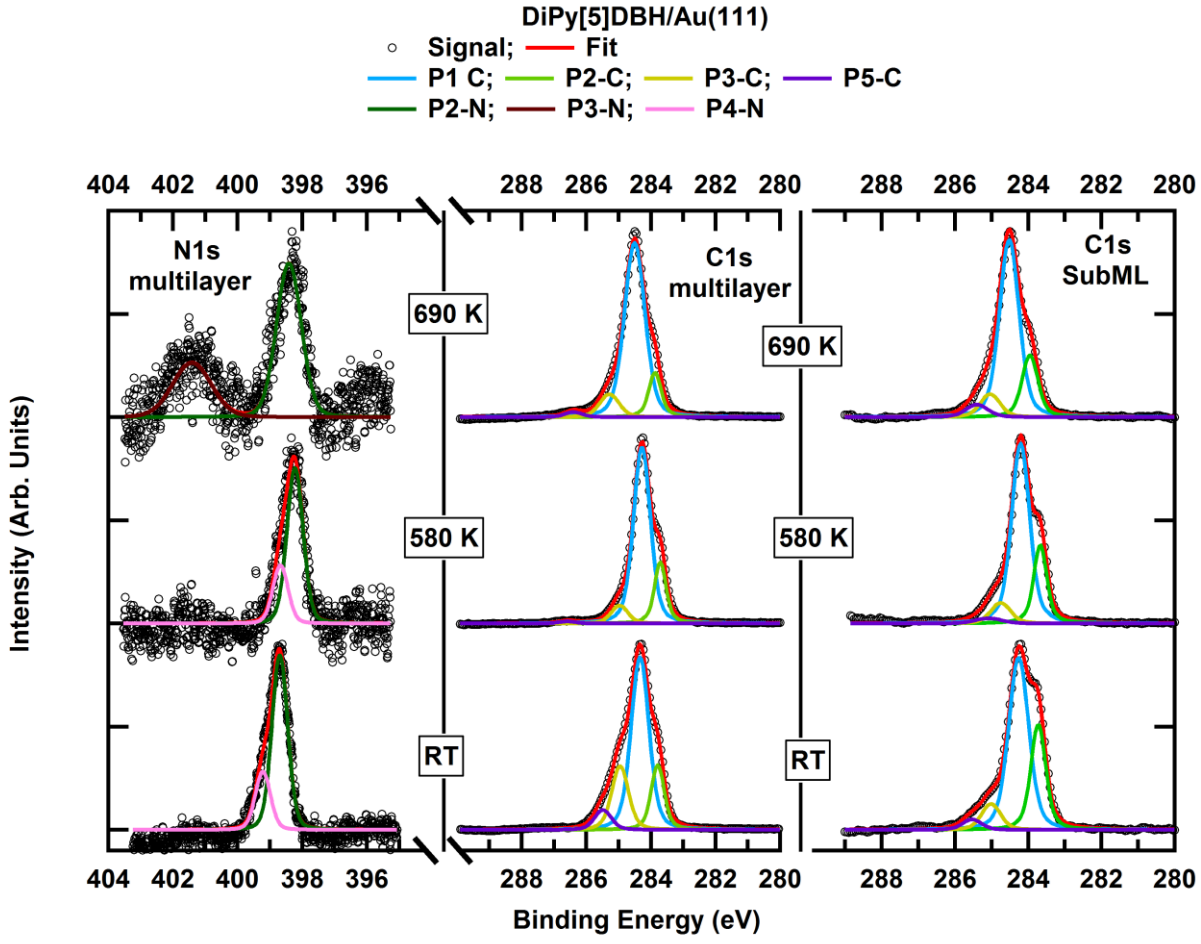

Figure 4.2.29 – *XPS of DiPy[5]DBH/Au(111).* *The left panel shows the N1s peak for multilayer coverage in terms of temperature; the middle panel shows the C1s peak for multilayer coverage; the right panel shows the submonolayer C1s peak. We measured the XPS for RT (moving molecules), 590 K (moving molecules + partial dehydrogenation) and 690 K (molecular chains). The intensity y-axis is not in scale for C1s and N1s.*

Let us first discuss the C1s peaks, using the same connotations as for the previous substrates. First of all, the C1s peak has now four components, since P4-C (the one that indicates the bonding between C and the metal) is not present. Qualitatively, the multilayer and the submonolayer C1s peaks are similar: the evolution of the areas (Figure 4.2.30) proves it. In both cases, P1-C (the carbon from the aromatic rings) increases, while P2-C (C-H) decreases when the molecules dehydrogenate.

Throughout this chapter, we have been relating P3-C to the carbon in the pyridinic rings; however, P3-C in the room temperature multilayer scan on Au has a relative intensity of 25%, much higher than the 10-20% of DiPy[5]DBH on the Cu(110), Cu(111) and submonolayer Au(111). The rise of P3-C is due to the charge effect of the molecules in the upper levels which are insulating and are not in direct contact with the gold: therefore part of P1-C moves to higher binding energy. The decrease in P3-C of the multilayer after the soft annealing at 580 K means that this temperature is enough to desorb the molecules on the top layers, leaving only one monolayer.

The main component of the N1s peak at RT (Figure 4.2.29, bottom left panel) is related to the pyridinic nitrogen (P2-N at 398.7 eV); however, one component is now not enough to fit the peak since a shoulder at higher binding energy appears (P4-N at 399.2 eV). This shoulder has the same origin as the rise in P3-C for the C1s peak: due to the multilayer coverage, the molecules of the upper layers are not in contact with the metal, revealing an insulating character and their binding energy increases due to charge effects.

Upon annealing to 580 K, P3-N rises at 401.4 eV, as the formation of the chains leads to an increase in the graphitic N peak, as the case of the molecule on previous metals.

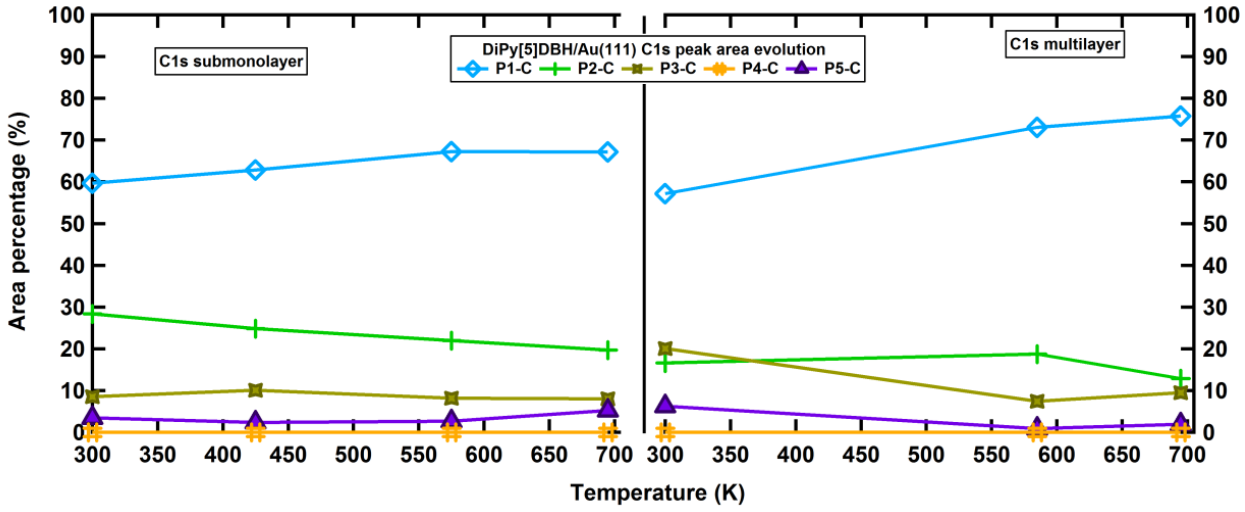

Figure 4.2.30 – *Relative area of each component of the C1s peak for DiPy[5]DBH/Au(111) in terms of temperature.* *This figure shows how the five components of C1s for the submonolayer (left panel) and for the multilayer (right panel) change upon annealing*

4.2.4 Discussion: DiPy[5]DBH on coinage metals

In the previous Sections we have discussed the results for DiPy[5]DBH on different coinage metals, and in this Section we will summarise the results, referring to Figure 4.2.31. The similarity of the STM and the spectroscopic results indicate that the molecules follow similar trends upon annealing on the three different surfaces.

We can identify three main stages upon annealing: as represented in Figure 4.2.31, in stage 1, the molecules are diffusing; in stage 2, polymeric networks form; in stage 3 there is full molecular decomposition and graphene prevails. DiPy[5]DBH on Au(111) was not observed to form graphene, possibly because we did not reach the needed temperature for graphene formation to avoid deteriorating the surface.

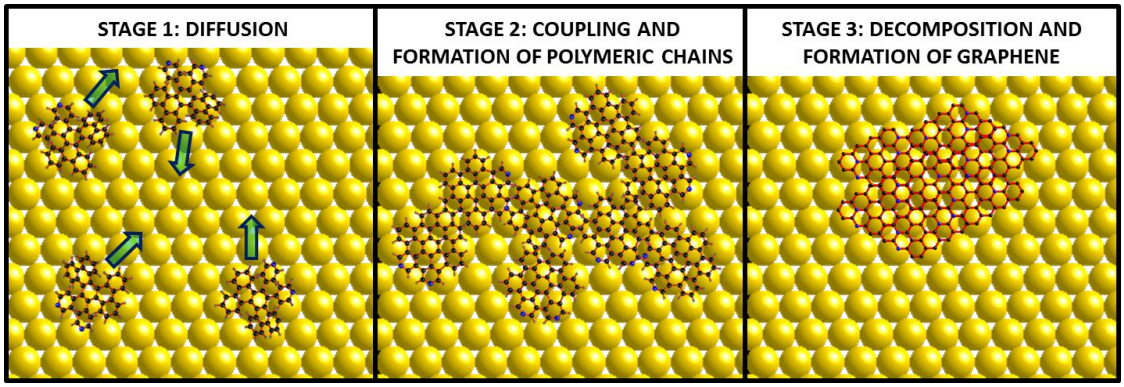

Figure 4.2.31 – ***The three main stages undergone by DiPy[5]DBH on coinage metals upon annealing.*** *At room temperature, the molecules diffuse (stage 1). Upon annealing cyclodehydrogenation and dehydrogenative polymerisation allows the formation of chains of N-doped nanographene monomers (stage 2). Further annealing allows the decomposition and formation of N-doped graphene (stage 3).*

Stage 1 – Diffusing molecules:

The as-deposited molecules cannot be observed by STM because they diffuse faster than the scanning speed. However, we confirm their presence both by NEXAFS and by XPS. Other than the very intense narrow feature at around 284-285 eV due to the transitions of C1s electrons of the aromatic rings to the π* levels, the NEXAFS exhibits smaller peaks between 286 and 289 eV due to transitions of C1s electrons related to the C-H groups. The presence of these peaks is very important since it suggests that the molecules do not dehydrogenate inside the crucible or on the sample at room temperature.

The lack of complete dichroism in the C K-edge NEXAFS shows that the non-annealed molecules maintain their three-dimensional shape caused by their helical structure, and are therefore intact. On Au(111), the N K-edge NEXAFS allow calculating the angle between the pyridinic rings and the surface, which were tilted by 64.5º. The estimation of this angle is possible because N atoms are present only in the pyridinic rings, however it may be misleading because the two pyridinic rings of a single molecule may be oriented in different ways, as for the case of Pt(111), and the NEXAFS would only show the average angle of the two.

For both copper and gold, the C1s XPS peak of the diffusing molecules show three main components: P1-C, due to C-C bonds in the aromatic rings; P2-C representing C-H bonds of the aromatic rings; P3-C indicating the C atoms connected to the N in the pyridinic rings. No interaction between the molecule and the metal is observed nor expected.

The N1s XPS spectra show that only one sharp component at about 399 eV exists on the surface. Indeed the two N atoms in each molecule are identical and belong to pyridinic rings: hence P2-N is the signature of pyridinic N in an aromatic ring, not interacting with the metal surface or with other molecules.

Stage 2 – N-doped chains:

As the annealing temperature is increased, surface-assisted cyclodehydrogenation and dehydrogenative polymerisation take place. On Cu(111) and Au(111), we observe two types of chains: we will refer to the chains where the monomers are distinguishable, which also exist in Cu(110) (such as those in Figure 4.2.2, Figure 4.2.12, Figure 4.2.15 and Figure 4.2.25) as polymeric chains, and the ones where bright and dim chains coexist (only visible in Cu(111) and Au(111)), where no monomers are discernible (exhibited in Figure 4.2.16 and Figure 4.2.26) as graphene nanoribbon chains. This name is usually employed to describe long covalent aromatic sp^2 carbon chains, with a constant width. The ribbons we show in this thesis do not have an unchanging width, but they are indeed covalent aromatic sp^2 carbon chains.

Let us first focus on the polymeric chains, observed in the three precursors. The most striking change of the C-K NEXAFS of the chains with respect to the diffusing molecules is the complete dichroism between p- and s-polarised light scans. Since DiPy[5]DBH is a PAH, it comprises aromatic rings with π and σ molecular orbitals, and the dichroism indicates that the molecules in the chains lay flat on the surface. Due to steric constraints, the only way that DiPy[5]DBH can lay flat on a surface is if the molecule cyclodehydrogenates, by breaking the eight C-H internal bonds, and forming four new C-C bonds giving rise to new aromatic rings, and to N-doped nanographene, as discussed in Chapter 3 and in Section 4.1 of Chapter 4.

Moreover, the C-H peaks disappear upon annealing, indicating a (partial) dehydrogenation. The dehydrogenation is also reflected by a decrease in the C-H component (P2-C) in the C1s XPS peak upon annealing. These results confirm that polymeric chains are formed by N-doped nanographene monomers. These monomers unify by dehydrogenative polymerisation, which means that the C-H bonds at the edge of the molecules break and allow different molecules to bind together by forming new C-C bonds from the dangling C bonds.

On copper, the formation of polymeric chains goes along with the rise of a new component in the C1s XPS spectrum, namely P4-C, the signature of a (covalent) interaction with the metal surface. This interaction is absent for the case of Au, up to 690 K, the maximum temperature reached for the spectroscopic experiments. Hence, on Cu as the precursors dehydrogenate and polymeric chains form, the surface-adsorbate interaction rises. The interaction of the metal is further confirmed by the broadening of the peak at 284-285 eV in the C K-edge of NEXAFS.

Two new components arise and coexist with P2-N in the N1s XPS peaks of the polymeric chains: P1-N at around 398 eV and P3-N at about 401 eV. The first peak indicates an increase in the interaction with the surface, and it is absent for the case of Au. The last peak represents substitutional N in a graphitic network. P3-N shows that the N-doped nanographene monomers unify not only by the link of two C dangling bonds,

but also by the bonding of lone pairs of N atoms with a C dangling bond. This is also confirmed by the rise of a new peak at 401 eV (P4-N) in the N K-edge NEXAFS of DiPy[5]DBH/Au(111) annealed at 690 K, which has been reported as the hallmark of graphitic N. The dichroism existing between the non-annealed and the annealed N K-edge of DiPy[5]DBH/Au(111) confirms that also the pyridinic rings flatten upon surface-assisted cyclodehydrogenation.

The second type of chains, the so-called graphene nanoribbons, only appear on the (111) faces of Cu and on Au when annealing at a higher temperature than the polymeric chains. Here the monomers are no longer discernible, as if the building blocks of these chains had fused together to form a long single unit, similar to a graphene nanoribbons,[17] but of variable width. The XPS and the NEXAFS on Cu(111) and on Au(111) have only been recorded up to 690 K, and this temperature is too low to achieve nanoribbons. However, from the spectroscopic information on Cu(110), we know that the XPS and NEXAFS of the polymeric chains and of graphene are very similar, therefore we expect the nanoribbons to behave likewise.

The most interesting feature of the nanoribbons is that they show two different apparent heights: indeed bright and dim chains coexist with a height difference of about 0.18±0.03 nm. The origin of these features may be either electronic or topographic, and the evidence discussed in Section 4.2.2 and 4.2.3 suggests that the bright and the dim chains are equal but sitting on different terraces, hence they exhibit different apparent height. Indeed the apparent height of graphene on Cu has been reported to be 0.07 nm,[111] similar to the value of the dim chains on Cu, while the one of graphene on gold is negative,[70] meaning that its apparent height is less than the one of Au.

The existence of graphene nanoribbons on different terraces may hence be caused by surface erosion and mass transport of the metal underneath (etching). Some large aromatic molecules such as C_{60}[117] and the Lander molecule[46] have been reported to induce a rearrangement of the close-packed metal surface underneath. The same may be happening here: the surface atoms may rearrange and form vacancies, and this may be the cause of the apparent height gap between bright and dim chains. As for the case of C_{60} (see Chapter 6), the presence of the aromatic molecule may induce the rearrangement of surface metal atoms, and this structural change has then the effect of decreasing the apparent height of the ribbon. However not all the ribbons catalyse the vacancy formation, hence bright and dim ribbons coexist.

Stage 3 – N-doped graphene:

In the final stage of the (cyclo)dehydrogenation process, the polymeric chains and the nanoribbons transform into graphene. We observe this phase only on the two copper surfaces, not on Au(111), which is not annealed above 825 K to prevent damaging the surface. Even though neither moiré nor atomic resolution is achieved in most cases, the spectroscopic information on Cu(110) confirm that what we observe is in fact graphene. The C1s XPS peak narrows, which is typical of graphene.[118] Moreover, the graphitic N component (P3-N) in the N1s XPS spectra rises, hence confirming the presence of N-dopants in the network. The C K-edge of NEXAFS also recalls the one of graphene, as reported by Preobrajenski *et al*.[80] On Cu(110) we observe a linear moiré.

It is important to notice that the shape of the C K-edge of NEXAFS is similar for polymeric chains and for graphene, which indicates that the chains are composed of N-doped nanographene bricks. As for the case of

nanoribbons, vacancies on the metal surfaces are likely to originate the presence of coexisting bright and dim graphene islands

Binding energy variations of P1-C upon annealing

The binding energies' change upon annealing are important to understand changes in the interaction of the molecules with the surface, therefore we will now track the changes with temperature of the submonolayer C1s main peak – P1-C, the carbon atoms in the aromatic rings – for the three surfaces analysed with XPS (Cu(110), Cu(111) and Au(111)).

As Figure 4.2.32 indicates, the value of the binding energy of P1-C for the molecule at room temperature on each surface is different, namely 284.3 for Au(111), 284.7 eV for Cu(111) and 285.3 eV for Cu(110). The binding energy of the sp^2 C-C bond in Highly Ordered Pyrolytic Graphite (HOPG) has been reported to lay at 285.5 eV,[119] hence the corresponding peak for DiPy[5]DBH on the studied metals varies from this standard value. The difference in binding energy at room temperature shows that even though the molecules are moving on all the surfaces, they interact differently with the substrate. The reason for this different behaviour is likely to be the different charge transfer to or from the surface to the formed nanostructure. DiPy[5]DBH behaves as an electron donor on Cu(110) and to a lesser extent on Cu(111), while it behaves as an electron acceptor on Au(111).

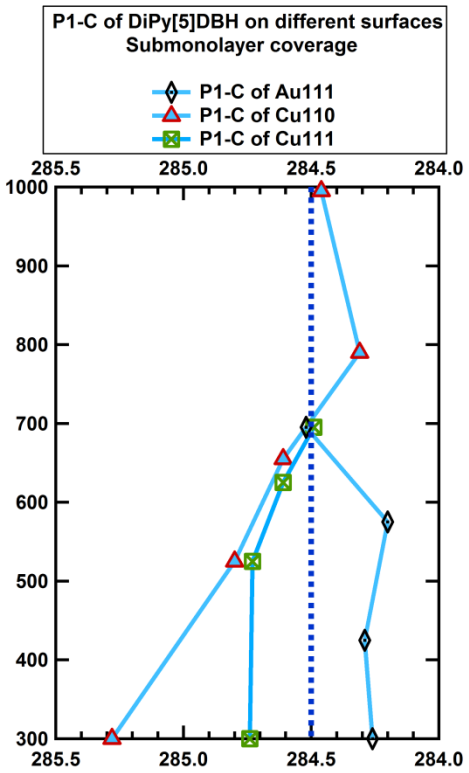

Figure 4.2.32 – *Binding Energy shifts of P1-C with temperature for the different surfaces (submonolayer coverage).* *The black rhombi represent Au(111), the red triangles Cu(110) and the green squares Cu(111). The blue shaded line indicates the standard value of the binding energy of HOPG (284.5 eV).*

Upon annealing, the peaks of the molecule on Cu(110) and Cu(111) shift towards lower BE as opposed to the one of DiPy[5]DBH on Au(111) which shifts towards higher binding energy. At about 700 K, the energy of all the three peaks converges at 284.5 eV, meaning that the electronic structure of the molecules start to look alike and to resemble the one of HOPG, or graphene.

Hence, the starting point of the binding energy differs, because of the different interaction between the pristine molecule and the coinage metals. However, upon annealing the electronic structure of the dehydrogenate molecules converge. Unfortunately, we have no higher temperature measurements of Au(111) and Cu(111); however, P1-C on Cu(110) moves to even lower binding energy before adjusting to its final graphene state.

Phase diagram on the four different surfaces

To provide a comprehensive view on the role of the adsorbate-surface interaction on the (cyclo)dehydrogenation of the hetero-aromatic precursor as a function of annealing temperature, we construct a phase diagram for DiPy[5]DBH on the different surfaces studied here

The construction of this diagram is possible because the same structures form on the coinage metals. DiPy[5]DBH/Pt(111) is also included here. Within a temperature range of 300-825 K, intriguing differences emerge in the behaviour of the precursor on the Pt(111) *versus* Cu(110), Cu(111) and Au(111). These differences manifest in terms of different phase-transition temperatures and different outcomes of the (cyclo)dehydrogenation, which is shown in Figure 4.2.33.

On Pt(111) (column 1 of Figure 4.2.33 and insets) no diffusion is present and we can see three main phase transitions. First, at the threshold temperature of 400 K, the pristine molecule **1** (light orange) undergoes partial cyclodehydrogenation, and the helicene part of the precursor flattens forming **2** (orange), and the four bright lobes of the molecular orbitals turn into two protrusions. At about 600 K, the conversion of **2** to N-doped nanographene **3** occurs (red) by a completion of cyclodehydrogenation. Further annealing allows the formation of N-doped domes **4** (dark red) as the C-H bonds at the edges of **3** break. A fourth phase transition occurs at 850 K (not shown in Figure 4.2.33) to form N-doped nanographene.

In stark contrast to that, DiPy[5]DBH diffuses on the coinage metals (light blue zone of columns 2-4 of Figure 4.2.33-a and Figure 4.2.33-f) at room temperature, hence favouring its conversion into networks. The phase transition from moving molecules (light blue) to chains (lilac) is gradual: the precursors undergo an intermediate phase where diffusing molecules coexist with the chains (blue, Figure 4.2.33-e).

Moreover, the phase transition into polymeric networks (lilac in Figure 4.2.33-a and -d) occurs at a different threshold temperature for each coinage metal, namely 580 K for Cu(110), 620 for Cu(111) and 670 for Au(111).

The next phase transition only occurs for Cu(111) at 690 K and Au(111) at 720 K: the polymeric networks complete the cyclodehydrogenation and transform into graphene nanoribbons (purple zone, Figure 4.2.33-a and -c). Here, the building blocks forming the polymers are no longer distinguishable, and dark and bright ribbons are observed. The origin of coexisting dark and bright chains is likely to be the induction of an etching of the metal surface indicating mass transport and rearrangement of the uppermost atoms.

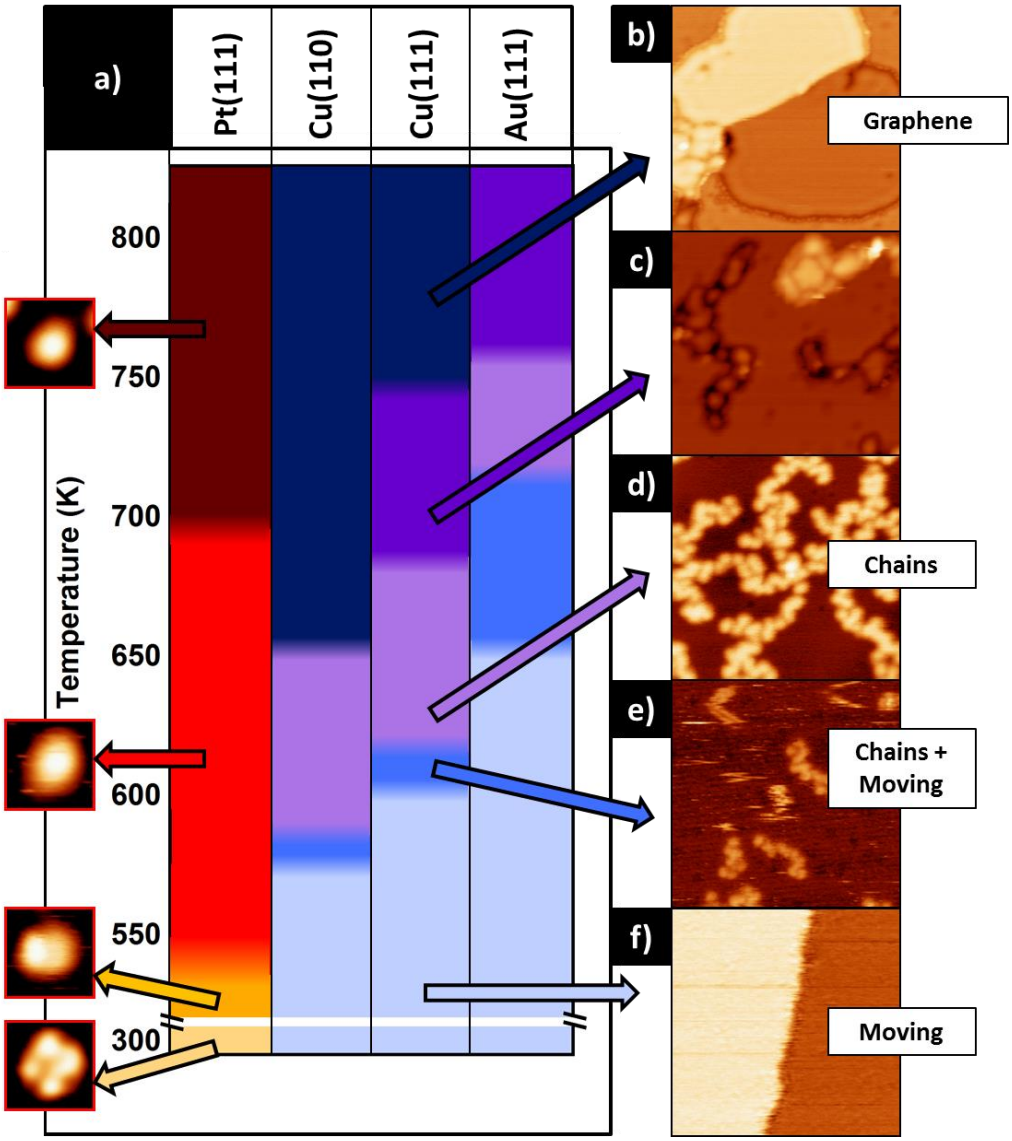

Figure 4.2.33 – ***Phase diagram and STM images of the different nanostructures formed by surface assisted cyclodehydrogenation of DiPy[5]DBH on four different metals.*** *a) The different colours indicate different nanoarchitectures. Column 1 shows the precursor deposited on Pt(111) (light orange zone), which undergoes three phase transitions upon annealing to form an intermediate stage (orange), 2N-HBC (red zone) and nano-domes (dark red zone). The insets show the STM images of all phases (3x3 nm^2; V_s = 2.0 V). The N-doped graphene grown at 850 K is not shown in column 1. The diffusion of DiPy[5]DBH on Cu(110), Cu(111) and Au(111) is indicated by the light blue region in columns 2-4 respectively. Upon annealing, after the first transition temperature, the polymeric chains start to form, coexisting and for a range of temperature they coexist with diffusing molecule (blue zone in columns 2–4). Further annealing allows the formation of chains (lilac). At higher temperature, Cu(111) and Au(111) exhibit dark and bright chains (purple zone in columns 3 and 4). Further heating transforms the precursors in an N-doped graphene layer (dark blue zone in columns 2 and 3). b) The dark blue zone refers to the N-doped graphene phase (20x20 nm^2; V_s = -0.05 V). c) The purple zone refers to the dark and bright chains (20x20 nm^2; V_s = -3.5 V). d) The lilac zone refers to the polymeric chain (20x20 nm^2; V_s = -2.0 V). e) The blue zone refers to diffusing molecules coexisting with the seeds of the chains (20x20 nm^2; V_s = -2.0 V) f). The light-blue zone refers to the freely diffusing molecules (20x20 nm^2; V_s = -2.0 V).*

A fourth phase transition results in the growth of a N-doped graphene layer as supported by the N1s-XPS. The determined threshold temperatures for this N-graphene phase are 660 K for Cu(110) and 750 K for

Cu(111) (dark blue in Figure 4.2.33-a and -b, columns 2 and 3). We have not observed formation of N-doped graphene on Au(111) below the upper limit of 825 K (Figure 4.2.33-a, column 4).

The substrate-dependent transformation of DiPy[5]DBH supports the concept of metal catalysis in on-surface dehydrogenation processes. The (110) face of Cu is the most catalytically active in transforming the precursor to N-doped graphene. As mentioned above, the (110) face exhibits close-packed rows of the Cu atoms, which are more reactive and, therefore, dehydrogenation and graphenisation reactions are boosted here. Moreover, we find gold to be less catalytically active towards cyclodehydrogenation than the copper surfaces. The precursor cyclodehydrogenates on this metal but it needs a greater injection of external energy (provided in terms of higher temperature) to complete the process.

4.3 DiPy[5]DBH on different transition metals: conclusions

The aim of this chapter is to uncover all the details of the (cyclo)dehydrogenation of DiPy[5]DBH to achieve N-doped nanographene/nanodomes, hetero-aromatic polymeric networks and N-doped nanographene.

In Chapter 3 we discussed how the control over on-surface diffusion can be achieved by changing the nature of the substrate, and we demonstrated how the state of the as-deposited precursor is crucial to determine the final outcome. Here we introduce an extensive research of DiPy[5]DBH on four different metals. The combination of theoretical calculations, STM, XPS and NEXAFS allows us to follow the structural and chemical transformations step by step.

On Pt(111), the non-annealed precursor is intact and exhibits a four-lobes molecular orbital structure. Upon annealing, the precursor undergoes three phase transitions. At 450 K an intermediate cyclodehydrogenated phase occurs. At 650 K, 2N-HBC (N-doped nanographene) is formed via cyclodehydrogenation of the precursor. Further annealing allows the complete breakage of the C-H bonds and the bending of the molecules into N-doped nano-domes covalently bonded with the surface. The final phase transition results in the decomposition of the molecule to form N-doped graphene at 850 K.

The behaviour of the precursor on the coinage metals is different, due to the diffusion at room temperature. We follow the formation of covalently bonded polymeric networks with STM, XPS and NEXAFS. The XPS and the NEXAFS are particularly useful to track the breakage of the C-H bonds.

Curiously, on Cu(111) and Au(111) dark and bright chains form: no molecules are observable within the chains, which seems more like graphene nanoribbons than polymeric chains. The dark and bright chains stand on two different terraces and this is what causes the apparent height gap between the two types of chains. This is surprising because it involves an unexpected mass transport of the metal atoms.

Finally, the phase diagram in Figure 4.2.33 shows how the different reactivity of the coinage metals induces the achievement of similar outcomes at different temperatures, and therefore suggests that among the surface studied, gold is the least catalytic metal for promoting (cyclo)dehydrogenation.

5. $C_{57}H_{33}N_3$: on-surface cyclodehydrogenation steps towards the formation of triaza-fullerenes

One of the main goals of on-surface chemistry with adsorbed molecular precursors is the achievement of new organic nanostructures which cannot be fabricated with conventional chemical synthesis methods. The formation of triaza-fullerene ($C_{57}N_3$) from its planar precursor $C_{57}H_{33}N_3$ is a very good example of the power of the bottom-up approach:[21] *in this case, the catalytic properties of the Pt(111) surface were exploited to cyclodehydrogenate the molecular precursor to form triaza-fullerene, a molecule that was never obtained before.*

The complete cyclodehydrogenation of $C_{57}H_{33}N_3$ causes the folding of the planar precursor into the triaza-fullerene. The initial and the final state have already been previously described[120] *by our group. However many questions on the mechanism of the transformation are still unanswered. For instance, the partially dehydrogenated open-cage fullerene can either bend upwards or downwards with respect to the surface prior to full closure. If the fullerene bends upwards, in principle different materials can be included in the fullerene cage by deposition of an additional atomic element while the molecule is folding.*

In a large molecule, some of the C-H bonds are weaker than others, as for the case of DiPy[5]DBH/Pt(111) described in Chapter 4. Therefore, some H bonds break before others, leaving a partially dehydrogenated molecule: as new C-C bonds form, the molecule partially closes, and an open-cage fullerene arises. In this chapter we followed the steps of the cyclodehydrogenation by annealing $C_{57}H_{33}N_3$/Pt(111) at lower temperatures than the one needed to complete the cyclodehydrogenation. We recorded Scanning Tunneling Microscope (STM) images and X-ray Photoelectron Spectroscopy (XPS) spectra of the open cage fullerenes at different stages, to determine the mechanism of the folding.

Moreover, decomposition of hetero-aromatics has also been proved effective for the doping of graphene,[42] *by including foreign atoms such as N in the network. The introduction of foreign atoms in the graphene network is a very useful strategy to manipulate its band gap (see Chapter 4). One of the most common techniques to obtain N-doped graphene is the Chemical Vapour Deposition (CVD) of N-heteroaromatic hydrocarbons on a transition metal surface. In this chapter, we show how the deposition of $C_{57}H_{33}N_3$ on a hot Pt surface is an efficient methodology for the formation of N-doped graphene.*

5.1 Introduction

The synthesis of the heteroaromatic Polycyclic Aromatic Hydrocarbon (PAH) $C_{57}H_{33}N_3$ was accomplished by Gomez-Lor *et al*.[51] in 2004, as a follow up to their achievement of $C_{60}H_{30}$, an unfolded fullerene.[121] The 'crushed-fullerene' structure of these precursors was selected on purpose, to unveil new methods for the synthesis of fullerenes.

Figure 5.1.1 (modified from Otero *et al*.[21]) represents a scheme of the transformation of $C_{57}H_{33}N_3$ into triaza-fullerene $C_{57}N_3$.

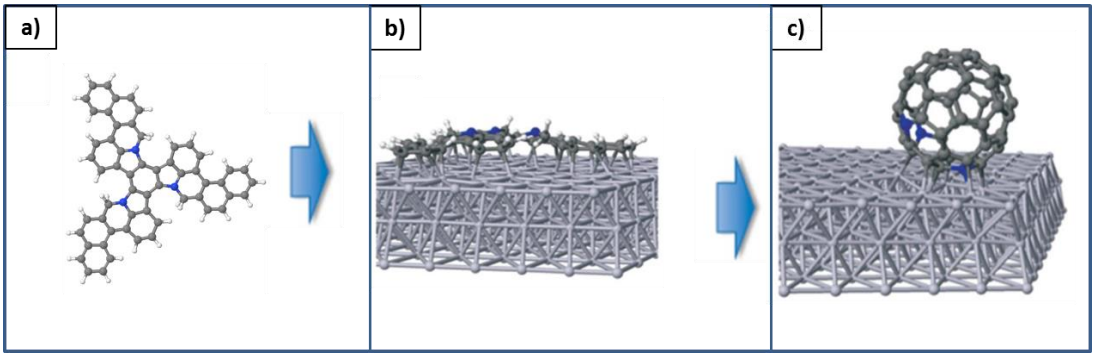

Figure 5.1.1 – *Scheme of the transformation of $C_{57}H_{33}N_3$ into triaza-fullerene.* *Modified from Otero et al.*[21] *The triangular precursor in (a) is deposited on Pt(111) (b); upon annealing at 720 K, the molecule undergoes cyclodehydrogenation and the precursor transforms into a triaza-fullerene (c). The blue balls indicate the N atoms in the molecules.*

$C_{57}H_{33}N_3$ (Figure 5.1.1-a) contains three branches, each of which is composed by two limbs, a shorter one and a longer one. The branches consist of aromatic C hexagons and pentagons surrounded by H atoms, and they are joined by a central benzene ring. Each branch contain one N atom near the centre, which is shared by a pentagon and a hexagon.[120]

The precursor (Figure 5.1.1-a) was deposited under UHV conditions on a clean Pt(111) surface (Figure 5.1.1-b): upon annealing at 720 K, it underwent a complete surface-catalysed cyclodehydrogenation and transformed into $C_{57}N_3$ (Figure 5.1.1-c). The same procedure was repeated, and the same result was obtained, using the similar precursor $C_{60}H_{30}$. STM images before and after annealing at 720 K showed that both the shape and the size of the molecules changed. The shape of the triangular precursor transformed into a round one due to the loss of H and the subsequent creation of new C-C bonds and the consequent folding of the molecule. Moreover the width and the Apparent Height (AH) of the molecules changed from 0.14 to 0.38 nm and from 2.2 to 1.5 nm respectively. The apparent height of commercial fullerenes deposited on Pt(111) is about 0.48 nm (see Chapter 6), which is slightly higher than the one observed by creating a triaza-fullerene from its planar precursor. The AH gap is probably due to a higher hybridization of $C_{57}N_3$ with Pt(111), which can cause the molecule to flatten slightly.

In addition, Otero *et al*.[67] proved that the deposition of the undoped 'crushed fullerene' $C_{60}H_{30}$ on Pt(111) induces a surface mediated recognition which leads to enantiomeric discrimination. The precursor can either land on one side or on the other, and this leads to a prochiral symmetry break.

There are two possible mechanisms of forming a fullerene through cyclodehydrogenation, namely by upwards or downwards molecular folding. Figure 5.1.2-a represents a conjectural scheme of a possible path undergone by a planar precursor: here the intact molecule on the left partially dehydrogenates and as it does so, the molecule bends downwards with respect to the surface. However, this is not the only possible way of forming a fullerene: the precursor can also bend upwards with respect to the surface as shown in Figure 5.1.2-b. In principle, both routes are allowed. One of the aims of this work is to investigate the steps of cyclodehydrogenation, to understand which of the paths proposed here is the correct one.

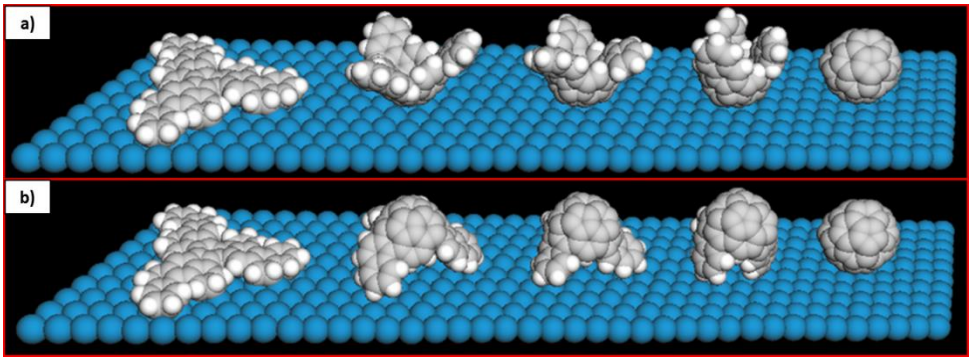

Figure 5.1.2 – *Possible paths of cyclodehydrogenation towards fullerene formation.* *The planar precursor can either bend (a) downwards or (b) upwards as folding to form a (triaza)fullerene. The paths show conjectural intermediate steps with partially dehydrogenated molecules, from a fully hydrogenated planar precursor to the dehydrogenated fullerene.*

Amsharov and collaborators[24] have also been investigating formation of fullerenes from similar precursors.

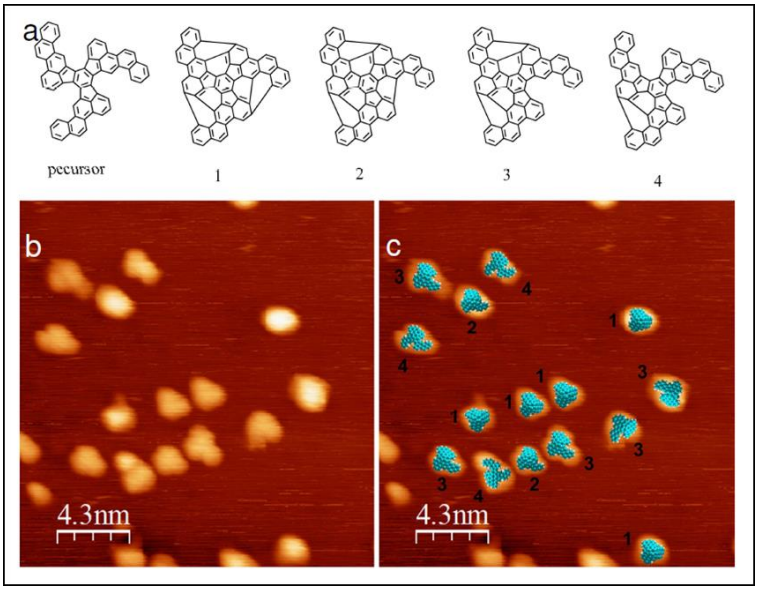

Figure 5.1.3 – *Open-cage fullerenes from a modified $C_{60}H_{30}$ precursor.* *From Amsharov et al.[24] a) Four possible ways of cyclodehydrogenating the modified $C_{60}H_{30}$ precursor. b) An STM image of the precursor annealed to 750 K. c) The models of the four different open-cage fullerenes have been superimposed to the molecules of the STM image of (b).*

In particular, they achieved the on-surface synthesis of the higher fullerene C_{84} from cyclodehydrogenation of $C_{84}H_{42}$. In their work, Amsharov *et al*. focused on the importance of the design of the precursor for achieving the desired result. They provided evidence that only the correctly programmed precursor can transform into the desired outcome. They synthesized two different isomers of $C_{60}H_{30}$ molecules, and showed that only one of them can turn into a fullerene via on-surface cyclodehydrogenation. Therefore they proved that the surface catalysed cyclodehydrogenation processes do not involve C-C bond rearrangement, and that the "cage formation proceeds through dehydrogenation and the zipping of newly formed bonds at preselected positions only".[24] In the Supplementary Information,[24] the authors showed how the cyclodehydrogenation of the modified $C_{60}H_{30}$ precursor led to open-cage fullerene (Figure 5.1.3-a, -b and -c).

The authors discerned four types of open-cage fullerenes, depending on which C-H bonds broke to form new C-C bonds. Therefore they were able to superimpose the models of open-cage fullerenes to the STM images. Importantly, they found that the molecules bend upwards upon annealing. Due to its shape, this particular $C_{60}H_{30}$ isomer cannot undergo a complete cyclodehydrogenation.

In this chapter we will get insights on the formation mechanisms of the structures, by showing STM images of $C_{57}H_{33}N_3$ at different temperatures, from the open molecule to open-cage fullerenes to fullerenes. This information is complemented by high resolution XPS measured at the SuperESCA beamline at ELETTRA (Trieste, Italy).

5.2 Scanning Tunneling Microscopy of $C_{57}H_{33}N_3$/Pt(111): the formation of triaza-fullerenes in steps

To understand the formation of triaza-fullerenes from its planar precursor, we analyse the system by STM in temperature steps. To do so, we deposit submonolayer coverage of $C_{57}H_{33}N_3$ (0.4 ML) on a clean Pt(111) surface, and we anneal the sample. We can divide the results into four main stages: (i) open molecules up to 500 K; (ii) open-cage fullerenes (Temperature T = 550-650 K); (iii) triaza-fullerenes (T = 700-950 K); (iv) N-doped graphene (T > 950 K). We hence divide this section into three sub-sections, one for each stage of the evolution.

5.2.1 Planar molecules: crushed fullerenes

Room temperature (RT) deposition of $C_{57}H_{33}N_3$ on Pt(111) allows the observation of triangular objects on the surface. Figure 5.2.1-a represents a 17x17 nm^2 STM image of the non-annealed planar precursor: we can see up to 11 different molecules. Curiously, all precursors look different; in this colour scale, red corresponds to the highest apparent height (about 0.26 nm in Figure 5.2.1-a), and the bright lobes in the centre of the molecules changes drastically from one to the other.

Taking a closer look, we can divide the molecules into symmetric and non-symmetric. The symmetric molecules (the two red circles highlight the only two examples in Figure 5.2.1-a, plus the three molecules in Figure 5.2.1-b) enclose symmetric submolecular lobes. The non-symmetric molecules (the large majority in

Figure 5.2.1-a) are triangular in shape, but the bright lobes in the middle are disordered. We will show after that the symmetric molecules can be related to non-dehydrogenated flat species.

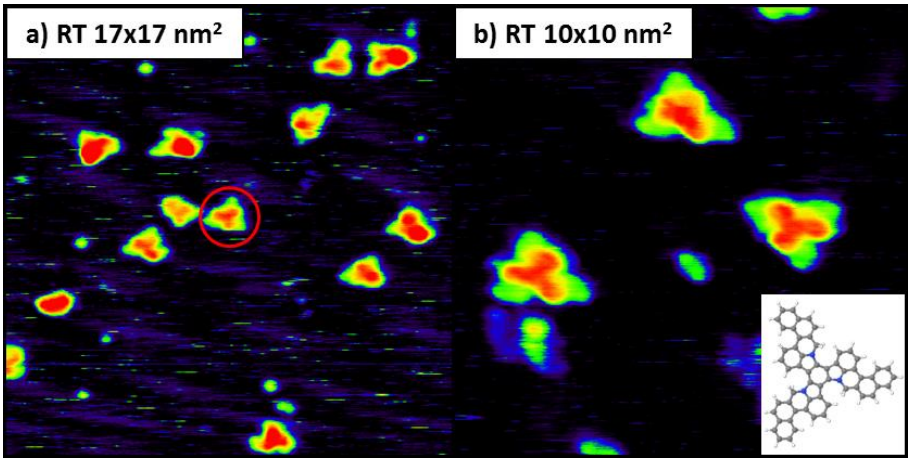

Figure 5.2.1 – *STM images of $C_{57}H_{33}N_3$, the open planar precursors of triaza-fullerenes at room temperature.* *a) Each triangular feature is a different molecule; however, it is clear that all the molecules are different (17x17 nm^2; sample voltage V_s = 0.5 V); the red circle represents an example of a symmetric molecule. b) High resolution STM image of three molecules: three bright (red) lobes can be seen in two molecules, while only two in one of them (10x10 nm^2; V_s = 1.0 V); the inset represents a ball-and-stick model of the precursor.*

Figure 5.2.1-b represents a typical image of three symmetric $C_{57}H_{33}N_3$s, where intramolecular resolution is achieved. The bright lobes in the centre of the molecule represent the short limbs of the branches of the molecule. In the STM image, we can discern three bright lobes in the two molecules at the bottom. However, we can only distinguish two bright lobes in the top molecule: the third lobe is present but it is fainter.

Figure 5.2.2 shows the apparent height of one asymmetrical (red) and two symmetrical (brown and black) molecules.

For the symmetrical molecules, the AH of the bright lobes for both precursors is 0.16 nm, while the fainter parts corresponding to the long limbs of the molecules are 0.08-0.09 nm tall. The width of the molecule from vertex to side is about 1.9 nm, while the side alone is 2.2 nm long. The asymmetrical molecule shown in the inset of Figure 5.2.2-a is about 0.05 nm higher than the other two, as its maximum height is 0.21 nm. However, the side is shorter (1.3 nm) as the vertex to side width (1.6 nm). These height and width differences may indicate a partial folding due to partial cyclo-dehydrogenation, or it may mean that the asymmetric molecules do not land flat on the surface but exhibit a different adsorption geometry.

Figure 5.2.3 shows five high resolution STM images of examples of typical symmetric molecules. Figure 5.2.3-a and -b show two molecules such as the ones we observed so far, with the three bright lobes in the centre corresponding to the short limbs surrounded by dimmer features related to the large limbs. We can notice how these molecules are the mirror images of each other: the bright lobes sit either to the right (Figure 5.2.3-a, called 3-R) or to the left (Figure 5.2.3-b, named 3-L) of the dim ones. As shown by Otero *et al.*,[67] these molecules are prochiral and the difference arise from how the precursors land.

Figure 5.2.3-c is a high resolution image of a molecule with two bright lobes, oriented on the right of the dim limbs (2-R). The presence of only two bright limbs instead of three is due to the partial cyclodehydrogenation of the precursor, which causes a different imaging of the molecule.

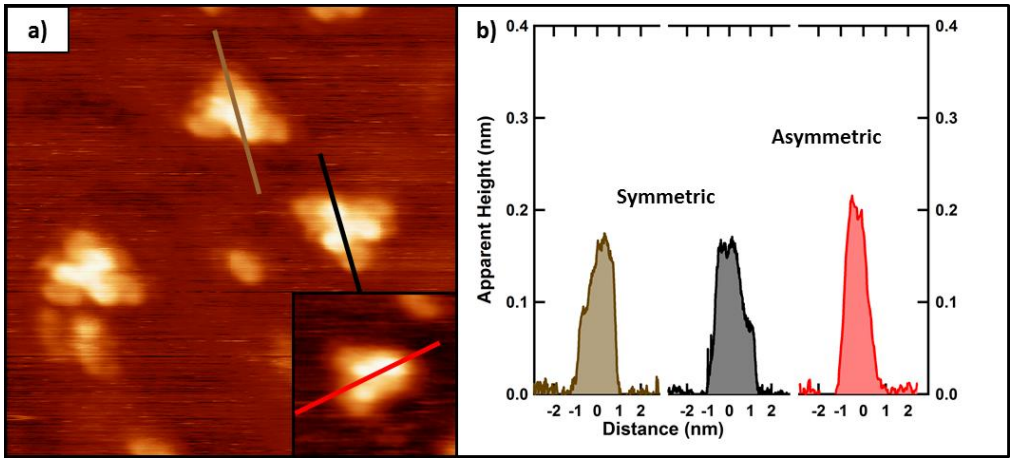

Figure 5.2.2 – *Apparent height of one symmetric and two asymmetric molecules at RT.* *a) An STM image of $C_{57}H_{33}N_3$/Pt(111) at RT (10x10 nm^2; V_s = 1.0 V); the brown and black lines represent the zone where the apparent height profile was traced. The inset shows an asymmetric molecule and the red line its apparent height profile (3.1x3.1 nm^2). b) The apparent height profile of the three molecules in (a).*

Figure 5.2.3Figure 5.2.3-d and -e indicate a different type of symmetric molecules: these precursors exhibit a spiral shape. These molecules also reveal bright lobes in the center. As before, the spiral-shaped molecules are also chiral: depending on how they land on the surface, the bright lobes lay either on the left (S-R) in the clockwise or on the right (S-L) in the anticlockwise conformation. The size is very similar to the molecules discussed so far, but the shape is diverse.

The difference between the triangular molecules (Figure 5.2.3-a, -b and -c) and the spiral-shaped ones (Figure 5.2.3-d and -e) cannot be related to a tip effect, since they coexist in the same image. It is likely that this dissimilarity is again caused by partial cyclodehydrogenation. However, to confirm this hypothesis, theoretical simulations of STM images should be performed.

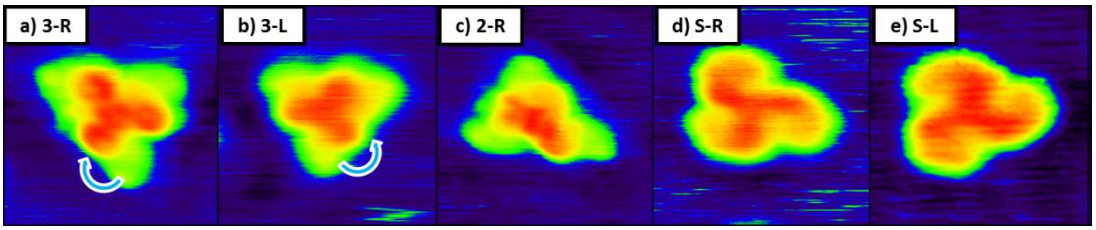

Figure 5.2.3 – *Five examples of typical symmetric molecules at RT.* *The size of all images is 2.9x2.9 nm^2 and the sample voltage between 0.5 and 1.0 V. a) Three bright lobes appear to the right of the dim limbs (3-R). b) Three bright lobes are shifted to the left of the dim limbs (3-L). c) Two bright lobes are tilted to the right of the dim limbs (2-R). d) A clockwise spiral-shaped molecule (S-R) presents here three central lobes and fainter limbs. e) The anti-clockwise spiral-shaped molecule (S-L) is the mirror image of (d).*

Up to about 500 K, we observe only slight changes to the system upon annealing the sample. The STM tip images of the molecules still show flat triangles on the surface; however a deep analysis shows that the system is actually changing. Figure 5.2.4 shows the evolution of the precursor with temperature upon soft annealing, to 380 K (Figure 5.2.4-b), to 420 K (Figure 5.2.4-c) and to 480 K (Figure 5.2.4-d). These images are compared with one of the non-annealed system (Figure 5.2.4-a).

To a first glance, the main effect of the soft annealing is the desorption of part of the numerous fragments observed at room temperature. The STM images when heating the sample show much less small objects on the surface: these objects are likely to be due to contamination from the synthesis process and in particular to broken portions of molecule. Due to their small mass, they desorb easily and therefore a soft annealing is enough to get rid of them.

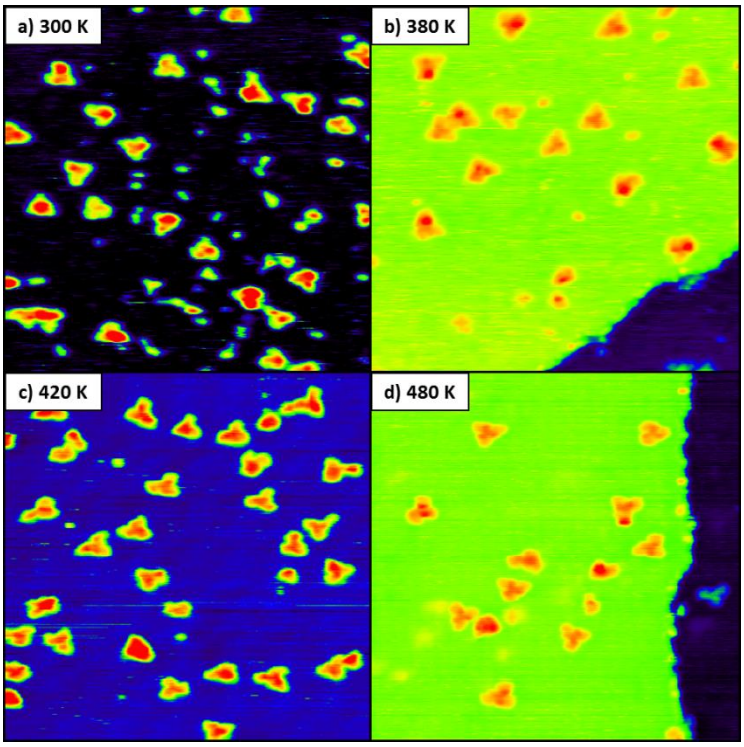

Figure 5.2.4 – *STM images of $C_{57}H_{33}N_3$/Pt(111) after soft annealing.* *The size of all images is 20x20 nm^2 and the sample voltage between 0.5 V and 1.0 V. a) A RT STM image is presented to facilitate the comparison with the rest. In the other images, the sample has been annealed to: b) 380 K; c) 420 K; d) 480 K.*

The shape of the molecules upon soft annealing is triangular, showing that only minor (if any) cyclodehydrogenation is occurring. However, the heating of the sample is associated with an increase in the observation of symmetric molecules in the system. A simple statistical calculation based on the images of Figure 5.2.4 reveals that at room temperature only 10% of the molecules are symmetric. However, when annealing to 380 K, 420 K and 480 K this percentage increases respectively to 33%, 42% and 70%. This trend is qualitatively representative of the general behaviour of these precursors upon soft annealing.

The shape of the molecules upon soft annealing is triangular, showing that only minor (if any) cyclodehydrogenation is occurring. However, the heating of the sample is associated with an increase in the

observation of symmetric molecules in the system. A simple statistical calculation based on the images of Figure 5.2.4 reveals that at room temperature only 10% of the molecules are symmetric. However, when annealing to 380 K, 420 K and 480 K this percentage increases respectively to 33%, 42% and 70%. This trend is qualitatively representative of the general behaviour of these precursors upon soft annealing.

The existence of asymmetric molecules upon deposition can be caused by three factors: (i) they can adsorb in different sites or forms, either in a planar configuration or by leaning on one side; (ii) the molecules can partially cyclodehydrogenate in the evaporator or as they touch the surface and therefore partially fold to form open-cage fullerenes; (iii) they can partially dehydrogenate and bond covalently with the Pt surface.

The Pt(111) surface is known to be highly reactive, therefore it is expected that upon deposition the surface induces the molecules to maximise the number of favourable adsorption positions for all the individual rings. This was shown for the case of the similar precursor $C_{60}H_{30}$.[67] Hence, the precursors are expected to flatten as much as possible upon deposition, to "touch" the surface with all the aromatic rings. However, we observe that most as-deposited molecules differ from each other, and that soft annealing steps produce the observation of increasingly more 'symmetric' molecules. Thus, this fact suggests that the symmetric molecules correspond to non-dehydrogenated flat precursors, which do not adsorb flat on the surface. The increase in the relative amount of these molecules with temperature means that the energy provided by the soft annealing is not enough to cyclodehydrogenate the precursors but it is sufficient to allow them to move towards a stable site at the surface, and therefore, to maximise the number of aromatic rings in contact with it, favouring like that the flattening of the adsorbed molecules.

5.2.2 Open-cage triaza-fullerenes

The effect of further annealing to about 550-650 K is the partial cyclodehydrogenation of the molecule and the formation of open-cage fullerenes. The cleavage of the weakest C-H bonds allows the formation of new C-C bonds, preserving the strongest C-H bonds.

As discussed in Chapter 4, the cyclodehydrogenation of PAHs is likely to occur in steps. This was first showed by Treier *et al.*[23]: they elegantly explained how some C-H bonds are weaker than others and these are the first to break upon surface-assisted cyclodehydrogenation; therefore a relatively soft annealing can leave the precursor in an intermediate state between the pristine molecule and the final result. In our case, these will lead spontaneously to a partially closed fullerene.

Figure 5.2.5-a and -b represent two images of submonolayer coverage of $C_{57}H_{33}N_3$ on Pt(111) annealed at 600 K. The shape of the molecules is no longer triangular. Moreover the molecules seem smaller if compared to the previous results of Section 5.2.1.

Another remarkable consequence of annealing to 600 K is the fact that all the PAHs have now a different shape. Figure 5.2.5-c shows the apparent height profiles of four representative molecules of Figure 5.2.5-a and -b: it is clear how after annealing the width and the height of these molecules differ. The apparent height ranges from about 0.16 nm (the same as the flat non-dehydrogenated molecules) up to 0.30 nm (similar to the one of closed fullerenes, see next Section). Moreover, the lateral size of the measured objects varies between 1.9 to 1.3 nm. Importantly, the molecules with the largest apparent height are also the ones with the smaller width.

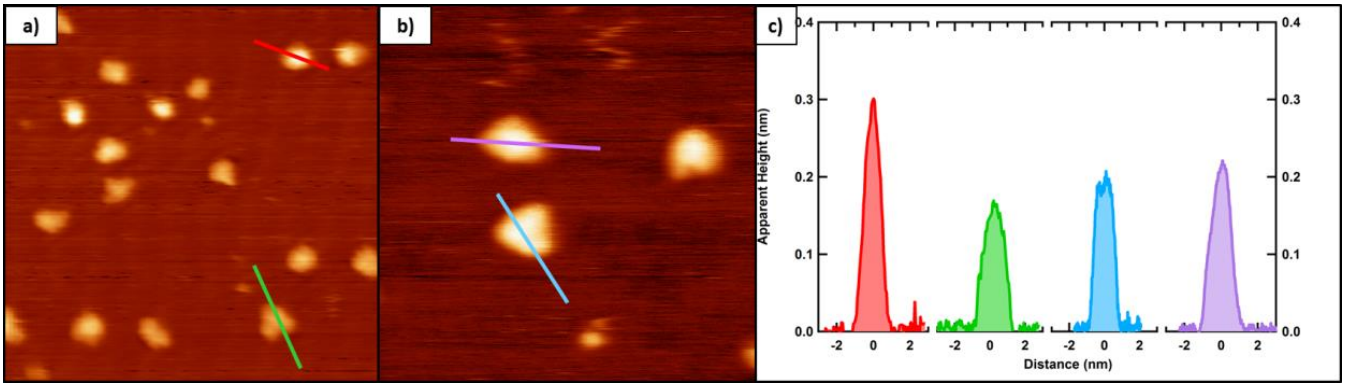

Figure 5.2.5 – *STM images and apparent height of open-cage triaza-fullerenes.* *a) 20x20 nm^2 image of $C_{57}H_{33}N_3$ on Pt(111) annealed to about 600 K (V_s = 0.5 V). b) 10x10 nm^2 image of the same sample as (a) (V_s = 0.5 V). c) The apparent height of four molecules: the coloured lines in (a) and (b) correspond to the profiles in (c).*

We can see six examples of high resolution images of open-cage fullerenes in Figure 5.2.6-a to -f. Figure 5.2.6 clearly reveals that the shape and the size of the molecules can differ greatly. This variety is caused by the fact that the all the molecules cyclodehydrogenate in different ways. The final outcome of all the precursors is the formation of triaza-fullerene. However, the annealing to 600 K does not provide enough energy for all the C-H bonds to break and allow the complete folding. Only some H atoms detach and allow for new C-C bond formation. The fact that the molecules differ at this stage means that for each molecule different C-H bonds break at this stage, therefore allowing different types of open-cage triaza-fullerenes to coexist. Amsharov *et al*.[24] observed similar results.

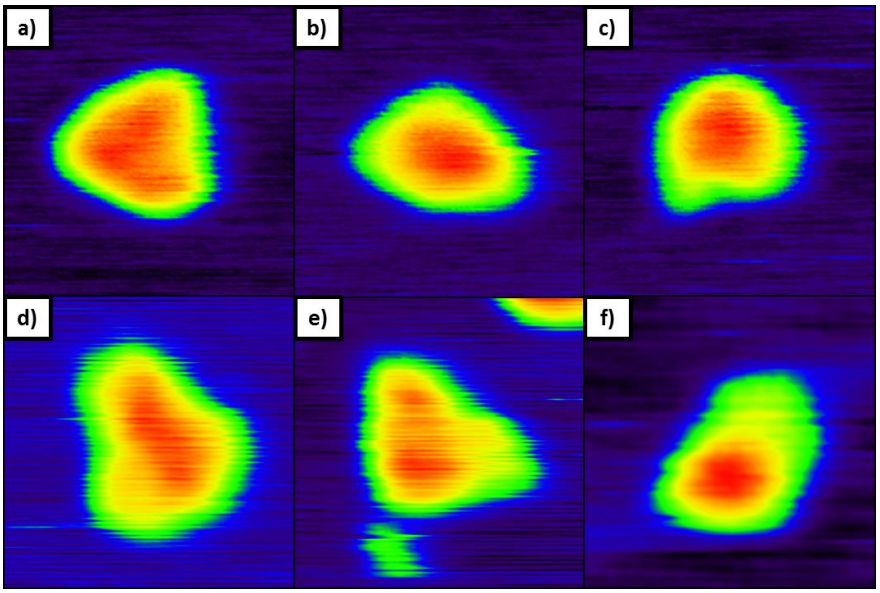

Figure 5.2.6 – *STM images of individual open-cage triaza-fullerenes.* *The size of all the images (a-f) is 2.8x2.8 nm^2 and the sample voltage 0.5-1.0 V.*

Importantly, the increase in apparent height with respect to the one of the pristine PAH is always observed in the central part of the molecules. This suggests that the molecules bend by lifting their core: this is consistent with the cyclodehydrogenation path of Figure 5.1.2-b.

5.2.3 The formation of triaza-fullerenes

The complete surface-promoted cyclodehydrogenation of $C_{57}H_{33}N_3$ into $C_{57}N_3$ is achieved upon annealing at more than 700 K.

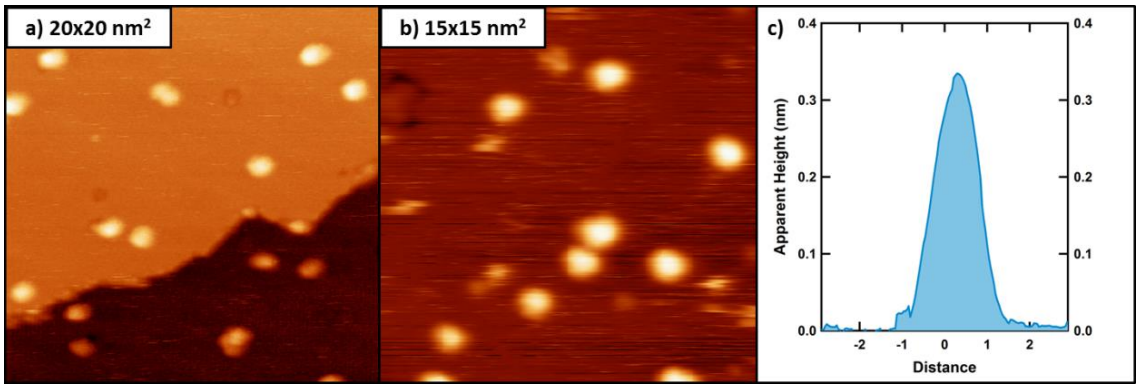

Figure 5.2.7 – *Annealing $C_{57}H_{33}N_3$ at more than 700 K on Pt leads to the formation of triazafullerenes.* *a) 20x20 nm^2 of the sample annealed at about 700 K (V_s = 1.0 V). b) 15x15 nm^2 image of the system annealed at 750 K (V_s = 2.0 V). c) The apparent height profile of a typical triaza-fullerene shows a full width at half maximum of 1.2 nm and an apparent height of 0.33 nm.*

The STM is a very powerful tool to track these changes, since the evolution of the structure of the precursor undergoes drastic transformation. Figure 5.2.7-a and -b show two STM images of the sample annealed respectively at 700 and 750 K. The topographic images of the molecule are identical at these two temperatures. The pristine triangular molecules transform upon annealing into round objects whose lateral size decreases from 2.2 to about 1.1-1.4 nm. Moreover, the apparent height also increases to about 0.33±0.05 nm, as shown in Figure 5.2.7-c.

Figure 5.2.8-a and -b represents two high resolution images of $C_{57}N_3$, both with apparent height of about 0.30 nm. These round molecules are clearly very different from the pristine PAH of Section 5.2.1: the molecule is round in shape, as opposed to being triangular before annealing, moreover the internal molecular orbital resolution is lost.

When depositing commercial C_{60} on Pt(111) (see Chapter 6), molecular orbitals features are seldom seen, and from the STM observation we can understand how the molecule is rotated on the surface,[122] for example whether it is sitting on a hexagon or on a pentagon. The observation of molecular orbitals of the triaza-fullerenes build by its planar precursor is very difficult and was not achieved in this set of experiment. The reason may be that these molecules are too hybridised with the surface to show molecular electronic states by STM.

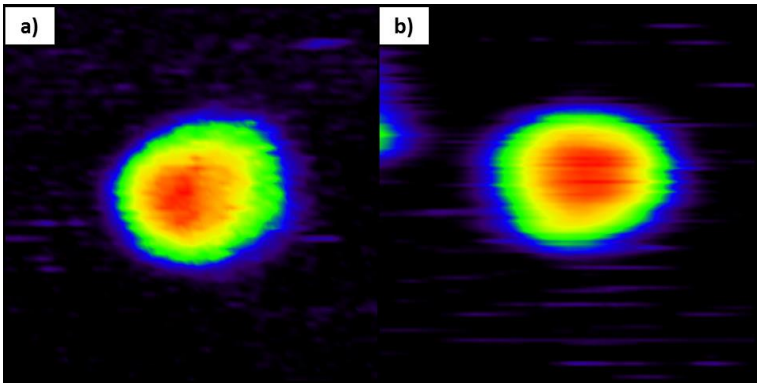

Figure 5.2.8 – *Examples of high resolution STM images of $C_{57}N_3$.* *2.9x2.9 nm^2 V_s = 0.5-1.0 V.*

The apparent height of commercial C_{60}/Pt(111) after annealing at 700 K is about 0.48 nm, while the height of the triaza-fullerenes was found to range between 0.30 to 0.37 nm. The difference of more than 0.1 nm between the two is likely to be caused either by a large hybridisation with the substrate of the triaza-fullerene built from its planar precursor or by the formation of a large vacancy on the surface (see Chapter 6). Commercial C_{60} is known to covalently bind with the Pt surface with $6^{123,124}$ or 12^{44} C atoms. For the case of the triaza-fullerene, the metal surface can interact covalently with even more C atoms in the precursors: the more atoms interact with the Pt, the more deformed the triaza-fullerene should be, therefore its apparent height would also be affected.

5.2.4 N-doped graphene

Further heating (T>950 K) causes the disruption of the triaza-fullerenes and the formation of N-doped-graphene. As discussed in Chapter 4, the inclusion of dopants in the precursor is an adequate method of growing doped nano-objects. This allows extra control over the electronic properties of the outcome. The STM images of N-doped graphene in this Section have been obtained with the Low Temperature STM of the IMDEA-Nanociencia group. Graphene was grown on Ir(111) and on Ru(0001) instead of Pt(111), because of the unavailability of the latter substrate. Figure 5.2.9 displays three STM images of N-doped graphene (NG) on these two metals, which have been manually compressed in the vertical direction by 50%, as during the acquisition a piezoelectric was fissured.

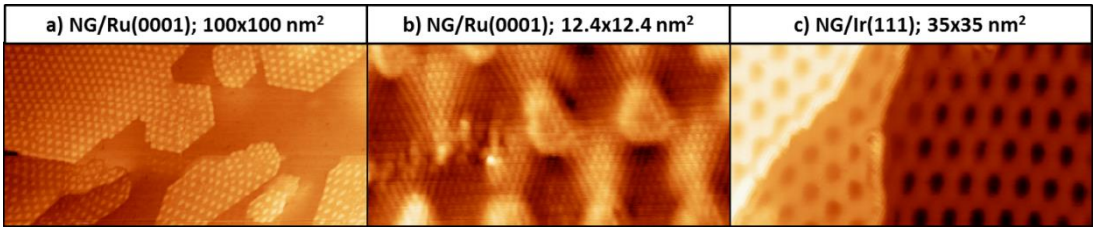

Figure 5.2.9 – *N-doped graphene grown with $C_{57}H_{33}N_3$ on Ru(0001) and Ir(111).* *a) A panoramic image of submonolayer NG/Ru(0001) (V_s = -1.0 V; 100x100 nm^2). b) An atomic resolution image of the border between two moiré domains of NG/Ru(0001) (V_s = -0.05 V; 12.4x12.4 nm^2). c) NG/Ir(111) (V_s = 0.01 V; 35x35 nm^2).*

Since Ir and Ru belong to the platinum group of metals the three have similar chemical and physical properties. Hence it is correct to assume that to a certain extent similar results will be achieved on these metal surfaces, even if the conditions (such as the annealing temperature for graphene formation) may change slightly.

Figure 5.2.9-a and -b show NG grown on Ru(0001). The first one is a panoramic 100x100 nm^2 STM image of a sample with submonolayer coverage; here moirés with different periodicity and orientation coexist. The low annealing temperature (about 950 K) is to blame for the high amount of defects of this graphene network. Indeed, a defect-less graphene moiré should be perfectly hexagonal, and Figure 5.2.9-a shows that this is not the case. Figure 5.2.9-b displays a 12.4x12.4 nm^2 STM image of NG/Ru(0001): here the border between two moiré domains is represented with atomic resolution. NG/Ru(0001) is observed to be bias dependant.[74]

Figure 5.2.9-c shows a 35x35 nm^2 STM of NG/Ir(111) scanned at a sample voltage of 0.1 V. The sample was annealed to about 950 K, which is the lowest possible temperature to form graphene with $C_{57}H_{33}N_3$ as a precursor. The moiré is bias dependant (not shown here), since when the sample voltage is increased to 3 V, what we see as dark bulges appear as bright protrusions. As for the case of NG/Ru(0001), the amount of defects is very high, because of the low annealing temperature.

In the literature, nitrogen dopants in a graphene STM image are visualised as bright defects.[71] In our experiment we are not able to observe such effect. The reason why we are not able to resolve such features may be that the moiré corrugation is much higher than the corrugation induced by the dopants. To this matter, Zhao *et al*. reported a maximum atomic corrugation of 0.06 nm for the N atom included in the graphene network, which is less than half the corrugation of the moiré. The presence of NG was confirmed by XPS spectra on Pt(111), as we will discuss in the next Section.

5.3 High resolution and temperature programmed XPS

The C1s, N1s and $Pt4f_{7/2}$ high resolution (HR) and the C1s temperature programmed (TP) XPS spectra are recorded at the SuperESCA beamline (ELETTRA, Trieste). The HR-XPS scans of the sample at different temperatures are obtained by keeping the sample at room temperature, while the TP-XPS on the hot sample.

First of all, the surface is cleaned and checked by XPS, and then submonolayer coverage of $C_{57}H_{33}N_3$ is deposited on it. The sample is kept at room temperature during the deposition of molecule for the TP-XPS and HR-XPS. HR-XPS is also recorded for a sample prepared by evaporating the molecules on the hot surface (990 K).

All XPS spectra are fitted by a convolution of a Lorentzian and a Gaussian function. For C1s, we use the typical Lorentzian widths of 180 meV and Gaussian widths 350-500 meV (190 meV for the case of graphene). The N1s peak is fitted with similar Lorentzian width and a broader Gaussian (about 850 meV). The Binding Energy of each scan is corrected by subtracting the error in the Fermi edge.

5.3.1 Temperature Programmed XPS of C1s

We set the TP scans (shown in Figure 5.3.1) to increase the temperature at a rate of 1 K/s, and as each C1s spectrum lasted less than 10 seconds, each scan would represent a very specific temperature. The assignation of the specific components peaks will be discussed in the next Section; we will now focus on the overall binding energy shifts that the system molecule undergoes upon annealing.

Figure 5.3.1 shows the intensity of the C1s XPS peak (colour code: blue/green = low; white = high) variations in terms of the binding energy (x-axis) and the annealing temperature (y-axis). 15x15 nm^2 STM images of the four main stages are depicted at the right, and the black line indicates the maximum temperature reached by each phase. At room temperature up to about 500 K intact pristine molecules are present on the surface, and the C1s peak is very broad, meaning that the carbon atoms in the molecule belong to many different chemical environments. The binding energy of the main peak lays at 284.2 eV. In particular, at 286 eV we can see a small carbon monoxide contamination peak, which disappears at about 400 K.

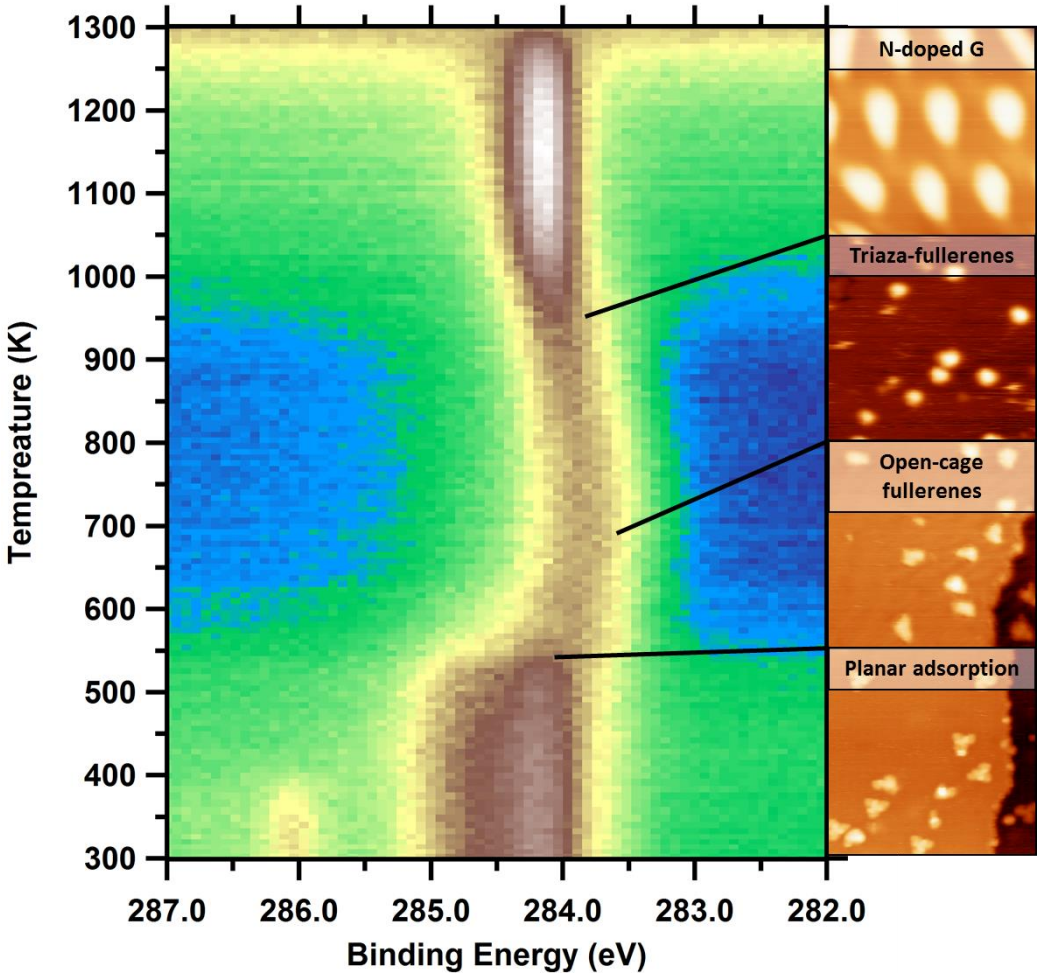

Figure 5.3.1 – ***TP-XPS C1s spectrum of $C_{57}H_{33}N_3$/Pt(111).*** *The temperature of the sample was increased from RT to 1320 K at a rate of 1 K/s. The x-axis represents the corrected binding energy and the y-axis the temperature; the colour-code indicates the intensity of the peak (blue/green = low; white = high). The STM images on the right (15x15 nm_2) indicate the four main different stages undergone by the molecule. Planar triangular precursors exist up to about 500 K; open-cage fullerenes up to 700 K; triaza-fullerenes up to 950 K; N-doped graphene exists above 950 K. The black lines indicate the maximum temperature reached by a given phase.*

At 550 K, the C1s peak narrows and shifts towards lower binding energies by about 0.15 eV. This peak shift coincides with the beginning of the cyclodehydrogenation and the formation of the open-cage fullerenes, as indicated by the STM image on the right. As we will discuss in the next Section, an increase in the intensity of low binding energy components (283.7 eV) takes place, and the component at this binding energy is related to the interaction of the C atoms of the molecule with the Pt surface:[55,100,101] therefore, as the molecule begins to cyclodehydrogenate, the interaction of the Pt increases. Figure 5.3.1 suggests that the overall binding energy shift is hence due to a modification of the relative intensity of the components rather than to a charge transfer from the Pt. This figure shows that a new component arises, and another one loses its intensity. This differs from the TP-XPS of DiPy[5]DBH/Cu(110), as the much greater binding energy shift could in that case justify charge transfer.

A variation of the intensity is expected when recording TP-XPS and due to photoelectron diffraction effects.[20,55] For $C_{57}H_{33}N_3$ on Pt(111), the intensity of the peak diminishes from about 550 K to 1000 K. Another possible explanation for the drop of intensity is the loss of material; however, the intensity is recovered at 1000 K, and this indicates that the source of this variation is a photoelectron diffraction effect.

When the cyclodehydrogenation completes at about 700 K, and the triaza-fullerenes form, the binding energy does not varies greatly with respect to the open-cage fullerenes. This means that the fullerenes are also highly interacting with the surface. The STM images of the closed molecules also suggested this result, since the apparent height of the closed fullerenes is lower than the one of the commercial C_{60}s.

The next significant change occurs at about 1000 K, where N-doped graphene starts to form. The peak narrows and shifts to higher binding energy, returning to the value of the open molecule. This indicates that the interaction of the graphene layer with the surface is less than the one of the molecule.[80] Moreover, the intensity increases as a result of photoelectron diffraction effects.

If we take the main peak of graphene situated at 284.4 eV as the reference for sp^2 C atoms not interacting with the metal, we can see that the main peak of the triaza-fullerenes is shifted by about 0.15 eV towards lower binding energy. This clearly indicates a charge transfer from the surface to the molecules, which confirms the stronh hybridisation of the triaza-fullerene with the platinum surface.

5.3.2 High-resolution XPS

The HR-XPS gives detailed chemical information on the surface and it helps to complement and explain the steps that the molecule undergoes which we observed with the STM. From the STM measurements, we know that up to about 500 K the open molecule lays intact on the surface; cyclodehydrogenation begins at about 550 K forming open-cage fullerenes which transforms into triaza-fullerenes at about 700 K, when the cyclodehydrogenation completes. The triaza-fullerenes are stable up to the graphene formation. We show the results from two different XPS experiment. In the first one, we deposit the $C_{57}H_{33}N_3$ precursor on the sample at room temperature. In the second one, we evaporate the precursor on the hot sample.

Room temperature deposition

Figure 5.3.2 represents the N1s and C1s XPS peak of the molecule deposited on the surface at RT; Figure 5.3.3 shows the changes in the relative area of the components of each N1s and C1s peak with temperature;

Figure 5.3.4 represents the $Pt4f_{7/2}$ XPS peak upon annealing; Figure 5.3.5 is a visual scheme of the different components of the peaks. We will first focus on the C1s peak then on the N1s one.

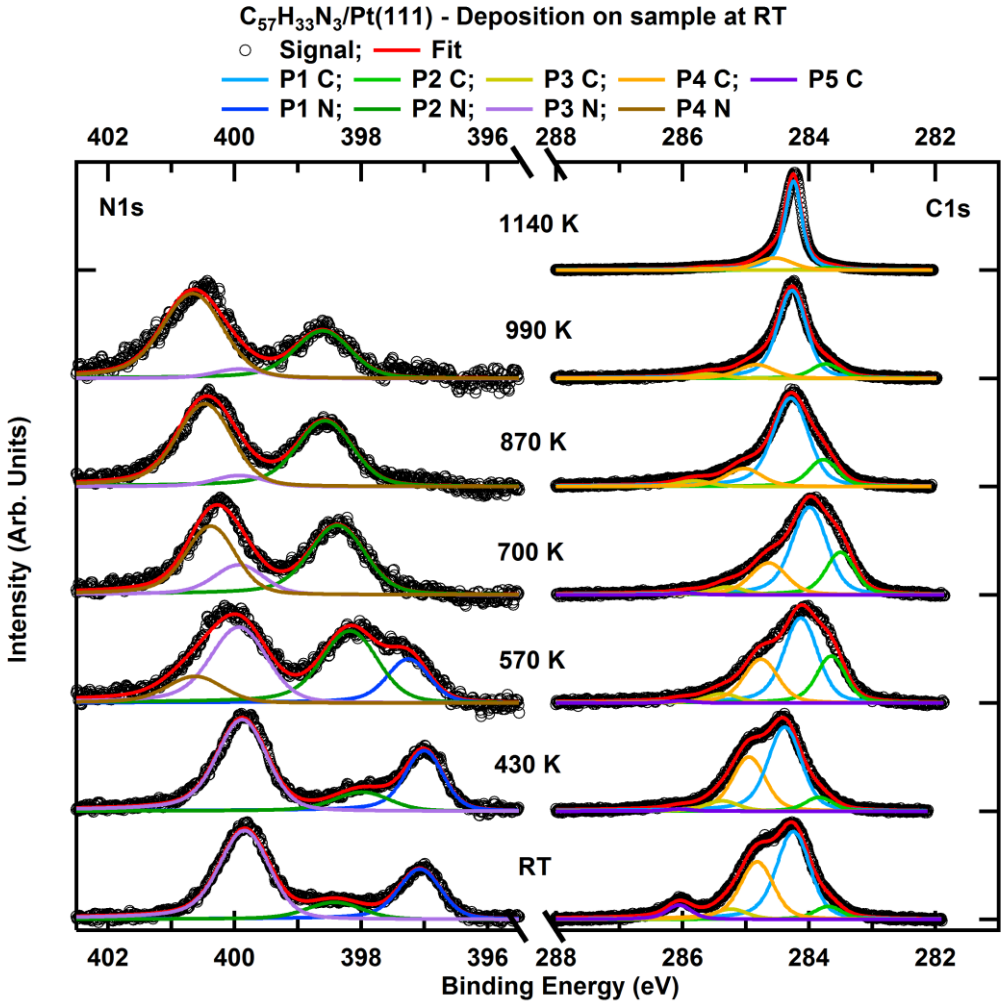

Figure 5.3.2 – ***N1s and C1s HR-XPS of $C_{57}H_{33}N_3$/Pt(111) at various temperatures.*** *The XPS was recorded in steps from RT to 1140 K, therefore we were able to record the spectroscopic information for all the molecular stages. The N1s intensity is not normalized to the one of C1s.*

We fitted the room temperature C1s peak (Figure 5.3.2, right panel) with five components. Their relative proportion is indicated in the top panel of Figure 5.3.3.

The most intense component (P1-C, light-blue) is laying at 284.24 eV. It is present throughout the whole annealing procedure, and it is always the most intense contribution, therefore it is related to the C-C bond of C atoms in the aromatic hexagon/pentagon configuration, as indicated by Figure 5.3.5-a.[55,77,92,96,100] As opposed to the case of DiPy[5]DBH on the coinage metals, in this case we cannot distinguish the C-C and the C-H peak, which are both enclosed in a single P1-C component.

As discussed in Section 5.3.1, the low binding energy component at 283.68 eV (P2-C, light green) represents the C atoms interacting covalently with the Pt surface (Figure 5.3.5-e).[55,100,101] Curiously, this component is

not zero at room temperature, indicating some covalent bonding with the metal upon deposition. We then assign the intense peak at 284.81 (P4-C, orange) to the C atoms bonded with N.[95–97,99] Figure 5.3.5-a represents the model of the open molecule: we can see that only nine C atoms bond directly with N, therefore P4-C is too intense to account for only nine C atoms in the molecule. However, the presence of the N dopants does not only affect these nine nearest neighbour C atoms, but all the twenty-four atoms in the adjacent rings containing the N, and this explains its large area.

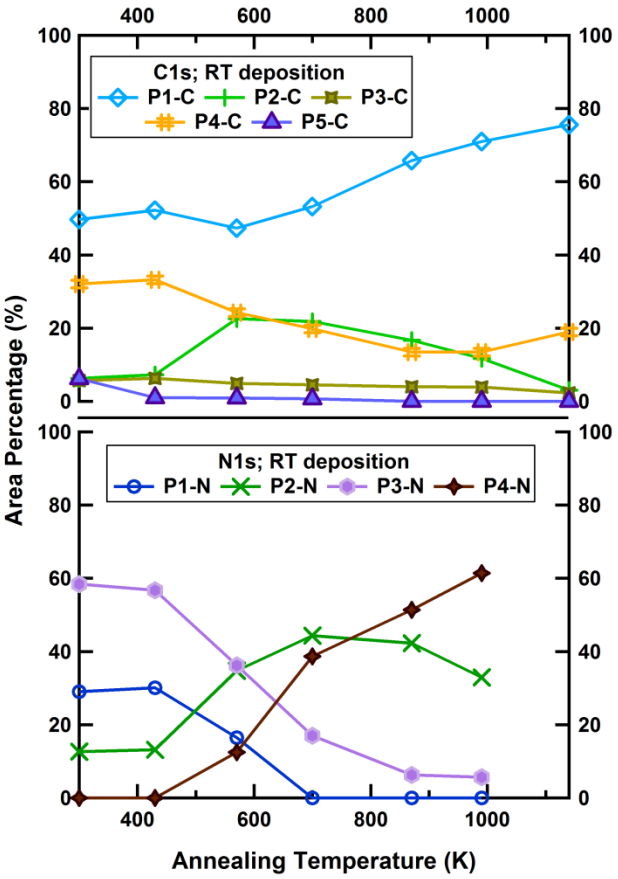

Figure 5.3.3 – ***Relative abundance of the area of each N1s and C1s peak in terms of temperature (deposition at room temperature).*** *The C1s peaks are shown in the top panel and the N1s in the low panel. The colour code follows the one of Figure 5.3.2.*

We tentatively assign the small peak at 285.83 (P3-C, ochre) to a shake-up feature of P1. Finally, the component at 286.04 eV (P5-C, purple) is related to oxygen contamination present on the surface, which desorbs completely at 400 K, as shown in Figure 5.3.5-a.[77,94,96]

The evaluation of the relative percentage of the area of the peaks with temperature is a very useful tool for confirming the previous assignation of the peaks.

The evolution of the components of the C1s peak of the molecule deposited at RT is shown in the top panel of Figure 5.3.3. P1-C (corresponding to the C-C interaction of the aromatic hexagons and pentagons) is the most intense throughout the whole process; upon annealing to high temperature (above 800 K), its relative

importance increases as a consequence of partial N desorption and the drop in the surface-adsorbate interaction. As discussed in Section 5.3.1, the formation of graphene decouples the C atoms from the surface.

We can monitor the strength of the surface-adsorbate interaction upon annealing by tracking the relative importance of P2-C with temperature. As discussed in Section 5.3.1, the interaction with the metal surface suddenly increases at 550 K, when the molecules partially cyclodehydrogenate. This rise is caused by a covalent interaction between the C dangling electrons and the Pt surface, both before and after the formation of a new C-C bond as an aromatic ring.

The area of P4-C (C-N) decreases slightly upon annealing. This can be related to a minor loss of N during the annealing process. P4-C is still present above 1000 K, indicating the presence of N-doped graphene. The C1s peaks of the sample annealed at 990 K and 1140 K are thinner than the ones of the sample heated to lower temperature: this reduction is the hallmark of graphene formation which always shows a very narrow peak.[106,118] This is because graphene is a highly ordered system with respect to the adsorbed molecules.

We can infer more on the surface-adsorbate interaction by looking at the fitting of the $Pt4f_{7/2}$ peak, shown in Figure 5.3.4.

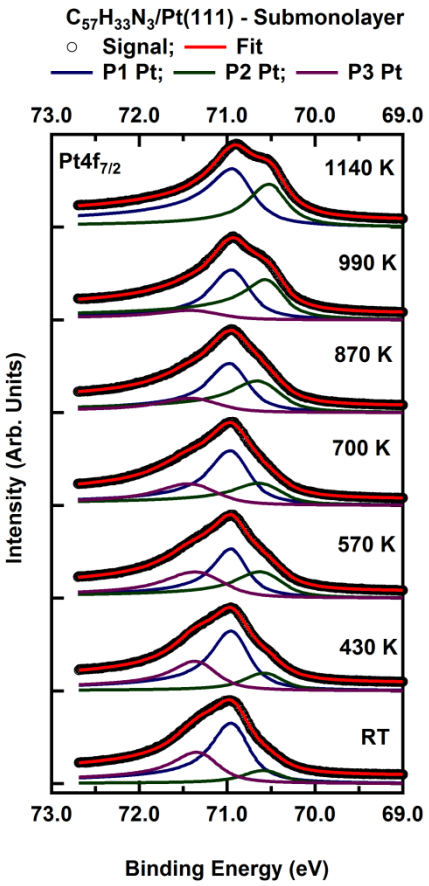

Figure 5.3.4 – *$Pt4f_{7/2}$ peak of $C_{57}H_{33}N_3$ on Pt(111) at different temperatures.* *The bulk and surface component are both present, together with a third component, which accounts for the interaction with the surface.*

As we will discuss in Chapter 7, the Pt4f peak shows three main components. P1-Pt (dark blue) at 70.92 eV corresponds to the bulk atoms of the metal. The second, P2-Pt (dark green) at 70.57 eV is related to the Pt atoms on the surface. As Lizzit and collaborators[55] describe, the presence of the surface peak is due to the reduced coordination of surface atoms with respect to the bulk. The so-called Surface Core Level Shift (SCLS) indicates the distance between the two peaks, and for this case is 350 meV.

The adsorption of $C_{57}H_{33}N_3$ allows for a new component to raise, namely P3-Pt at 71.28 eV (purple). P3-Pt is the hallmark of a prominent surface-adsorbate interaction,[81,125,126] and we can see that it is very intense up to 870 K. Curiously, its intensity slightly decreases from RT to 700 K, as opposed to the metal-molecule interaction component P2-C of the C1s XPS. A possible cause may be the fact that since the molecule is folding, the quantity of Pt atoms actually interacting with the molecules is decreasing, since the width of the molecule is becoming smaller.

As the temperature rises, P3-Pt shrinks and the surface component P2-Pt intensifies. When graphene is formed at 1140 K, a spectrum almost identical to the clean Pt one is achieved, indicating that the metal-graphene interaction is very small. Preobrajenski *et al.*[80] recorded the C1s XPS of graphene on Pt(111) and other transition metals, and they found a lack of interaction between the graphene grid and the platinum surface, which is also reflected in our results.

We will now focus on the evolution of the N1s peak upon annealing, for the molecule deposited at room temperature, represented in Figure 5.3.2. The relative abundance of the components of this peak is shown in the bottom panel of Figure 5.3.3. We can fit the RT N1s peak with four components. The first one, P1-N (blue) at 397.05 eV, corresponds to the N in the molecule interacting covalently with the Pt surface, as represented by Figure 5.3.5-d.[42,105] Curiously, its importance decreases with temperature, and it disappears at about 700 K.

However, from the previous analysis of the P2-C for the C1s and P3-Pt for the Pt4f peaks we know that the interaction between the molecule and the metal is increasing with temperature, and it actually peaks at about 700 K. Even so, the N-Pt interaction decreases, indicating that the interaction of the molecule with the surface arises mainly from the C atoms. The STM images reveal that upon cyclodehydrogenation the molecule folds downwards, since we found the highest apparent height of all the molecules in the central region. This means that as the core of the molecules bend upwards, the N which are positioned in the centre of the molecule detach from the Pt, and hence their interaction with the metal decreases. When the cyclodehydrogenation is completed and the triaza-fullerene is achieved, no N atoms are touching the surface. This is an elegant hint on how the triaza-fullerene orients on the surface and it is a further proof that the cyclodehydrogenation process of the molecule occurs as in Figure 5.3.2-b.

The most intense N1s peak at RT is P3-N (lilac) at 399.82 eV; it is related to the N atoms in the open molecules, which are shared by a hexagon and a pentagon and directly bonded with three C atoms (see Figure 5.3.5-a).

The N1s peak of a nitrogen atom bonded with carbon is highly sensitive to its surrounding: therefore a slight change in the environment may cause a large shift in its XPS peak. For example, the iminic N in porphirines usually lies at about 398 eV, while pyrrolic N in the same molecule at about 400 eV.[102,116,127] Different studies confirm that the environment is crucial for determining the binding energy of N in carbonaceous rings.[77,128,129]

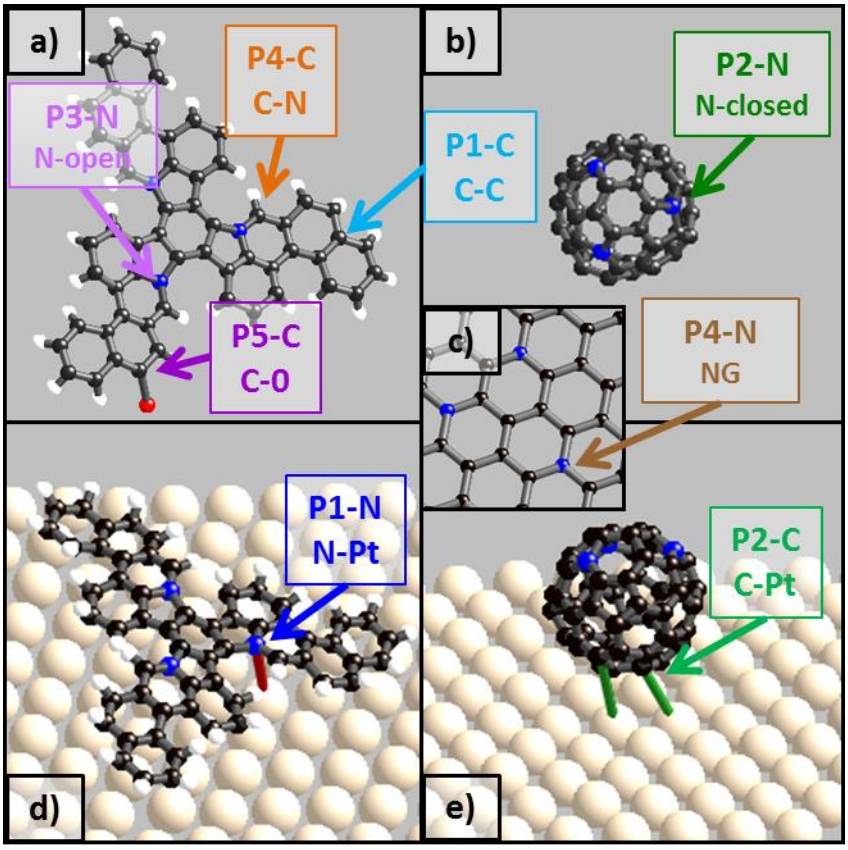

Figure 5.3.5 – *Visual scheme of the different XPS components of the N1s and C1s peaks.* *The black atoms represent the C, the blue ones the N, the white ones the H, the red one the O and the large pale spheres the Pt atoms. a) In the representation of the open molecule we can observe P1-C (the sp^2 and sp^3 C-C component) in light blue, P4-C (C bonded to N) in orange, P5-C (C bonded to O contamination in red) in purple and P3-N (N in the open molecule shared by a pentagon and a hexagon) in fuchsia. b) The closed molecule shows P2-N, the N divided by one pentagon and two hexagons (green). c) N-doped graphene indicates the substitutional N in a graphene network, P4-N in brown. d) The red bond shows the covalent interaction between the N in the open molecule and the Pt (P1-N). e) The green bond represents the covalent bond between C and Pt (P2-C): this component is present both for the open and for the closed molecule.*

We hence assigned P3-N as caused by the N in the open molecule. The bottom panel of Figure 5.3.3 reveals that the relative importance of this component decreases as the temperature increases. This is consistent with the fact that as the molecule transforms, the N environment also changes. As Figure 5.3.5-b shows, when the cyclodehydrogenation completes and the $C_{57}N_3$ forms, the N atom passes from being shared by one pentagon and one hexagon to being shared by one pentagon and two hexagons: this explains the drop of the area of P3-N with temperature.

As P3-N decreases, another component arises, namely P2-N (green) at 398.39 eV. This component is also present at RT, but its relative importance increases with temperature, peaking at 700 K, when the cyclodehydrogenation has completed and triaza-fullerenes have formed. Therefore we can relate P2-N to the N shared by one pentagon and two hexagons in the closed molecule, as indicated by Figure 5.3.5-b.

The presence of P2-N at RT and of P3-N at high temperature reveals that the cyclodehydrogenation process is not perfect and that a few defects are present. These defects may be caused by molecular fragments or by partial cyclodehydrogenation occurring in the evaporator. The presence of defects can also explain the large

apparent height range of the closed molecules revealed in Section 5.2.3: possibly due to contamination, some molecules are not able to close so their apparent height remains low (0.30 nm).

P4-N (brown) appears as a faint shoulder at 570 K, and becomes more and more important upon annealing, up to a point (at 870 K) where it becomes the primary contribution to the N1s peak. This component is therefore related to N atoms substituting C atoms in the graphene network,[42,96,103] and it is the hallmark of the growth of N-doped graphene following this recipe. This is represented in Figure 5.3.5-c. The high quality N XPS peak faints at 1140 K, as most N atoms desorb from the surface.

Hot sample deposition – N-doped graphene

To try to achieve a better recipe for the growth of N-doped graphene, we deposited $C_{57}H_{33}N_3$ on the hot Pt surface, by keeping it at 990 K (Figure 5.3.6). The relative abundances of the peak components with temperature are visible in Figure 5.3.7 (top panel for C1s and bottom panel for N1s): the components of the peaks follow the same colour code as Figure 5.3.6.

The deposition on the hot sample allows the N1s signal to be present in a constant fashion up to 1260 K. Hence, the intensity of P4-C is constant up to the final annealing temperature.

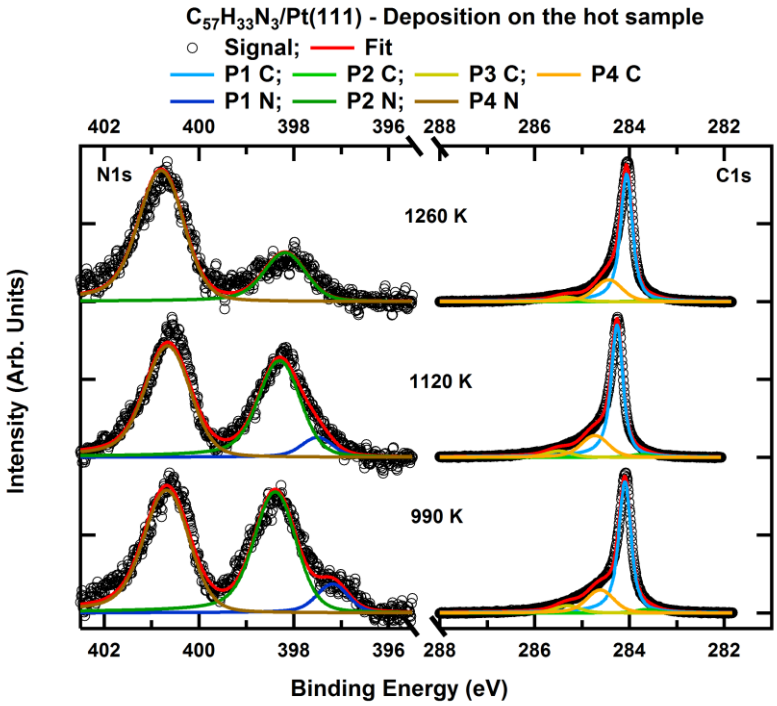

Figure 5.3.6 – ***XPS C1s and N1s peak of $C_{57}H_{33}N_3$ deposited on the hot Pt surface kept at 990 K.*** *The N1s peak is represented on the left panel and the C1s on the right panel. The N1s intensity is not normalized to the one of C1s.*

The N1s peak at 990 K shows the presence of some P1-N traces related to the interaction of N with Pt which disappears upon annealing, indicating a covalent bond of the N in the graphene network with the Pt. The presence of P2-C (a N shared by a pentagon and two hexagons in the closed triaza-fullerene) indicates the presence of defects in the N-doped graphene, which is not unusual.[42,130]

The effect of the increase in annealing temperature is to improve the quality of the N-doped graphene, since the relative abundance of P4-N (substitutional N in the graphene network) increases. The P1-C component (C-C bond) of the C1s peak is very narrow throughout the whole process, indicating that the deposition at 990 K allows the formation of graphene.

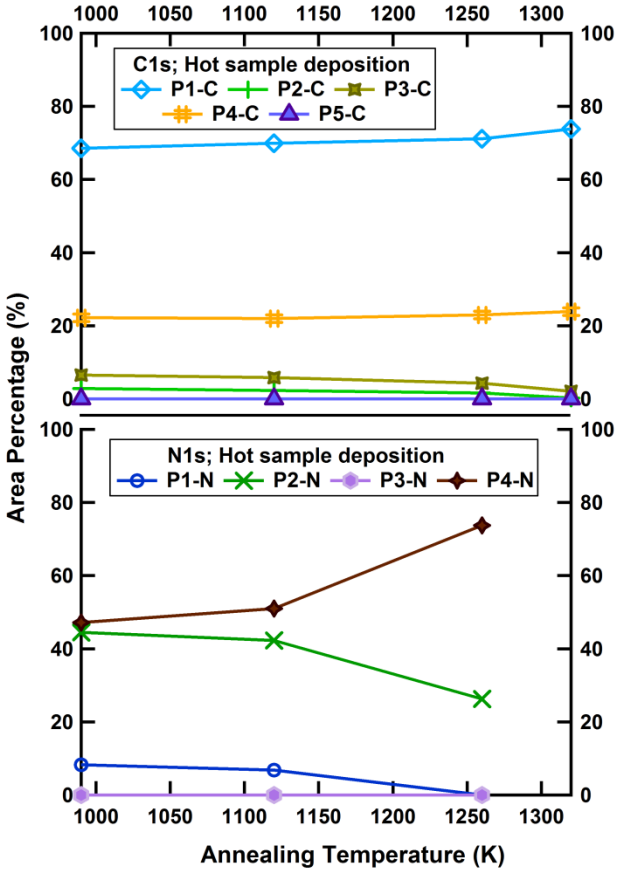

Figure 5.3.7 – ***Relative abundance of the area of each N1s and C1s peak in terms of temperature (deposition on the sample kept at 990 K).*** *The C1s peaks are shown in the top panel and the N1s in the low panel. The colour code follows the one of Figure 5.3.6.*

Discussion – XPS

The XPS is a powerful tool for understanding the evolution of the molecule with temperature. As opposed to the cases presented in Chapter 4, where DiPy[5]DBH was deposited on coinage metals and was interacting weakly with the surface, here the precursor $C_{57}H_{33}N_3$ is evaporated on a highly reactive metal, namely Pt(111). The high resolution C1s, N1s and Pt4f peaks indicate an on-going change of the chemical state of the molecule depending on the thermal energy provided to the system. According to the STM, the molecule starts to cyclodehydrogenate at about 550 K, and as a consequence open-cage N-doped fullerenes form; further annealing allows the complete cleavage of C-H bonds and the consequent total folding of the precursors into triaza-fullerenes at 700 K. Heating to 1000 K causes the molecular disruption into N-doped graphene.

The TP-XPS of the C1s peak reveals an increase in the interaction with the Pt surface occurring between 550 and 1000 K, *i.e.* in the same temperature range in between the beginning of the cyclodehydrogenation and the formation of graphene. This rise in the interaction is reflected as an overall shift of 0.15 eV of the C1s peak towards lower binding energy and it is correlated to an increase in the surface-adsorbate interaction. The C1s HR-XPS reflects this increase in the interaction as an increase of the relative importance of the peak at 283.68 eV, namely P2-C: upon annealing, it rises with respect to P1-C (the C atoms bonded with another C atoms in aromatic rings). The Pt4f peak also gives information on this matter. The Pt4f peak of a clean sample has two components, at 70.9 and at 70.5 eV: the first one arises from the contribution of Pt atoms from the bulk, while the second one from the reduced coordination of surface atoms. The existence of extra peaks, such as the one we observe at 71.28 eV, and the decrease in intensity of the surface component, indicates a high interaction with an adsorbate, which in this case is $C_{57}H_{33}N_3$. Interestingly, the Pt4f peak of the system annealed at more than 1000 K resembles the one of the clean sample: this indicates a small interaction of the graphene with the surface.

A summary of all the different components of the C1s and the N1s XPS peaks is reported in Table 5.3.1. P4-C, arising at 284.81 eV indicates those carbon atoms bonded with a nitrogen atom: its intensity decreases slightly throughout the annealing due to a possible small loss of some material upon annealing. The C1s peak also shows a CO contamination peak at room temperature (P5-C at 286.01 eV) which disappears with a light annealing, and the presence of a shake-up peak at 285.23 eV (P3-C).

Peak	BE (eV) at RT	Assignation
P1-C	284.24	C-C in hexagons and pentagons
P2-C	283.68	C-Pt
P3-C	285.23	Shake-up
P4-C	284.81	C-N
P5-C	286.01	CO contamination
P1-N	397.04	N-Cu
P2-N	398.39	N in closed molecule
P3-N	399.82	N in open molecule
P4-N	400.62	Graphitic (substitutional) N

Table 5.3.1 – *Description of each XPS peak for $C_{57}H_{33}N_3$/Pt(111).* *Each peak is described in terms of the Binding Energy (BE) at RT and of its assignation as discussed in the text.*

The evolution of the N component with temperature is equally interesting. At room temperature, the molecule exhibits three components, namely P1-N at 397.04, P3-N at 399.82 eV and traces of P2-N at 398.39 eV. Of these, P1-N and P3-N tend to zero upon annealing, and disappear at about 700 K: they indicate respectively a covalent interaction with the surface, and the N in the open triangular molecule geometry (shared between one organic pentagon and one hexagon). When the cyclodehydrogenation starts above 550 K, P2-N starts to grow: P2-N indicates the chemical environment of N in the (partially) closed molecule, shared by two organic hexagons and one pentagon. Its contribution grows up to about 800 K, at which points its importance starts to descend, as a new contribution rises, namely P4-N at 400.62 eV. P4-N indicates the presence of substitutional N in a graphene network, namely a nitrogen atom shared by three benzene rings of graphene. As the thermal energy provided to the system is increased and as graphene is

formed, the contribution of P4-N rises continuously, and this proves the presence of NG on the surface. Moreover, the fact that P1-N disappears upon formation of the triaza-fullerenes shows that the molecule is folding downwards and that the N atoms (which are positioned in the centre of the molecule) are detaching from the surface.

Moreover, the temperature of the sample during deposition is crucial for the final output: the quality of NG increases if the deposition takes place at 990 K. The relative importance of P4-N (*i.e.* the N in a graphene network) is much higher in this situation.

5.4 Conclusions

In this chapter, we unveiled by STM and XPS the mechanisms of the formation of triaza-fullerene from its planar precursor $C_{57}H_{33}N_3$. The process can be divided in three stages: (i) the open intact molecule (RT – 500 K); open-cage fullerene (500 – 700 K); (iii) triaza-fullerene (700 – 950 K). Further annealing allows the growth of N-doped graphene.

Upon deposition, the molecules do not land horizontal on the surface, but a soft anneal is enough to allow the intact molecules to maximise the number of aromatic rings touching the surface, hence flattening the precursor. The surface-catalysed cyclodehydrogenation begins at about 500 K. The presence of open-cage fullerenes increases the interaction of the molecules with the surface, as we showed by TP-XPS. The combination of STM and XPS results clarifies that the molecules bend upwards upon folding.

The closed fullerenes have an average apparent height of about 0.33±0.05 nm, but the range of AH of the molecules is wide. This is again because of the strong hybridisation with the surface which deforms the doped fullerenes.

We tracked the chemical changes of the molecules by HR-XPS. Table 5.3.1 summarises the C1s and N1s peaks of $C_{57}H_{33}N_3$ as described in the text and visually represented in Figure 5.3.2. In the Table 5.3.1 we report the binding energy at room temperature (when available) for P1-C to P5-C and from P1-N to P4-N and schematically describe its assignation.

We found that annealing the surface above 950 K produces N-doped graphene, and its quality increased if the molecules were deposited on the hot surface.

6. The mechanism of the atomic vacancy formation on the C_{60}/Pt(111) system

C_{60} is the parent molecule of the fullerene family. It is a symmetric spherical molecule made up by 60 carbon atoms divided into 20 hexagons and 12 pentagons. It has been proposed for many applications, such as superconductivity (for example bulk K_3C_{60} presents a superconductive transition at 19 K[131]), solar cells[132] and in medicine as antibacterial agents, antioxidants and for drug delivery.[133] Moreover, free C_{60} can act both as an electron acceptor and as an electron donor,[117] which enhances its potential for applications.

Surface scientists analysed thin films and adlayers of fullerenes on different surfaces (mostly metals[44,108,134–137] and semi-conductors[138]) in Ultra High Vacuum (UHV). It is a model system to explore the interaction of cyclic organic molecules with surfaces, also due to its remarkable ability of self-assembling into close-pack structures due to van der Waals interactions. Fullerenes are different from the other molecules studied in this thesis because they lack of hydrogen atoms, and are much more stable.

Felici et al.[44] discovered by Surface X-ray Diffraction that when a fullerene layer is deposited in UHV on a Pt(111) surface and annealed, the top layer of the metal reconstructs and one atomic vacancy forms below each molecule. The presence of the molecule catalyses the vacancy formation, by lowering the energy needed for this process to occur.[123]

We have been investigating the mechanism of the vacancy formation by LEED, STM, XPS and TPD and found that the fullerenes undergo three phase transitions upon annealing. The as-deposited molecule is weakly bound to the surface, and this is likely to be due to the presence of passivating H atoms on the surface; as the H desorbs upon annealing, the molecule undergoes an excited intermediate phase in which the vacancy is formed, but the molecule cannot sit on top of it because of the ejected Pt adatom which binds to the molecule and prevents its full relaxation. When further thermal energy is provided, the adatom migrates to the Pt steps and the fullerene can shift to sit on top of the vacancy. This configuration is stable up to the formation of graphene at 1000 K.

6.1 Introduction

In 2005, Felici and his collaborators published the first experimental evidence of the formation of a vacancy on a metal surface induced by C_{60},[44] previously proposed by Stengel *et al*.[139] When the C_{60}/Pt(111) system is subjected to annealing, the interface between the Pt and the observed (√13x√13)R13.9º C_{60} domains reconstruct and one single-atom vacancy is observed on the Pt(111) surface below each C_{60} molecule. This nano-patterning of the surface is a breakthrough that established a new point of view of the effect of organic molecules and C_{60} in particular on metals. Figure 6.1.1 (from Felici *et al*.[44]) represents the model of the top view and side view of the reconstruction induced by C_{60} on the Pt(111) surface.

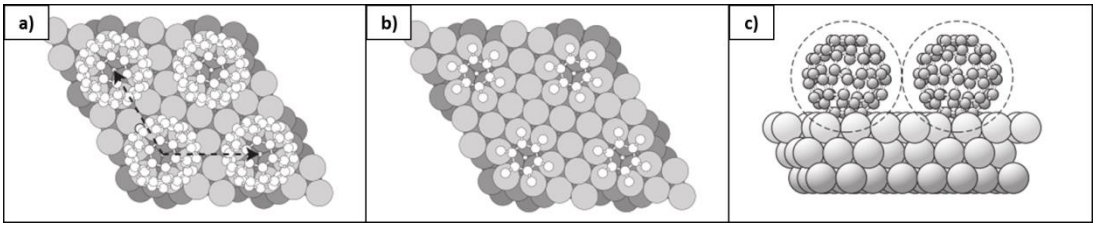

Figure 6.1.1 – *Model of the reconstruction induced by C_{60} on Pt(111).* *From Felici et al.[44] According to this scheme, the fullerene sits on top of a vacancy, and it covalently binds with the platinum surface. (a) A top view of the model where the dashed arrows indicate the unit cell of the reconstructed surface. (b) Same as (a) but only the twelve C atoms nearest to the Pt are indicated. (c) Side view of the model.*

This discovery set a trend of experiments on similar systems, and it was found that in most of them the surface experienced a single- or multi-atom vacancy. The vacancies have been characterized with many techniques, such as Surface X-ray Diffraction (SXRD), Low Energy Electron Diffraction Current Voltage curves (LEED-IV), Density Functional Theory (DFT) calculations and Scanning Tunneling Microscopy and Spectroscopy (STM/S). Li *et al*.[108] defined the formation of the vacancy on the metal as "the rule rather than the exception for C_{60} monolayers on close-packed metal surfaces".

The list of other metals undergoing the C_{60} induced reconstruction includes Au(111)[140], Cu(111)[45,131,141], Au(110)[142], Ag(111)[108,143] and Pt(110)[144] to name a few. In particular, (111) faces of face-centred cubic metals undergo a one- or a seven-atoms vacancy reconstruction depending on the geometry of the surface.[45,117] In some systems, such as Pt, the energy cost for forming a vacancy on the metal is lowered by the presence of a covalent bond with the molecule.[123]

Depending on the interaction, many transition metals transfer charge to the C_{60}, [124,131,140,145–154] even though some works are controversial, as explained by Gardener *et al*. [140] In general, bonding between the organic molecule and the metal allows a charge transfer from the surface, *i.e.*, the fullerene behave as electron acceptor.[155,156] Pai *et al*. [131] demonstrated that optimal electron doping for C_{60} can be induced by the 7-atom pit induced by C_{60} on the Cu(111) surface. C_{60}^{3-} is the optimal electron doping for fullerenes, as it is the one required by superconductivity.

Some of the works mentioned above use STM images to understand the orientation of the molecule with respect to the substrate by achieving molecular orbital (MO) resolution. A molecularly resolved STM image of an individual C_{60} molecule recorded at positive sample voltages shows the large electron density confined in the pentagons of the fullerene cage.[135] Figure 6.1.2, from Schull *et al.*,[135] indicates STM images of three C_{60}s oriented in different ways, namely sitting on a pentagon (1, one bright lobe), sitting on a 6:6 bond (2, two bright lobes) or sitting on a hexagon (3, three bright lobes). Intermediate rotations are simply displayed as with partially visible pentagons.

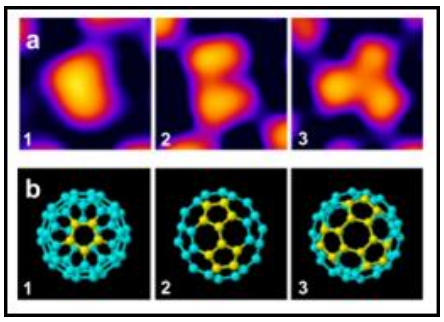

Figure 6.1.2 – *The resolution of molecular orbitals helps to deduce the orientation of the C_{60}.* *C_{60}/Au(111), from Schull et al.[135] a) STM images of fullerenes with different orientation. b) Corresponding top view models. Since the tunneling current mainly arises from the pentagons (highlighted in yellow), when the molecule is sitting on a pentagon only one lobe appears; when sitting on a 6:6 dimer, two lobes occur; when a hexagon ring is facing downwards, a three-leaved clover shape follows.*

When applying different sample bias, different molecular orbitals are contributing to the tunneling current, as represented in Figure 6.1.3.

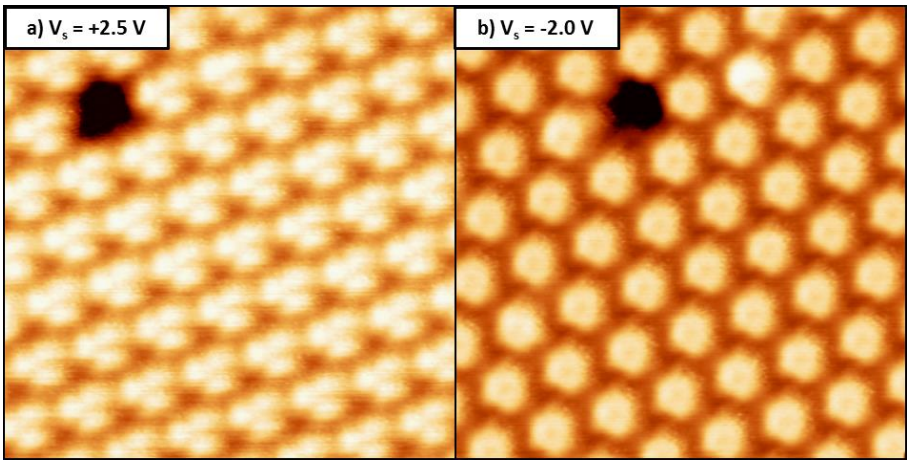

Figure 6.1.3 – *Images at different sample voltages allows observing different molecular orbitals.* *The hole represents the reference point for the two images. a) 7x7 nm^2 STM image of the LUMO + 1, measured at V_s = +2.5 V. b) 7x7 nm^2 STM image of the HOMO, measured at V_s = -2.0 V.*

By scanning at V_{sample} (V_s) = +2.5 V we can see spatial features related to the Lowest Unoccupied Molecular Orbital (LUMO) + 1, as the three-clover shape; by measuring at V_s = -2.0 V, we observe the Highest Occupied Molecular Orbital (HOMO) as a round feature with a dark hole in the middle. STS can be employed to characterize the energy position of the LUMO, the LUMO + 1 and the HOMO. According to the literature, on different metals the LUMO is positioned between 0.2 and 0.7 V, the LUMO + 1 between 1.4 and 2.2 V and the HOMO between -1.6 and -1.9 V, depending on the system.[131,145,157]

Other STM experiments on numerous systems,[140,141,143,154,156,158–163] revealed the presence of two families of molecules with different apparent height, namely bright (B) and dim (D). The origin of such features has been debated for the past few years but the scientific community is more and more keen to justify the height divergence as due to a surface reconstruction of the substrate which causes some molecules to 'sink' with respect to others, as it may be the presence of a vacancy. In some cases, such as Au(111),[140,160] the apparent height difference between B and D molecules (which is usually about 1.5-2 Å) depends on the bias voltage applied to the sample, being maximum at positive voltage and almost zero at negative voltage: this means that the difference between B and D molecules is not only topographic but also electronic. Other experiments confirm that when measured at RT, some molecules are allowed to flip between B and D on Au(111) and on other surfaces such as Ag(111), which infers that the substrate below is dynamic. In general, the relative proportions of B and D molecules increase with T, which means that there is an energy barrier to overcome for the system.[161]

In this work, we will focus on the case of C_{60}/Pt(111), which is the transition metal with the highest workfunction.[44,122] As discussed above, Felici *et al*.[44] confirmed the formation of the vacancy on the (√13x√13)R13.9º superstructure of C_{60} on Pt(111). This system forms two different superstructures: even though there is no full agreement on the precise temperature of formation of the different phases, according to most authors,[122,124,152] C_{60} on Pt(111) exhibits two mirror domains of (√13x√13)R13.9º and one domain of (2√3x2√3)R30º which occurs only after annealing at high temperature (above 500 K). Other authors[150,164] only report the existence of (√13x√13)R13.9º. According to these results, it is very difficult to determine an exact recipe for the formation of these domains since they seem to be very sensitive to any slight change of the experimental conditions (such as temperature of the sample, rate of deposition and coverage). Moreover, the temperature of formation of the vacancy is also a matter of debate.

In the literature, another controversy arises from the charge transfer of electrons (e^-): according to Cepek *et al*.[164] 0.8 e^-/molecule are transferred to the C_{60} from Pt, according to Swami at al.[150] 2.0 e^-/molecule and for Shi and collaborators[124] 0.25 e^-/molecule. This discrepancy may be explained of the different measuring conditions, *i.e.* Cepek annealed the sample to 900 K, Swami performed the experiment at room temperature and Shi calculated the charge transfer. Moreover, the authors employed different techniques in calculating or extracting experimentally this number: Cepek used vibrational modes, Swami High Resolution Electron Energy Loss Spectroscopy (HREELS) and Shi the Bader charge analysis.

STM images revealed that C_{60}/Pt(111) sits in five different ways on the surface at room temperature, as Figure 6.1.4 – from Liu *et al*.[122] – reveals. According to Liu's study, the apparent height of the molecules is 0.53 nm, and the only domain present at room temperature is the (√13x√13)R13.9º. The molecule sits either on a pentagon (1), or on a 6:6 bond (2), or on a hexagon (3), or on a 5:6 bond (4) or in an intermediate position between sitting on a hexagon and on a 6:6 bond (5).

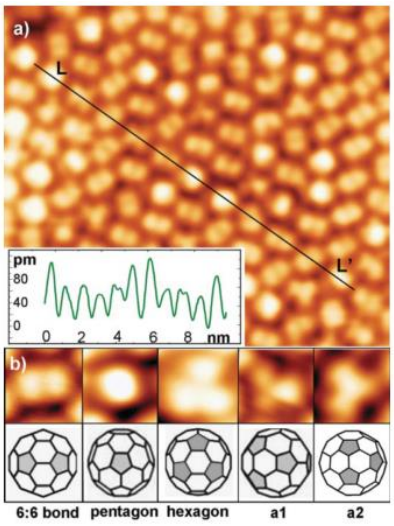

Figure 6.1.4 – *Orientation of C_{60} on Pt(111) at room temperature.* *From Liu et al.*[122] *a) This high resolution image shows the molecular orbital orientation and the inset shows the apparent height of the molecules along the black line (V_s = 2 V; 12x10 nm^2). b) Five different orientations are allowed on Pt(111) at room temperature and are shown here: the molecule can be sitting on a 6:6 bond (1), on a pentagon (2), on a hexagon (3), on a 5:6 bond (4) or on an intermediate stage between a hexagon and a 6:6 bond (5).*

According to Liu, after thermal activation at 500 K only two orientations survive, namely (4) and (5) with an apparent height drop to 0.50 nm; when increasing the temperature to 700 K all the molecules rotate to sit on a hexagon. Upon annealing, the (2√3x2√3)R30º domain appears, and since the apparent height and the orientation is exactly the same as the ones of the other domains, the authors suggest that this domain also undergoes the vacancy formation.

Other studies confirm that upon annealing C_{60} on Pt(111) sits on a hexagon.[44,123,124,165] In particular Huang[123] and Shi[124] performed DFT calculations and agree that in the presence of a vacancy the molecule sits in a atop configuration. They both corroborate that the C_{60} binds covalently with the Pt, and that this bonding lowers the energy formation of the vacancy on the metal, which would be much higher in the absence of the molecule. In particular, Huang's calculations suggest that the energy of formation of a vacancy is 1.75 eV lower directly below a C_{60} molecule. The extracted Pt atom then becomes an adatom located at an interstitial region between the Pt(111) surface and the C_{60} molecules and a covalent bond between the adatom and the fullerene forms, as shown in Figure 6.1.5.

Sogo *et al.*[166] confirm a strong hybridisation of the molecule's π orbitals with the Pt5d electrons, which transform the whole C_{60} molecule in a good mediator of metal-wave function.

In this work, we shed some light on the mechanism of the vacancy formation by combining LEED-IV, STM, High Resolution XPS, Temperature Programmed XPS and Temperature Programmed Desorption. The molecules' apparent height varies with thermal activation, and we observe three types of molecules, namely, medium height, bright and dim. The medium height molecule corresponds to the weakly interacting fullerene, while the bright and the medium height correspond respectively to a molecule sitting on an adatom and the molecule sitting on a vacancy. Hence this apparent height evolution is due to the presence

of the adatoms suggested by Huang. We also show an increase in the interaction between Pt and C_{60} during the vacancy formation.

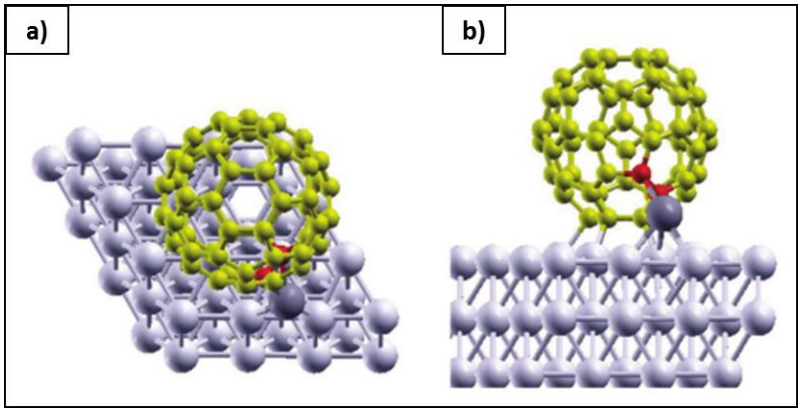

Figure 6.1.5 – *Model of the adatom-vacancy pair suggested by Huang.* *From Huang.*[123] *The top view (a) and side view (b) for the relaxed structure of C_{60}/Pt(111) with an adatom–vacancy pair. The Pt adatom (a dark grey sphere) is located at the hcp hollow site; the C atoms forming Pt–C bonds with Pt adatom are shown as small red spheres.*

6.2 Results

6.2.1 STM

To unveil the mechanisms of the vacancy formation, we monitor by STM the changes with temperature of submonolayer coverage of C_{60}/Pt(111). Two STM setups have been employed for this section: a room temperature STM (ESISNA, ICMM-CSIC) and a Low Temperature STM (M2N, Technical University of Eindhoven): the results are alike although the molecular orbital resolution improves at low temperature.

At room temperature, domains of ordered C_{60} with a (√13x√13)R13.9º periodicity are observed. The monoatomic Pt steps saturate with molecules, as Figure 6.2.1-a indicates. Once all the steps are fully decorated, the exceeding molecules form islands, arising from the step. Some small islands nucleate in the middle of a large terrace, probably due to contamination traces which react with a fullerene and act as a seed for the island formation. The formation of ordered islands is possible because the interaction with the surface is low enough to permit diffusion of the molecules, so the intermolecular forces act to attract the fullerenes to each other.[7] However the surface-adsorbate interaction is high enough to avoid diffusion of the islands.

In Figure 6.2.1-b the spatial resolution of the LUMO + 1 indicates that the fullerenes orient in five different ways, highlighted in Figure 6.2.1-c. Liu *et al.*[122] observed the same result, as discussed in Section 6.1. Next to each high resolution image, a model represents the fullerene orientation. The configuration at the bottom

represents the molecule sitting on a hexagon: we observed two rotations of the three-leaved clover features with respect to the Pt, with an angle difference of 60º.

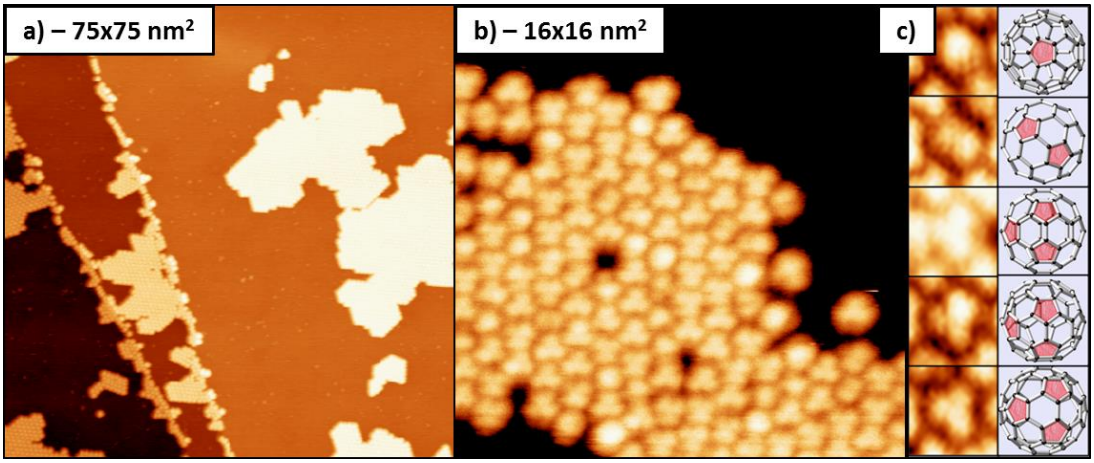

Figure 6.2.1 – *STM of C_{60}/Pt(111) at room temperature: M molecules.* *a) Panoramic image (75x75 nm^2; V_s = 2.0 V) of C_{60} decorating the steps and forming islands. b) Molecular orbital resolution (16x16 nm^2; V_s = 2.5 V) of the system. c) The five possible orientations of C_{60} on Pt(111) at room temperature are here shown in high resolution images (2x2 nm^2) and compared with a model; the red pentagons show the feature observed in the image.*

Upon thermal activation at 400 K, a new domain arises, namely the (2√3x2√3)R30º superstructure: Figure 6.2.2-a shows a 28x28 nm^2 image of three different domains of C_{60}. Domain A represents the (2√3x2√3)R30º superstructure, and domains B and C the two mirroring forms of the (√13x√13)R13.9º superstructure. Other than the rise of a new domain, the landscape does not change with respect to the RT image, as Figure 6.2.2-b shows that the molecules still orientate in the same five different ways as at room temperature, and the apparent height (AH) of the molecules (see inset) with respect to the Pt is 6.6 ± 0.3 Å, which is the same as at room temperature (not shown).

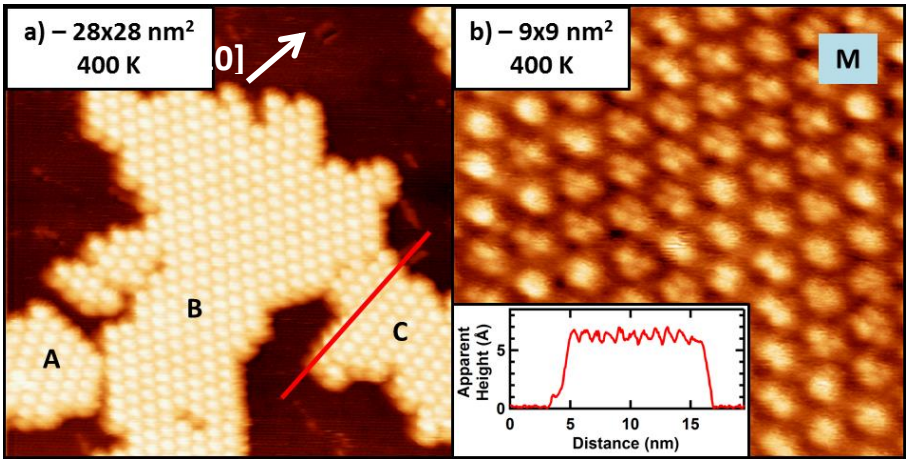

Figure 6.2.2 – *C_{60}/Pt(111) annealed to 400 K: M molecules.* *a) Three domains coexist in this image, namely A, the (2√3x2√3)R30º one, B and C, the two mirrors of (√13x√13)R13.9º (28x28 nm^2; V_s = -2.5 V); the white arrow indicates the Pt(111) crystallographic*

direction. b) Molecular orbitals are resolved in this 9x9 nm^2 image (V_s = 2.5 V); the inset shows the apparent height of the molecules in the red line in (a).

The AH is a crucial parameter in this analysis: from now on, we will refer to molecules exhibiting any of the five different orientations and apparent height of 6.6 ± 0.3 Å as Medium height molecules (M). The value of the AH of M-type molecules has been determined after analysing tens of images ranging from RT to about 450 K.

When annealing at 500 K, the sample changes drastically (Figure 6.2.3-a): the apparent height of certain molecules changes and brighter and dimmer molecules coexist. M molecules with an apparent height of 6.6 ± 0.3 Å oriented in five different ways are still present (emphasised in Figure 6.2.3-c). However, we can also see Bright (B) molecules with apparent height of 7.5 ± 0.3 Å and Dim (D) molecules with AH = 4.8 ± 0.5 Å. Molecular orbital resolution from Figure 6.2.3-b indicates that all the B and D molecules sit on a hexagon facing the same direction. Figure 6.2.3-d and -e highlight this aspect.

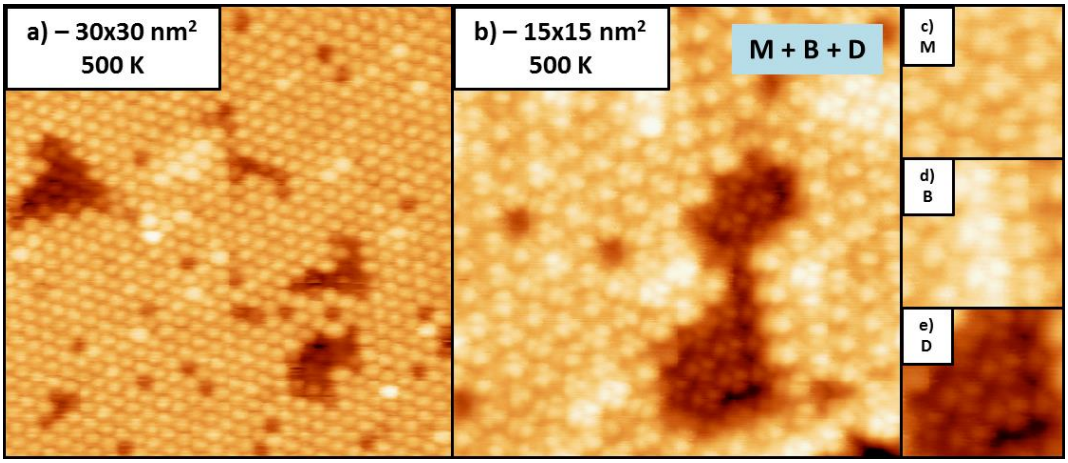

Figure 6.2.3 – *C_{60}/Pt(111) at 500 K: M, B and D molecules.* *a) This image shows that three different types of molecules coexist after annealing at 500 K, namely M, B and D (30x30 nm^2; V_s = 2.0 V). b) Molecular orbitals of M, B and D are resolved: both B and D are always sitting on a hexagon (15x15 nm^2; V_s = 1.5 V). c)-d)-e) are high resolution image of respectively M, B and D (3.2x3.2 nm^2; V_s = 1.5 V).*

The apparent height is a delicate parameter to characterise. However, the difference between M, B and D is clear from Figure 6.2.4, which shows the height profile of the three types of molecules coexisting on the same sample.

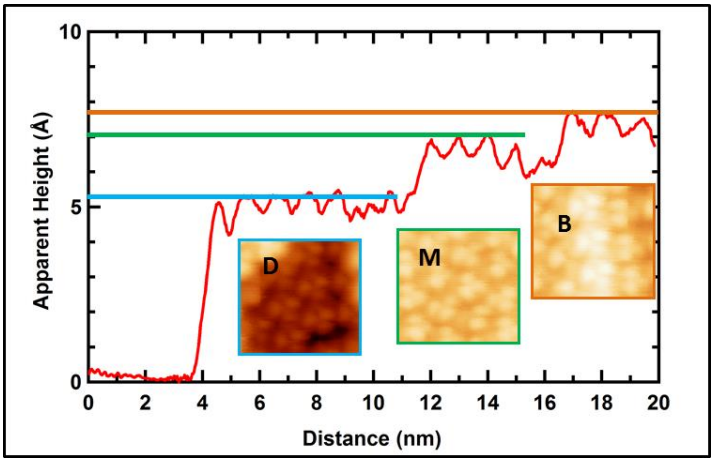

Figure 6.2.4 – *A comparison of the apparent height of M, B and D molecules.* *We measured this profile on a sample where the three molecules coexisted. The apparent height is measured by considering the Pt surface as the 'zero' and the highest part of the molecule as its height.*

Upon annealing at 600 K, we can only spot two types of molecules (Figure 6.2.5-a) since all the M molecules transformed into B and D molecules. The resolved molecular orbitals in Figure 6.2.5-b indicate that all the fullerenes are sitting on a hexagon, since we see the three-leaved clover features for the LUMO + 1, and the B and D molecules are all facing the same direction. Moreover, we can notice how in general the bright molecules are surrounded by dim molecules.

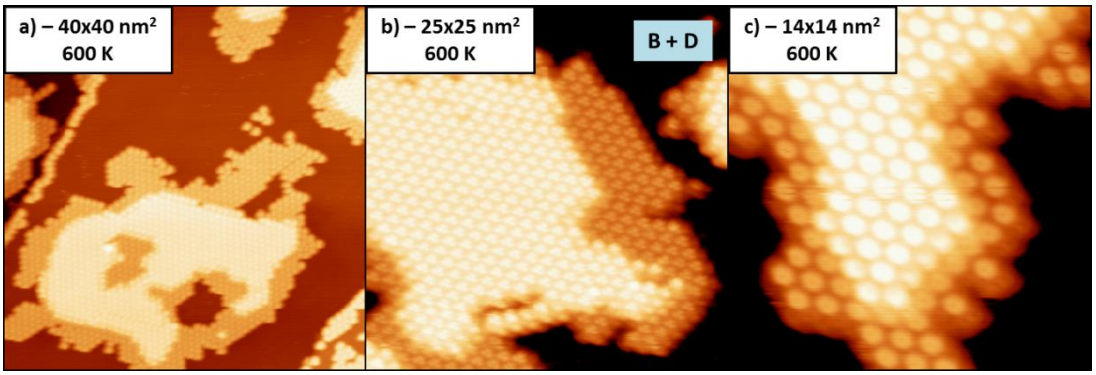

Figure 6.2.5 – *C_{60}/Pt(111) at 600 K: B and D molecules.* *Now no more M molecules appear, and only B fullerenes coexist with D ones. a) 40x40 nm^2; V^s = 2.0 V. b) 25x25 nm^2; V^s = 2.0 V. c) 14x14 nm^2; V^s = -2.5 V*

Figure 6.2.5-c clearly shows the HOMO of the molecule since the image was scanned at a sample voltage of -2.5 V. Even so, the apparent height of the HOMO and of the LUMO + 1 is the same. Curiously, Figure 6.2.5 shows that the D molecules start to appear at the edges of the islands.

Other than the apparent height, the B and D molecules differ for another aspect: the 2D crystallographic networks they belong to are identical in periodicity, but are shifted. The green lines in Figure 6.2.6 represent the 2D lattice of the of B fullerenes. These lines extend to the D molecules of the same islands: the

intersections of the lines fall exactly on the middle of the B molecules, but are shifted from the centre of the D ones. The **a** and **b** vectors indicate the unit cell of the B lattice, while **a'** and **b'** the one of the D grid: the shift (measured with the WSxM software[167]) is 0.14 nm for both vectors.

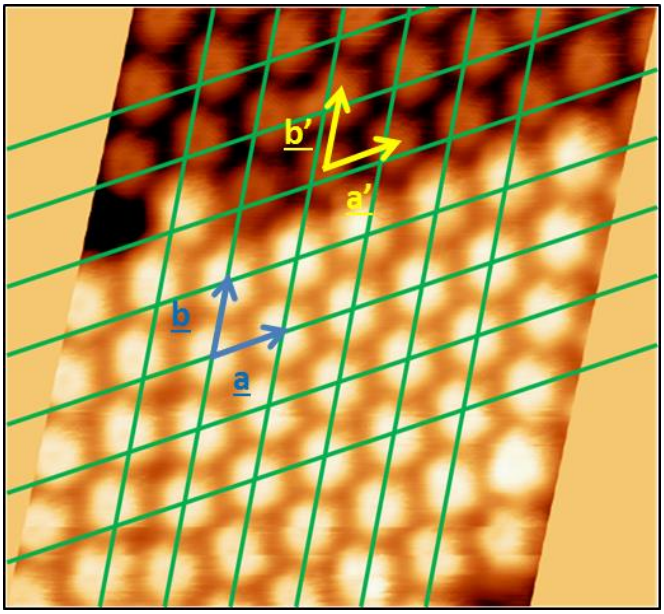

Figure 6.2.6 – *The grids of the B and D molecules are shifted by 0.14 nm.* *The drift of the image was corrected with a homemade program. The green lines represent the hexagonal grid of the bright molecules, and each crossing between vertical and horizontal lines falls on top of the centre of a molecule (9.7x8.9 nm^2; V_s = -2.5 V). The blue vectors **a** and **b** show the unit cell of the B fullerenes, while the yellow vectors **a'** and **b'** represent the unit cell of the D molecules, shifted 0.14 nm in both directions.*

The nearest neighbour distance between Pt atoms is 0.277 nm: the shift between grids is about half of the interatomic distance of the metal. Therefore, the adjustment when passing from B to D must involve a change in the relative position of the fullerene with the surfaces, such as the passage from a hollow or bridge to atop site.

Further heating transforms all the molecules of the sample to Dim molecules: Figure 6.2.7-a only shows one type of molecules, and the inset clarifies that the AH of the molecules is about 4.8 Å. The LUMO + 1 resolution (Figure 6.2.7-b) confirms that all the fullerenes sit on a hexagon and face the same direction, as expected for D molecules.

Figure 6.2.7-c indicates that a slight increase in annealing temperature (750 K) is enough to decompose the fullerenes into graphene (G): indeed a trained eye can spot a graphene patch in the middle of the image, nucleating at the step. The graphene coexist with intact molecules, and a few detach from the island and are isolated. Graphene and dim fullerenes coexist up to about 1000 K; at this point, the temperature is enough to disrupt all the molecules and form graphene sheets: since C_{60} comprises hexagons and pentagons, its bonds must break to form the hexagonal network of graphene.

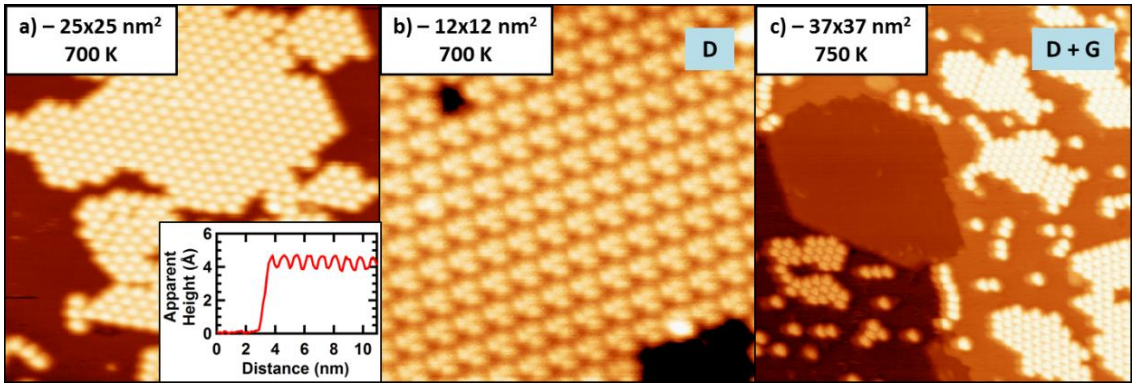

Figure 6.2.7 – *C_{60}/Pt(111) annealed to 700 and 750 K: D molecules.* *a) Upon annealing to 700 K, all the molecules look the same; the inset represents the apparent height of 9 molecules and shows that they are indeed all D (25x25 nm^2; V_s = 0.25 V). b) Resolution of the LUMO + 1 indicates that all the molecules are sitting on a hexagon (12x12 nm^2; V_s = 2.5 V. c) When annealing to 750 K, some fullerenes start to decompose into graphene, like in the patch in the middle (37x37 nm^2; V_s = 2.0 V).*

The use of large precursors and annealing at the lowest possible temperature favours the growth of multiple domains of graphene.[73,106] Figure 6.2.8 represents different islands of graphene; Figure 6.2.8-a reveals two coexisting moiré islands, namely α graphene and o graphene (this nomenclature refers to Merino *et al*.[73]). α graphene, also known as a (√3x√3)R30º or as a 2x2 superstructure, is a special moiré since it is the only one that bonds covalently with Pt(111) and it induces an ordered vacancy network on the Pt(111) surface similar to the one induced by the fullerenes.[106] Upon annealing C_{60} to form graphene, we observed 19 different domains of different periodicity and angles with the surfaces (Figure 6.2.8-b displays an atomic resolution image of ε graphene).

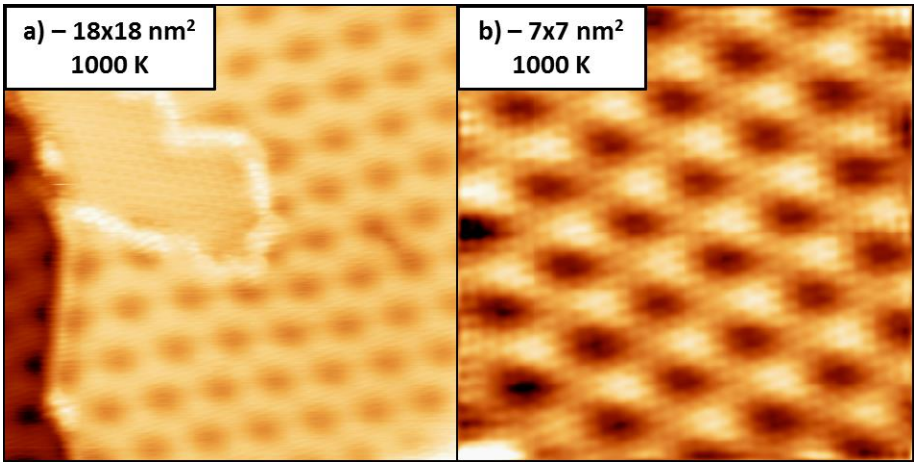

Figure 6.2.8 – *C_{60}/Pt(111) at 1000 K: formation of graphene.* *a) Graphene Moiré patterns corresponding to the coexisting phases α and o graphene following the nomenclature of ref.[73] (18x18 nm^2; V_s = 0.1 V). b) Atomic resolution on an island of ε graphene (7x7 nm^2: V_s = 0.15 V).*

As a summary, Figure 6.2.9-a represents the evolution of the apparent height of the molecules in terms of temperature: this is achieved after quantifying the apparent height of hundreds of molecules, to be

statistically relevant. Related to that, Figure 6.2.10 consists of six STM images at each important temperature. At room temperature, Figure 6.2.9-a shows that all the molecules are about 6.6 ± 0.3 Å tall, and this is true up to about 490 K (steps a and b in Figure 6.2.10): therefore we can classify them as M molecules, represented in green in the plot. M molecules are present up to about 590 K, but at 490 K the panorama changes and dimmer and brighter molecules begin to show, respectively 4.8 ± 0.5 Å (yellow in the plot) and 7.5 ± 0.3 Å (red in the plot) tall (step c in Figure 6.2.10). Upon further annealing, at about 600 K, the bright and dim molecules take over, and no more medium height C_{60}s survive (step d in Figure 6.2.10). At 700 K, all the bright molecules turn into dim molecules, and at 750 K they start to decompose into graphene (respectively, steps e and f in Figure 6.2.10). Unfortunately, due to the experimental set up, the error in measuring the temperature is estimated to be about 30 K.

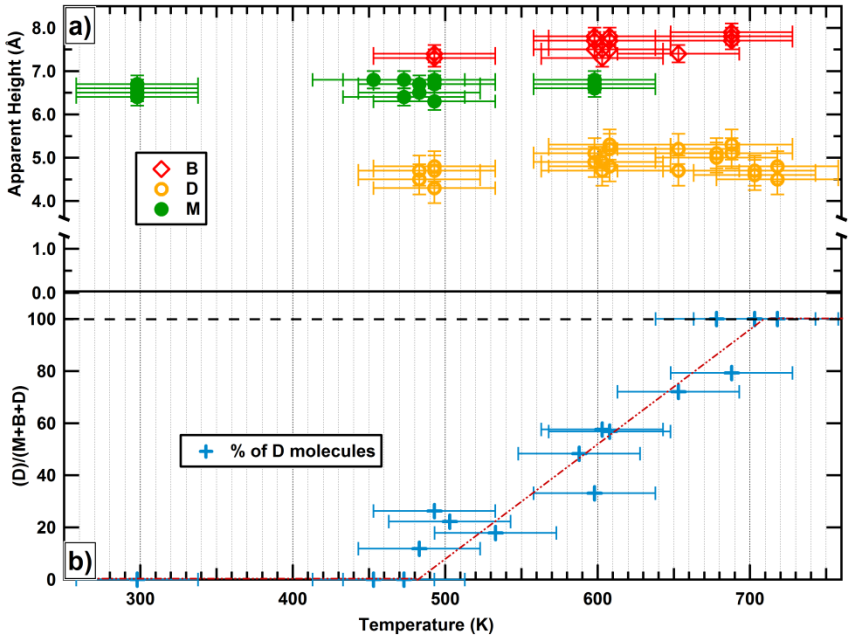

Figure 6.2.9 – *The apparent height variation and the percentage of D molecules is shown in terms of temperature.* *a) The apparent height of the molecules is represented as a function of the annealing temperature; we can distinguish three different AH, namely medium height molecules (green), dim ones (yellow) and bright (red). b) We can see the percentage of M+B molecules with respect to the total number of molecules as the temperature is increased. These graphs were produced after recording the apparent height of hundreds of images.*

Figure 6.2.9-b represents how the percentage of dim molecules increases with temperature: as we just discussed, these fullerenes start to appear at 480 K, then their relative amount increases up to 700 K, where 100% of the molecules are dim. From Figure 6.2.9-b, it is clear that the percentage of D molecules increases linearly as the sample is heated up.

Hence, fullerenes on Pt(111) undergo a double phase change upon annealing before forming graphene: three types of molecules arise according to the temperature. M molecules turn into B fullerenes, which in turn transform into D molecules. The difference does not stand only on the apparent height, but also on the

orientation: all the medium height molecules lean in five different ways, as indicated in Figure 6.2.10-a by coloured circles, while all the bright and dim molecules sit on a hexagon facing the same crystallographic direction. Also, the B and D molecules do not possess the same position with respect to the Pt atoms since their grids are shifted by 0.14 nm both horizontally and vertically.

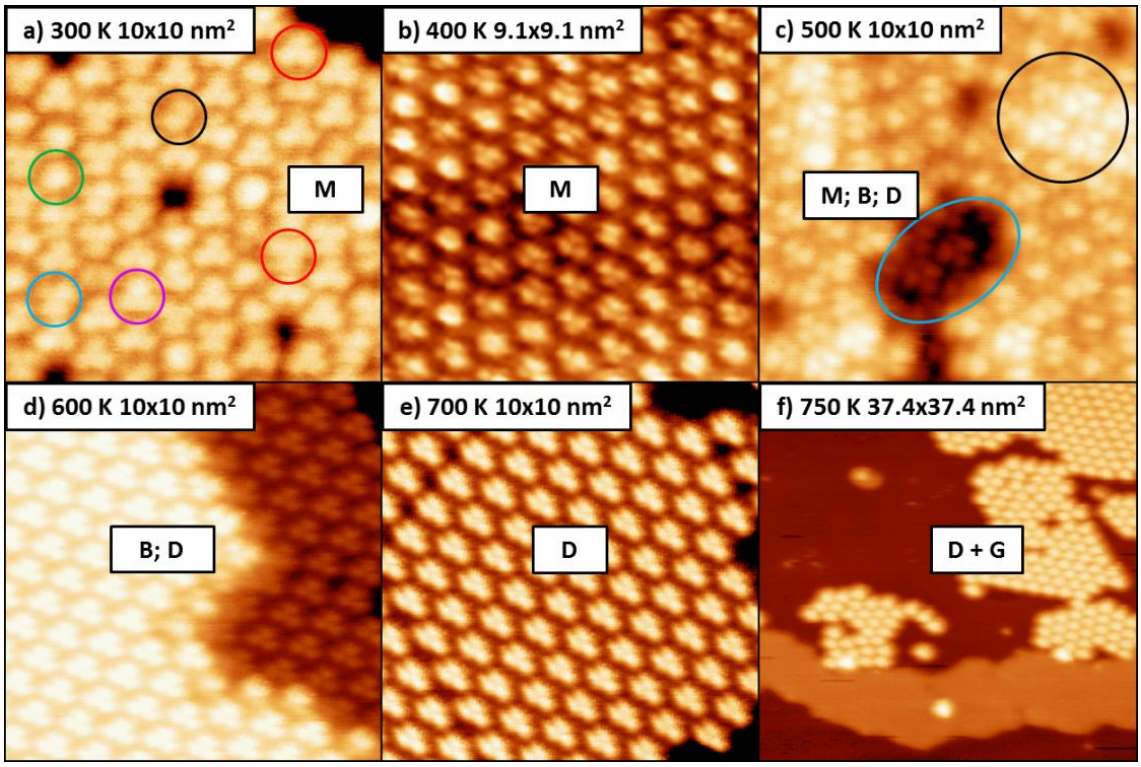

Figure 6.2.10 – *Summary image of all the stages that are observed by STM for C_{60}/Pt(111) upon annealing.* *The sample voltage of each image is between 2.0 and 2.5 V, and the size is written in the inset. a) At room temperature, all the molecules are M and are rotated in five different ways, indicated by the coloured circles: the red circle shows two molecules sitting on a hexagon, rotated by 30º. b) At 400 K the panorama is the same as at RT. c) At 500 K, B and D molecules sitting on a hexagon start to appear. d) Further annealing at 600 K implies that all the M molecules transformed into D and B C_{60}. e) At 700 K, the D molecules take over and they are the only ones remaining on the surface. f) At 750 K, some D molecules start to decompose into graphene, as indicated by the patch in the bottom of the image.*

In terms of AH, it could be natural to assign the change from M to D to the formation of a vacancy. Other authors also connected the height gap of fullerenes to the vacancy formation,[131,140] and it is consistent with a structural transformation of the surface. The loss of an atom on the surface is indeed likely to be in part to blame for the sinking of the adsorbed molecule. Also, most authors assess that the fullerenes bond covalently to the platinum when the vacancy is formed (D molecules) with either the six[123,124] or the twelve[44] bottom carbon atoms. However, the M fullerenes at room temperature are free to diffuse until they meet other molecules to form ordered structures nucleated at the steps: ordered patterns can only form if the substrate-adsorbate interaction is low enough to allow them to diffuse but high enough to hold them in place; also, the intermolecular interaction plays the fundamental role to bind them together.[7] All of this suggests that C_{60} weakly interacts with the surface upon deposition. Since when the vacancy forms, the

molecules covalently bond to the surface, there is a phase transition between weak interaction and chemisorption, which coincides with the vacancy formation.

The role of the B molecule is still not mentioned in this picture even though each M fullerene undergoes an intermediate (metastable) stage where its apparent height increases before becoming D: as always when analysing STM results, this alteration can either be caused by electronic effect or by geometrical and topographical causes, or even by a combination of the two. As the AH shift is as large as 0.2 nm, it is likely to be an electronic effect rather than purely topographic.

To acquire additional information on the process with a slightly different approach, we investigate the role of the surface temperature upon deposition, that is, to deposit the fullerenes keeping the sample at different temperatures, rather than evaporating the molecules at room temperature and annealing subsequently. The results are shown in Figure 6.2.11. The change in the kinetics of the system may lead the molecules to a different structure or final state. As a general trend we observe an increase in the population of molecules at the steps of the sample, together with a decrease in the size of the islands.

It is clear that the steps are much less decorated if the evaporation of C_{60} takes place with the sample at RT (Figure 6.2.1). The presence of so many molecules at the steps when deposition occurs on the hot sample can be explained from the fact that the vacancy formation is a slow process. Indeed, the phase transition does not occur suddenly but instead the passage from a surface with no vacancies (no D molecules) to a sample where all the C_{60} molecules sit on vacancies occurs over a range of about 200 K. Therefore some molecules have enough energy to form a vacancy, and those molecules will just stay where they land, if the sample is hot, and will not contribute to the decoration of the steps. All the other molecules which do not form a vacancy, due to the high mobility at this temperature will move towards a favourable spot to stay, and they find it by the step. This explains the high population at the steps and the small islands, and the increasingly small size or lack of the islands upon increasing the temperature.

The second characteristic of depositing the molecules on the sample at 480 K (Figure 6.2.11-a) is that the fullerene islands are smaller than when depositing at room temperature and then annealing, which further confirms the higher metal-molecule interaction competing with the intermolecular one. In this sample, most molecules exhibit B and D character however some M molecules are also present. When depositing at room temperature, B and D molecules started to appear at 490 K, a slightly higher temperature than the one observed here. Thus, deposition on the hot sample seems to be more efficient in favouring the growth of B and D molecules.

Deposition at 550 K (Figure 6.2.11-b) results in an even higher population of the steps; moreover, most molecules segregate in disordered chains or agglomerate in small isolated islands. This confirms that the hot sample interacts more with the fullerenes and this interaction prevails on the intermolecular forces. Most molecules are D type, with some B exceptions in the middle of larger islands. RT deposition and annealing to similar temperature still reveals the presence of M molecules, thus reinforcing the argument that a hot sample is more effective in producing B and D fullerenes.

The sample kept at 715 K (Figure 6.2.11-c) during evaporation favours the growth of D molecules at the step and isolated molecules or small islands in the terraces. Ordered triangular agglomerations decorate the

steps. At this stage, the sample matches the room temperature deposition and annealing to 700 K of Figure 6.2.7, even though the steps are now more decorated.

Figure 6.2.11-d shows how depositing fullerenes on the sample at 750 K results in scattered D molecules and small islands and in lack of population at the steps. This means that the interaction with the surface is so high that the molecules stick where they land or they diffuse slightly to meet other few fullerenes to form small agglomerations. Moreover – as for room temperature deposition – the molecules start to decompose into graphene and a small graphene patch is visible in Figure 6.2.11-d. The presence of D molecules is related to the formation of a vacancy on the Pt surface, the lack of molecules at the steps and the small islands mean that the high temperature catalyses the formation of the vacancy as soon as the molecule lands, hence the molecules are anchored to the sample where they arrive, and no further diffusion is allowed.

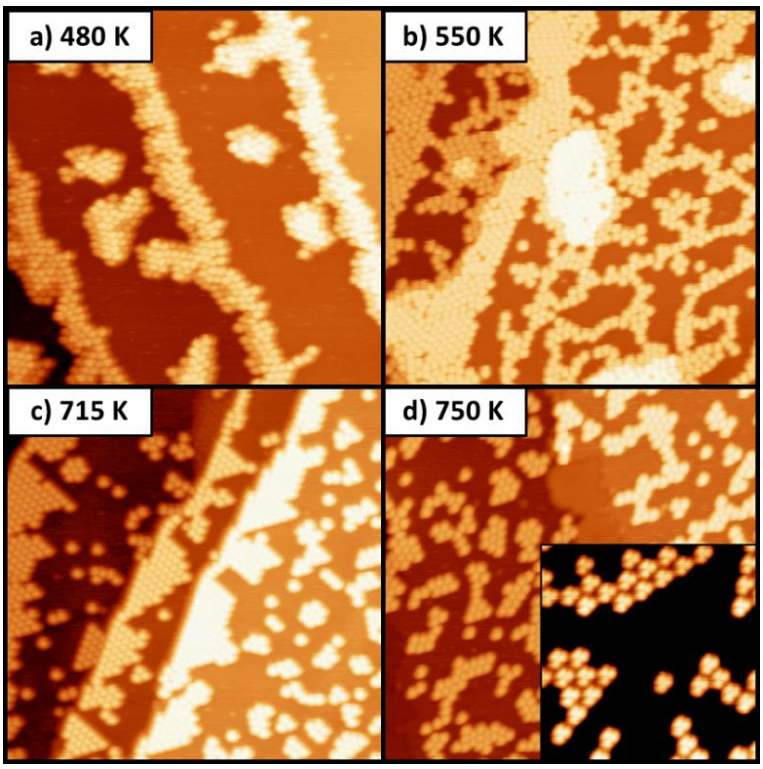

Figure 6.2.11 – C_{60} deposited on the hot sample at four different temperatures. *a) When the sample is kept at 480 K during deposition mostly B and M molecules are observed, but also some D are present (35x35 nm^2; V_s = 2 V). b) Deposition on Pt at 550 K leads to mostly D molecules with a few B molecules in the centre of large islands (35x35 nm^2; V_s = 2 V). c) At 715 K, all molecules are D and mostly scattered around (35x35 nm^2; V_s = 2 V). d) An increase in sample temperature to 750 K all molecules are D and some decomposed into graphene (35x35 nm^2; V_s = 2 V).*

To summarize, the STM depicts a process for which the adsorbed molecules can be either weakly interacting M molecules, or covalently bonded D fullerenes sitting on a vacancy or B molecules. Two questions arise: what are B molecules and how can we understand the room temperature weak interaction for M molecules, as the DFT calculations predict a strong surface-adsorbate interaction for this system. We have been using other experimental techniques to answer these questions.

6.2.2 LEED

To understand by diffraction methods the mechanism of formation of the vacancy, we carry out LEED-IV measurements. In particular, we are interested in discovering whether the vacancy can also be related to B molecules or only to the D ones. Our LEED results confirm the STM appreciation of the existence of the two mirror domains of the (√13x√13)R13.9º, which coexist with the superstructure after annealing the sample at 480 K. Figure 6.2.12-a, -b, -c and -d display a series of LEED patterns measured at 58-62 eV on the sample annealed at different temperatures, respectively 300, 480, 610 and 810 K. The two domains of the (√13x√13)R13.9º superstructure are always present, and the (2√3x2√3)R30º domain appears at 480 K as faint spots as indicated by the inset of Figure 6.2.12-d, and its intensity increase with temperature.

When comparing the first two LEED patterns with the last two, a clear difference arises: the LEED patterns at 300 and 480 K show that all the 12 dots in the inner ring present the same brightness, while if the sample is annealed to a higher temperature (at least 610 K), six spots are brighter than the others. This proofs that there is a structural transition with temperature. Up to 480 K the system presents six-fold symmetry and all the spots behave in the same way, while if we anneal further, three-fold symmetry appears. An important structural change occurs in the system between 480 K and 610 K.

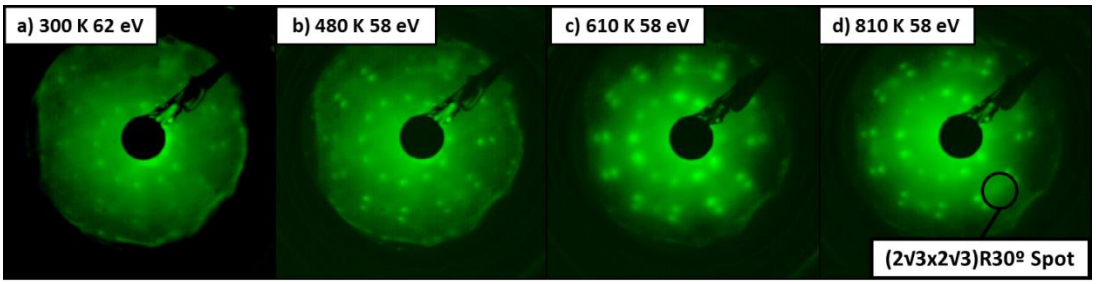

Figure 6.2.12 – *The LEED patterns of C_{60}/Pt(111) at different annealing temperatures.* *a) represents the sample annealed to 300 K: here the two mirror domains of the (√13x√13)R13.9º superstructure are measured at 62 eV. b) is the LEED pattern of the sample annealed to 480 K, at 58 eV: faint spots of the (2√3x2√3)R30º arise and coexist with the (√13x√13)R13.9º domains . c) 58 eV LEED pattern of the (2√3x2√3)R30º and (√13x√13)R13.9º domains annealed to 610 K. d) At 810 K, the intensity of the(2√3x2√3)R30º spots increases (58 eV).*

This was confirmed by LEED-IV measurements. Figure 6.2.13-a shows a model of the LEED pattern obtained with the three superstructures at high temperature. The white dots represent the positive and negative domains of (√13x√13)R13.9º, while the lilac dots show the (2√3x2√3)R30º superstructure of C_{60}/Pt(111). The reference are the first order Pt spots, white dots surrounded by a circle.

Figure 6.2.13-c shows the changes with energy for different temperatures of the intensity of non-equivalent spots of the inner circle of the (√13x√13)R13.9º domain, for two different sets of spots defined in Figure 6.2.13-b. 'A' is the average of two spots with reciprocal space coordinates (3/13, 4/13) and (4/13, 3/13), while 'B' is the average of four spots, namely (-1/13, 3/13), (1/13, 4/13), (4/13, 1/13) and (3/13,-1/13), as defined in Figure 6.2.13-b.

We measure IV curves with a home-made program which records the intensity; the background has been subtracted manually with the same program. Spots A and spots B show the same behaviour with respect to each other at RT at 480 K, while the curves of both spots slightly change from RT to 480 K. However, the differences in the shape of the intensity curves is very small and the position of the peaks is still the same, (A(RT)=B(RT)≈A(480K)=B(480K)). On the other hand, at 610 K the LEED-IVs change radically, both within the same set of spots and when comparing the two: within the same temperature range, a difference in the intensity curves of spots A and spots B relative to each other also arises, which indicates a structural change. This behaviour remains constant up to 810 K (A(610K)=A(810K)≠B(610K)=B(810K)).

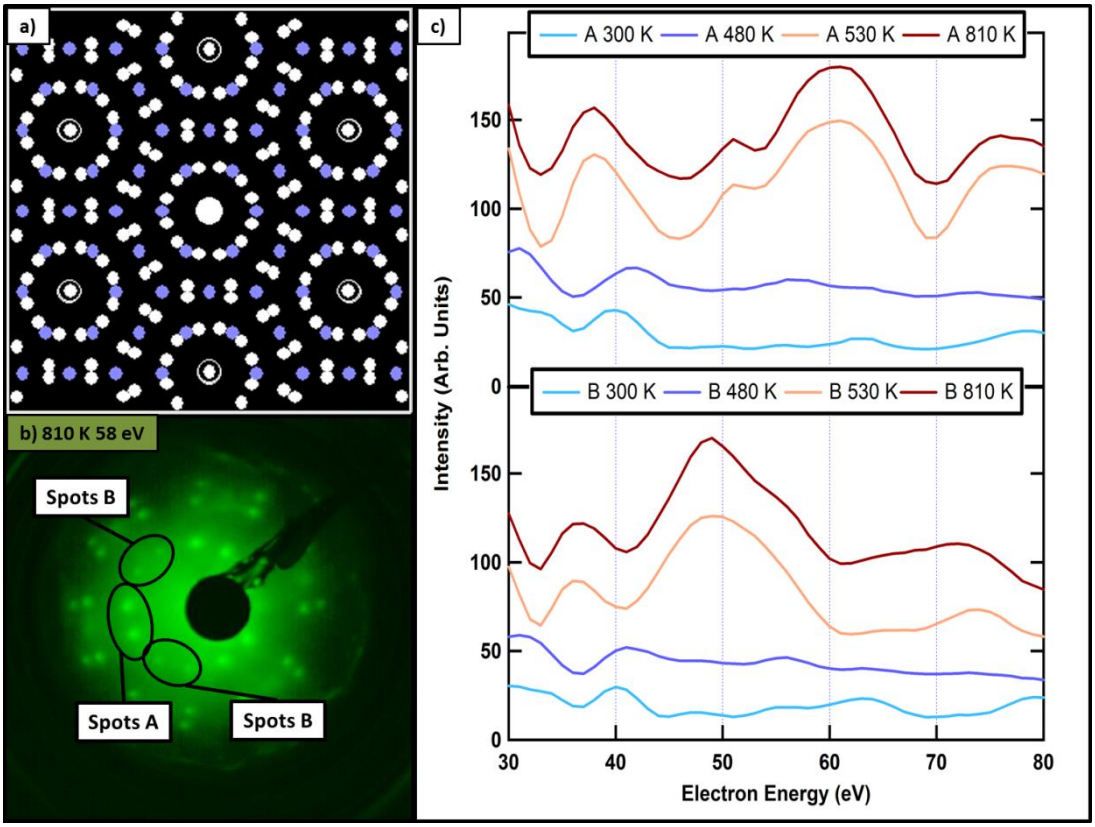

Figure 6.2.13 – *Model and LEED-IV of C_{60}/Pt(111) from 30 to 80 eV.* *a) This is a model of the LEED pattern of the superstructures that C_{60} forms on Pt(111): the white dots represent the two domains of the (√13x√13)R13.9º phase, while the lilac dots show the (2√3x2√3)R30º phase; the white dots surrounded by a ring represent the first order Pt(111) spots. b) This is an image of the LEED pattern of C_{60}/Pt(111) annealed at 610 K at an electron energy of 58 eV; we are defining here two sets non-equivalent spots (A) and (B) whose intensity is measured as a function of energy in (c). c) LEED-IV measurements of non-equivalent spots (spots A in the upper panel and spots B in the lower panel) at different temperatures from 30 to 80 eV*

Shi and his colleagues[124] also performed LEED-IV measurements and calculations on the same system to shed some light on the vacancy formation. They recorded the curves by keeping the sample at 83 K, which gives better results than RT since at higher temperature there is strong suppression of the signal due to Debye-Waller. Therefore they are able to analyse a total energy range of 4860 eV for the (√13x√13)R13.9º and 3080 eV for the (2√3x2√3)R30º superstructure.

The IV-curves in Shi's word did not consider electron energies lower than 150 eV, and quoting from the paper: "Lower energy (<150 eV) are not used in the intensity analysis because they are less sensitive to the C_{60}/metal interface structure, which is buried about 0.7 nm below the surface". Calculations from the results on our system confirmed that the IV curves for the system with and without vacancy in this range are very hard to distinguish, as the structures of the two systems are very similar. Therefore the change in the shape of the LEED-IV curves must be due to something else. According to the STM results, thermal activation causes all the molecules to rotate to sit on a hexagon, as bright and dim molecules start to appear. This effect has the result of changing the symmetry of the system to threefold. Hence three sets of spots behave differently than the other three, and this leads to the observation of different IV curves upon annealing.

6.2.3 XPS

To shed some light on the on-going electronic processes and in particular on the existence of B molecules, we recorded XPS. The experiment was performed at the SuperESCA beamline, in the ELETTRA synchrotron (Trieste, Italy). First, we recorded a Temperature Programmed (TP) XPS of the C1s peak, from 300 to 1300 K, then the high resolution C1s and $Pt4f_{7/2}$ XPS at four key temperatures.

6.2.3.1 TEMPERATURE PROGRAMMED XPS

The TP-XPS consists of hundreds of fast XPS scans obtained as increasing the temperature of the sample, at a rate of 1 K/s. The energy resolution of the beamline $E/\Delta E$ is about 10^4 therefore also the slightest changes in the electronic configuration of the analysed system are recorded. The temperature of the sample was monitored by a Chromel-Alumel thermocouple spot-welded to the back of the sample. Figure 6.2.14 represents the TP-XPS of the C1s peak: the colour scale (blue = low; red = high) reveals the intensity of the peak in terms of binding energy (x-axis) and temperature (y-axis). An attentive reader can notice a loss of the signal upon annealing from room temperature to 1000 K, caused by photoelectron diffraction effects and by the variation of the atomic density.[55] Figure 6.2.14 also relates each temperature of the photoemission with the stage of the molecule at that same temperature, to facilitate the visualisation of the stage of the molecules. However, the XPS spectra have been recorded ex-situ with respect to the STM, so the inaccuracy in measuring the temperature between the two chambers causes an error which was estimated to be about 40 K.

Upon thermal activation, the first striking feature of the TP-XPS is a sudden core-level shift in binding energy, occurring at about 450 K. The main peak moves 0.16 eV towards lower binding energy, from 284.05 eV to 283.89 eV. The binding energy of the system stabilises up to about 650 K, where the main peak shifts 0.10 eV towards higher binding energy, reaching 283.99 eV. As the temperature is increased, the peak's intensity falls (due to the photoelectron diffraction effects) but remains constant in binding energy up to 1000 K. At this point, the intensity of the peak increases and the binding energy shifts by 0.07 eV, reaching its final stage at 284.06 eV, very close to the initial value.

By combining the spectroscopic and the microscopic information, we can relate (within error) the first binding energy shift at 450 K to the rise of dim and bright molecules on the surface. The x-rays of the XPS shine on the whole sample, hence the information obtained with this technique is an averages of the whole surface while the STM is a localised technique. The binding energy shift indicates an electronic alteration in the molecules which we interpret as related to a charge transfer from the Pt to the fullerenes.

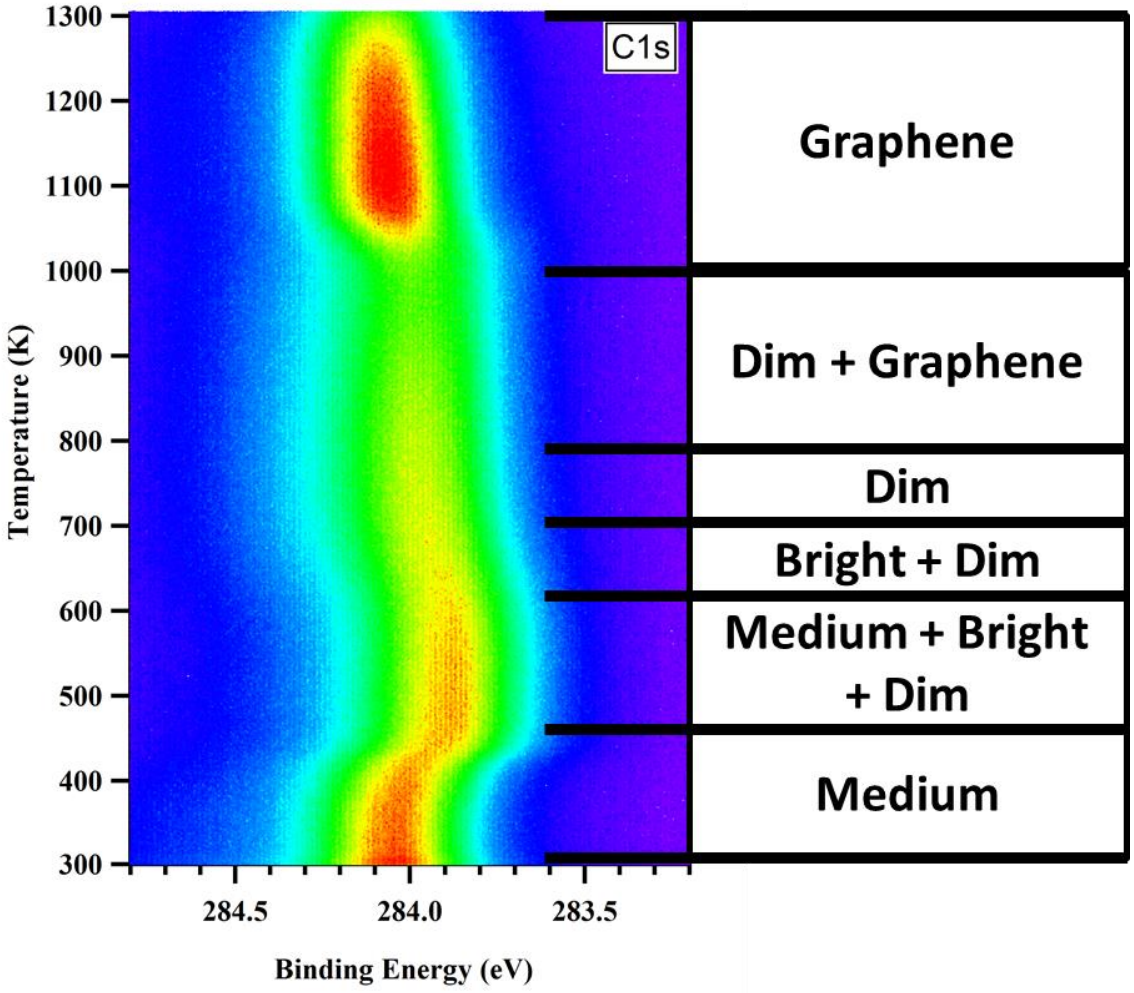

Figure 6.2.14 – ***Temperature Programmed XPS of the C1s peak of C_{60}/Pt(111) annealed at a rate of 1 K/s.*** *The intensity of the C1s peak is plotted in a colour scale (blue is low and red is high intensity) in terms of annealing temperature on the y-axis and binding energy on the x-axis. The insets on the right represent each stage observed with the STM for each temperature.*

The second binding energy shift (0.1 eV towards higher BE) occurs at 650 K, when almost all of the molecules turned from bright to dim. So, the D fullerenes 'give back' the extra charge to the metal and settle in a stable configuration, covalently bonded to the surface. The dim molecules are sitting on a Pt vacancy, which therefore must form during one of these charge transferring processes. The final BE shift (+0.07 eV) occurs at about 1000 K, when the typical sharp peak of graphene arises at 284.06 eV.

6.2.3.2 *C1s AND Pt4f$_{7/2}$ HIGH RESOLUTION XPS*

The TP-XPS enlightens on the core level shifts in binding energy with temperature, and in order to appreciate the chemical alterations occurring to the molecule we measure the high resolution C1s XPS after annealing the sample at different critical temperatures, and cooling it down to room temperature for the scans.

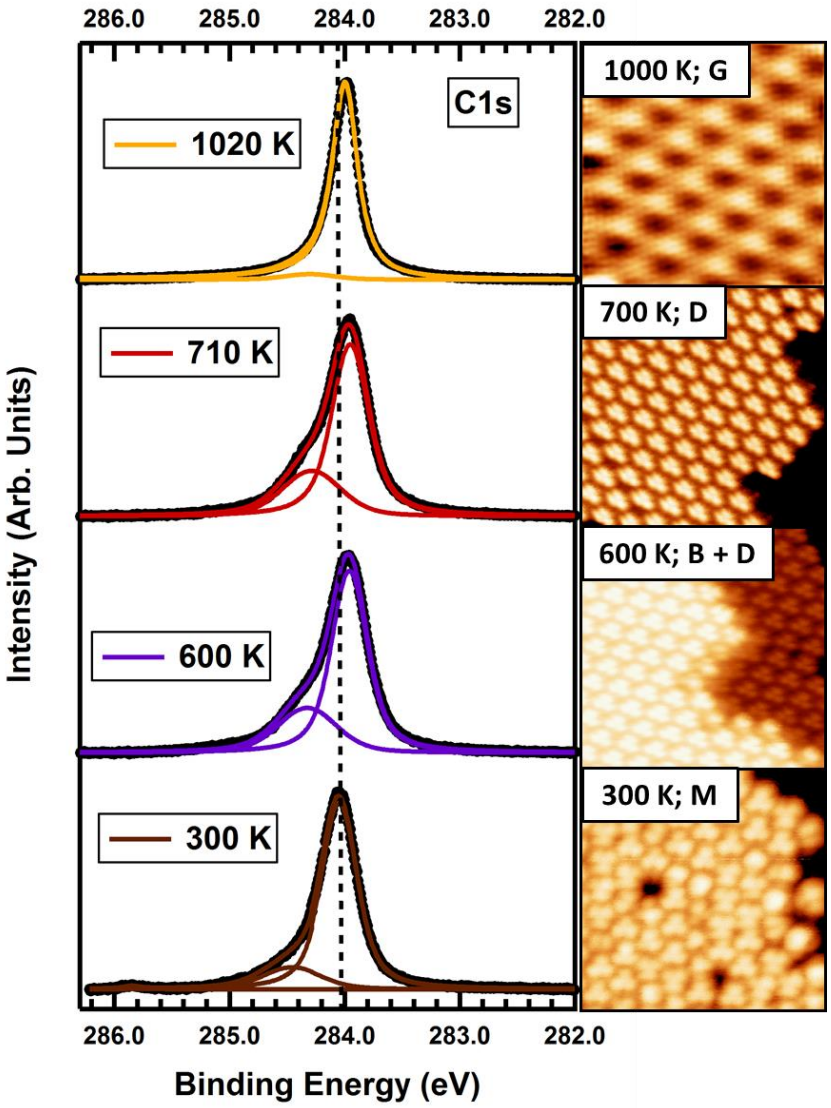

Figure 6.2.15 – ***C1s XPS peak of C_{60}/Pt(111) at various temperatures, compared with the corresponding STM image.*** *All the STM images' size is 10x10 nm^2 and sample voltage between 2.0 and 2.5 V, except the graphene one (7x7 nm^2; V_s = 0.15 V). All the XPS exhibit one main peak and a smaller one at higher binding energy, and the room temperature peak also has a shake-up contribution.*

Figure 6.2.15 represents the high resolution XPS C1s peak of C_{60}/Pt(111) at different temperatures (increasing the temperature bottom to top), and the corresponding STM image. At room temperature, the

main peak corresponding to the sp^2 and sp^3 carbon forming the hexagons and the pentagons of the molecules rises at 284.05 eV, and a second peak at higher binding energy follows at 284.46 eV. The presence of the higher binding energy peak at about 0.4 eV from the main one has been observed on different surfaces such as Cu(111)[168,169], Ag(110)[155], Au(110)[170] and others[152], and most authors related it to an asymmetry of the main peak due to non-equivalent carbon sites or to non-uniform distribution of valence electron charge due to hybridisation/chemisorption effects. A shake-up feature emerges at room temperature at 285.26 eV, 1.81 eV higher than the main peak: this value is very similar to the one found by Swami *et al*.[150] on the same system (1.9 eV). Curiously, the shake-up only exists at room temperature: according to Pedio *et al.*,[152] the satellite washes out because there is an increase in the bonding interaction with the surface, corresponding to a more covalent bond.

Remarkably, the fine lineshape of the RT high resolution C1s core-level peak of C_{60} on Pt(111) is very similar to the one of the same molecule on TiO_2(110).[171] C_{60}/TiO_2 is very weakly interacting, as it has been shown to diffuse and to rotate azimuthally on this surface. However, even in the case of the weakly interacting TiO_2 surface, the XPS still shows a minor peak 0.4 eV higher in binding energy than the main peak, related to the charge redistribution within the molecule due to the presence of the surface.

As discussed above, upon annealing both components shift towards lower binding energy; also, the high energy peak becomes more important. The peaks at 600 K and 710 K are very similar. Figure 6.2.15 also exhibits the corresponding STM image next to the XPS spectra, that is, B and D fullerenes at 600 K and only D fullerenes at 710 K. It is therefore very interesting that the XPS peaks are alike: D molecules are sitting upon a vacancy on the surface and they are covalently bonded with it, therefore the fact that a sample with B molecules is almost identical to a sample with D molecules means that the B molecules are also covalently bonded to the surface.

Table 6.2.1 represents the binding energy and the relative area of each C1s peak at all the annealing temperatures, from M molecules at 300 K, to B and D at 600 K, to only D at 710 K and finally to graphene at 1020 K. We already discussed the shifts in binding energy when showing the real time XPS. At room temperature, the secondary peak P2 represents 15.1% of the total, while the main peak P1 84.9%. Upon annealing, the relative importance of P2 grows to 27.1% with a corresponding decrease of P1 to 72.9%, and these percentages remain almost unchanged at 710 K.

The formation of graphene when annealing to 1020 K causes a drastic decrease in the relative importance of P2 to only 4.4%. The behaviour of P2 upon annealing is crucial to identify its nature: its importance increases when B and D molecules form, as the molecules covalently bond to the surface as the vacancy forms. P2 therefore corresponds to the C atoms interacting covalently with the Pt surface. The different position of atoms in the fullerene cage is therefore to blame for the existence of two components in the C1s peaks, since some atoms are covalently bonded with the surface and some are not.

In their XPS characterisation of graphene on different transition metal surfaces, Preobrajenski and its collaborators[80] found that on some metals the moiré interacts strongly with the surface, and this interaction induces the rise of a secondary component in the C1s XPS spectrum. As for the system discussed here, this component arises at higher binding energy than the main peak, and it is due to graphene atoms covalently bonded with the surface.

Temperature (K)	BE P1 (eV)	BE P2 (eV)	BE shake up (eV)	% A P1	% A P2
300	284.05	284.46	285.86	84.9	15.1
600	283.96	284.32	-	72.9	27.1
710	283.95	284.28	-	72.5	27.5
1020	283.99	284.29	-	95.6	4.4

Table 6.2.1 – *Binding energy (BE) and relative area (% A) of all the C1s peaks of Figure 6.2.15.* *At room temperature, three peaks are present (two main peaks, P1 and P2, and the shake-up), and upon annealing the shake-up peak disappears. The relative area of the peak is indicated as a percentage over the sum of the area of the peaks.*

The C1s peak narrows significantly when graphene forms (when annealing at 1020 K), and its Full Width at Half Maximum (FWHM) decreases from 390 meV at room temperature to 260 meV. This is typical of the formation of a more ordered phase, namely graphene, however the reported FWHM for graphene grown with ethylene on a hot Pt(111) surface is even thinner, being 130 meV;[80] moreover, as opposed to the present case, the peak can usually be fitted with only component. As discussed above, the experimental protocol for growing graphene can greatly affect the quality of the graphene on a metal surface, and the use of large aromatic molecules and low temperatures increases the number of domains and defects, which would therefore increase the width of the peak.[73] Moreover, one particular phase of graphene, namely the α graphene, also known as the (√3x√3)R30º or 2x2 domain, covalently bonds with the surface and this is the reason of the survival of P2 on graphene samples.[106]

The $Pt4f_{7/2}$ XPS peak provides great information on the state of the metal, so we recorded it as the sample was annealed. The XPS of the clean Pt (Figure 6.2.16, bottom spectrum) exhibits two components, a more intense one at 70.97 eV and the other at 70.54 eV: the first one arises from the bulk atoms, while the second one from the surface atoms. The presence of this extra component is very common in transition metals, and the distance between the two is known as the Surface Core Level Shift (SCLS) – which in this case is 0.43 eV. The low binding energy component arises from a reduced coordination of surface atoms with respect to the bulk.[118] Note that at this particular photon energy, the intensity of both is of the same order.

C_{60} adsorption at 300 K (Figure 6.2.16 brown spectrum) has two main effects. First of all, the surface component diminishes: its intensity lowers because of the interaction of the molecules with the metals[55]. Secondly, two new peaks appear at 71.28 eV and 71.89 eV: these peaks are typical of depositing molecules on Pt and they signify an interaction of the fullerenes with the metal.[125,126,172]

The XPS peaks of the C_{60}/Pt sample annealed to 600 and 710 K are very similar, and these spectra also present evidence of the high interaction of the molecules with the metal. The peak at 71.89 eV disappears but the surface peak at 70.57 eV is still less intense than the one of the clean surface and the peak at 71.39 eV is present (it shifted slightly).

When graphene forms at 1100 K, the surface peak recovers the intensity of the clean Pt peak and the extra peak at higher binding energy disappears. This is very typical of a graphene layer which is almost free standing.[55,80]

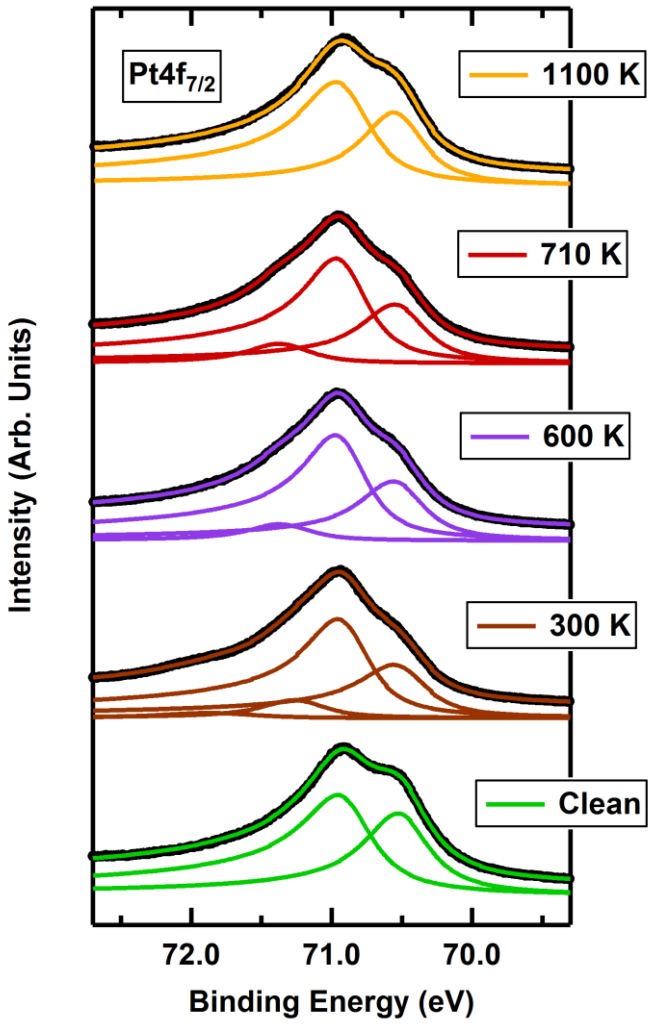

Figure 6.2.16 – *Pt4f$_{7/2}$ XPS peak of C$_{60}$/Pt(111) at various temperatures.* *The bottom (green) peak indicates the clean Pt peak, with the surface component at 70.54 eV and the bulk component at 70.97 eV; the rest of the peaks represent 0.5 ML of C60/Pt(111) annealed to different temperatures and extra components arise at higher binding energy.*

6.2.4 TPD

The transition from a weakly interacting to a chemisorbed state requires an activation energy that is provided by temperature. The existence of a purely physisorbed system is very unlikely, because these systems usually desorbs as temperature is increased. Moreover DFT calculations[173] predict a strong C-Pt bonding even at very low temperature. Therefore, somehow, the C_{60} molecule has to be decoupled from the surface at RT to form this weakly interacting overlayer. A possible candidate for passivating the Pt(111)

surface and allowing the existence of a weakly bound state at room temperature may be the presence of invisible atomic H on the surface from the residual pressure of the chamber. A paper from Swami *et al*.[174] analyses the behaviour of 1 ML of C_{60} on four different modified surfaces. In one of the experiments, they expose the surface to H_2, obtaining 0.4 ML and 0.8 ML. After this modification, they observed that HREELS disorder peaks reported on the unexposed C_{60}/Pt(111) system have a much lower intensity compared with the unexposed case. Their conclusion is that due to the absence of charge transfer between the surface and the C_{60}, the molecules are able to move around and form ordered islands (they did not measure LEED and therefore were not able to determine which superstructures were obtained).

Christmann *et al*.[175] exposed a clean Pt(111) sample to H_2 at 150 K and measured Temperature Programmed Desorption (TPD). From their experiment it is clear that H_2 sticks to the surface, and this adsorbed gas could passivate the Pt surface atoms and forbids the C_{60} to interact with the surface. Let's not forget that in a UHV chamber the main residual gas is always H_2. According to their experiment, all the residual H desorbs from the surface at 430 K.

These facts have motivated us to repeat the experiment of Christmann *et al*., in order to see whether or not the deposition of C_{60} was affected by the hydrogen on the surface. In the TPD laboratory of the Graz Technical University, with the help of Prof. Robert Schennach, we expose a clean Pt(111) sample held at 100 K to 3 L of H_2, and then deposited 1 ML of C_{60} and measure TPD from 100 - 870 K (Figure 6.2.17). We compare this with the TPD of 1 ML on clean Pt(111).

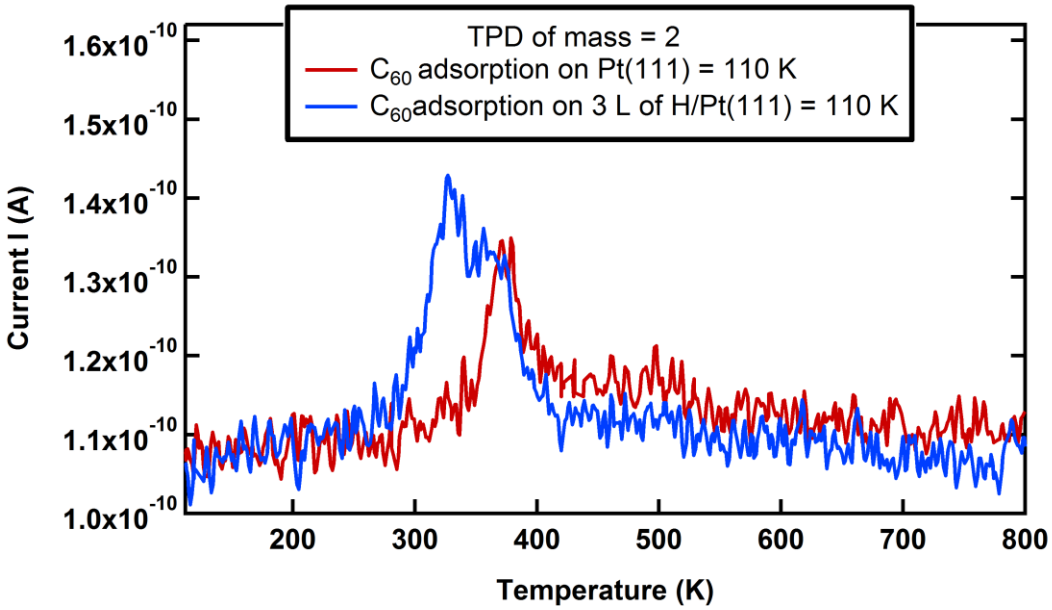

Figure 6.2.17 – ***Mass = 2 TPD peaks of C_{60}/clean Pt(111) (red) and of C_{60}/H_2/Pt(111) (blue).*** *The clean sample shows presence of H on the surface, however less than when depositing 3 L of H.*

TPD of mass = 1 has also been recorded, however no peak has been observed because the H atoms, which dissociate on the surface, recombine and form H_2 molecules. First of all, we notice from Figure 6.2.17 that all the hydrogen on the surface desorbs after annealing at about 430 (± 30 estimated) K, even in the case in

which the sample was exposed just to the residual gas of the UHV chamber (for 1 hour, adding up to 0.1 L). So, even the clean sample possesses some atomic H on the surface which is invisible with both XPS and STM. Christmann *et al*.[175] interpreted this as the recombination of H_2 molecules from H atoms with an empty (high temperature peak) or occupied (low temperature peak) neighbouring adsorption site.

As we can see from Figure 6.2.17, at about 430 ± 30 K the sample is free from hydrogen. This temperature is (within error) comparable with the initial temperature of formation of B and D molecules, and of the BE shift observed with the real time XPS. This suggests that a possible candidate for the phase transition from a weakly bound to a chemisorbed state may be the existence of invisible H on the surface, between the Pt and the C_{60}: at RT, the H passivates the metal, preventing the interaction with the molecules, but when the H desorbs, the molecules touch the Pt and this is what causes the transition between weak interaction and chemisorption. However, the deposition of molecules on the hot sample and their STM characterisation can help us to interpret the TPD results: if the hypothesis is correct, no M molecules should be observed when depositing the fullerenes at temperature higher than the H desorption temperature. We presented the results of the deposition on the hot surface in Section 6.2.2 (Figure 6.2.11). When depositing the molecules by keeping the surface at 480 K, a few M molecules were still observed. However, as their number was very small, it is likely that the presence of invisible atomic H is the cause of the phase transition between a weakly adsorbed and a chemisorbed state, and that the presence of a few remnants of M molecules is due to an error in comparing the temperature between the chambers where the STM images were recorded and the one where TPD was acquired.

Further experiments showed that saturation on the Pt surface (*i.e.* a 1x1 superstructure) was achieved with 50 L of H_2 exposure (not shown here). However, as little as one H atom between a C_{60} molecule and the Pt underneath can prevent their interaction, hence in principle much less H atoms (about 0.15 ML) are required to passivate the surface.

6.3 DISCUSSION

The STM and XPS experiments reveal that the molecule converts from a weakly interacting to a chemisorbed state upon thermal activation. We propose that the desorption of an intermediate submonolayer of invisible hydrogen on the surface could be responsible for this change. H cannot be detected with the STM nor with the XPS, hence this element may have been partially passivating the surface and it therefore could have been the reason for the weak interaction. TPD results indeed showed that H was present on the surface even in a clean environment, and that it desorbed completely at 430 K.

The STM reveals that each molecule passes from a stable weakly interacting state (M) to a chemisorbed excited state (B), to a chemisorbed stable phase (D). In this process, a vacancy forms on the Pt surface. Moreover, the network of D molecules is shifted by 0.14 nm with respect to the one of D molecules (which coincides with the network of M molecules). Our XPS results reveal the presence of a charge transfer from the surface to the molecule as a shift of 0.16 eV towards lower binding energy at 450 K, that is, when the B and D molecules start to appear, *i.e.* just after the H desorption. This goes along with an increase in the interaction with the metal surface, observed on both the high resolution C1s and Pt4f peaks.

A possible explanation for the formation of a vacancy in terms of all the experimental observations and for the appearance of the B molecule is related with the existence of an adatom-vacancy pair first proposed by Huang[123] and described in Figure 6.1.5. Our interpretation of the experimental evidence combined with other authors' work for the mechanism of vacancy formation is described in Figure 6.3.1, which is a model of the atomistic configuration for the M, B and D stage.

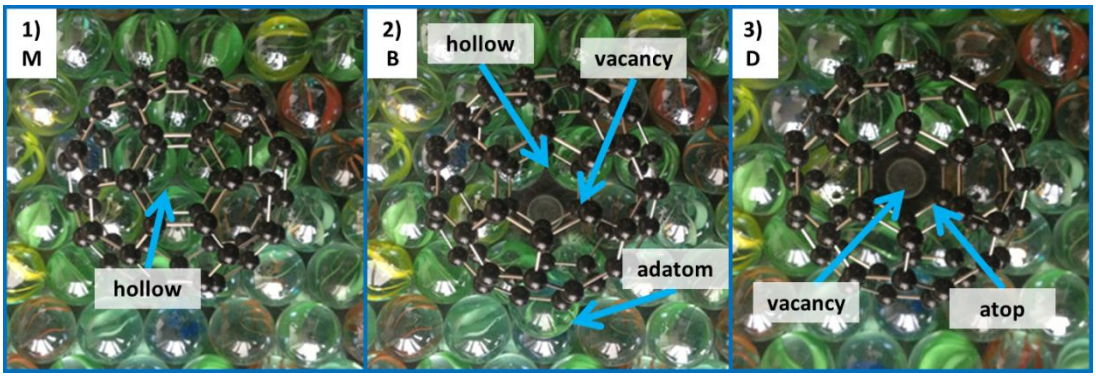

Figure 6.3.1 – *Model of the three steps of the mechanism of vacancy formation of C_{60}/Pt(111).* *a) The weakly interacting M molecule is sitting on a hollow configuration, and a H atom is passivating the surface preventing a high interaction. b) Upon thermal activation, the H desorbs and an adatom-vacancy is formed next to the hollow configuration and due to charge transfer effect the molecule is B. c) With further annealing, the molecule 'slides' to the more favourable configuration on top of the vacancy and the Pt adatom migrates to the steps.*

Figure 6.3.1-a reveals the model of a M fullerene sitting on a hollow position, with a H atom passivating the surface and preventing a strong interaction. In this example, the M fullerene is sitting on a hexagon, but it is allowed to sit in five different configurations as the STM shows. According to the theoretical works,[123,124] the most energetically favourable sites for the molecule on the unreconstructed surface to sit on are the atop, the bridge and the fcc-hollow configuration. On the other hand, the most stable arrangement on reconstructed surface (D molecule) in the presence of a vacancy is on the atop site. The STM shows that the D molecules cannot be sitting on the same configuration as the M and the B molecule, as the networks are shifted by 0.14 nm (Figure 6.2.6). Hence, if the D molecules are sitting on the atop site, the M and D molecules must be sitting on either the bridge or the fcc-hollow sites. We cannot determine which configuration is the real one; according to Huang, the fcc-hollow configuration is more favourable when no vacancy is present, hence for the purpose of this description we assume that the C_{60} is sitting on the fcc-hollow site on the unreconstructed surface.

Upon annealing, the interaction between the Pt and the fullerene rises due to the desorption of the H, and charge is transferred to the molecule as the vacancy forms. The B molecule (Figure 6.3.1-b) is an intermediate phase between M and D. According to our model, the ejected Pt adatom remains next to the vacancy, and it also bounds to the C_{60}. Hence this could be the reason why the C_{60} cannot accommodate quickly on top of the vacancy as the vacancy is formed: this adatom is sterically blocking the fullerene to slide on the more favourable configuration on top of the vacancy. The adatom covalent bond is reflected in the high-resolution XPS as an increase in the C-Pt interaction. The rise in apparent height is likely to be due

to an electron redistribution at this energy due to the charge transferred to the molecule due to the adatom and to the desorption of H.

Upon further thermal activation, the adatom migrates to the Pt steps and the fullerene is free to shift on top of the vacancy, maximising the interaction with the surface and decreasing its apparent height to the D state (Figure 6.3.1-c). The shift from hollow to atop configuration justifies the network mismatch of the B and D molecules. In the model, the B and the D molecules are both sitting on a hexagon and are facing the same direction, as observed with the STM. Their orientation may be the same as the M molecules or not. In fact, in Figure 6.3.1 the M molecule is rotated 60º with respect to the B and D ones.

The D molecules maintain the stable configuration on top of a vacancy upon annealing up to about 1000 K: at this point, the molecules break and graphene forms. This transformation is also observed by the XPS, which shows a narrowing of the C1s peak and a drastic decrease of the C-Pt interaction, typical of graphene formation.

6.4 Conclusions

Understanding the mechanism of formation of the vacancy in the C_{60}/Pt(111) system is a complex problem to tackle. According to the experiments we performed, we found that the molecules undergo three phase transitions upon annealing. The as-deposited so-called medium-height M fullerenes are weakly bound to the Pt, as they are able to diffuse to form ordered structures. With no further annealing, all the molecules have the same apparent height (6.6 ± 0.3 Å) and orient in five ways. Upon annealing, the M molecules transform into bright molecules B, as their apparent height rises to 7.5 ± 0.3 Å. The weak interaction of the M molecule is possibly due to the presence of H on the surface, passivating the metal. The first phase transition from M to B occurs as the H desorbs and a vacancy-adatom pair forms very close to the fullerene: due to the presence of the ejected Pt adatom covalently bonded with the fullerene, the molecule cannot accommodate on the more favourable site on top of the vacancy. At this stage the interaction between the molecule and the Pt increases, and charge is transferred to the molecule.

Further thermal activation allows the Pt adatom to migrate to the Pt steps, and the fullerene is free to shift to sit on top of the vacancy. Hence its apparent height decreases to 4.8 ± 0.5 Å (dim fullerene D), and the molecule is now chemisorbed on the surface as it covalently bonds with the neighbouring metal atoms. This state is stable up to the formation of graphene at about 1000 K.

Summary and conclusions

This thesis aims to unravel the catalytic role of different transition metal surfaces on cyclo- and de-hydrogenation reactions of Polycyclic Aromatic Hydrocarbons (PAH) and to understand the possible effects of these molecules on the surface of the substrate. We selected three molecules for our research, namely DiPy[5]DBH, $C_{57}H_{33}N_3$ and C_{60}. The first two molecules utterly differ from the last one, as they are hetero-aromatics which can modify their structure via (cyclo)dehydrogenation, whereas the fullerene lacks of H atoms and it is much more stable than the other two. The two hetero-aromatics can undergo both cyclodehydrogenation and dehydrogenation: these two mechanisms differ as the first one involves the cleavage of one or more C-H bonds and the subsequent formation of an aromatic ring, while in the second one involves the simple cleavage of one or more C-H bonds with no aromatic ring creation. These precursors have been deposited on four surfaces of three transition metals, namely Pt(111), Cu(110), Cu(111) and Au(111). The reactivity of each metal varies due to the occupation of their d-band which allows different interaction with the molecules; moreover, different faces of the same crystal (as for the case of Cu(110) and Cu(111)) can also have unalike effect on a particular molecule as an effect of the geometrical distribution of the atoms. The introduction of dopants in the precursor is an elegant way of creating doped nanostructures. Many of the N-doped nanostructures described in this thesis have never been obtained before.

A more specific summary of the results of each chapter of this thesis follows.

Tailored formation of N-doped nanoarchitectures by diffusion-controlled on-surface (cyclo)dehydrogenation of heteroaromatics. The reactivity of transition metals depends on their electronic and geometric structure. By depositing DiPy[5]DBH and $C_{57}H_{33}N_3$ on Pt(111) and Au(111), we reveal that surface diffusion of the PAH is perhaps the most important process for the formation of different structures. On highly reactive surfaces such as Pt(111), diffusion of the as-deposited precursor is prevented, due to a strong surface-adsorbate interaction. Hence cyclodehydrogenation (intramolecular structural modification) is the main mechanism undergone by the precursor upon thermal activation. In this sense, DiPy[5]DBH and $C_{57}H_{33}N_3$ transform respectively into N-doped nanographene and into a triaza-fullerene. When the same molecules are deposited on a weakly reactive substrate such as Au(111), they diffuse as the substrate-adsorbate interaction is not strong enough to stick the molecules where they land. Hence, as they cyclo- and de-hydrogenate upon annealing (intra- and intermolecular modification), the molecules 'see' and link with other precursors forming oligo- or polymeric chains, whose building blocks are intact of partially cyclodehydrogenated molecules.

DiPy[5]DBH on Pt(111). DiPy[5]DBH does not diffuse when deposited on Pt(111), hence at low coverage no intermolecular interaction is expected: indeed, only intramolecular modification occurs upon annealing. The precursor undergoes three main structural transformations, which have been unveiled by combining experimental STM images with theoretical simulations and DFT calculations. The first transformation occurs upon thermal activation at 650 K. It involves cyclodehydrogenation of the internal C-H bonds: due to steric factors, the energy needed to cleave these H atoms is substantially lower than the energy needed to cleave the H atoms at the edges of the molecule, hence N-doped nanographene electrostatically bound to the system is formed. The second transformation occurs when applying about 100 K more (770 K) to the sample: the C-H bonds at the edges have now enough energy to break, leaving dangling C bonds which bind

covalently with the Pt atom, bending the molecule and forming N-doped nanodomes. The different activation energy required to remove the internal and the external C-H bonds allows hierarchical growth of two structures, which can be discerned easily by applying a different thermal activation. The third structural transformation undergone by the molecule is the formation of N-doped graphene when annealing at about 830 K.

DiPy[5]DBH on coinage metals. When DiPy[5]DBH is deposited on coinage metals (Cu(110), Cu(111) and Au(111)), it diffuses as a consequence of the weak surface-adsorbate interaction. The pristine molecule undergoes different phase transitions which have been identified by combining STM with synchrotron-based spectroscopic techniques as XPS and NEXAFS. The main effect of diffusion is to allow intermolecular interaction: as the internal and external C-H bonds cleave upon thermal activation, the molecules can meet and link with each other forming oligomers or polymers. On Cu(111) and Au(111) further annealing triggers the formation of 'bright' and 'dim' chains, whose structure recalls the one of graphene nanoribbons. An explanation for the apparent height gap between the chains is to be found in the probable formation of a vacancy network underneath the polyaromatic structures, so that the PAH induces an atomic etching process on the metal surfaces. Further annealing prompts the graphene growth on Cu(110) and Cu(111). On Au(111) the graphene formation temperature is not achieved to avoid deteriorating the sample. The combination of STM with XPS and NEXAFS allows a complete description of the C and N environments from the electronic point of view. For instance, the NEXAFS spectra show that the molecule flattens upon oligo- and polymerisation, hence the building blocks of the polymers are N-doped nanographene flakes. Moreover the XPS shows that at room temperature the molecules behave differently depending on the surface: on copper (especially on the (110) face) they behave as donors, while on gold as mild acceptors. As the molecule undergoes similar structural phases on the three coinage metal surfaces, we are able to combine the result into a single phase diagram which informs of the temperature of formation of a particular structure on a particular metal. The coinage metal which catalyses polymerisation and the other structural changes at the lowest temperature is the best catalyser, and the phase diagram is a rapid method to establish Cu(110) as the best catalyser, followed by Cu(111) and then by Au(111). Even though for the case of the two faces of copper the metal is the same (and therefore the occupation of its d-band is constant), Cu(110) is a better catalyser because its rows are catalytically active sites.

$C_{57}H_{33}N_3$: On-surface cyclodehydrogenation steps to the formation of triaza-fullerenes. The crushed-triaza-fullerene precursor $C_{57}H_{33}N_3$ is known to transform into triaza-fullerene upon surface-assisted cyclodehydrogenation on highly reactive surfaces such as Pt(111). This transformation can be divided into four main steps: (i) intact molecule; (ii) open-cage fullerene; (iii) triaza-fullerene; (iv) N-doped graphene formation. These stages are achieved by different thermal activation steps, and are explored by STM and high-resolution and temperature programmed XPS. Upon deposition, the intact molecule does not diffuse and lays in different configurations, and with a small thermal activation it flattens and maximises the number of rings in contact with the surface. Annealing above 550 K triggers a partial cyclodehydrogenation of the precursor, leading to open-cage fullerenes. The interior C-H bonds are sterically favoured to break first, and different shapes are observed on the surface with the STM: different interior C-H bonds are cleaved as their energy is comparable. As the central part of the open-cage fullerenes is much higher in height than the edges, we conclude that the molecule bends upwards as the fullerene forms. Thermal activation to more than 700 K completes the cyclodehydrogenation progression leading to the formation of triaza-fullerenes, whose shape is spherical as opposed to the triangular shape of the pristine molecule. The

XPS shows an increase in the interaction between the C and the Pt between 550 and 950 K indicating an active role of the metal surface in the cyclodehydrogenation. Above 950 K, N-doped graphene forms. The quality of N-doped graphene is improved by depositing the precursor on the hot sample, as determined by XPS.

The mechanism of the atomic vacancy formation on the C_{60}/Pt(111) system. C_{60} differs from the other two precursors described in this thesis as it lacks of H atoms, and it is very stable due to its symmetric shape and to the strength of the C-C double and single bonds. This organic molecule is well known to induce a single- or a multi-atom vacancy on transition metal surfaces. For the present case, C_{60} forces a one-atom vacancy reconstruction on the metal surface below each molecule upon thermal activation. The energy needed for the surface to reconstruct is noticeably lower in the presence of the fullerene, and according to a theoretical work by Huang mentioned in Chapter 6, the vacancy is triggered by a previous creation of an adatom-vacancy pair on the substrate. STM images of C_{60}/Pt(111) at various temperatures reveal that each molecule undergoes three phases before disrupting to form graphene: (i) medium height molecule (physisorbed); (ii) bright molecule (chemisorbed); dim molecule (chemisorbed). Upon deposition, with no further annealing, the molecule physisorbs on the surface and forms ordered domains, and each molecule is about 6.6 ± 0.3 Å high (medium height molecule). Thermal activation at about 500 K instigates the formation of an adatom-vacancy pair on the surface, which results in an increase in apparent height of the molecule to about 7.5 ± 0.3 Å (bright molecules). This process results in a charge transfer from the substrate to the molecule and a consequent rise in the surface-adsorbate interaction as observed by high-resolution and temperature programmed XPS. With further energy injection, the bright molecules then shifts to sit on top of the vacancy, thereby its apparent height decreases to 4.8 ± 0.5 Å (dim molecules). The percentage of dim molecules increases linearly with temperature, and at about 700 K all molecules are dim, as all the fullerenes are sitting on top of a vacancy. The fullerenes are then stable up to the disruption of C-C bonds when graphene forms, at about 1000 K.

Conclusiones

El objetivo de esta tesis es entender el papel catalítico de la superficie de diversos metales de transición en el caso de reacciones de ciclodeshidrogenación y deshidrogenación de hidrocarburos policíclicos aromáticos (PAH) y llegar a determinar los posibles efectos de estas moléculas sobre dichas superficies. Para esta investigación, hemos seleccionado tres precursores: DiPy[5]DBH, $C_{57}H_{33}N_3$ and C_{60}. Los dos primeros se diferencian del segundo ya que son hetero-aromáticos que pueden (ciclo)deshidrogenar y cambiar su estructura, mientras que el fullereno no posee átomos de H siendo además mucho más estable que los otros dos. Hay que tener en cuenta que las reacciones de ciclodeshidrogenación y deshidrogenación, que pueden ocurrir en el caso de los dos precursores hetero-aromáticos, siguen mecanismos diferentes. En el primer caso, ciclodeshidrogenación, la formación de un anillo aromático sigue a la ruptura de uno o más enlaces C-H mientras que el segundo caso, deshidrogenación, es la simple ruptura de uno o más enlaces C-H. Los precursores moleculares se han depositado sobre cuatro superficies de tres metales de transición, Pt(111), Cu(110), Cu(111) y Au(111). La reactividad de estos metales depende de la ocupación de la banda d, que permite distintas interacciones con las moléculas; asimismo, la reactividad de distintas caras del mismo metal (como el caso de Cu(110) y Cu(111)) puede ser diferente, debido al efecto que una particular distribución geométrica de los átomos puede tener en la molécula. Por otro lado, la introducción de dopantes en el precursor es una manera elegante de crear nanoestructuras dopadas. Así, algunas de las estructuras dopadas con N aquí descritas no se encuentran en la literatura científica y se han observado por primera vez en esta tesis.

A continuación se expone un resumen más específico de cada capítulo de esta tesis.

Formación de nano-arquitecturas dopadas con N a través de (ciclo)deshidrogenación de hetero-aromáticos controlada por la difusión sobre superficies. La reactividad de los metales de transición depende de sus propiedades electrónicas y estructurales. Cuando depositamos DiPy[5]DBH o $C_{57}H_{33}N_3$ sobre los metales, vemos que el grado de difusión del PAH sobre la superficie es el parámetro más importante para determinar la formación de distintas estructuras. Así, la falta de difusión en un sustrato reactivo como el Pt(111) no va a permitir la interacción entre moléculas, y por tanto la ciclodeshidrogenación (transformación estructural intramolecular) va a ser el principal mecanismo de modificación de la molécula bajo activación térmica. De esta manera, DiPy[5]DBH y $C_{57}H_{33}N_3$ evolucionan respectivamente en nano-grafeno dopado con N y en triaza-fullerenos. Cuando depositamos las mismas moléculas en un sustrato poco reactivo como el Au(111), las moléculas difunden ya que la baja interacción entre el sustrato y el adsorbato lo permite. Proporcionando energía térmica al sistema, los precursores ciclodeshidrogenan y deshidrogenan y las moléculas activadas se enlazan con otros precursores formando cadenas oligo- o poliméricas.

DiPy[5]DBH sobre Pt(111). DiPy[5]DBH no difunde sobre Pt(111), y esto causa que no haya interacción intermolecular a bajo recubrimiento. Por eso, tras calentar, solo se observa una modificación intramolecular. La combinación de imágenes experimentales de STM con simulaciones y cálculos DFT demuestra que se pueden lograr tres estructuras a partir de este sustrato. La primera transformación resulta en nano-grafeno dopado con N, y se obtiene ciclodeshidrogenando la molécula tras calentar a 650 K. Debido a factores estéricos, la energía necesaria para romper los enlaces C-H interiores es mucho menor respecto a la energía necesaria para romper los mismos enlaces del borde de las moléculas. Por ello, los enlaces C-H interiores se

rompen a más baja temperatura que los exteriores, y se forman nuevos anillos aromáticos que dan lugar al nano-grafeno. La segunda modificación se obtiene con una activación térmica a 770 K, y consiste en la deshidrogenación de los átomos en los bordes de las moléculas. Este proceso causa la formación de nuevos enlaces entre C y Pt y origina la curvatura del precursor que resulta en la formación de nano-cúpulas dopadas con N. La distinta energía de activación necesaria para romper los enlaces C-H interiores y exteriores nos permite obtener jerárquicamente dos estructuras distintas simplemente cambiando la temperatura de calentamiento del sustrato. Calentando a unos 830 K podemos crear la tercera estructura, es decir, grafeno dopado con N.

DiPy[5]DBH sobre Cu(110), Cu(111) y Au(111). DiPy[5]DBH difunde sobre cobre y oro debido a la débil interacción entre sustrato y adsorbato. Las transformaciones estructurales de la molécula se determinaron a través de la combinación de imágenes de STM con técnicas espectroscópicas usando radiación sincrotrón, como XPS y NEXAFS. El efecto principal de la difusión es permitir la interacción intermolecular. Así, mientras los enlaces C-H interiores y exteriores se rompen debido a activación térmica, las moléculas se encuentran y se unen formando oligómeros y polímeros. Subiendo la temperatura, se logra que sobre Cu(111) y Au(111) se formen cadenas con distinta altura aparente, cuya estructura recuerda la de los nanoribbons de grafeno. La diferencia de altura es debida a la posible formación de una red de vacantes debajo de la estructura poliaromática, inducida por el mismo PAH. Otro aumento de la temperatura en el sistema, aporta la activación térmica para crear grafeno sobre Cu(110) y Cu(111). La temperatura de formación de grafeno sobre Au(111) no se ha podido alcanzar, para evitar el deterioro del sustrato. La combinación de STM con XPS y NEXAFS nos permite obtener una descripción completa del entorno de los carbonos y nitrógenos desde un punto de vista electrónico. Por ejemplo, los espectros de NEXAFS demuestran que las moléculas se aplanan cuando forman oligómeros y polímeros, comprobando así que están formados por la unión de nano-grafenos. Combinando los cambios estructurales del precursor sobre las tres superficies estudiadas, podemos obtener un diagrama de fase que nos facilita la temperatura de formación de cada estructura. Según este diagrama de fase, el mejor catalizador es el Cu(110), ya que la (ciclo)deshidrogenación y la consecuente formación de oligómeros y polímeros ocurre en este substrato a la temperatura más baja, seguido por Cu(111) y siendo Au(111) el peor caso. En el caso de Cu(110) y Cu(111), el metal es el mismo, así que la ocupación de la banda-d también es la misma. Sin embargo, el primero es mejor catalizador ya que su estructura geométrica basada en filas de átomos aumenta los sitios activos de la superficie.

$C_{57}H_{33}N_3$: pasos en la ciclodeshidrogenación catalizada por superficies para formar triaza-fullerenos. En superficies catalíticas como Pt(111), se conoce que $C_{57}H_{33}N_3$ se transforma en triaza-fullereno debido a la ciclodeshidrogenación catalizada por la superficie. Esta metamorfosis ocurre en cuatro pasos principales obtenidos por distinta activación térmica: (i) precursor intacto; (ii) fullereno abierto; (iii) triaza-fullereno; (iv) grafeno dopado con N. Hemos explorado estas cuatro fases por STM y XPS. Las moléculas depositadas no difunden, y se observan en varias configuraciones. A través de una pequeña activación térmica, se aplanan y maximizan el número de anillos en contacto con la superficie. La ciclodeshidrogenación empieza tras calentar a más de 550 K y, dado que no todos los enlaces C-H tienen la misma energía de ruptura, podemos observar fases intermedias de ciclodeshidrogenación parcial, llamadas fullerenos 'open-cage'. Los enlaces interiores son estéricamente favorables a romperse a más baja temperatura, y los fullerenos parcialmente deshidrogenados tienen distintas formas. En el proceso, la parte central de las moléculas tiene una altura aparente más alta que los bordes, por lo que se deduce que los fullerenos 'open-cage' se doblan hacia abajo en el proceso de cierre de las moléculas. Un nuevo incremento de temperatura a más de 700 K aporta la

activación térmica necesaria para completar la ciclodeshidrogenación, y se forman triaza-fullerenos de forma esférica, radicalmente distintos al precursor triangular. Los datos de XPS nos indican una mayor interacción con el sustrato entre 550 y 950 K, y eso demuestra el papel activo que tiene el metal en el proceso de ciclodeshidrogenación. A más de 950 K, las moléculas se rompen y se forman islas de grafeno dopado con N. La calidad de este material mejora notablemente si el precursor se deposita directamente sobre un sustrato caliente.

El mecanismo de formación de la vacante en el sistema de C_{60}/Pt(111). El C_{60} se distingue de los otros precursores utilizados en esta tesis ya que no posee átomos de hidrógeno, y es muy estable debido a su forma simétrica y a la fuerza de los enlaces C-C. Esta molécula orgánica es también conocida por inducir una vacante de uno o más átomos en la superficie de varios metales de transición. Gracias a una activación térmica, en el caso de C_{60}/Pt(111) el fullereno fuerza una reconstrucción en la superficie del metal formada por una vacante monoatómica debajo de cada molécula. La energía necesaria para la reconstrucción de la superficie baja en presencia del fullereno, y según el trabajo de Huang descrito en el capítulo 6, la formación de una vacante es favorecida por la creación de un 'adatom-vacancy pair' en la superficie del sustrato. Las imágenes de STM a varias temperaturas nos indican que cada molécula pasa por tres fases antes de romperse para formar grafeno: (i) altura mediana (fisisorbida); (ii) brillante (quimisorbida); (iii) oscura (quimisorbida). A temperatura ambiente, sin activación térmica, la molécula está fisisorbida en la superficie y forma dominios ordenados, en los que cada molécula tiene una altura de 6.6 ± 0.3 Å. El calentamiento a 500 K induce la formación de algunos 'adatom-vacancy pair' sobre la superficie. El resultado es un aumento de la altura aparente de la molécula a 7.5 ± 0.3 Å (brillante). Este proceso da lugar a una transferencia de carga del sustrato a la molécula y a un consecuente aumento de la interacción entre superficie y adsorbato, como se observa por XPS. Inyectando más energía en el sistema, la molécula brillante se mueve y se coloca encima de la vacante, bajando su altura aparente a 4.8 ± 0.5 Å (oscuras). El porcentaje de moléculas oscuras aumenta linealmente con la temperatura, siendo el 100% de las moléculas oscuras a 700 K. Esto quiere decir que, en ese caso, todos los fullerenos están encima de una vacante. Los fullerenos son estables hasta 1000 K, cuando se forma grafeno.

Bibliography

(1) Feynman, R. There's Plenty of Room at the Bottom. *Eng. Sci.* **1960**, *23*, 22–36.

(2) Binnig, G.; Rohrer, H.; Gerber, C.; Weibel, E. Surface Studies by Scanning Tunneling Microscopy. *Physical Review Letters* **1982**, *49*, 57–61.

(3) Kroto, H. W.; Heath, J. R.; O'Brien, S. C.; Curl, R. F.; Smalley, R. E. C60: Buckminsterfullerene. *Nature* **1985**, *318*, 162–163.

(4) Iijima, S. Helical microtubules of graphitic carbon. *Nature* **1991**, *354*, 56–58.

(5) Iijima, S.; Ichihashi, T. Single-shell carbon nanotubes of 1-nm diameter. *Nature* **1993**, *363*, 603–605.

(6) Novoselov, K. S.; Geim, A. K.; Morozov, S. V; Jiang, D.; Zhang, Y.; Dubonos, S. V; Grigorieva, I. V; Firsov, A. A. Electric field effect in atomically thin carbon films. *Science* **2004**, *306*, 666–9.

(7) Bartels, L. Tailoring molecular layers at metal surfaces. *Nature chemistry* **2010**, *2*, 87–95.

(8) Méndez, J.; López, M. F.; Martín-Gago, J. A. On-surface synthesis of cyclic organic molecules. *Chemical Society reviews* **2011**, *40*, 4578–90.

(9) Bieri, M.; Nguyen, M.; Gro, O.; Cai, J.; Treier, M.; Aït-Mansour, K.; Ruffieux, P.; Pignedoli, C. A.; Passerone, D.; Kastler, M.; Mu, K. Two-Dimensional Polymer Formation on Surfaces : Insight into the Roles of Precursor Mobility and Reactivity. *Journal of the American Chemical Society* **2010**, *132*, 16669–16676.

(10) Lipton-Duffin, J. A.; Ivasenko, O.; Perepichka, D. F.; Rosei, F. Synthesis of polyphenylene molecular wires by surface-confined polymerization. *Small* **2009**, *5*, 592–7.

(11) Kanuru, V. K.; Kyriakou, G.; Beaumont, S. K.; Papageorgiou, A. C.; Watson, D. J.; Lambert, R. M. Sonogashira coupling on an extended gold surface in vacuo: reaction of phenylacetylene with iodobenzene on Au(111). *Journal of the American Chemical Society* **2010**, *132*, 8081–6.

(12) Lafferentz, L.; Ample, F.; Yu, H.; Hecht, S.; Joachim, C.; Grill, L. Conductance of a Single Conjugated Polymer as a Continuous Function of Its Length. *Science* **2009**, *323*, 1193–1198.

(13) Grill, L.; Dyer, M.; Lafferentz, L.; Persson, M.; Peters, M. V; Hecht, S. Nano-architectures by covalent assembly of molecular building blocks. *Nature nanotechnology* **2007**, *2*, 687–91.

(14) Bieri, M.; Treier, M.; Cai, J.; Aït-Mansour, K.; Ruffieux, P.; Gröning, O.; Gröning, P.; Kastler, M.; Rieger, R.; Feng, X.; Müllen, K.; Fasel, R. Porous graphenes: two-dimensional polymer synthesis with atomic precision. *Chemical communications (Cambridge, England)* **2009**, 6919–21.

(15) Bieri, M.; Blankenburg, S.; Kivala, M.; Pignedoli, C. a; Ruffieux, P.; Müllen, K.; Fasel, R. Surface-supported 2D heterotriangulene polymers. *Chemical communications (Cambridge, England)* **2011**, *47*, 10239–41.

(16) Gutzler, R.; Walch, H.; Eder, G.; Kloft, S.; Heckl, W. M.; Lackinger, M. Surface mediated synthesis of 2D covalent organic frameworks: 1,3,5-tris(4-bromophenyl)benzene on graphite(001), Cu(111), and Ag(110). *Chemical communications* **2009**, 4456–8.

(17) Cai, J.; Ruffieux, P.; Jaafar, R.; Bieri, M.; Braun, T.; Blankenburg, S.; Muoth, M.; Seitsonen, A. P.; Saleh, M.; Feng, X.; Müllen, K.; Fasel, R. Atomically precise bottom-up fabrication of graphene nanoribbons. *Nature* **2010**, *466*, 470–3.

(18) Talirz, L.; Söde, H.; Cai, J.; Ruffieux, P.; Blankenburg, S.; Jafaar, R.; Berger, R.; Feng, X.; Müllen, K.; Passerone, D.; Fasel, R.; Pignedoli, C. a Termini of bottom-up fabricated graphene nanoribbons. *Journal of the American Chemical Society* **2013**, *135*, 2060–3.

(19) Blankenburg, S.; Cai, J.; Ruffieux, P.; Jaafar, R.; Passerone, D.; Feng, X.; Müllen, K.; Fasel, R.; Pignedoli, C. a Intraribbon heterojunction formation in ultranarrow graphene nanoribbons. *ACS nano* **2012**, *6*, 2020–5.

(20) Fuhrmann, T.; Kinne, M.; Tränkenschuh, B.; Papp, C.; Zhu, J. F.; Denecke, R.; Steinrück, H.-P. Activated adsorption of methane on Pt(111) —an in situ XPS study. *New Journal of Physics* **2005**, *7*, 107–107.

(21) Otero, G.; Biddau, G.; Sánchez-Sánchez, C.; Caillard, R.; López, M. F.; Rogero, C.; Palomares, F. J.; Cabello, N.; Basanta, M. a; Ortega, J.; Méndez, J.; Echavarren, A. M.; Pérez, R.; Gómez-Lor, B.; Martín-Gago, J. A. Fullerenes from aromatic precursors by surface-catalysed cyclodehydrogenation. *Nature* **2008**, *454*, 865–869.

(22) Rim, K. T.; Siaj, M.; Xiao, S.; Myers, M.; Carpentier, V. D.; Liu, L.; Su, C.; Steigerwald, M. L.; Hybertsen, M. S.; McBreen, P. H.; Flynn, G. W.; Nuckolls, C. Forming aromatic hemispheres on transition-metal surfaces. *Angewandte Chemie (Int. ed.)* **2007**, *46*, 7891–5.

(23) Treier, M.; Pignedoli, C. A.; Laino, T.; Rieger, R.; Müllen, K.; Passerone, D.; Fasel, R. Surface-assisted cyclodehydrogenation provides a synthetic route towards easily processable and chemically tailored nanographenes. *Nature chemistry* **2011**, *3*, 61–7.

(24) Amsharov, K.; Abdurakhmanova, N.; Stepanow, S.; Rauschenbach, S.; Jansen, M.; Kern, K. Towards the isomer-specific synthesis of higher fullerenes and buckybowls by the surface-catalyzed cyclodehydrogenation of aromatic precursors. *Angewandte Chemie (International ed. in English)* **2010**, *49*, 9392–6.

(25) Treier, M.; Richardson, N. V; Fasel, R. Fabrication of surface-supported low-dimensional polyimide networks. *Journal of the American Chemical Society* **2008**, *130*, 14054–5.

(26) Treier, M.; Fasel, R.; Champness, N. R.; Argent, S.; Richardson, N. V Molecular imaging of polyimide formation. *Physical chemistry chemical physics* **2009**, *11*, 1209–14.

(27) Weigelt, S.; Busse, C.; Bombis, C.; Knudsen, M. M.; Gothelf, K. V; Strunskus, T.; Wöll, C.; Dahlbom, M.; Hammer, B.; Laegsgaard, E.; Besenbacher, F.; Linderoth, T. R. Covalent interlinking of an aldehyde and an amine on a Au(111) surface in ultrahigh vacuum. *Angewandte Chemie (Int. ed.)* **2007**, *46*, 9227–30.

(28) Dinca, L. E.; Fu, C.; MacLeod, J. M.; Lipton-Duffin, J.; Brusso, J. L.; Szakacs, C. E.; Dongling, M.; Perepichka, D. F.; Rosei, F. Unprecedented Transformation of Tetrathienoanthracene into Pentacene. *ACS nano* **2013**.

(29) Schlickum, U.; Decker, R.; Klappenberger, F.; Zoppellaro, G.; Klyatskaya, S.; Auwa, W.; Neppl, S.; Kern, K.; Brune, H.; Ruben, M.; Barth, J. V Chiral Kagomé Lattice from Simple Ditopic Molecular Bricks. *Journal of the American Chemical Society* **2008**, *130*, 11778–11782.

(30) Böhringer, M.; Morgenstern, K.; Schneider, W.; Berndt, R.; Mauri, F.; De Vita, A.; Car, R. Two-Dimensional Self-Assembly of Supramolecular Clusters and Chains. *Physical Review Letters* **1999**, *1*, 324–327.

(31) Schlickum, U.; Decker, R.; Klappenberger, F.; Zoppellaro, G.; Klyatskaya, S.; Ruben, M.; Silanes, I.; Arnau, a; Kern, K.; Brune, H.; Barth, J. V Metal-organic honeycomb nanomeshes with tunable cavity size. *Nano letters* **2007**, *7*, 3813–7.

(32) Alvarez, L.; Peláez, S.; Caillard, R.; Serena, P. a; Martín-Gago, J. a; Méndez, J. Metal-organic extended 2D structures: Fe-PTCDA on Au(111). *Nanotechnology* **2010**, *21*, 305703.

(33) Heim, D.; Ecija, D.; Seufert, K.; Auwärter, W.; Aurisicchio, C.; Fabbro, C.; Bonifazi, D.; Barth, J. V Self-assembly of flexible one-dimensional coordination polymers on metal surfaces. *Journal of the American Chemical Society* **2010**, *132*, 6783–90.

(34) Walch, H.; Dienstmaier, J.; Eder, G.; Gutzler, R.; Schlögl, S.; Sirtl, T.; Das, K.; Schmittel, M.; Lackinger, M. Extended two-dimensional metal-organic frameworks based on thiolate-copper coordination bonds. *Journal of the American Chemical Society* **2011**, *133*, 7909–15.

(35) In't Veld, M.; Iavicoli, P.; Haq, S.; Amabilino, D. B.; Raval, R. Unique intermolecular reaction of simple porphyrins at a metal surface gives covalent nanostructures. *Chemical communications* **2008**, 1536–8.

(36) Matena, M.; Riehm, T.; Stöhr, M.; Jung, T. A.; Gade, L. H. Transforming surface coordination polymers into covalent surface polymers: linked polycondensed aromatics through oligomerization of N-heterocyclic carbene intermediates. *Angewandte Chemie (Int. ed.)* **2008**, *47*, 2414–7.

(37) Franc, G.; Gourdon, A. Covalent networks through on-surface chemistry in ultra-high vacuum: state-of-the-art and recent developments. *Physical chemistry chemical physics* **2011**, *13*, 14283–14292.

(38) Ourdjini, O.; Pawlak, R.; Abel, M.; Clair, S.; Chen, L.; Bergeon, N.; Sassi, M.; Oison, V.; Debierre, J.-M.; Coratger, R.; Porte, L. Substrate-mediated ordering and defect analysis of a surface covalent organic framework. *Physical Review B* **2011**, *84*, 1–9.

(39) Lipton-Duffin, J. A.; Miwa, J. A.; Kondratenko, M.; Cicoira, F.; Sumpter, B. G.; Meunier, V.; Perepichka, D. F.; Rosei, F. Step-by-step growth of epitaxially aligned polythiophene by surface-confined reaction. *Proceedings of the National Academy of Sciences* **2010**, *107*, 11200–11204.

(40) Jiang, L.; Sun, Y.; Chen, X. Chemical reaction on a solid surface with nanoconfined geometry. *Small* **2012**, *8*, 333–5.

(41) Lafferentz, L.; Eberhardt, V.; Dri, C.; Africh, C.; Comelli, G.; Esch, F.; Hecht, S.; Grill, L. Controlling on-surface polymerization by hierarchical and substrate-directed growth. *Nature chemistry* **2012**, *4*, 215–20.

(42) Usachov, D.; Vilkov, O.; Grüneis, A.; Haberer, D.; Fedorov, A.; Adamchuk, V. K.; Preobrajenski, A. B.; Dudin, P.; Barinov, A.; Oehzelt, M.; Laubschat, C.; Vyalikh, D. V Nitrogen-doped graphene: efficient growth, structure, and electronic properties. *Nano letters* **2011**, *11*, 5401–7.

(43) Imamura, G.; Saiki, K. Synthesis of Nitrogen-Doped Graphene on Pt(111) by Chemical Vapor Deposition. *J. Phys. Chem. C* **2011**, 6–11.

(44) Felici, R.; Pedio, M.; Borgatti, F.; Iannotta, S.; Capozi, M.; Ciullo, G.; Stierle, A. X-ray-diffraction characterization of Pt(111) surface nanopatterning induced by C60 adsorption. *Nature materials* **2005**, *4*, 688–92.

(45) Shi, X.-Q.; Van Hove, M.; Zhang, R.-Q. Adsorbate-induced reconstruction by C60 on close-packed metal surfaces: Mechanism for different types of reconstruction. *Physical Review B* **2012**, *85*, 1–7.

(46) Rosei, F.; Schunack, M.; Jiang, P.; Gourdon, A.; Laegsgaard, E.; Stensgaard, I.; Joachim, C.; Besenbacher, F. Organic molecules acting as templates on metal surfaces. *Science* **2002**, *296*, 328–31.

(47) ESISNA group, www.icmm.csic.es/esisna.

(48) Nanotec, www.nanotec.es.

(49) University of Virginia, www.virginia.edu.

(50) Jančařík, A.; Stará, I. G.; Starý, I. To be published.

(51) Gómez-Lor, B.; Echavarren, A. M. Synthesis of a triaza analogue of crushed-fullerene by intramolecular palladium-catalyzed arylation. *Organic letters* **2004**, *6*, 2993–6.

(52) Lüth, H. *Solid Surfaces, Interfaces and Thin Films*; Springer, 2001.

(53) Woodruff, D. P.; Delchar, T. A. *Modern Techniques of Surface Science*; Cambridge University Press, 1994.

(54) Vickerman, J. C. *Surface Analysis, the principal techniques*; Wiley, 1997.

(55) Lizzit, S.; Baraldi, A. High-resolution fast X-ray photoelectron spectroscopy study of ethylene interaction with Ir(111): From chemisorption to dissociation and graphene formation. *Catalysis Today* **2010**, *154*, 68–74.

(56) Hähner, G. Near edge X-ray absorption fine structure spectroscopy as a tool to probe electronic and structural properties of thin organic films and liquids. *Chemical Society reviews* **2006**, *35*, 1244–55.

(57) Stöhr, J. *NEXAFS spectroscopy*; Springer, 1996.

(58) Cossaro, A.; Puppin, M.; Cvetko, D.; Kladnik, G.; Verdini, A.; Coreno, M.; De Simone, M.; Floreano, L.; Morgante, A. Tailoring SAM-on-SAM Formation. *The Journal of Physical Chemistry Letters* **2011**, *2*, 3124–3129.

(59) Tkatchenko, A.; Scheffler, M. Accurate Molecular Van Der Waals Interactions from Ground-State Electron Density and Free-Atom Reference Data. *Physical Review Letters* **2009**, *102*, 6–9.

(60) Tkatchenko, A.; DiStasio, R.; Car, R.; Scheffler, M. Accurate and Efficient Method for Many-Body van der Waals Interactions. *Physical Review Letters* **2012**, *108*, 1–5.

(61) Kittelmann, M.; Rahe, P.; Nimmrich, M.; Hauke, C. M.; Ku, A. On-Surface Covalent Linking of Organic Building Blocks on a Bulk Insulator. *ACS Nano* **2011**, *5*, 8420–8425.

(62) Gourdon, A. On-surface covalent coupling in ultrahigh vacuum. *Angewandte Chemie (Int. ed.)* **2008**, *47*, 6950–3.

(63) Lackinger, M.; Heckl, W. M. A STM perspective on covalent intermolecular coupling reactions on surfaces. *Journal of Physics D: Applied Physics* **2011**, *44*, 1–14.

(64) Palma, C.-A.; Samorì, P. Blueprinting macromolecular electronics. *Nature chemistry* **2011**, *3*, 431–6.

(65) Zhong, D.; Franke, J.-H.; Podiyanachari, S. K.; Blömker, T.; Zhang, H.; Kehr, G.; Erker, G.; Fuchs, H.; Chi, L. Linear alkane polymerization on a gold surface. *Science* **2011**, *334*, 213–6.

(66) Violi, A. Cyclodehydrogenation reactions to cyclopentafused polycyclic aromatic hydrocarbons. *The journal of physical chemistry. A* **2005**, *109*, 7781–7.

(67) Otero, G.; Biddau, G.; Ozaki, T.; Gómez-Lor, B.; Méndez, J.; Pérez, R.; Martín-Gago, J. A. Spontaneous discrimination of polycyclic aromatic hydrocarbon (PAH) enantiomers on a metal surface. *Chemistry, A European Journal* **2010**, *16*, 13920–4.

(68) Weiss, K.; Beernink, G.; Dötz, F.; Birkner, A.; Müllen, K.; Wöll, C. Template-Mediated Synthesis of Polycyclic Aromatic Hydrocarbons: Cyclodehydrogenation and Planarization of a Hexaphenylbenzene Derivative at a Copper Surface. *Angewandte Chemie (Int. ed.)* **1999**, *38*, 3748–3752.

(69) Beernink, G.; Gunia, M.; Dötz, F.; Öström, H.; Weiss, K.; Müllen, K.; Wöll, C. Synthesis of Polycyclic Aromatic Hydrocarbons and Graphite Islands via Surface-Induced Reaction of Small Molecules. *ChemPhysChem* **2001**, *2*, 317–320.

(70) Martínez-Galera, A. J.; Brihuega, I.; Gómez-Rodríguez, J. M. Ethylene irradiation: a new route to grow graphene on low reactivity metals. *Nano letters* **2011**, *11*, 3576–80.

(71) Zhao, L.; He, R.; Rim, K. T.; Schiros, T.; Kim, K. S.; Zhou, H.; Gutierrez, C.; Chockalingam, S. P.; Arguello, C. J.; Palova, L.; Nordlund, D.; Hybertsen, M. S.; Reichman, D. R.; Heinz, T. F.; Kim, P.; Pinczuk, a.; Flynn, G. W.; Pasupathy, a. N. Visualizing Individual Nitrogen Dopants in Monolayer Graphene. *Science* **2011**, *333*, 999–1003.

(72) Ugeda, M.; Fernández-Torre, D.; Brihuega, I.; Pou, P.; Martínez-Galera, a.; Pérez, R.; Gómez-Rodríguez, J. Point Defects on Graphene on Metals. *Physical Review Letters* **2011**, *107*, 1–5.

(73) Merino, P.; Svec, M.; Pinardi, A. L.; Otero, G. Strain-Driven Moire Superstructures of Epitaxial Graphene on Transition Metal Surfaces. *ACS Nano* **2011**, *5*, 5627–5634.

(74) Vázquez de Parga, a.; Calleja, F.; Borca, B.; Passeggi, M.; Hinarejos, J.; Guinea, F.; Miranda, R. Periodically Rippled Graphene: Growth and Spatially Resolved Electronic Structure. *Physical Review Letters* **2008**, *100*, 1–4.

(75) Levy, N.; Burke, S. a.; Meaker, K. L.; Panlasigui, M.; Zettl, a.; Guinea, F.; Neto, a. H. C.; Crommie, M. F. Strain-Induced Pseudo-Magnetic Fields Greater Than 300 Tesla in Graphene Nanobubbles. *Science* **2010**, *329*, 544–547.

(76) Fedorov, A. V.; Varykhalov, A. Y.; Dobrotvorskii, A. M.; Chikina, A. G.; Adamchuk, V. K.; Usachov, D. Y. Structure of graphene on the Ni(110) surface. *Physics of the Solid State* **2011**, *53*, 1952–1956.

(77) Hellgren, N.; Guo, J.; Luo, Y.; Såthe, C.; Agui, A.; Kashtanov, S.; Nordgren, J.; Ågren, H.; Sundgren, J.-E. Electronic structure of carbon nitride thin films studied by X-ray spectroscopy techniques. *Thin Solid Films* **2005**, *471*, 19–34.

(78) Bavdek, G.; Cossaro, A.; Cvetko, D.; Africh, C.; Blasetti, C.; Esch, F.; Morgante, A.; Floreano, L. Pentacene nanorails on Au(110). *Langmuir : the ACS journal of surfaces and colloids* **2008**, *24*, 767–72.

(79) Kikuma, J.; Yoneyama, K.; Nomura, M.; Konishi, T.; Hashimoto, T.; Mitsumoto, R.; Ohuchi, Y.; Seki, K. Surface analysis of CVD carbon using NEXAFS, XPS and TEM. *Journal of Electron Spectroscopy and Related Phenomena* **1998**, *88-91*, 919–925.

(80) Preobrajenski, A. B.; Ng, M. L.; Vinogradov, A. S.; Mårtensson, N. Controlling graphene corrugation on lattice-mismatched substrates. *Physical Review B* **2008**, *78*, 2–5.

(81) Ng, M. L.; Balog, R.; Hornekær, L.; Preobrajenski, A. B.; Vinogradov, N. A.; Mårtensson, N.; Schulte, K. Controlling Hydrogenation of Graphene on Transition Metals. *The Journal of Physical Chemistry C* **2010**, *114*, 18559–18565.

(82) Nikitin, A.; Näslund, L. A.; Zhang, Z.; Nilsson, A. C-H bond formation at the graphite surface studied with core level spectroscopy. *Surface Science* **2008**, *602*, 2575–2580.

(83) Oji, H.; Mitsumoto, R.; Ito, E.; Ishii, H.; Ouchi, Y.; Seki, K.; Yokoyama, T.; Ohta, T.; Kosugi, N. Core hole effect in NEXAFS spectroscopy of polycyclic aromatic hydrocarbons: Benzene, chrysene, perylene, and coronene. *The Journal of Chemical Physics* **1998**, *109*, 10409–10418.

(84) Zhang, W.; Nefedov, A.; Naboka, M.; Cao, L.; Wöll, C. Molecular orientation of terephthalic acid assembly on epitaxial graphene: NEXAFS and XPS study. *Physical chemistry chemical physics* **2012**, *14*, 10125–31.

(85) Weiss, K.; Gebert, S.; Wühn, M.; Wadepohl, H.; Wöll, C. Near edge x-ray absorption fine structure study of benzene adsorbed on metal surfaces: Comparison to benzene cluster complexes. *Journal of Vacuum Science & Technology A: Vacuum, Surfaces, and Films* **1998**, *16*, 1017–1022.

(86) Lee, V.; Park, C.; Jaye, C.; Fischer, D. a.; Yu, Q.; Wu, W.; Liu, Z.; Bao, J.; Pei, S.-S.; Smith, C.; Lysaght, P.; Banerjee, S. Substrate Hybridization and Rippling of Graphene Evidenced by Near-Edge X-ray Absorption Fine Structure Spectroscopy. *The Journal of Physical Chemistry Letters* **2010**, *1*, 1247–1253.

(87) Schultz, B. J.; Patridge, C. J.; Lee, V.; Jaye, C.; Lysaght, P. S.; Smith, C.; Barnett, J.; Fischer, D. a; Prendergast, D.; Banerjee, S. Imaging local electronic corrugations and doped regions in graphene. *Nature communications* **2011**, *2*, 372.

(88) Urquhart, S. G.; Gillies, R. Rydberg-valence mixing in the carbon 1s near-edge X-ray absorption fine structure spectra of gaseous alkanes. *The journal of physical chemistry. A* **2005**, *109*, 2151–9.

(89) Dedkov, Y. S.; Sicot, M.; Fonin, M. X-ray absorption and magnetic circular dichroism of graphene/Ni(111). *Journal of Applied Physics* **2010**, *107*, 09E121.

(90) Schmidt, N.; Fink, R.; Hieringer, W. Assignment of near-edge x-ray absorption fine structure spectra of metalloporphyrins by means of time-dependent density-functional calculations. *The Journal of chemical physics* **2010**, *133*, 054703.

(91) El-Sayed, A.; Mowbray, D. J.; García-Lastra, J. M.; Rogero, C.; Goiri, E.; Borghetti, P.; Turak, A.; Doyle, B. P.; Dell'Angela, M.; Floreano, L.; Wakayama, Y.; Rubio, A.; Ortega, J. E.; De Oteyza, D. G. Supramolecular Environment-Dependent Electronic Properties of Metal–Organic Interfaces. *The Journal of Physical Chemistry C* **2012**, *116*, 4780–4785.

(92) Baldacchini, C.; Allegretti, F.; Gunnella, R.; Betti, M. G. Molecule–metal interaction of pentacene on copper vicinal surfaces. *Surface Science* **2007**, *601*, 2603–2606.

(93) Lipton-Duffin, J.; Miwa, J. A.; Urquhart, S. G.; Contini, G.; Cossaro, A.; Casalis, L.; Barth, J. V; Floreano, L.; Morgante, A.; Rosei, F. Binding geometry of hydrogen-bonded chain motif in self-assembled gratings and layers on Ag(111). *Langmuir* **2012**, *28*, 14291–300.

(94) Gustafsson, J.; Zhang, H.; Moons, E.; Johansson, L. Electron spectroscopy studies of PTCDA on Ag/Si(111)-3×3. *Physical Review B* **2007**, *75*, 155413–155419.

(95) Castellarin-Cudia, C.; Borghetti, P.; Di Santo, G.; Fanetti, M.; Larciprete, R.; Cepek, C.; Vilmercati, P.; Sangaletti, L.; Verdini, A.; Cossaro, A.; Floreano, L.; Morgante, A.; Goldoni, A. Substrate influence for the Zn-tetraphenyl-porphyrin adsorption geometry and the interface-induced electron transfer. *ChemPhysChem* **2010**, *11*, 2248–55.

(96) Lv, R.; Li, Q.; Botello-Méndez, A. R.; Hayashi, T.; Wang, B.; Berkdemir, A.; Hao, Q.; Elías, A. L.; Cruz-Silva, R.; Gutiérrez, H. R.; Kim, Y. A.; Muramatsu, H.; Zhu, J.; Endo, M.; Terrones, H.; Charlier, J.-C.; Pan, M.; Terrones, M. Nitrogen-doped graphene: beyond single substitution and enhanced molecular sensing. *Scientific reports* **2012**, *2*, 1–8.

(97) Serkovic Loli, L. N.; Hamoudi, H.; Gayone, J. E.; Martiarena, M. L.; Sánchez, E. A.; Grizzi, O.; Pasquali, L.; Nannarone, S.; Doyle, B. P.; Esaulov, V. A. Growth of N,N'-Bis(1-ethylpropyl)perylene-3,4,9,10-tetracarboxdiimide Films on Ag(111). *J. Phys. Chem. C* **2009**, 17866–17875.

(98) Zahn, D. R. T.; Gavrila, G. N.; Salvan, G. Electronic and vibrational spectroscopies applied to organic/inorganic interfaces. *Chemical reviews* **2007**, *107*, 1161–232.

(99) Evangelista, F.; Ruocco, A.; Gotter, R.; Cossaro, A.; Floreano, L.; Morgante, A.; Crispoldi, F.; Betti, M. G.; Mariani, C. Electronic states of CuPc chains on the Au(110) surface. *The Journal of chemical physics* **2009**, *131*, 174710.

(100) Lacovig, P.; Pozzo, M.; Alfè, D.; Vilmercati, P.; Baraldi, A.; Lizzit, S. Growth of Dome-Shaped Carbon Nanoislands on Ir(111): The Intermediate between Carbidic Clusters and Quasi-Free-Standing Graphene. *Physical Review Letters* **2009**, *103*, 14–17.

(101) Grüneis, A.; Kummer, K.; Vyalikh, D. V Dynamics of graphene growth on a metal surface: a time-dependent photoemission study. *New Journal of Physics* **2009**, *11*, 073050.

(102) Klappenberger, F.; Weber-Bargioni, a; Auwärter, W.; Marschall, M.; Schiffrin, a; Barth, J. V Temperature dependence of conformation, chemical state, and metal-directed assembly of tetrapyridyl-porphyrin on Cu(111). *The Journal of chemical physics* **2008**, *129*, 214702.

(103) Kondo, T.; Casolo, S.; Suzuki, T.; Shikano, T.; Sakurai, M.; Harada, Y.; Saito, M.; Oshima, M.; Trioni, M.; Tantardini, G.; Nakamura, J. Atomic-scale characterization of nitrogen-doped graphite: Effects of dopant nitrogen on the local electronic structure of the surrounding carbon atoms. *Physical Review B* **2012**, *86*, 035436.

(104) Kang, X.; Song, Y.; Chen, S. Nitrene-functionalized ruthenium nanoparticles. *Journal of Materials Chemistry* **2012**, *22*, 19250.

(105) Soto, G. Synthesis of PtNx films by reactive laser ablation. *Materials Letters* **2004**, *58*, 2178–2180.

(106) Otero, G.; González, C.; Pinardi, A.; Merino, P.; Gardonio, S.; Lizzit, S.; Blanco-Rey, M.; Van de Ruit, K.; Flipse, C.; Méndez, J.; De Andrés, P.; Martín-Gago, J. Ordered Vacancy Network Induced by the Growth of Epitaxial Graphene on Pt(111). *Physical Review Letters* **2010**, *105*, 1–4.

(107) Xu, G.; Shi, X.-Q.; Zhang, R.; Pai, W.; Jeng, H.; Van Hove, M. Detailed low-energy electron diffraction analysis of the (4×4) surface structure of C60 on Cu(111): Seven-atom-vacancy reconstruction. *Physical Review B* **2012**, *86*, 1–7.

(108) Li, H.; Pussi, K.; Hanna, K.; Wang, L.-L.; Johnson, D.; Cheng, H.-P.; Shin, H.; Curtarolo, S.; Moritz, W.; Smerdon, J.; McGrath, R.; Diehl, R. Surface Geometry of C60 on Ag(111). *Physical Review Letters* **2009**, *103*, 1–4.

(109) Yamada, T.; Shibuta, M.; Ami, Y.; Takano, Y.; Nonaka, A.; Miyakubo, K.; Munakata, T. Novel Growth of Naphthalene Overlayer on Cu(111) Studied by STM, LEED, and 2PPE. *J. Phys. Chem. C* **2010**, 13334–13339.

(110) Han, P.; Weiss, P. S. Electronic substrate-mediated interactions. *Surface Science Reports* **2012**, *67*, 19–81.

(111) Chen, X.; Liu, S.; Liu, L.; Liu, X.; Liu, X.; Wang, L. Growth of triangle-shape graphene on Cu(111) surface. *Applied Physics Letters* **2012**, *100*, 163106.

(112) Zhao, L.; Rim, K. T.; Zhou, H.; He, R.; Heinz, T. F.; Pinczuk, a.; Flynn, G. W.; Pasupathy, a. N. Influence of copper crystal surface on the CVD growth of large area monolayer graphene. *Solid State Communications* **2011**, *151*, 509–513.

(113) Bader, M.; Haase, J.; Ocal, C.; Puschmann, A. Near-Edge X-ray Absorption Fine-Structure studies of ring molecules adsorbed on single crystal surfaces. *Journal de Physique* **1986**, *47*.

(114) Bader, M.; Haase, J.; Puschmann, A.; Otto, A. Orientational Phase Transition in the System Pyridine/Ag(111): A Near-Edge X-ray-Absorption Fine-Structure Study. *Physical Review Letters* **1986**, 20–23.

(115) Polzonetti, G.; Carravetta, V.; Iucci, G.; Ferri, a.; Paolucci, G.; Goldoni, a.; Parent, P.; Laffon, C.; Russo, M. V. Electronic structure of platinum complex/Zn-porphyrinato assembled macrosystems, related precursors and model molecules, as probed by X-ray absorption spectroscopy (NEXAFS): theory and experiment. *Chemical Physics* **2004**, *296*, 87–100.

(116) Diller, K.; Klappenberger, F.; Marschall, M.; Hermann, K.; Nefedov, a; Wöll, C.; Barth, J. V Self-metalation of 2H-tetraphenylporphyrin on Cu(111): an x-ray spectroscopy study. *The Journal of chemical physics* **2012**, *136*, 014705.

(117) Shi, X.-Q.; Van Hove, M. A.; Zhang, R.-Q. Survey of structural and electronic properties of C60 on close-packed metal surfaces. *Journal of Materials Science* **2012**, *47*, 7341–7355.

(118) Lizzit, S.; Zampieri, G.; Petaccia, L.; Larciprete, R.; Lacovig, P.; Rienks, E. D. L.; Bihlmayer, G.; Baraldi, A.; Hofmann, P. Band dispersion in the deep 1s core level of graphene. *Nature Physics* **2010**.

(119) Riggs, C. D.; W.M., W.; Davis, L. E.; Moulder, J. F.; Muilenberg, G. E. *Handbook of X-ray Photoelectron Spectroscopy*; Perkin-Elmert Corporation, 1979.

(120) Otero-Irurueta, G. G. Ciclodeshidrogenación catalizada por superficies: Fullerenos a partir de precursores aromáticos, Universidad Autónoma de Madrid, 2010.

(121) Gómez-Lor, B.; De Frutos, Ó.; Echavarren, A. M. Synthesis of " crushed fullerene " C60H30. *ChemComm* **1999**, 2431–2432.

(122) Liu, C.; Qin, Z.; Chen, J.; Guo, Q.; Yu, Y.; Cao, G. Molecular orientations and interfacial structure of C60 on Pt(111). *The Journal of chemical physics* **2011**, *134*, 044707.

(123) Huang, M. First-principles study on the reconstruction induced by the adsorption of C60 on Pt(111). *Physical chemistry chemical physics* **2012**, *14*, 4959–63.

(124) Shi, X.; Pang, A.; Man, K.; Zhang, R.; Minot, C.; Altman, M.; Van Hove, M. C60 on the Pt(111) surface: Structural tuning of electronic properties. *Physical Review B* **2011**, *84*, 1–6.

(125) Nilsson, A.; Tillborg, H.; Bennich, P.; Sandell, A.; Hernnäs, B.; Puglia, C.; Martensson, N. Overlayer structure from adsorbate and substrate core level binding energy shifts : CO, CCH, and 0 on Pt (111). *Surface Science* **1994**, *315*, 983–989.

(126) Baetzold, R. C.; Apai, G.; Shustorovich, E.; Jaeger, R. Surface core-level shifts for Pt single-crystal surfaces. *Physical Review B* **1982**, *26*, 4022–4027.

(127) Di Santo, G.; Sfiligoj, C.; Castellarin-Cudia, C.; Verdini, A.; Cossaro, A.; Morgante, A.; Floreano, L.; Goldoni, A. Changes of the molecule-substrate interaction upon metal inclusion into a porphyrin. *Chemistry (Weinheim an der Bergstrasse, Germany)* **2012**, *18*, 12619–23.

(128) Pels, J. R.; Kapteijn, F.; Moulijn, J. A.; Zhu, Q.; Thomas, M. Evolution of Nitrogen Functionalities in Carbonaceous Materials During Pyrolisis. *Carbon* **1995**, *33*, 1641–1653.

(129) Gammon, W. J.; Kraft, O.; Reilly, A. C.; Holloway, B. C. E xperimental comparison of N(1s) X-ray photoelectron spectroscopy binding energies of hard and elastic amorphous carbon nitride films with reference organic compounds. *Carbon* **2003**, *41*, 1917–1923.

(130) Wei, D.; Liu, Y.; Wang, Y.; Zhang, H.; Huang, L.; Yu, G. Synthesis of N-doped graphene by chemical vapor deposition and its electrical properties. *Nano letters* **2009**, *9*, 1752–8.

(131) Pai, W. W.; Jeng, H. T.; Cheng, C.-M.; Lin, C.-H.; Xiao, X.; Zhao, A.; Zhang, X.; Xu, G.; Shi, X. Q.; Van Hove, M. a.; Hsue, C.-S.; Tsuei, K.-D. Optimal Electron Doping of a C60 Monolayer on Cu(111) via Interface Reconstruction. *Physical Review Letters* **2010**, *104*, 1–4.

(132) Chan, S.-H.; Lai, C.-S.; Chen, H.-L.; Ting, C.; Chen, C.-P. Highly Efficient P3HT: C60 Solar Cell Free of Annealing Process. *Macromolecules* **2011**, *44*, 8886–8891.

(133) Bakry, R.; Vallant, R. M.; Najam-ul-Haq, M.; Rainer, M.; Szabo, Z.; Huck, C. W.; Bonn, G. K. Medicinal applications of fullerenes. *International journal of nanomedicine* **2007**, *2*, 639–49.

(134) Lu, X.; Grobis, M.; Khoo, K.; Louie, S.; Crommie, M. Spatially Mapping the Spectral Density of a Single C60 Molecule. *Physical Review Letters* **2003**, *90*, 7–10.

(135) Schull, G.; Berndt, R. Orientationally Ordered (7×7) Superstructure of C60 on Au(111). *Physical Review Letters* **2007**, *99*, 1–4.

(136) Schull, G.; Frederiksen, T.; Brandbyge, M.; Berndt, R. Passing Current through Touching Molecules. *Physical Review Letters* **2009**, *103*, 11–14.

(137) Schull, G.; Frederiksen, T.; Arnau, A.; Sánchez-Portal, D.; Berndt, R. Atomic-scale engineering of electrodes for single-molecule contacts. *Nature nanotechnology* **2011**, *6*, 23–7.

(138) Moriarty, P. J. Fullerene adsorption on semiconductor surfaces. *Surface Science Reports* **2010**, *65*, 175–227.

(139) Stengel, M.; Vita, a.; Baldereschi, a. Adatom-Vacancy Mechanisms for the C60/Al(111)-(6×6) Reconstruction. *Physical Review Letters* **2003**, *91*, 2–5.

(140) Gardener, J. A.; Briggs, G. A. D.; Castell, M. R. Scanning tunneling microscopy studies of c60 monolayers on Au(111). *Physical Review B* **2009**, *80*, 1–9.

(141) Pai, W.; Hsu, C.-L.; Lin, M.; Lin, K.; Tang, T. Structural relaxation of adlayers in the presence of adsorbate-induced reconstruction: C60/Cu(111). *Physical Review B* **2004**, *69*, 1–7.

(142) Hinterstein, M.; Torrelles, X.; Felici, R.; Rius, J.; Huang, M.; Fabris, S.; Fuess, H.; Pedio, M. Looking underneath fullerenes on Au(110): Formation of dimples in the substrate. *Physical Review B* **2008**, *77*, 1–4.

(143) Pussi, K.; Li, H.; Shin, H.; Serkovic Loli, L.; Shukla, A.; Ledieu, J.; Fournée, V.; Wang, L.; Su, S.; Marino, K.; Snyder, M.; Diehl, R. Elucidating the dynamical equilibrium of C60 molecules on Ag(111). *Physical Review B* **2012**, *86*, 205406.

(144) Torrelles, X.; Langlais, V.; De Santis, M.; Tolentino, H. C. N.; Gauthier, Y. Nanostructuring surfaces: Deconstruction of the Pt(110)-(1×2) surface by C60. *Physical Review B* **2010**, *81*, 1–4.

(145) Lu, X.; Grobis, M.; Khoo, K.; Louie, S.; Crommie, M. Charge transfer and screening in individual C60 molecules on metal substrates: A scanning tunneling spectroscopy and theoretical study. *Physical Review B* **2004**, *70*, 1–8.

(146) Wang, P.; Zhang, H.-J.; Li, Y.-J.; Sheng, C.-Q.; Shen, Y.; Li, H.-Y.; Bao, S.-N.; Li, H.-N. Effect of charge transfer on the geometric structure of a C70 monolayer on the surface of Ag(111). *Physical Review B* **2012**, *85*, 205445.

(147) Daughton, D. R.; Gupta, J. a. Orientation dependence of charge transfer for C60 on Cu(100). *Applied Physics Letters* **2011**, *98*, 133303.

(148) Tzeng, C.; Lo, W.; Yuh, J.; Chu, R.; Tsuei, K. Photoemission, near edge x-ray absorption spectroscopy and low energy electron diffraction study of C60 on Au(111) surfaces. *Physical Review B* **2000**, *61*, 2263–2272.

(149) Tsuei, K.-D.; Yuh, J.-Y.; Tzeng, C.-T.; Chu, R.-Y.; Chung, S.-C.; Tsang, K.-L. Photoemission and photoabsorption study of C60 adsorption on Cu(111) surfaces. *Physical Review B* **1997**, *56*, 15412–15420.

(150) Swami, N.; He, H.; Koel, B. Polymerization and decomposition of C60 on Pt(111) surfaces. *Physical Review B* **1999**, *59*, 8283–8291.

(151) Franke, K. J.; Pascual, J. I. Effects of electron-vibration coupling in transport through single molecules. *Journal of physics. Condensed matter : an Institute of Physics journal* **2012**, *24*, 394002.

(152) Pedio, M.; Hevesi, K.; Zema, N.; Capozi, M.; Perfetti, P.; Gouttebaron, R.; Pireaux, J. J.; Cadauno, R.; Rudolf, P. C60/metal surfaces: adsorption and decomposition. *Surface Science* **1999**, *437*, 249–260.

(153) Larsson, J.; Elliott, S.; Greer, J.; Repp, J.; Meyer, G.; Allenspach, R. Orientation of individual C60 molecules adsorbed on Cu(111): Low-temperature scanning tunneling microscopy and density functional calculations. *Physical Review B* **2008**, *77*, 1–9.

(154) Zhang, X.; He, W.; Zhao, A.; Li, H.; Chen, L.; Pai, W.; Hou, J.; Loy, M.; Yang, J.; Xiao, X. Geometric and electronic structure of a C60 monolayer on Ag(100). *Physical Review B* **2007**, *75*, 1–8.

(155) Magnano, E.; Vandré, S.; Cepek, C.; Goldoni, A.; Laine, A.; Curró, G.; Santaniello, A.; Sancrotti, M. Substrate-adlayer interaction at the C60/Ag(110) interface studied by high-resolution synchrotron radiation. *Surface Science* **1997**, *379*, 1066–1070.

(156) Hsu, C.-L.; Pai, W. Aperiodic incommensurate phase of a C60 monolayer on Ag(100). *Physical Review B* **2003**, *68*, 1–12.

(157) Schull, G.; Néel, N.; Becker, M.; Kröger, J.; Berndt, R. Spatially resolved conductance of oriented C60. *New Journal of Physics* **2008**, *10*, 065012.

(158) Pai, W.; Hsu, C.-L. Ordering of an incommensurate molecular layer with adsorbate-induced reconstruction: C60/Ag(100). *Physical Review B* **2003**, *68*, 1–4.

(159) Tang, L.; Guo, Q. Orientational ordering of the second layer of C(60) molecules on Au(111). *Physical chemistry chemical physics* **2012**, *14*, 3323–8.

(160) Tang, L.; Xie, Y.; Guo, Q. Complex orientational ordering of C(60) molecules on Au(111). *The Journal of chemical physics* **2011**, *135*, 114702.

(161) Yamada, Y.; Yamada, S.; Nakayama, T.; Sasaki, M.; Tsuru, T. Electronic Modification of C60 Monolayers via Metal Substrates. *Japanese Journal of Applied Physics* **2011**, *50*, 08LB06.

(162) Pai, W.; Hsu, C.; Chiang, C.; Chang, Y.; Lin, K. Origin of peculiar STM molecular contrast in C60/Ag(100). *Surface Science* **2002**, *519*, L605–L610.

(163) Grobis, M.; Lu, X.; Crommie, M. Local electronic properties of a molecular monolayer: C60 on Ag(001). *Physical Review B* **2002**, *66*, 5–8.

(164) Cepek, C.; Goldoni, A.; Modesti, S. Chemisorption and fragmentation of C60 on Pt(111) and Ni(110). *Physical review. B* **1996**, *53*, 7466–7472.

(165) Giovanelli, L.; Cepek, C.; Floreano, L.; Magnano, E.; Sancrotti, M.; Gotter, R.; Morgante, A.; Verdini, A.; Pesci, A.; Ferrari, L.; Pedio, M. Molecular orientation of C60 on Pt(111) determined by X-ray photoelectron diffraction. *Applied Surface Science* **2003**, *212-213*, 57–61.

(166) Sogo, M.; Sakamoto, Y.; Aoki, M.; Masuda, S.; Yanagisawa, S.; Morikawa, Y. C60 Adsorbed on Platinum Surface: A Good Mediator of Metal Wave Function. *The Journal of Physical Chemistry C* **2010**, *114*, 3504–3506.

(167) Horcas, I.; Fernández, R.; Gómez-Rodríguez, J. M.; Colchero, J.; Gómez-Herrero, J.; Baro, a M. WSXM: a software for scanning probe microscopy and a tool for nanotechnology. *The Review of scientific instruments* **2007**, *78*, 013705.

(168) Goldoni, A.; Cepek, C.; Larciprete, R.; Sangaletti, L.; Pagliara, S.; Floreano, L.; Gotter, R.; Verdini, A.; Morgante, A.; Luo, Y.; Nyberg, M. C70 adsorbed on Cu(111): Metallic character and molecular orientation. *The Journal of Chemical Physics* **2002**, *116*, 7685.

(169) Rowe, J. E.; Rudolf, P.; Tjeng, L. H.; Malic, R. A.; Meigs, G.; T, C. C.; J, C.; W, P. E. Synchrotron Radiation and Low Energy Electron Diffraction Studies of Ultrathin C60 Films Deposited on Cu(100), Cu(111) and Cu(110). *International journal of modern physics B* **1992**, *6*, 3909–3913.

(170) Maxwell, A. J.; Brühwiler, P. A.; Nilsson, A.; Martensson, N.; Rudolf, P. Photoemission, autoionization, and x-ray absorption spectroscopy of ultrathin-film C60 on Au(110). *Physical Review B* **1994**, *49*, 10717–10727.

(171) Sanchez Sanchez, C. Structure and Electronic Properties of Different Adsorbates on the rutile TiO2(110) surfaces, 2011, Vol. 2.

(172) Lin, T. H.; Huang, T. P.; Liu, Y. L.; Yeh, C. C.; Lai, Y. H.; Hung, W. H. Adsorption and reaction of methanethiol on Pt(111). *Surface Science* **2005**, *578*, 27–34.

(173) Biddau, G. From Hydrocarbons to Carbon Nanostructures: a Theoretical Analysis of Surface-Catalysed Cyclodehydrogenation, 2011.

(174) He, H.; Swami, N.; Koel, B. E. Control of the growth of ordered C60 films by chemical modification of Pt(111) surfaces. *Thin Solid Films* **1999**, *348*, 30–37.

(175) Christmann, K.; Ertl, G.; Pignet, T. Adsorption of Hydrogen on a Pt(111) surface. *Surface Science* **1976**, *54*, 365–392.